Journal of the CERAMIC SOCIETY of Japan, International Edition 第99集 第1151号 平成3年6月25日発行(毎月1回25日発行) ISSN 0912-9200

Journal of the CERAMIC SOCIETY of Japan, International Edition

Vol.99 June 1991

■ 19 Papers from Nippon Seramikkusu Kyokai Gakujutsu Ronbunshi, Vol. 99 No.6 1991

NIPPON SERAMIKKUSU KYOKAI GAKUJUTSU RONBUNSHI Vol. 99 1991

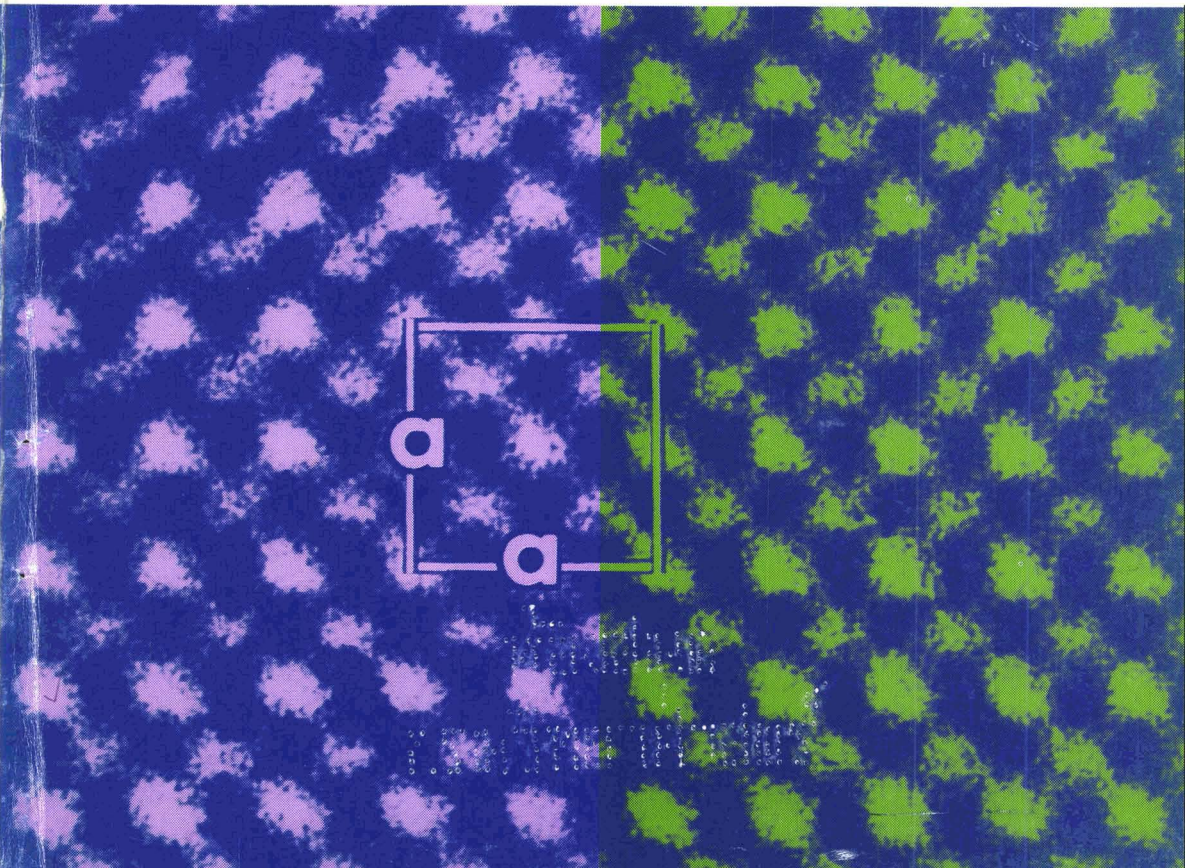

Journal of Ceramic Society of Japan, *International Edition*

Vol.99 No.6
June 1991

Published Monthly by
FUJI TECHNOLOGY PRESS LTD.
7F Daini Bunsei Bldg.
11-7, Toranomon 1-chome
Minato-ku, Tokyo 105, Japan
Tel:81-3-3508-0051
Fax:81-3-3592-0648

One year subscription
Air Mail ¥200,000

CONTENTS

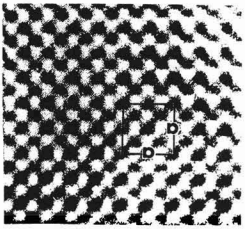

Cover:

This picture shows a high-resolution structure image of zirconia (ZRO_2) projected along the a-axis of a cubic lattice (a=5.1). As indicated by arrowheads in the micrograph, both zirconium (Zr) and oxygen (O) atom positions appear as strong and weak dark dots, respectively. This is the first electron microscope data in which individual oxygen positions in inorganic compounds can be directly observed as weak dark dots.

The microgram was obtained by the ultra-high-resolution, high-voltage electron microscope (Model: H-1500) developed in 1990 as NIRIM's second high-voltage electron microscope. The device has the world's highest resolution of 1.0Å, which was achieved by employing operating and applicable voltages of 1300kV and 1500kV, respectively. A very low spherical aberration coefficient for the objective (C_S=1.85mm at 1300kV) was realized by computer-aided design of the electron-magnetic lens system. This new apparatus permits the imaging of not only metal atoms but also light atoms (such as oxygen) in many inorganic materials by means of high-resolution electron microscopy.

Papers, Letters and Notes

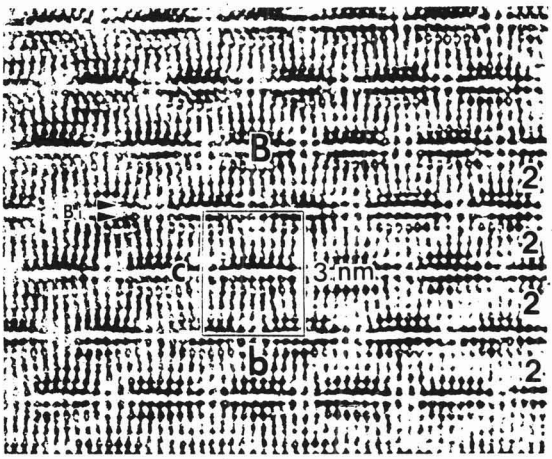

High resolution electron microscope photograph of the modulation doped structure of $Bi_2Sr_2CaCu_2O_y$ (T_c=80K) in the [100] direction. Figures at right side indicate number of copper layers, symbol B indicates bismuth rich region.

Crystal Chemistry of Copper-Based Oxide Superconductors and Related Compounds
-An Approach to Material Design-

Takahiro Wada, Ataru Ichinose, Hisao Yamauchi and Shoji Tanaka

Superconductivity Research Laboratory, International Superconductivity Technology Center
10-13 Shinonome 1-Chome, Koto-ku, Tokyo, 135 Japan

The crystal structure of copper oxide superconductors and their related compounds is described in terms of three basic structural blocks. The main block is the perovskite ($ACuO_{3-z}$), and the others are the rock salt block (AO) and the fluorite block (AO_2). The perovskite block has for types, full perovskite structure ($ACuO_3$) and three types of oxygen deficient perovskite structure of $ACuO_{2.5}$, $ACuO_2$ and $ACuO_{1+z}$. $Ba_2YCu_3O_{6+Z}$ consists of two types of perovskite blocks and the series of superconducting compounds such as $La_2Ca_{n-1}Cu_nO_{2n+2}$ and $M_mA_2Ca_{n-1}Cu_nO_{2n+m+2}$ (M=T1 or Bi and A=Ba or Sr) consist of perovskite blocks and rock salt blocks. The copper oxide series such as (Pb, Cu)$A_2(R,Ce)_nCu_2O_{2n+5}$ and $A_2(R,Ce)_nCu_3O_{2n+4+z}$ (R: rare earth element, A=Ba or Sr) consist of perovskite blocks, rock salt blocks and fluorite blocks.

The electroneutrality condition in the crystal was taken into account. The characteristic charge for each structural block was calculated using an ionic model. In La_2CuO_4, the perovskite block $[La^{3+}Cu^{2+}(O^{2-})_3]$ has a negative charge and the rock salt block $[La^{3+}O^{2-}]$ a positive charge. Therefore, the negative perovskite block is considered to be a hole acceptor. On the other hand, in Nd_2CuO_4, the oxygen deficient perovskite block $[Nd^{3+}Cu^{2+}(O^{2-})_2]$ is positively charged and the fluorite block $[Nd^{3+}(O^{2-})_2]$ is negatively charged. Consequently, the perovskite block readily accepts an electron. The rock salt block usually has a positive charge and works as a hole donor for the CuO_2 planes in the perovskite block. The fluorite block has usually a negative charge and so works as a hole acceptor.

A variety of new layered copper oxides which may turn into new high-T_c superconductors can be designed by employing the basic principles of the present block model and taking into account the lattice constant matching and the electroneutrality condition between the blocks. Thus the block model provides a guiding principle for the preparation of new layered copper compounds.

[Received December 20, 1990; Accepted February 20, 1991]

Key-words: Oxide superconductor, Crystal chemistry, Material Design, Copper oxide, Crystal structure, Perovskite structure, Rock salt structure, Fluorite structure

1. Introduction

Since the discovery of superconductivity in $(La,Ba)_2CuO_4$,[1,2] a number of copper-based oxide superconductors and their related compounds have been discovered.[3,4] New types of copper oxide superconductors and their related compounds have been constantly discovered in recent years.[5-15] Meanwhile, various methods of classification and compilation for these copper oxide superconductors and their related compounds have been proposed from the viewpoint of crystal structure.[10,16-18]

Our proposal in this paper concerns the improvement and further development of a conventional method for the classification and compilation of copper oxide superconductors and their related compounds, based on the latest data and knowledge on crystal chemistry. We believe the method here proposed should provide a guiding principle for exploring novel copper oxide superconductors.

2. Basic Structural Blocks Which Compose Copper Oxide Superconductors and Related Compounds

Copper oxide superconductors and their related compounds can be composed of three types of basic structural blocks, i.e. perovskite block ($ACuO_{3-\delta}$), rock salt block (AO) and fluorite block (AO_2). Here, A indicates an alkali earth ion or a rare earth ion, which has a larger ionic radius than Cu^{2+} ion.

2.1. Perovskite Block

Figure 1 shows four types of the perovskite block which appear in copper oxide superconductors. Figure 1(a) shows a normal perovskite block without oxygen deficiency ($ACuO_3$). A typical copper oxide superconductor which contains a block of this type as a unit cell is $LaCuO_3$, which can be synthesized under a high oxygen partial pressure.[19] We indicate this type perovskite block by a symbol of $^{+}P^{+}$ in our rule. Here, the plus sign (+) as a superscript of P means that oxygen exists in the same plane to the A ion. Among the two signs to the right and left of P, the left indicates whether oxygen is deficient or not in the upper A ion plane, and the right does the same in the lower A ion plane. The symbol $^{+}P^{+}$ here accordingly indicates that oxygen exists in both upper and lower A ion planes.

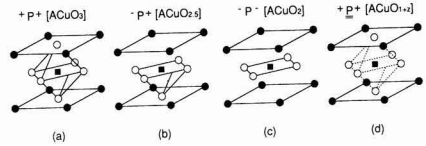

Fig. 1. Four basic perovskite blocks. ●: A atom, ■: Cu atom, ○: oxygen atom.

Figure 1(b) shows the oxygen-deficient perovskite block $ACuO_{2.5}$, in which one among the six oxygen atoms coordinated to a Cu is deficient. One oxygen atom is deficient in the upper A ion plane above Cu in this perovskite structure, therefore, this oxygen-deficient perovskite block is symbolized as $^{-}P^{+}$.

Figure 1(c) shows an oxygen-deficient perovskite block $ACuO_2$, in which two among the six oxygens coordinated to a Cu are deficient in both upper and lower A ion planes. $(Ca_{0.9}Sr_{0.1})CuO_2$ is a typical compound which contains this structural block as a unit cell.[20,21] Oxygen is deficient in both upper and lower A ion planes, therefore, this perovskite block is symbolized as $^{-}P^{-}$.

Figure 1(d) shows the special perovskite block $ACuO_{1+z}$. This appears in the crystal structures of $Ba_2YCu_3O_{6+z}$ and $(Eu, Ba)_2(Eu, Ce)_2Cu_3O_{8+z}$, and shows a characteristic behavior that oxygen moves in and out, depending on the changes in temperature and oxygen partial pressure. Oxygen is present in both upper and lower A ion planes, therefore, this special perovskite block is symbolized as $^{+}P^{+}$.

2.2. Rock Salt Block

Figure 2(a) shows a unit of the rock salt structure (NaCl). Both BaO and SrO are known as the oxide which takes the rock salt structure. When the rock salt block composes a part of copper oxide superconductors and their related compounds, it becomes a unit which takes a half area of the previous unit of rock salt structure, as shown by dotted lines in the figure. There are three types of rock salt blocks having different layer thickness, as single layer block (R), double layer one (R^2) and triple layer one (R^3). They respectively contain 1, 2 and 3 units of AO. These structures are shown in **Fig.3**.

The rock salt block always contains oxygen in the same plane for the A ion, therefore, it should be symbolized as $^{+}R^{+}$; but as a matter of abbreviation, the plus signs next to R are usually omitted.

As Santro et al.[18] pointed out, a rock salt block can be coupled with a perovskite block ($^{+}P^{+}$) by commonly occupying a plane. Taking an example of La_2CuO_4, which is a compound composed of a rock salt block and a perovskite block, we show the coupling of these two different blocks in **Fig.4(a)**. According to the method for the compilation of crystal structure using these basic structural blocks, each element in a compound, if its chemical formula is given, can be divided and assigned to the respective structural blocks. La_2CuO_4, for instance, can be divided and assigned to a perovskite block ($^{+}P^{+}[LaCuO_3]$) and a rock salt block (R[LaO]).

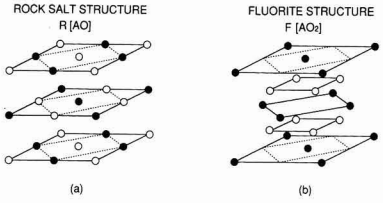

Fig. 2. Relations between the rock-salt block and the unit cell of rock-salt-type structure and those between the fluorite block and the unit cell of fluorite-type structure. ●: A atom, ○: oxygen atom.

2.3. Fluorite Block

Figure 2(b) shows a unit of the fluorite structure (CaF_2). CeO_2 is known as an oxide taking the fluorite structure. The fluorite block, shown by dotted lines in the figure, is a unit which takes a half area of a unit cell of fluorite structure, in a manner similar to the case of the rock salt, block. In the case of the fluorite block, as in the case of the rock salt block (which composes copper oxide superconductors and their related compounds), single layer block (F) and double layer block (F^2) respectively containing 1 and 2 units of AO_2 are known to exist. However, a triple layer fluorite block (F^3) has not been identified yet.

In the fluorite block, oxygen does not always exist in the same plane to A ion, thereby, minus superscripts are usually omitted from F and F^2. These fluorite blocks can be coupled with $^{+}P^{-}$ or $^{-}P^{-}$ perovskite block by commonly occupying an A ion plane where no oxygen exists. This coupling between different blocks is shown in Fig.4(b) in the case of Nd_2CuO_4, for example, which is a compound composed of a fluorite block and an oxygen-deficient perovskite block. Nd_2CuO_4 can be divided and assigned to a perovskite block ($^{-}P^{-}[NdCuO_2]$) and a fluorite block ($F[NdO_2]$).

3. Classification of Copper Oxide Superconductors and Related Compounds, in Terms of the Basic Structural Blocks

Based on the concept of the afore-mentioned basic structural blocks, we compiled the major copper oxide supercon-

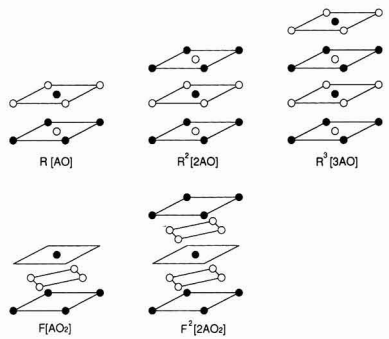

Fig. 3. Structures of various rock-salt blocks and fluorite blocks. ●: A atom, ○: oxygen atom.

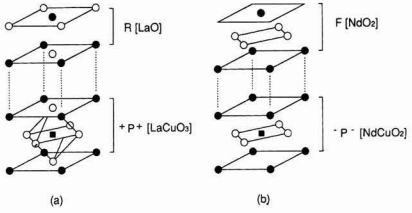

Fig. 4. Matching of the rock-salt and the perovskite blocks in the La_2CuO_4 structure (a) and that of the fluorite and the perovskite blocks in the Nd_2CuO_4 structure (b). ●: A atom, ■: Cu atom, ○: oxygen atom.

ductors and their related compounds, including the recently discovered ones. They are listed in **Tables 1 and 2**. Table 1 concerns the group of compounds which are derived from the couplings between the perovskite block ($^{+}P^{+}$, $^{-}P^{+}$, $^{-}P^{-}$ or $^{+}p^{+}$) and the rock salt block (R, R^2 or R^3). Table 2 concerns the group of compounds which contain the fluorite block (F or F^2). (Those shown at the left end are the basic compounds before being coupled with the fluorite blocks.)

The copper oxides compiled in Table 1 are composed of the perovskite block and the rock salt block, and are basically classified into two series. One is a series of compounds in which the number of the perovskite block is fixed, while the number of rock salt block to make coupling with the perovskite block varies (in such manner as to build up the multi-layer structure) as shown in the series of $LaCuO_3[^{+}P^{+}] \rightarrow La_2CuO_4[^{+}P^{+}\text{-}R] \rightarrow TlBa_2CuO_5[^{+}P^{+}\text{-}R^2] \rightarrow Tl_2Ba_2CuO_6[^{+}P^{+}\text{-}R^3]$.

Figure 5 shows the crystal structures of various compounds which belong to this series. It is observed in this figure that $LaCuO_3$ (which does not contain the rock salt block) and TlB_2CuO_5 (which contains the double layer rock salt block) are respectively constructed in a full unit cell, while La_2CuO_4 and $Tl_2Ba_2CuO_6$ (which respectively contain the single layer rock salt block and the triple layer one) are

Table 1. List of copper oxide superconductors and their related compounds which consist of either perovskite blocks or perovskite blocks and rock-salt blocks. The underlined compounds are non-superconductors or parent materials for superconductors.

[X]	[X-R]	[X-R^2]	[X-R^3]
[$^{+}P^{+}$]	[$^{+}P^{+}$-R]	[$^{+}P^{+}$-R^2]	[$^{+}P^{+}$-R^3]
$\underline{LaCuO_3}$	$(La,Sr)_2CuO_4$	$Tl(Sr,La)_2CuO_5$	$Tl_2Ba_2CuO_6$
		$(Pb,Cu)(Sr,La)_2CuO_5$	
	[$^{+}P^{+}$--$^{+}P^{+}$-R]	[$^{+}P^{+}$--$^{+}P^{+}$-R^2]	[$^{+}P^{+}$--$^{+}P^{+}$-R^3]
	$(La,Sr)_2CaCu_2O_6$	$(Tl,Pb)Sr_2Ca_1Cu_2O_7$	$Tl_2Ba_2Ca_1Cu_2O_8$
		$(Pb,Cu)Sr_2(Y,Ca)Cu_2O_7$	$Bi_2Sr_2Ca_1Cu_2O_8$
		[$^{+}P^{+}$--$^{+}P^{+}$--$^{+}P^{+}$-R^2]	[$^{+}P^{+}$--$^{+}P^{+}$--$^{+}P^{+}$-R^3]
		$(Tl,Pb)Sr_2Ca_2Cu_3O_8$	$Tl_2Ba_2Ca_2Cu_3O_{10}$
	[$^{+}P^{+}$-R-$^{+}\underline{P}^{+}$-R]		
	$(Pb_2Cu)(Sr,La)_2CuO_6$		
[$^{-}P^{+}$-$^{+}\underline{P}^{+}$-$^{+}P^{-}$]	[$^{-}P^{+}$-R-$^{+}\underline{P}^{+}$-R-$^{+}P^{-}$]		
$Ba_2YCu_3O_{6+x}$	$(Pb_2Cu)Sr_2(Y,Ca)Cu_2O_{6+x}$		

Table 2. List of copper oxide superconductors and their related compounds which contain fluorite blocks. The compounds at left side are basic compounds without fluorite block. The underlined compounds are non-superconductors or parent materials for superconductors.

[Y]	[Y-F]	[Y-F^2]
[$^{-}P^{-}$]	[$^{-}P^{-}$-F]	
$\underline{(Sr,Ca)CuO_2}$	$(Nd,Ce)_2CuO_4$	
[$^{-}P^{+}$-$^{+}\underline{P}^{+}$-$^{+}P^{-}$]	[$^{-}P^{+}$-$^{+}\underline{P}^{+}$-$^{+}P^{-}$-F]	[$^{-}P^{+}$-$^{+}\underline{P}^{+}$-$^{+}P^{-}$-F^2]
$Ba_2YCu_3O_{6+x}$	$(Eu,Ba)_2(Eu,Ce)_2Cu_3O_{8+x}$	$\underline{Sr_2(Ho,Ce)_2Cu_2O_{10+x}}$
[$^{-}P^{+}$-R-$^{+}P^{-}$]	[$^{-}P^{+}$-R-$^{+}P^{-}$-F]	
$(La,Sr)_2CaCu_2O_6$	$(La,Sr)GdCuO_4$	
[$^{-}P^{+}$-R^2-$^{+}P^{-}$]	[$^{-}P^{+}$-R^2-$^{+}P^{-}$-F]	[$^{-}P^{+}$-R^2-$^{+}P^{-}$-F^2]
$TlBa_2CaCu_2O_7$	$\underline{Tl(Ba,Tl)_2Pr_2Cu_2O_8}$	$\underline{(Tl,Cu)Sr_2(Ho,Ce)_2Cu_2O_{11}}$
$(Pb,Cu)Sr_2(Y,Ca)Cu_2O_7$	$(Pb,Cu)(Sr,Eu)_2(Eu,Ce)_2Cu_2O_8$	$\underline{(Pb,Cu)Sr_2(Ho,Ce)_2Cu_2O_{11}}$
[$^{-}P^{+}$-R^3-$^{+}P^{-}$]	[$^{-}P^{+}$-R^3-$^{+}P^{-}$-F]	
$Tl_2Ba_2CaCu_2O_8$	$\underline{Tl_2Ba_2(Eu,Ce)_2Cu_2O_{10}}$	
$Bi_2Sr_2CaCu_2O_8$	$Bi_2Sr_2(Eu,Ce)_2Cu_2O_{10}$	
[$^{-}P^{+}$-R-$^{+}\underline{P}^{+}$-R-$^{+}P^{-}$]	[$^{-}P^{+}$-R-$^{+}\underline{P}^{+}$-R-$^{+}P^{-}$-F]	
$(Pb_2Cu)Sr_2(Y,Ca)Cu_2O_{6+x}$	$\underline{(Pb_2Cu)Sr_2(Eu,Ce)_2Cu_2O_{10+x}}$	

constructed in a half of the unit cell. Consequently, we can assume that both unit cells of $LaCuO_3$ and $TlBa_2CuO_5$ are plain lattices (P), but both unit cells of La_2CuO_4 and $Tl_2Ba_2CuO_6$, which respectively contain the single layer rock salt block and the triple layer one, are body-centered lattices (I).

The other is the series of compounds in which the number of the rock salt block is fixed, while the number of the perovskite block varies, as typically shown in the series of $TiBa_2Ca_{n-1}Cu_nO_{2n+3}$. When the number of the double layer rock salt block contained is fixed, this series of compounds changes in such manner as: $TlBa_2CuO_5[^{+}P^{+}\text{-}R^{-}{}^{2}] \rightarrow TiBa_2CaCu_2O_7[^{+}P^{-}\text{-}P^{+}\text{-}R^{2D]128\text{Å}TlBa}{}_2Ca_2Cu_3O_{9D}[^{+}P^{-}\text{-}P^{-}\text{-}P^{+}\text{-}R^{2}] \rightarrow TlBa_2CaMV3Cu_4O_{11}[^{+}P^{-}\text{-}\wedge\text{-}P^{-}\text{-}P^{-}\text{-}P^{+}\text{-}R^{2}]$. **Figure 6** shows the crystal structures of these copper oxides in the order of increasing content of perovskite blocks. The respective series of $Tl_2Ba_2Ca_{n-1}Cu_nOV2n+4$ and $Bi_2Sr_2Ca_{n-1}Cu_nOV2n+4$, which contain the triple layer rock salt block, are also well-known as the series of compounds of similar kind.

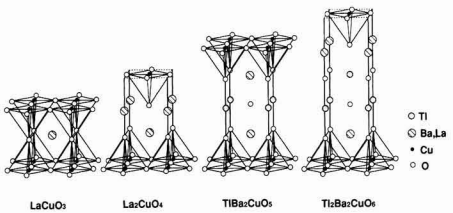

Fig. 5. Crystal structures of the series copper oxides which consist of a perovskite block and various rock-salt blocks.

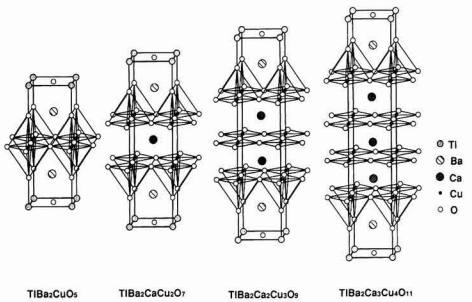

Fig. 6. Crystal structures of the $TlBa_2Ca_{n-1}CunO_{2n+3}$ series compounds which consist of a double rock-salt block and various perovskite blocks.

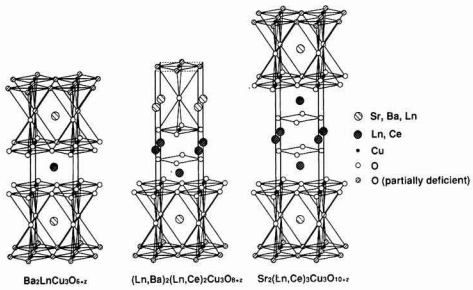

Fig. 7. Crystal structures of (Ba, Sr, Ln)$_2$(R, Ce)$_n$Cu$_3$O$_{2n+4+z}$ (R: rare earth element) series compounds which consist of perovskite blocks and various fluorite blocks.

Table 2 shows a compiled list of various series of fluorite block-containing copper oxide superconductors and their related compounds. In these series, the number of fluorite block varies in such manner, for instance, as: $Ba_2YCu_3O_{6+z}[^{+}P^{+}\text{-}^{+}P^{+}\text{-}^{+}P^{-}] \rightarrow (Ba,Eu)_2(Eu,Ce)_2Cu_3O_{8+z}[^{+}P^{+}\text{-}\underline{^{+}P^{+}}\text{-}^{+}P^{-}\text{-}F] \rightarrow Sr_2(Ho, Ce)_3Cu_3O_{10+z}[^{+}P^{+}\text{-}\underline{^{+}P^{+}}\text{-}^{+}P^{-}\text{-}F^{2}]$. **Figure 7** shows the crystal structures of these compounds. It is observed in this figure that (Ba, Eu)$_2$(Eu, Ce)$_2$Cu$_3$O$_{8+z}$, which contains the single layer fluorite block, is constructed in half of the unit cell, and the unit cell of this compound is a body-centered lattice. The series of (M, Cu)Sr$_2$(Ho, Ce)$_n$Cu$_2$O$_{2n+5}$ (M=Tl, Pb) is also well-known to be similar to the series mentioned above.[14,15]

There are other types of copper oxide superconductors which contain the double CuO chains, such as $Ba_2YCu_4O_8$ and $Ba_4Y_2Cu_7O_{14+z}$. They are not included in Tables 1 and 2. The crystal structures of $Ba_2YCu_4O_8$ (T_c=80K) and $Ba_2YCu_3O_7$ (T_c=90K) are compared in Fig.8. It is seen that $Ba_2YCu_3O_7$ which contains the single CuO chain is constructed in a full unit cell, but $Ba_2YCu_4O_8$ is in half of the unit cell. Santro et al.[16] assumed that the double CuO chains (Cu_2O_2) contained in the crystal structure of $Ba_2YCu_4O_8$ took the shear structure, which is observed in the crystal structures of V_nO_{2n-1} and Ti_nO_{2n-1}. We assume from the illustrations in Fig.9 that the double Cu_2O_2 chain was formed by the coupling of two $^{+}P^{+}$ $BaCuO_2$ blocks, during which a (BaO) plane was lost and a (CuO) lane slid slightly (by 1/2 in the axis direction).

$Pb_3Sr_3Cu_3O_{8+z}Cl$, recently discovered by Cava et al.,[22] is a layered copper compound (oxychloride) having a special crystal structure, which was not included in either Table 1 or Table 2. The crystal structure of this compound is shown in **Fig.10**. We can assume that the crystal structure of this chlorine-containing copper compound was formed as the combined structure of $(Pb_2Cu)Sr_2(Y, Ca)Cu_2O_{8+z}$, which is an 80K class superconductor, and a cell of cesium chloride

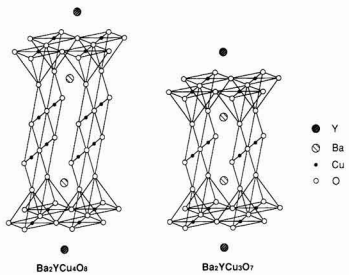

Fig. 8. Crystal structures of $Ba_2YCu_4O_8$ and $Ba_2YCu_3O_7$.

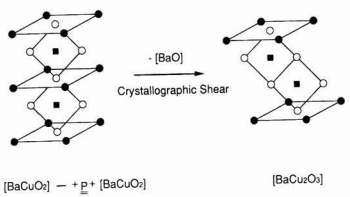

Fig. 9. Structural relationship between single CuO chain and double Cu_2O_2 chain. ●: Ba atom, ■: Cu atom, ○: oxygen atom.

(CsCl) type. We expressed this cesium chloride block as C[AX], and showed its crystal structure in **Fig.11.** In the case of this cesium chloride block, oxygen is not present in the same plane to A ions, as in the case of the fluorite block, therefore, we simply use C without minus superscripts. By introducing this new block of cesium chloride C, we can express $Pb_3Sr_3Cu_3O_{8+z}Cl$ in modified form as C(Pb, Sr)Cl-$^{+}$P^{+}(Pb, Sr)$CuO_{2.5}$-R(Pb, Sr)O-$^{+}$P^{+}$PbCuO_{1+z}$-$^{+}$P$^{-D(Pb, Sr)CuO_{2.5}}$. This indicates that the cesium chloride block (C block) can make coupling with the perovskite blocks of $^{+}$P^{-} and $^{-}$P^{-} and the fluorite block F by commonly occupying an A ion plane which did not exist with oxygen. As far as our limited understanding at present is concerned, this cesium chloride block is assumed to be involved only in compounds which contain halogen elements like chlorine.

4. Valencies of Individual Blocks Contained in Copper Oxide Superconductors and Related Compounds

When we intend to introduce carriers into a perovskite block (CuO_2 plane), or to work out the actual crystal structure of perovskite compounds, it is very useful to regard the blocks (composed of copper oxide superconductors and their related compounds) as ions, and based on this, to take account of the signs and valencies of these blocks (ions). On one hand, there are some complex perovskite compounds (like $Sr_{n+1}Ti_nO_{2n+1}$ (n=1, 2, 3)) which are known to be composed of the perovskite and rock salt blocks.[23] However, the rock salt block[SrO] and the perovskite block [$SrTiO_3$] composing these compounds are neutral blocks without electric charge. On the other hand, the blocks which compose the layered copper oxides we have discussed have a positive or negative electric charge depending on the kind of component element and oxygen content, and can be regarded as equivalent to ions. This should be the feature of these blocks. We assume that this feature is attributed to the variable valences of Cu ion, which can be not only plus 2, but also easily be plus 1 or plus 3, depending on the surroundings. (Here, we regard that an oxygen ion takes a fixed valency of minus 2.)

Following is the procedure for determination of the valence of respective blocks, based on the assumption that each block is equivalent to an ion. We assume in our calculation of the valency of each block (ion) that the composing elements of the block exist as ions. We deem that Cu in any perovskite block ($^{+}$P^{+}, $^{+}$P^{-} and $^{-}$P^{-}) which has a CuO_2 plane normally has plus 2 valencies, and that oxygen (0) always has minus 2 valencies. Based on these assumptions, we calculated the valency of individual blocks (ions), which we chose as the representative compounds among those listed in Table 1 and 2, obtaining the results shown in **Table 3.**

4.1. Perovskite Blocks

As seen in Table 3, there are three types of perovskite blocks (ions) in terms of electric charge–namely plus, minus and neutral.

A basic compound La_2CuO_4 in the p-type superconductor $(La, Sr)_2CuO_4$ is composed of a rock salt block R[LaO] and a perovskite block $^{+}$P^{+}[$LaCuO_3$]. Since each composing element in the block was assumed to exist as an ion, the rock salt block R[$La^{3+}O^{2-}$] is calculated as having plus 1 valency and the perovskite block $^{+}$P^{+}[$La^{3+}Cu^{2+}(O^{2-D})_3$] is calculated as having minus 1 valency. It is generally accepted that electric charge in a crystal tends to change in such manner as to make the electrostatic localization minimum, therefore we can understand that the perovskite block $^{+}$P^{+}[{$LaCuO_3$}$^{-}$] accepts a hole when part of La^{3+} in this block is substituted with Sr^{2+}. In addition, we assume from the viewpoint of crystal structure that the oxygen atoms shift from the perovskite block toward the rock salt block so that the electrostatic partialization between these two blocks is eased as much as possible. This oxygen shift implies that 6 oxygens coordinated at the octohedral sites of a Cu in La_2CuO_4 move toward both upper and lower directions.[4]

A basic compound Nd_2CuO_4 in the n-type superconductor $(Nd, Ce)_2CuO_4$ is composed of a fluorite block F[NdO_2] and an oxygen-deficient perovskite block $^{-}$P^{-}[$NdCuO_2$]. Then, the fluorite block F[$Nd^{3+}(O^{2-})_2$] is calculated as having

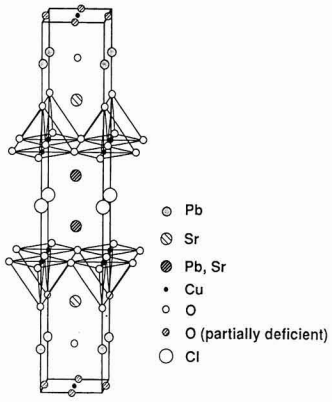

Fig. 10

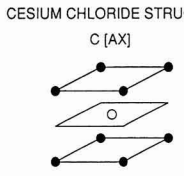

Fig. 11

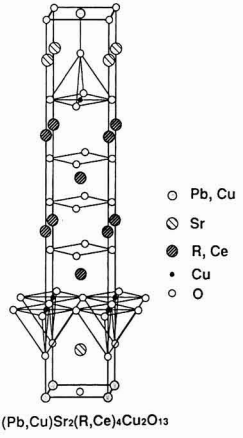

Fig. 12

Fig. 10. Crystal structure of a layered copper oxychloride, $Pb_3Sr_3Cu_3O_{8+z}Cl$.

Fig. 11. Structure of cesium chloride block, C(AX). ●: A atom, ○: halogen atom.

Fig. 12. Crystal structure of a plausible layered copper oxide, (Pb, Cu)Sr_2(R, $Ce)_4Cu_2O_{13}$ (R: rare earth element).

Table 3. Charges of different blocks found in the typical copper-oxide superconductors and their related compounds.

$LaCuO_3$	$^{+}P^{+}[\{LaCuO_3\}^{-}]$
La_2CuO_4	$^{+}P^{+}[\{LaCuO_3\}^{-}] - R[\{LaO\}^{+}]$
$Tl(Sr_{1/2}La_{1/2})_2CuO_5$	$^{+}P^{+}[\{(Sr_{1/2}La_{1/2})CuO_3\}^{3/2-}] - R^{2}[2\{(Tl_{1/2}Sr_{1/4}La_{1/4})O\}^{3/4+}]$
$Tl_2Ba_2CuO_6$	$^{+}P^{+}[\{BaCuO_3\}^{2-}] - R^{2}[2\{(Ba_{1/2}Tl_{1/2})O\}^{1/2+}+\{TlO\}^{+}]$
$Tl_2Ba_2CuO_6$	$^{+}P^{+}[\{BaCuO_3\}^{2-}] - R^{2}[2\{(Ba_{1/2}Tl_{1/2})O\}^{1/2+}+\{TlO\}^{+}]$
$Tl_2Ba_2Ca_1Cu_2O_8$	$^{-}P^{+}[\{(Ba_{1/2}Ca_{1/2})CuO_{2.5}\}^{-}] - R^{2}[2\{(Ba_{1/2}Tl_{1/2})O\}^{1/2+}+\{TlO\}^{+}] - {}^{+}P^{-}[\{(Ba_{1/2}Ca_{1/2})CuO_{2.5}\}^{-}]$
$Tl_2Ba_2Ca_2Cu_3O_{10}$	$^{-}P^{-}[\{CaCuO_2\}] - {}^{-}P^{+}[\{(Ba_{1/2}Ca_{1/2})CuO_{2.5}\}^{-}] - R^{2}[2\{(Ba_{1/2}Tl_{1/2})O\}^{1/2+}+\{TlO\}^{+}] - {}^{+}P^{-}[\{(Ba_{1/2}Ca_{1/2})CuO_{2.5}\}^{-}]$
$Tl_2Ba_2Ca_3Cu_4O_{10}$	$^{-}P^{-}[\{CaCuO_2\}] - {}^{-}P^{-}[\{CaCuO_2\}] - {}^{-}P^{+}[\{(Ba_{1/2}Ca_{1/2})CuO_{2.5}\}^{-}] - R^{2}[2\{(Ba_{1/2}Tl_{1/2})O\}^{1/2+}+\{TlO\}^{+}] - {}^{+}P^{-}[\{(Ba_{1/2}Ca_{1/2})CuO_{2.5}\}^{-}]$
$Ba_2YCu_3O_{6+x}$	$^{-}P^{+}[\{(Ba_{1/2}Y_{1/2})CuO_{2.5}\}^{1/2-}] - {}^{+}\underline{P}^{+}[\{BaCuO_{1+z}\}^{2-2z}] - {}^{+}P^{-}[\{(Ba_{1/2}Y_{1/2})CuO_{2.5}\}^{1/2-}]$
$(Eu_{2/3}Ba_{1/3})_2(Eu_{1/3}Ce_{2/3})_2Cu_3O_{8+x}$	$F[\{(Eu_{2/3}Ce_{1/3})O_2\}^{2/3-}] - {}^{-}P^{+}[\{(Eu_{1/2}Ce_{1/6}Ba_{1/3})CuO_{2.5}\}^{1/6-}] - {}^{+}\underline{P}^{+}[\{(Eu_{1/3}Ba_{2/3})CuO_{1+z}\}^{(7/3-2z)+}] - {}^{+}P^{-}[\{(Eu_{1/2}Ce_{1/6}Ba_{1/3})CuO_{2.5}\}^{1/6-}]$
$Sr_2(Ho_{1/3}Ce_{2/3})_3Cu_3O_{10+x}$	$F^{2}[2\{(Ho_{1/3}Ce_{2/3})O_2\}^{1/3-}] - {}^{-}P^{+}[\{(Ho_{1/6}Ce_{1/3}Sr_{1/2})CuO_{2.5}\}^{1/6-}] - {}^{+}\underline{P}^{+}[\{SrCuO_{1+z}\}^{(2-2z)+}] - {}^{+}P^{-}[\{(Ho_{1/6}Ce_{1/3}Sr_{1/2})CuO_{2.5}\}^{1/6-}]$

minus 1 valency, and the perovskite block $^{-}P^{-}[Nd^{3+}Cu^{2+}(O^{2-})_2]$ is calculated as to have plus 1 valency. Since this perovskite block (ion) has a positive charge in contrast to a negative charge in the perovskite block La_2CuO_4, we can understand that it tends to accept an electron.

The oxygen-deficient perovskite block (ion) $^{+}P^{+}[ACuO_{1+z}]$, which block composed of $Ba_2YCu_3O_{6+z}$ superconductor and has no CuO_2 plane, has various electric charges depending on the oxygen content (1+z). When A ion is a 2 valency cation like Ba, this perovskite block (ion) has positive charges in the oxygen content (1+z) range of less than 2, and has negative charges in the range of more than 2. Therefore, in order for this perovskite block $^{+}P^{+}$ to couple with a CuO_2 plane-containing perovskite block and donate a hole, the oxygen content (1+z) must be less than 2. Concerning the role of the oxygen-deficient perovskite block (ion) $^{+}P^{+}[ACuO_{1+z}]$ in the $Ba_2YCu_3O_{6+z}$ superconductor, Tokura et al. presented an interesting report.[24)]

4.2. Rock Salt Blocks

As seen in Table 3, the rock salt block (ion) takes a positive charge. Therefore, when a rock salt block is coupled with a perovskite block, we can usually expect holes to be introduced into the perovskite block.

The reason why the rock salt block (ion) takes a positive charge is that, although this block is basically expressed by AO, which is composed of a cation A with plus 2 valencies and an anion 0 with minus 2 valencies, a cation with plus 3 valencies (like a rare earth element ion) is usually contained in the form of solid solution at the site of Cation A with plus 2 valencies. Accordingly, if we can arrange for a cation with plus 1 valency like alkali metal element to be contained in the form of solid solution at the site of cation A in the rock salt block, we could presumably obtain a rock salt block with a negative charge.

4.3. Fluorite Blocks

As also seen in Table 3, the fluorite block (ion) takes a negative charge. Therefore, when a fluorite block is coupled with a perovskite block, we can ordinarily expect that an electron is donated from the fluorite block to the perovskite block. The superconductors of the $(Eu, Ba)_2(Eu, Ce)_2Cu_3O_{8+z}$ type have the coupled structure of p-type superconductor $Ba_2YCu_3O_{6+z}$(T_c~90K) and single layer fluorite block, and show T_c of around 40K at best even after heat-treatment under high oxygen gas pressure.[5,6)] Meanwhile, the superconductors of the $Bi_2Sr_2(Eu, Ce)_2Cu_2O_{10}$("2222") type and those of the $(Pb, Cu)Sr_2(Eu, Ce)_2Cu_2O_9$("1222") type are respectively composed by the coupling of $Bi_2Sr_2CaCu_2O_8$(T_c~80K) and $(Pb, Cu)Sr_2(Y, Ca)Cu_2O_7$($T_c$~60K) with a single layer fluorite block, and both show T_c as low as 20 to 30K.[8,11)] Neither the Tl based layered copper oxide which contains a single-layer fluorite block nor the oxide which contains a double-layer fluorite block show superconductivity.[7,8,14)]

The reason why these copper oxide superconductors showed decreased T_c's when they were coupled with the fluorite block, as afore-mentioned, is attributed to the decrease of holes in the perovskite block (CuO_2 plane), which was caused by the coupling of the perovskite block with the negative-charged fluorite block $F[\{(Ce, Eu)O_2\}^{8-}]$. In other expression, the holes in the CuO_2 plane shift their positions to some extent toward the fluorite block in order to keep the balance of electrostatic charge. We therefore think that the layered copper oxides which contain the fluorite block are not suitable materials for the preparation of high-T_c p-type copper oxide superconductors. On the contrary, we think the fluorite blocks are useful for the preparation of n-type superconductors like $(Nd, Ce)_2CuO_4$.

The reason why the fluorite block (ion) takes a negative charge, as above mentioned, is that although this block is basically expressed by AO_2 (composed of a cation A with plus 4 valencies and two anions 0 with minus 2 valencies

each) a cation with plus 3 valencies like rare earth elements is usually contained in the form of solid solution at the site of this 4-valency cation. Accordingly, if we can arrange for a cation with plus 5 valencies to be contained in the form of solid solution at the site of cation A in the fluorite block, we could presumably obtain a fluorite block with a positive charge.

5. Material Design of Layered Copper Oxides Having Novel Structures

According to the procedure proposed in this report, in which the individual structural blocks are deemed as the secondary unit cells and their valencies are summed up, we can easily derive compounds which have novel crystal structures. In our "material design" of layered copper oxides by using these blocks, we combine the basic principle for the block construction and the conventionally available knowledge of crystal chemistry.

5.1. Fundamental Requisite

The restricting condition of primary importance in the "material design" comes from the ordinary principle that the blocks can be coupled with each other only when the two blocks involved commonly possess either A ion plane with oxygen in it or an A ion plane without oxygen in it. In other words, if we explain by taking the plus and minus superscripts of block symbols such as P, R and F, we imply that any two blocks involved can be coupled with each other only between points on the respective blocks, where both are given with plus (+) or minus(-) signs in common. Consequently, we can couple the blocks between a plus position and a plus position or between a minus position and a minus position in as long a series as we want (for example $^{+}$P^{+}-R-$^{+}$P^{-}-F), but we cannot couple them between a plus position and a minus position (such as $^{+}$P^{+}-F, or $^{+}$P^{-}-R).

5.2. Matching of Lattice Constants Between Blocks

The second condition for the coupling of blocks is the matching of lengths of axes in a tetragonal lattice, when this lattice is assumed as the basic cell. That is, when the lengths of a side (equivalent to the length of axis a) of the plane common to the two blocks involved (this plane is basically assumed to be square) are close each other, these two blocks are easier to couple, but when they are largely different, these two blocks are difficult to couple.

Basic blocks in the copper oxide superconductors are the perovskite blocks such as $^{+}$P^{+} and $^{-}$P^{-}. $LaCu_3O$, which is a copper oxide compound having $^{+}$P^{+} block as a unit cell, has the a axis of 3.819Å (the c axis is 3.973Å).[19] Meanwhile, $(Ca_{0.9}Sr_{0.1})CuO_2$, which is a compound having $^{-}$P^{-} block as a unit cell, has the axis a with a length of 3.861Å (the axis c is 3.201Å).[20] It is worthwhile to note that the lengths of the axis a in these two compounds are respectively close to 3.9Å, which is twice the distance between Cu and O in CuO (in which Cu is bonded with the 4 coordinated Os in a square plane).[25]

If the rock salt block or the fluorite block can be coupled with one of these perovskite blocks, the length of its a axis must be close to 3.8Å to 3.9Å. BaO and SrO are compounds which respectively consist of a unit cell of the rock salt block. Both of them belong to the cubic system, and they have lattice constants of 5.539Å and 5.160Å respectively. Using these data we calculated the respective lengths of a axis of the rock salt blocks BaO and SrO, obtaining 3.92 (=5.539/2)Å and 3.65(5.160/2)Å. These values are fairly close to the length of a axis of the perovskite block, so we can understand that both of them are highly likely to be coupled with the perovskite blocks. CaO and MaO also take the crystal structure of the rock salt type. If they are supposed to have formed the rock salt blocks, the respective lengths of axis a are calculated as 3.4Å and 3.0Å, which widely differ from the 3.8Å to 3.9Å of the perovskite blocks. Thereby, we can predict the difficult coupling of CaO and MaO with the perovskite blocks.

CeO_2 is the compound which consists of a unit cell of the fluorite block. Rare earth oxides of three-two type R_2O_3 (R is rare earth element like Y, Nd, Sm, Eu, Gd, Tb, Dy, Ho, Er, Tm, Yb and Lu) take the anion-deficient lattice of fluorite type, which is commonly known as C type.[25] We calculated the lengths of a axis of the fluorite blocks of these compounds from their lattice constants, obtaining 3.83Å for CeO_2 and 3.75Å for Y_2O_3. Both values are found to be relatively close to the length of a axis of the perovskite blocks, thereby, we can predict that these fluorite blocks of CeO_2 and Y_2O_3 are easily coupled with the perovskite blocks. It was recently reported26) that $YBa_2Cu_3O_7$ was epitaxially grown on Y_2O_3 single crystals. This experiment was supported by the matching of lattice length between the blocks, as described above.

5.3. Electrostatic Conformity Between the Blocks

The third condition for the coupling of blocks is the electrostatic conformity between the blocks involved. When we examined the electrostatic connection between the blocks in the compounds listed in Table 3, we confirmed the existence of common characteristics among them.

5.3.1. Coupling Between Blocks of the Same Type

The coupling between two blocks of the same type can be made only on condition that these two blocks respectively possess electric charge of the same sign, or that one of them is electrically neutral. In the case of coupling between two perovskite blocks which respectively contain a CuO_2 plane, three kinds of block combinations in term of electric charge are found. First is the combination of perovskite blocks, both of which possess negative charge ($^{+}$P^{-}[$\{Ba_{0.5}Y_{0.5}CuO_{2.5}\}^{0.5-}$]-$^{-}$P^{+}[$\{Ba_{0.5DY0.5}CuO_{2.5}\}^{0.5-}$]), as observed in the case of the compound $Ba_2YCu_3O_{6+z}$. Second is the combination of blocks, one possessing negative charge and the other being neutral ($^{+}$P^{-}[$\{Ba_{0.5}Ca_{0.5}CuO_{2.5}\}^{-}$]-$^{-}$P^{-}[$\{CaCuO_2\}$]), as observed in the case of the compound $Tl2Ba_2Ca_3Cu_4O_{10}$. Third is the combination of blocks, both of which are neutral ($^{-}$P^{-}[$\{CaCuO_2\}$]-$^{-}$P^{-}[$\{CaCuO_2\}$]). The combination of two perovskite blocks, one possessing positive charge and the other negative charge, has not been identified at this time. Namely, the compound (Pb, Cu)Su_2(Y, Ca)$_2Cu_3O_9$ ["1223"compound of Pb system] has not been synthesized yet, although this compound is supposed to exist by taking the same crystal structure as (Tl, Pb)$Sr_2Ca_2Cu_3O_9$ "Tl-1223" compound already synthesized. We assume this "Pb-1223" compound of will include couplings between negative charged perovskite block ($^{+}$P^{-}) and positive-charged perovskite block, as $^{+}$P^{-}[{(Sr, Y, Ca)$CuO_{2.5}$}$^{\delta-}$]-$^{-}$P^{-}[{(Ca, Y)CuO_2}$^{\delta+}$)-$^{-}$P^{+}[{(Sr, Y, Ca)$CuO_{2.5}$}$^{\delta-}$].

5.3.2. Coupling Between Rock Salt Block and Perovskite Block

The rock salt blocks are normally charged positively, thereby, they couple with the negative-charged perovskite blocks.

5.3.3. Coupling Between Fluorite Block and Perovskite Block

The fluorite blocks are normally charged negatively, so they can couple with the positive-charged perovskite blocks ($(F^-[\{NdCuO_2\}^+]$, for instance), but not so often. Instead, they mostly couple with the negative-charged perovskite blocks.

Lastly, we present material design of a novel layered copper compound $(Pb_{0.5}Cu_{0.5})Sr_2(Ho_{1/4}Ce_{3/4})_4cu_2O_{13}$, which contained the triple layer fluorite blocks. This compound was a modification of the layered copper compound $(Pb_{0.5}Cu_{0.5})Sr_2(Ho_{1/3}Ce_{2/3})_3Cu_2O_{11}$, synthesized by us and containing the double layer fluorite blocks. This compound satisfies all of the required rules of thumb for material design outlined in this paper, therefore we think this material can be synthesized. **Figure 12** shows the crystal structure of this compound.

6. Conclusion

1) Crystal structures of copper oxide superconductors and their related compounds are usually composed of three types of structural blocks, namely, the perovskite blocks ($ACuO_{3-\delta}$), the rock salt blocks (AO) and the fluorite blocks(AO_2).
2) Based on the concept of these basic structural blocks, we classified and compiled the major copper oxide superconductors and their related compounds which were already known, and proved that there existed two compound series. One was the layered copper oxide series derived from the combination of the perovskite blocks and the rock salt blocks, and the other was the layered copper oxide series composed of the perovskite, rock salt and fluorite blocks.
3) Double Cu_2O_2 chains is observed in $Ba_2YCu_4O_8$ and $Ba_4Y_2Cu_7O_{14+z}$ can be understood as equivalent to the shear structure observed in V_nO_{2n-1} or Ti_nO_{2n-1}. Meanwhile, we proved the existence of the cesium chloride block, which was the characteristic block in halogen element-content compounds like $Pb_3Sr_3Cu_3O_{8+z}Cl$.
4) By deeming the blocks which composed the copper oxide superconductors and their related compounds as ions, we examined the electric charge possessed by the various blocks (ions). We proved through this examination that the rock salt blocks generally possess positive charge, thereby acting as hole donators to the perovskite blocks, and that the fluorite blocks possess negative charge, thereby acting as hole acceptors (electron donators) to the perovskite blocks.
5) By deeming the individual structural blocks as subunit cells and by piling them up, we can derive novel crystal structures. For the "material design" of novel layered copper oxides, not only the basic principle for block coupling, but also the matching of the lattice constants between the blocks involved and the electrostatic conformity (electroneutrality condition) between the blocks (ions) involved are important.

Acknowledgements

The authors are grateful to Mrs. Toshihiko Maeda, Yuji Yaegashi and Kazuyuki Hamada of the Superconductivity Research Laboratory of the International Superconductivity Technology Center; to Ms. Akiko Nara of Tokai University; and to Mr. Seiji Adachi of the Central Research Laboratory of the Matsushita Denki Co., Ltd.. All of them kindly helped us by discussing our study results before we complied this report.

References:

1) J.G. Bednortz and K.A. Muller, Z. Phys., B-Condensed Matter, 64, 189-193 (1986).
2) S. Uchida, H. Takagi, K. Kitazawa and S. Tanaka, Jpn. J. Appl. Phys., 26, L1-L2 (1987).
3) K. Yvon and M. Francois, Z. Phys. B-Condensed Matter, 76, 413-444 (1989).
4) H. Muller-Buschbaum, Angew. Chem. Int. Ed. Engl., 28, 1472-1493.
5) H. Sawa, K. Obara, J. Akimitsu, Y. Matsui and S. Horiuchi, J. Phys. Soc. Jpn., 58, 2252-2255 (1989).
6) T. Wada, A. Ichinose, Y. Yaegashi, H. Yamauchi and S. Tanaka, Phys. Rev. B, 41, 1984-1989 (1990).
7) C. Martin, D. Bourgault, M. Hervieu, C. Michel, J. Provost and B. Raveau, Mod. Phys. Lett. B, 3, 993-1000 (1989).
8) Y. Tokura, T. Arima, H. Takagi, S. Uchida, T. Ishigaki, H. Asano, R. Beyers, A.I. Nazzal, P. Lacorre and J.B. Torrance, Nature, 342, 890-893 (1989).
9) T. Rouillon, D.Groult, M. Herview, C. Michel, and B. Raveau, Physica C, 167, 107-111 (1990).
10) S. Adachi, O. Inoue, S. Kawashima, H. Adachi, Y. Ichikawa, K. Setsune and K. Wasa, ditto., 168, 1-7 (1990).
11) T. Maeda, K. Sakuyama, S. Koriyama, A. Ichinose, H. Yamauchi and S. Tanaka, ditto., 169, 133-136 (1990).
12) A. Tokiwa, T. Oku, M. Nagoshi, M. Kikuchi, K. Hiraga and Y. Shyono, ditto., 161, 459-467 (1990).
13) A. Tokiwa, T. Oku, M. Nagoshi, D. Shindo, M. Kikuchi, T. Oikawa, K. Hiraga and Y. Shyono, ditto., in press.
14) T. Wada, A. Ichinose, H. Yamauchi and S. Tanaka, ditto., 171, 344-347 (1990).
15) T. Wada, A. Ichinose, H. Yamauchi and S. Tanaka, Advance in Superconductivity III ed. by K. Kajima and H. Hayakawa, Springer, Tokyo, (1991) pp.327-330.
16) A. Santro, F. Beech, M. Marezio and R.J. Cava, Physica C, 156, 693-700 (1988).
17) Y. Tokura and T. Arima, Jpn. J. Appl. Phys., 29, 2388-2402 (1990).
18) J. Akimitsu, Oyo buturi 60, 466-467 (1991).
19) J.F. Bringley, B.A. Scott, S. J. La Placa, R.F. Boehme, T.M. Shaw, M.W. McElfresh, S.S. Trail and D.E. Cox, Nature, 347, 263-265 (1990).
20) T. Siegrist, S.M. Zahurak, D.M. Murphy and R.S. Roth, Nature, 334, 231-232 (1989).
21) H. Yamane, Y. Miyazaki and T. Hirai, J. Ceram. Soc. Jpn. Int. Ed. 97, 140-144 (1989).
22) R.J. Cava, P. Bordet, J.J. Capponi, C. Chaillout, J. Chenavas, T. Fournier, E.A. Hewat, J.L. Hodeau, J.P. Levy, M. Marezio, B. Batlogg and L.W. Rupp Jr., Phicica C 167, 67-74 (1990).
23) F.S. Galasso Structure and Properties of Inorganic Solis, Pergamon Press, New York, (1970) pp.188-192.
24) Y. Tokura, J.B. Torrance, T.C. Huang and A.I. Nazzal, Phys. Rev. B, 38, 7156-7160 (1988).
25) R. Kiriyama and H. Kiriyama, Kozo-Muki-Kagaku (structural non-organic chemistry) - I, Kyoritsu Publishing, Tokyo, (1985), Chapter 11.
26) A. Oishi, H. Teshima, H. Izumi, K. Ohata, S. Kawamoto, T.

Morishita and S. Tanak, Advances in Superconductivity III, ed. by K. Kajimura and H. Hayakawa, Springer, Tokyo, (1991) p.917-920.

Seramikkusu Kyokai Gakujutsu Ronbunshi (Japanese version), Vol.99, No.6, 1991.

This article is a full translation of the article which appeared in Nippon

Microstructure Development and Stacking Fault Annihilation in β-SiC Powder Compact

Won-Seon Seo, Chul-Hoon Pai, Kunihito Koumoto and Hiroaki Yanagida*

Department of Industrial Chemistry, Faculty of Engineering, The University of Tokyo
7-3-1 Hongo, Bunkyo-ku, Tokyo, 113 Japan
*Research Center for Advanced Science and Technology, The University of Tokyo
4-6-1 Komaba, Meguro-ku, Tokyo, 153 Japan

Beta-SiC specimens possessing 13% stacking fault density were annealed at various temperatures for various time periods in an Ar or a N_2 atmosphere; changes in microstructure and the annihilation of stacking faults were investigated. Stacking fault annihilation was found to occur parallel with the grain growth which is supposedly controlled by surface diffusion and/or vapor transport. Lattice strain enhanced by the incorporation of nitrogen into the SiC lattice was considered to be the most important factor in suppressing the mass transport rate.

[Received November 6, 1990; Accepted February 20, 1991]

Key-words: β-SiC, Stacking fault, Lattice strain, Surface diffusion, Nitrogen, Grain growth

1. Introduction

Silicon carbide is highly valued as an attractive material for its good electrical and mechanical properties. Silicon carbide exists in many polytypic forms, all based on various stacking sequences of the close-packed planes of covalently bonded tetrahedra (either SiC_4 or CSi_4). The only cubic polytype with the zinc blend structure is 3C,[1] in which the stacking of the planer units of Si and C in tetrahedral coordination is depicted as AbBcCaAbBcCa.... in the <111> direction. The other polytypes have either hexagonal or rhombohedral symmetries and have different stacking sequences of Si and C layer units. These polytypes are collectively known as α-SiC, and the 3C polytype is called β-SiC. Stacking fault is denoted as a disordered part of the above sequence, and it is generally classified into two types, i.e., growth fault (or twin fault) and deformation fault.[2]

There are few investigations on the stacking faults because of the experimental and computational difficulties resulting from the small energy difference between the ideal structure and the faulted structure. However, it has been reported that stacking faults greatly affect the properties such as thermoelectric conversion efficiency[3] and fracture toughness,[4] and also the solid state reaction like phase transformation.[5] We have already reported the results of qualitative characterization of stacking faults in β-SiC by means of X-ray diffraction (XRD) and high resolution electron microscopy.[6]

In the present study, we have quantitatively analyzed the annihilation of stacking faults and the change in microstructure of β-SiC during firing in an Ar or a N_2 atmosphere by means of XRD intensity measurements and scanning electron microscopy(SEM). As a result, the effect of nitrogen incorporation on the annihilation of stacking faults was clarified, and the mechanism of stacking fault annihilation in a β-SiC powder compact is proposed.

2. Quantitative Analysis of the Stacking Fault Density

Experimental determination of the amounts of different polytypes present in a SiC sample is not simple, because of the constant ambiguity caused by the differences in, for example, the degree of crystallity, particle size, and stacking fault density among polytypes involved. Hase et al. proposed an equation to calculate the quantities of 2H and 3C polytypes from the X-ray(CuK_α intensity ratio of 211 to 3C.[7] To calculate the theoretical peak intensity of 2H, they used the peak appearing at $2\theta=33.6°$, instead of that appearing at $2\theta=38.3°$. However, many researchers[3,8,9] have reported that the peak (CuK_α at $2\theta=38.3°$ and the (200) reflection peak near $2\theta=41.4°$ are closely related to the presence of stacking faults. Moreover, if 2H polytype is present, a much stronger reflection peak near $2\theta=38.3°$ ($CuK\alpha$ should be observed.[10] If 33.6° peak is only detected without the 38.3° peak appearing, the 33.6° peak must have resulted entirely from the stacking faults. Therefore, Hase's equation is considered to express the content of stacking faults, though it was initially derived to calculate 2H content.

Because stacking faults present in β-SiC usually have no periodic nature, we cannot determine the unit cell type, multiplicity factor, or structure factor only from X-ray powder profile measurement. Tateyama et al.[8] applied an advanced XRD intensity equation to SiC powders possessing stacking faults by carrying out XRD powder diffraction measurements and Rietveld (profile fitting) analysis. They succeeded in the simulation of XRD profiles by taking account of the stacking faults in both normal (ABCABC...) and inverse (ACBACB...) stacking sequences.

X-ray profile analysis of β-SiC powders shown that the 41.4° peak becomes broad and short, and the 33.6° peak coming from the stacking faults becomes larger, both with an increase in the stacking fault density. If the parameter X is defined as the ratio of 33.6° peak intensity to 41.4° peak intensity, the stacking fault density becomes dependent on X, while X is observed invariable with the X-ray apparatus conditions. In order to derive a quantitative equation to express the stacking fault density in β-SiC, the values of X were calculated from XRD patterns reported by Tateyama et al.[8] Then, we attempted to express the stacking fault

density Y obtained from the X-ray profile analysis[8] in terms of X using the following equation:

$$Y = \frac{x}{ax+b} + cx^3\,(\%) \quad \ldots\ldots\ldots\ldots\ldots (1)$$

Fitting operation has given the constants in eq.(1) as follows: a=6.82×10^{-2}, b=2.27×10^{-2}, and c=1.7. It can be seen in **Fig.1** that the fitting is fairly good, and eq.(1) was used throughout this study to calculate the stacking fault density.

3. Experimental Procedure

3.1. Heat Treatment of β-SiC Powder Compact

Beta-SiC powder (Central Glass Co., Ltd.) having 13% stacking fault density and synthesized by carbothermal reduction of SiO_2 was employed as a starting material. According to the chemical and spectroscopic analyses, the powder contained the following impurities in weight: free-carbon (0.3%), free-Si (0.1%), free-SiO_2 (0.2%), Fe (0.03%), Al (0.02%), Ca (0.01%), and Na (0.01%). The powder was isostatically pressed in a rubber mold after pre-pressing in a unidirectional mold, and was annealed at 1600° - 2000°C for 0 - 1h in an Ar or N_2 atmosphere, Gold was evaporated onto the fractured surface and SEM observations were conducted to examine the microstructure. The average grain size was calculated from the micrographs. Surface area of the annealed powder was measured by the single pint BET method using nitrogen gas.

3.2. XRD Analysis

XRD measurements of the crushed powders were conducted using CuKα radiation with a Ni filter and a graphite monochromator under the following conditions: scanning speed=1/4° (in 2θ) min^{-1}, time constant =5s, and receiving slit=0.15mm. The intensities of the peaks at 33.6° and 41.4° (2θ) were measured and eq.(1) was used to calculate the stacking fault density. The half-width of the (111) reflection peak was also measured and the Scherrer equation[11] was used to calculate the crystallite size. The Hall method[12] was used to measure the lattice strain introduced into the annealed β-SiC specimens. For this purpose, $CuK_{<DF128a1}$ peak positions of (111), (200), (220), (222), and (400) reflections were measured. Lattice parameter was calculated from the observed peak positions of (331), (420), and (422) reflections precisely determined by an internal method using high-purity silicon as a standard. A computer program which separates $K\alpha_1$ from $K\alpha_2$ by the Rachinger method[11] was used to calculate the precise lattice parameters of β-SiC, which showed only poor crystallity.

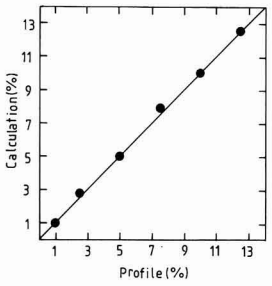

Fig. 1. Comparison of the calculated stacking fault density (eq.(1)) with the profile-fitted density reported by Tateyama et al.[8]

4. Results and Discussion

4.1. Annihilation of Stacking Faults

If the atoms existing in a faulted layer of SiC originally come from their normal lattice layer sites, all atoms in the faulted layer should have a stress field surrounding the layer. Hence, the energy of the system increases with increasing stacking fault density. The activation energy for the formation and annihilation of the stacking faults is considered to be rather low, because the difference in free energy among the various SiC polytypes formed through the rearrangement of stacking layers is small.[13] Since any system tends to become the minimum free energy state, there is a tendency for the stacking faults themselves to rearrange by moving the stacking layers, so that the overall strain energy may decrease. Stacking faults present in SiC are annihilated during annealing and the most stable polytype at that temperature would be formed.

In the present experimental temperature range (1600-2000°C) 3C polytype is stable and the stacking faults only become annihilated in the 3C matrix during annealing as was confirmed by XRD. **Figure 2** shows the stacking fault densities of β-SiC compacts after being annealed at various temperatures for 0.5h in a N_2 or Ar atmosphere. It appears that stacking fault density decreases with increasing annealing temperature. It can also be seen that the degree of decrease in the stacking fault density is larger in an Ar

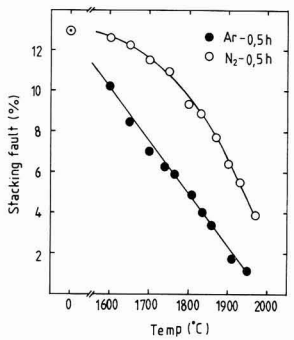

Fig. 2. Temperature dependence of the stacking fault density in β-SiC annealed for 0.5h in N_2 and Ar atmospheres.

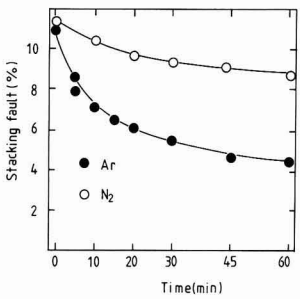

Fig. 3. Time dependence of the stacking fault density in β-SiC annealed at 1800°C in N_2 and Ar atmospheres.

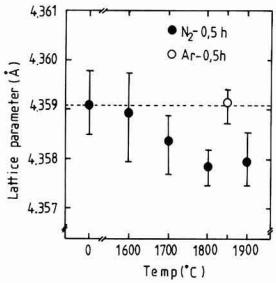

Fig. 4. Temperature dependence of the lattice parameter for β-SiC annealed for 0.5h.

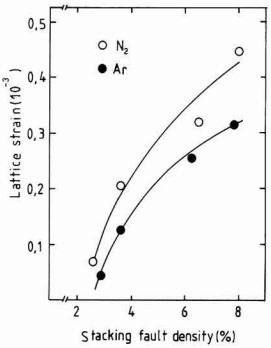

Fig. 5. Relation between stacking fault density and lattice strain in the β-SiC specimens.

atmosphere than in one of N_2. **Figure 3** shows the time dependence of the stacking fault density observed at 1800°C. The stacking fault density decreases with increasing annealing time both in N_2 and Ar atmospheres. The reason for the different rate of fault density change in different atmospheres could be attributed to the role of nitrogen incorporated into the SiC lattice, and this will be discussed further in the next section.

4.2. Incorporation of Nitrogen

It is already well known from the previous investigations on crystal growth,[14] diffusion,[15] and thermoelectric conversion[16] that nitrogen is easily incorporated into the SiC lattice during firing in a N_2 atmosphere at high temperatures. Even though the nitrogen incorporation has been widely recognized, the reported lattice parameters are not necessarily consistent. For instance, Kawamura[14] reported that the lattice parameter of the specimen grown in a pure nitrogen atmosphere was larger than that of the specimen grown in a pure argon atmosphere at 2200°C. However, Pai[16] reported that the lattice parameter of porous β-SiC ceramics sintered in a N_2 atmosphere decreased with increasing sintering temperature.

We measured the lattice parameters of the β-SiC specimens annealed at low temperatures (1600-1900°C) in N_2 and Ar atmospheres. The lattice parameter of β-SiC decreased with increasing annealing temperature in a N_2 atmosphere, while the lattice parameter remained practically unchanged in Ar as shown in **Fig.4.** It is postulated from the figure that the substitutional solid solution may be formed when nitrogen is incorporated into β-SiC lattice. This would be verified by the following considerations; atomic radii of nitrogen, carbon, and silicon are 0.075 nm, 0.077 nm, and 0.111 nm, respectively, and if incorporated nitrogen goes into a carbon site substitutionally, the lattice becomes squeezed owing to the difference in atomic radius.

Lattice strain is usually introduced by solid solution formation owing to the different atomic radii of solute atoms. In the present study the Hall method was employed to evaluate the lattice strain introduced into the annealed specimens. It is clearly seen in **Fig.5** that the incorporation of nitrogen does indeed enhance the lattice strain, and also, that the lattice strain increases with stacking fault density. Therefore, the lower rate of stacking fault annihilation in a N_2 atmosphere (Figs.2,3) than in an Ar atmosphere should be closely related to the incorporation of nitrogen and especially to the enhanced lattice strain.

4.3. Grain Growth and Crystallite Size

Figure 6 shows fractured surfaces of the β-SiC specimens. When annealed in an Ar atmosphere, small particles partially combine with each other during grain growth and neck growth. Relative density of the specimens (59-60%) does not change in spite of increasing annealing temperature since grains and pores grow concurrently. However, grain shapes in the annealed specimens are quite

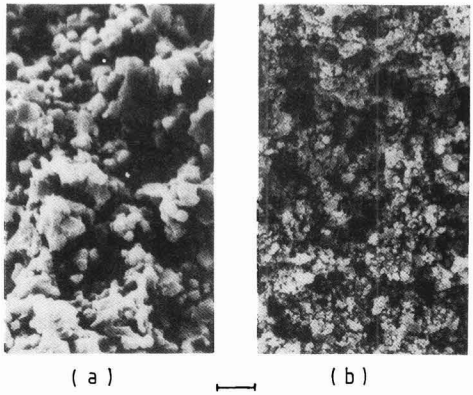

Fig. 6. Scanning electron micrographs of the fractured surfaces of the specimens annealed at 1800°C for 1h in (a) Ar and (b) N_2; bar=3μm.

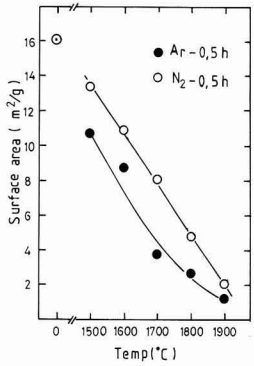

Fig. 7. Temperature dependence of the surface area in the β-SiC specimens annealed for 0.5h.

different; i.e, N_2-annealed specimens show angular grains, while Ar-annealed specimens have much rounder grains. This can be verified by surface area measurement as shown in **Fig.7**. As was expected, surface area decreases with increasing annealing temperature more rapidly in an Ar atmosphere than in a N_2 atmosphere. It is widely accepted that surface diffusion[17,18] or vapor-phase transport[19] causes formation and growth of inter-grain necks and grain coarsening in the sintering of SiC. In the present study, at least part of the decrease in the surface area during annealing might have been caused by surface diffusion, though the possibility of vapor transport via the evaporation-condensation process can not be overlooked. This difference must have been caused by a lower mass transport rate in a N_2 atmosphere than in an Ar atmosphere. Consequently, the difference in the mass transport rate between the two atmospheres might have appeared owing to the incorporation of nitrogen, which enhanced the lattice strain and suppressed the surface diffusivity and/or the vapor transport rate.

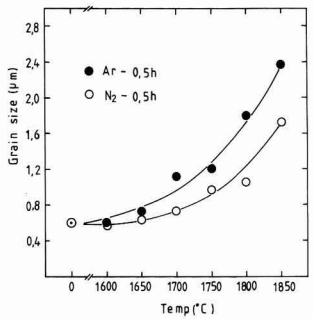

Fig. 8. Temperature dependence of the average grain size for the specimens annealed for 0.5h.

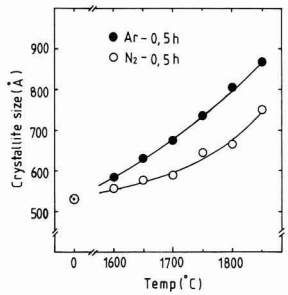

Fig. 9. Temperature dependence of the crystallite size for the specimens annealed for 0.5h.

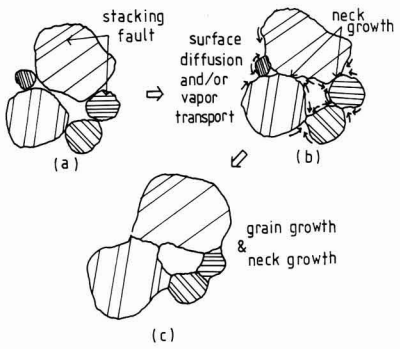

Fig. 10. Illustration of the proposed mechanism of stacking fault annihilation accompanied by the microstructure development; (a) initial packing state, (b) neck growth takes place via surface diffusion and/or vapor transport and (c) large grains grow further by the consumption of small grains. Diminishing in size and disappearance of small grains lead to a decrease in stacking fault density.

The stacking fault annihilation appears to be accompanied by grain growth as shown in **Fig.8**, which shows the average grain sizes of the annealed specimens. **Figure 9** shows the temperature dependence of the crystallite size measured by XRD. It is clearly seen that the crystallite size also increases with increasing annealing temperature. Therefore, grain growth and crystallite growth take place substantially at the same time. It is also seen that the rates of grain growth and crystallite growth in a N_2 atmosphere are both lower than in an Ar atmosphere. This observation can also be attributed to the role of incorporated nitrogen enhancing the lattice strain. Consequently, stacking fault annihilation, grain growth and crystallite growth all appear to take place cooperatively.

4.4. Mechanism of Stacking Fault Annihilation

In general, when a single-phase metal is annealed at a certain high temperature, a recovery process dissipating the strain energy takes place first. This recovery process does not involve any change in the grain shape, the only change being the rearrangement of the faulted parts within the existing grains. Strain-free grains then become nucleated and grow in the matrix.[20] However, in the present case, grain growth and annihilation of stacking faults simultaneously progress with annealing without any observable recovery process.

Taking the present experimental results into consideration, the mechanism of stacking fault annihilation in β-SiC powder compacts will be proposed as illustrated in **Fig.10**. Starting from the initial packing state (Fig.10(a)), surface diffusion and/or vapor transport becomes remarkable as the annealing temperature increases and the neck growth gradually begins to proceed (b). Further annealing gives rise to the growth of larger grains by the consumption of smaller grains (c). It should be noted that throughout the whole process considered here neck growth and grain growth take place without noticeable densification, so that the mass per unit volume (i.e. density) remains almost unchanged. Therefore, the diminishing in size and/or disappearance of small grains leads to a decrease in the stacking fault density, because the formation of new stacking faults within the growing large grains is presumed not to take place.

Crystallite growth as shown in Fig.9 is actually an apparent phenomenon according to the proposed model. Small grains with small crystallites usually become smaller or disappear during high-temperature annealing, and the average crystallite size in total appears to become larger. This is what was observed experimentally.

Summing up the present results and considerations, stacking fault annihilation is a phenomenon not induced by the direct slip of stacking layers within the grains, but is rather subject to a microstructure development where grain growth is controlled specifically by the surface diffusivity

and/or vapor transport rate.

Acknowledgments
The authors express their sincere thanks to Mr. T. Ono of Central Glass Co., Ltd. for supplying the specially ordered β-SiC powders, and to Dr. S.K. Jung of Korea New Ceramics Tech. Lab. for surface area measurement.

References:

1) P.T.B. Shaffer, Acta Crystallogr., Sect. B. Struct. Crystallog. Cryst. Chem., 25, 477-488 (1969).
2) M.S. Paterson, J. Appl. Phys., 23, 805-811 (1952).
3) K. Koumoto, M. Shimohigoshi, S. Takeda and H, Yanagida, Ceram. Trans., 2, 501-510 (1989).
4) G. Sasaki, K. Hiraga, M. Hirabayashi, k. Niihara and T. Hirai, J. Ceram. Soc. Jpn., 94, 779-783 (1986).
5) L.V. Ogbuji, T.E. Mitchell and A.H. Heuer, J. Am. Ceram. Soc., 64, 91-99 (1981).
6) K. Koumoto, S. Takeda, C.H. Pai, T. Sato and H. Yanagida, ibid. 72, 1985-1987 (1989).
7) T. Hase, H. Suzuki and T. Iseki, J. Ceram. Soc. Jpn., 87, 576-582 (1979).
8) H. Tateyama, N. Sutoh and N. Murakawa, ibid., 96, 1003-1011 (1988).
9) S. Hayashi, H. Toraya and T. Amino, Abst. 27th Sympo. Basic Sci. Ceram., Tokyo, (1989) pp.27.
10) Powder Diffraction File, Card No. 29-1126, Section 29-30 (Inorganic Volume), Joint Committee on Powder Diffraction Standards, Swarthmore, PA, (1987).
11) H.P. Klug and L.E. Alexander, X-ray Diffraction Procedures, J. Wiley and Sons, New York, (1974) pp. 618-708.
12) W.H/Hall, Proc. Phys. Soc., A62, 741-743 (1949).
13) N.W. Jepps and T.F. Page, J. Cryst. Growth Characterization, 7, 259-307 (1983).
14) T. Kawamura, Mineral. J., 4, 333-355 (1965).
15) J.D. Hong and R.F. Davis, J. Am. Ceram. Soc., 63, 546-552 (1980).
16) C.H. Pai, A Study on Microstructure Control and High Temperature Thermoelectric Properties of SiC Ceramics, Ph.D. Thesis, University of Tokyo (1990).
17) T. Hase, H. Suzuki, and I. Tomizuka, J. Ceram. Soc. Jpn., 87, 317-321 (1979).
18) C. Greskovich and J.H. Rosolowski, J. Am. Ceram. Soc., 59, 336-343 (1976).
19) W.K. Burton, N. Cabrera and F.C. Frank, Phil. Trans., A243, 299, (1951).
20) C.R. Barett, W.D. Nix and A.S. Teltelman, The Principles of Engineering Materials, Englewood Cliffs, (1973) pp.293-327.

This article appeared in English in Nippon Seramikkusu Kyokai Gakujutsu Ronbunshi (Japanese version), Vol.99, No.6, 1991.

Residual Stress in Glass Layer Coated on Ceramic Substrate

Zuyi Zhang and Naohiro Soga

Department of Industrial Chemistry, Faculty of Engineering, Kyoto University
Yoshida-honmachi, Sakyo-ku, Kyoto-shi, 606 Japan

In order to investigate a possible difference in the adhesion behavior of glass on ceramic substances between silicate and borate glasses, the residual stress in the glass layer of the glass-ceramic layered specimens was measured by a birefringenece method with changing temperature. The experimental results agreed with the calculation for silicate glass, but not for borate glass: the experimental stress for the specimens having a borate glass layer was about 30% lower than the calculated value. The discrepancy was attributed to the occurrence of possible plastic flow in borate glass by the existence of two-dimensional structural units.
(Received November 30, 1990; Accepted March 22, 1991)

Key-words: Residual stress, Glass-ceramic layered composite, Plastic flow, Fracture

1. Introduction

In the cohesion of glass and ceramic layers, the mismatch of their thermal expansion coefficients creates a large residual stress, leading sometimes to cracking or debonding. Such fracture behavior due to the residual stress has been investigated theoretically in the past,[1] and several ways to release the residual stress have been proposed. The introduction of a ductile layer or a fine grain layer is one effective method.[2]

In the author's previous study, alkali borate glasses, particularly ones with high alkali content, exhibited considerable inelastic deformation during stable fracture testing.[3] Therefore, unlike silicate glasses, they are expected to release the residual stress by inelastic deformation like a ductile material when they are coated on a ceramic substrate. In order to confirm this possible relaxation, the residual stress in glass-ceramic layered composites having a borate or silicate glass layer was investigated in the temperature range between room temperature and the softening temperature of the coated glass. The fracture pattern under such anisotropic compression condition was also observed.

2. Experimental Procedure

The two- and three-layered specimens shown in **Fig.1** were used in the present study. The two-layer specimens had $20Li_2O{\cdot}80B_2O_3$ and G11 glass layers on ZrO_2 and Al_2O_3 substrates, respectively. The composition of G11 glass was $58.5SiO_2{\cdot}22.0B_2O_3{\cdot}2.0Al_2O_3{\cdot}2.7ZnO{\cdot}14.7K_2O$(mole%).

The three-layer specimen was comprised of a soda lime silicate glass layer ($72.0SiO_2{\cdot}0.2Al_2O_3{\cdot}9.6CaO{\cdot}3.1Na_2O{\cdot}4.4MgO$), a thin low-melting $45PbO{\cdot}55B_2O_3$ glass layer and a MgO substrate. The substrate's thickness was 4 to 5.5mm.

The $20Li_2O{\cdot}80B_2O_3$ glass specimens were prepared in the following way. A sufficient amount of glass powder, which was prepared from reagent grade Li_2CO_3 and B_2O_3, was placed on a ZrO_2 substrate, and melted in an electric furnace at 800°C for about 10minutes. After the bubbles in the glass layer disappeared, they were cooled down to room temperature in an electric furnace. The glass layer was ground to the required thickness. The G11 glass specimen was prepared in a similar way at 1200°C. The glass layer was 1mm thick. The preparation method of the three-layer specimen is described in detail elsewhere.[6] An appropriate amount of $45PbO{\cdot}55B_2O_3$ glass was premelted and spread over the MgO substrate at 600°C. Then, a bent plate of soda lime silicate glass was placed to cover the melted $45PbO{\cdot}55B_2O_3$. The final thickness of $45PbO{\cdot}55B_2O_3$ glass was less than 0.1mm. All the specimens thus obtained were cut to 22×22mm surface area. In order to reduce scattering during stress measurement, two sides were polished by 1μm diamond paste. The stress was measured by using a polariscope, with the heating rate controlled at 5±0.5°C/min.

The commercial ZrO_2(ZR-11), MgO(MG-12) and Al_2O_3(SSA-S) substrates(Nippon Kagaku Togyo) were used in the present study. They were cut to an appropriate size. The surface used for the adhesion was polished using 800 grit silicon carbide paper, and cleaned ultrasonically in acetone.

3. Results

The variation of stress with temperature in the G11 glass layer is shown in **Fig.2.** The glass layer was considerably thin, compared with the substrate in the present specimens. Furthermore, the modulus of glass was smaller than that of the substrate by several factors, as shown in **Table 1**. Ac-

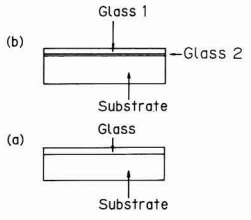

Fig. 1. Schematic illustrations of multilayered composites.
a: two-layer specimen, b: three-layer specimen

cording to the FEM (finite element method) calculation, carried out on a similar shape,[4] the stress in the glass layer can be considered two-dimensional and can be approximated as a finite broad case. Its magnitude at the free surface of the glass layer, is expressed by the following equation.[5]

$$\sigma = \frac{E_g}{1-\nu_g} \frac{2MN^3+3MN-1}{M^2N^4+4MN^3+6MN^2+4MN+1} \cdot \Delta\varepsilon_{th} \quad \cdots\cdots\cdots\cdots\cdots\cdots (1)$$

where E_g and ν are the Young's modulus and Poisson's ratio of glass, $\Delta\varepsilon_{th}$ is the thermal strain appearing from the difference between the thermal expansion of glass and that of substrate, N is the thickness ratio between the glass layer and the substrate, and M is the modulus ratio between the two. The calculation was carried out using eq.(1) by setting the stress at room temperature to the measurement value. The thermal expansion coefficients and elastic constants for G11 glass and Al_2O_3 were taken from pertinent literature.[7,8] Both experimental and theoretical results showed that the residual tensile stress at room temperature was released with increasing temperature at the beginning, but that tensile stress appeared again above 200°C, reflecting the difference in thermal expansion coefficient between G11 glass and Al_2O_3. Furthermore, the magnitude of the calculated stress mostly agreed with the experimental results in the entire temperature range, as observed by Scherer et al..[7] This result seems to confirm that the present stress measurement by a polariscope provides a reasonable stress value at elevated temperatures.

The results obtained from the $20Li_2O{\cdot}80B_2O_3$ specimen are shown in **Fig.3**. The parameters used in the calculation are listed in Table 1. In the calculation, the stress was set to 0 at the starting temperature of 510°C, where the stress was completely relaxed. In contrast to the G11 glass specimen, the slope of the stress vs temperature curve for $20Li_2O{\cdot}80B_2O_3$ glass was only about 70% of the calculated one.

Figure 4 illustrates the stress distribution across the 1.1mm thick glass layer in the $20Li_2O{\cdot}80B_2O_3$ glass specimen at room temperature. The stress decreased by about 10% towards the glass surface, in good agreement with the calculation. When the thickness of glass layer was less than 0.5mm, such variation could not be detected. The numerical calculation also indicated that there was only a change of 2% for the case of 0.5mm(t_s=5mm), which was below the resolution of the present measurement.

The stress variation with temperature for the three-layer specimen is shown in **Fig.5**. The generation of stress in the soda lime silicate glass layer was determined by the

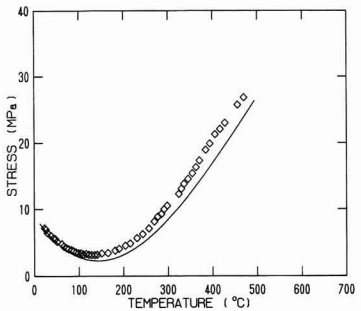

Fig. 2. Stress in G11 glass layer as a function of temperature. Experimental results are shown by square symbols, calculation results by a solid line.($t_{substrate}$=5mm, t_{glass}=1mm) The positive values signify tensile stress.

Table 1 Material Constants used in Stress Calculation

a: elastic constants

	Young's Modulus(GPa)	Poisson's Ratio
ZrO_2	211.2	0.30
MgO	294.8	0.20
Al_2O_3	399.0	0.24
$20Li_2O{\cdot}80B_2O_3$	59.32	0.28
SODA*	83.89	0.23
G11	72.6	0.30

*: Soda lime silicate glass

b: thermal expansion coefficients

	α (10^{-6} /°C)
ZrO_2	$6.56 + 2.60 \times 10^{-2} T - 4.61 \times 10^{-5} T^2$
MgO	$8.56 + 5.01 \times 10^{-2} T - 1.55 \times 10^{-5} T^2$
Al_2O_3	$5.26 + 1.19 \times 10^{-2} T - 1.00 \times 10^{-5} T^2$
$20Li_2O{\cdot}80B_2O_3$	$4.28 + 2.53 \times 10^{-2} T - 3.98 \times 10^{-5} T^2$
SODA	$6.72 + 2.39 \times 10^{-2} T - 6.49 \times 10^{-5} T^2$
G11	$6.47 + 2.00 \times 10^{-3} T$

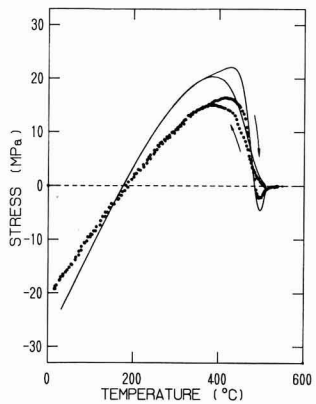

Fig. 3. Stress in $20Li_2O{\cdot}80B_2O_3$ glass layer. Experimental results are shown by circles, calculation results by a solid line.($t_{substrate}$=4.5mm, t_{glass}=0.52mm) The positive and negative values signify tensile and compressive stress, respectively.

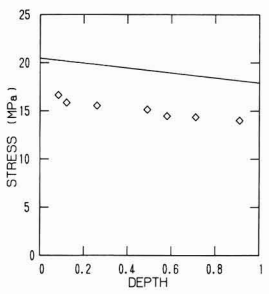

Fig. 4. Stress distribution across glass layer. Experimental results are shown by square symbols, calculation results by a solid line. ($t_{substrate}$=4.5mm, t_{glass}=1.1mm)

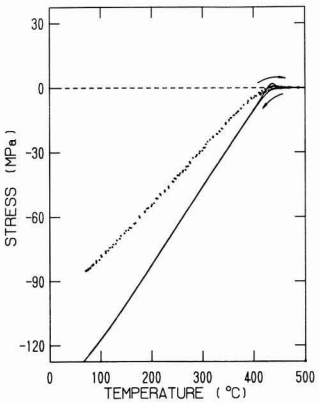

Fig. 5. Stress in soda lime silicate glass layer. Experimental results are shown by circles, calculation results by a solid line. ($t_{substrate}$=3.92mm, t_{glass}=0.67mm)

$45PbO{\cdot}55B_2O_3$ glass layer, because its glass transition temperature was lower than that of soda lime silicate glass by 100°C. In the calculation, the stress was set to 0 at 420°C. The thickness of the $45PbO{\cdot}55B_2O_3$ layer was estimated to be about 0.05mm, by means of EPMA. For such a thin layer, its influence on the stress change in the glass layer was negligible. Again, the measured stress was about 70% less than the calculated value.

4. Discussion

The stress appearing in the borate glass layer was found to be lower than that expected from the calculation. Judging from the good agreement between the experimental and calculated values for the G11 glass specimen, the measuring and calculating procedures used in the present study cannot account for the discrepancy observed in the borate glass specimens. Therefore, the following two possibilities are considered: (1) the changes in thermal expansion coefficient and elastic modulus from the values used in the calculation, due to the appearance of interface layer, and (2) the stress release in the glass layer arising from plastic or other process.

As for the interface layer, the dissolution of ceramic substrate into the glass layer was found to be very small by EPMA. Furthermore, no interface layer could be confirmed. Hence, the thermal expansion coefficient and elastic modulus should change little from those used in the calculation, and consequently the first possibility seems improbable.

Since the discrepancy was observed only on the borate glass specimen but not on the silicate glass specimen, the discrepancy may arise from the intrinsic properties of borate glass, which are different from those of silicate glasses. It is known that the borate network contains a large number of plane triangular BO_3 units, rather than three-dimensional tetrahedral units in silicate glass. These BO_3 units could assist shear deformation. According to recent results, alkali borate glasses show a large fraction of inelastic deformation during stable fracture.[3] B_2O_3 glass has also been found to behave uniquely in the process of deformation and crack formation, when impacted by a small steel ball at high speed.[9] A large degree of deformation/compaction was observed but no cone crack was generated, different from the normal behavior of glasses capable of densification.[10] These experimental facts suggest the occurrence of shear flow in borate glass to release the high stress. The same mechanism has been used to interpret the interference patterns caused by indentation for borate glasses.[11] In the present $20Li_2O{\cdot}80B_2O_3$ and $45PbO{\cdot}55B_2O_3$ glasses, a number of BO_4 units also exist in the forms of tetraborate and pentaborate groups, respectively.[13] The network structure becomes three-dimensional, compared with B_2O_3 glass. However, under applied stress even in the elastic region, the conversion among borate groups seems to occur easily, increasing the two-dimensional structures.[14,15] Hence, the structural conversion probably plays an important role as well in this stress release process.

During the preparation of the three-layer specimens, spherical cracks sometimes appeared in the glass layer from the MgO substrate, as shown in **Fig.6.** On cooling, large tensile stress arose in the MgO substrate, and cracks perpendicular to the interface were generated easily from the small flaws, which were caused by some mechanical damage. In layered specimens, stress concentration has been demonstrated by FEM calculation at the interface near edges.[4] It probably occurred in the present glass layer at such sites, and resulted in the extension of these cracks into the glass layer. This spherical crack growth is essentially equivalent to the decohesion of thin film deposited on a brittle substrate, in which the thin film was subjected to a tensile strain, different from the present case.[12] Due to the residual compressive strain, a planar crack propagated in the substrate parallel to the specimen surface, obeying a zero K_{II} criterion (K_{II}: a shear stress intensity factor). However, such a planar crack was not noticed in the present study. This may be associated with the fact that the glass layer was fairly thin in comparison with the substrate. The reason why the cracks grew in spherical manner rather than along the cracks in MgO substrate is not clear at this time, and should be investigated in the future.

5. Conclusion

The stress in the glass layer of glass-ceramic layered specimens was measured by a birefringenece method with changing temperature. There was satisfactory agreement between the experimental and calculated results for a silicate glass, while the specimens involving a borate glass layer revealed a lower value than the numerical calculation. This discrepancy was attributed to the structural difference between borate and silicate glasses. The two-dimensional

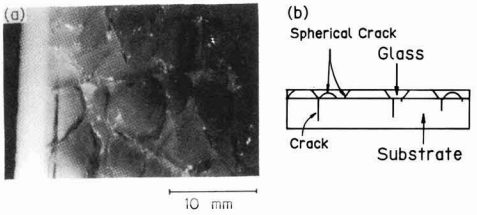

Fig. 6. a: Photograph of crack morphology in glass layer and b: Schematic demonstration of the specimen's section

units in borate glass are considered to assist shear flow, releasing high stress at the interface.

References:

1) M.D. Drory and A.G. Evans, J. Am. Ceram. Soc., 73, 634-638 (1990)
2) F. Wakai, H. Kato, S. Sakaguchi and N. Murayama, Yogyo-Kyokaishi, 94, 1017-1020 (1986).
3) K. Hirao, J. Matsuoka and N. Soga, J. Non-Cryst. Solids, 112, 336-340 (1989).
4) Y. Itoh, Y. Ishiwata and H. Kashiwaya, J. Ceram. Soc. Jpn., 97, 747-752 (1989)
5) T. Timoshenko and J.N. Goodier, Theory of Elasticity, McGraw-Hill, New York(1970), pp.433-435
6) Z. Zhang, K. Nakanishi, K. Hirao and N. Soga, J. Ceram. Soc. Jpn., 97, 365-369 (1989).
7) G.W. Scherer and S.M. Rekhson, J. Am. Ceram. Soc., 65, 399-406 (1982).
8) N. Soga, J. Soc. Mater. Sci. Jpn., 32, 229-236 (1983).
9) M.M. Chaudhri and C.R. Kurkjian, J. Am. Ceram. Soc., 69, 404-410 (1986).
10) J.T. Hagan, J. Mater. Sic., 14, 462-466 (1979).
11) K. Hirao, Z. Zhang, H. Morita and N. Soga, J. Soc. Mater. Sci. Jpn., in press
12) M.D. Thouless, A.G. Evans, M.F. Ashby and J. W. Hutchinson, Acta Metall., 35, 1333-1341 (1987).
13) B.N. Meera, A.K. Sood, N. Chandrahas and J. Ramakrishna, J. Non-cryst. Solids, 126, 224-230 (1990).
14) Z. Zhang and N. Soga, Phys. chem. Glasses, in press
15) N. Soga, Z. Zhang, K. Nakanishi and K. Hirao, J. Non-Cryst. Solids, 112, 377-380 (1989).

This article appeared in English in Nippon Seramikkusu Kyokai Gakujutsu Ronbunshi (Japanese version), Vol.99, No.6, 1991.

Injection Molding of Highly-Purified Hydroxylapatite and TCP Utilizing Solid Phase Reaction Method

Yoshimitsu Kankawa, Yasunari Kaneko* and Katsuyoshi Saitou

Kyoto Municipal Institute of Industrial Research
17, Chudouji-Minamimachi, Simogyo-ku, Kyoto-shi, 600 Japan
*Faculty of Science and Engineering, Ritsumeikan University
Tojiin-Kitamachi, Kita-ku, Kyoto-shi, 603 Japan

Injection molding of hydroxylapatite and TCP utilizing the solid phase reaction method was studied. Rod like test pieces (φ6×501) were produced by injection molding using two powder-binder compounds: (A) 6mol of calcium secondary phosphate (98.0%), 4mol of calcium carbonate (99.0%) and several organic binders; (B) 6mol of calcium secondary phosphate (98.0%), 3mol calcium carbonate (99.0%) and several organic binders. After the binder extraction process, the test pieces were heated up to 1000 to 1300°C at a rate of 100°C/hour.
When sintered at 1300°C, the sintered test piece (A) was found to consist of hydroxylapatite according to X-ray diffraction and FT-IR. On the other hand, the sintered test piece (B) was found to consist of α-TCP.
[Received August 24, 1990; Accepted March 22, 1991]

Key-words: Ceramics injection molding, Hydroxylapatite, TCP, Debinding, Sintering, Solid phase reaction, Calcium phosphate

1. Introduction

Calcium phosphate compounds have recently received considerable attention as substitute materials for bones of living bodies and as electronic ceramics used, for example, for sensors.[1-3] These materials, however, are unsuitable to high-volume molding of complex-shaped products with high dimensional accuracy because they are molded mainly with a press. Hydroxylapatite is usually synthesized by the wet method, so that the composition and physical properties of the resulting compound differ greatly with the synthesizing temperature and pH value. We reported the injection molding of less expensive calcium secondary phosphate, which is obtained from phosphoric acid produced as foam waste in the molding of plastic foam, and we also revealed the possibility of sintering of hydroxylapatite in a series of processes.[4] Afterwards, we found that the product sintered by the above method contains calcium oxide as a by-product, and the change of calcium oxide into calcium hydroxide reduces the strength of the sintered body. This report presents the reaction process and physical properties of a sintered body obtained by using calcium secondary phosphate of 98.5% or higher purity as a starting material to get highly-purified hydroxylapatite containing no calcium oxide. The reaction process and physical properties are also studied for sintered bodies that have been injection molded by changing the mixing ratio of calcium secondary phosphate and calcium carbonate to get β-TCP in sintering.

2. Experimental Method

2.1. Experimental Procedure

Calcium secondary phosphate (98.0% purity, Class 1 reagent) and calcium carbonate (99.0% purity, Class 1 reagent) were used as inorganic powders. The composition ratio in a mol of calcium secondary phosphate to calcium carbonate was taken as 6:4 from the solid phase reaction formula for hydroxylapatite. To obtain calcium tertiary phosphate, the composition ratio of calcium secondary phosphate to calcium carbonate was taken as 2:1. The organic binders used in this experiment were ethylene-vinyl acetate copolymer (EVA), poly-n-butyl methacrylate (PBMA), modified wax (WAX), amide lubricant (AMID), and dibutyl phthalate (DBP). **Table 1** gives the composition of the compound.

Hereafter, the compound of the composition ratio of 6:4 between calcium secondary phosphate and calcium carbonate is referred to as A, and that of 2:1 as B.

Figure 1 shows the experimental procedure. The heated kneading was performed in a kneader (supplied by Toshin) for 45 minutes. In the injection molding, Rod like test pieces (φ6×501) were produced at a molding temperature of 110°C by using a vertical plunger-type injection machine (supplied by Sanjou Seiki). The molded test pieces were kept at 50°C for 2 hours in the atmosphere by using a binder-extracting furnace (supplied by Fine), and then heated to 420°C at a rate of 6°C/h and kept at that temperature for 2 hours before being furnace cooled. The test pieces were sintered by heating from room temperature to 1000°C to 1300°C at a rate of 100°C/h in the atmosphere by using an

Table 1. The composition of the compound (part by weight).

	A	B
$CaHPO_4$	67	73
$CaCO_3$	33	27
EVA	7	7
PBMA	7	7
WAX	4	4
APP	2	2
AMID	1	1
DBP	2	2

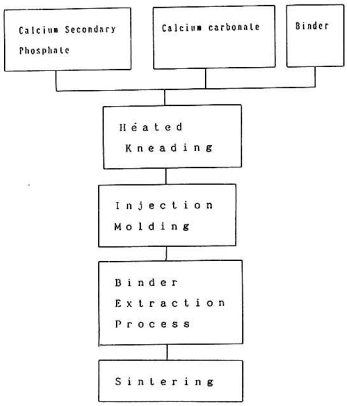

Fig. 1. Experimental procedure.

electric furnace (supplied by Chugai Ro) and kept at each temperature for 2 hours.

2.2. Determination of Physical Properties and Composition of Sintered Body

The change in weight of binder-extracted test pieces during sintering was measured in dry air at a heating rate of 10°C/min with thermogravimetric equipment (Perkin Elmer, TGA 7).

For the bending strength test of the sintered body, the sintered rod-like test pieces were used without being polished. The bending strength test was performed at room temperature five times for each point with a universal testing machine (Shimadzu Corporation, AG-5000D) with a cross-shead speed of 0.5mm/min. Density of the sintered body was measured by the Archimedean method.

For the identification of sintered body composition, the test pieces that had been subjected to the bending test were ground into powder and analyzed by using an X-ray diffractometer (Mac Science, MXP, Cu tube, 40kV, 20mA). The ground powder of sintered body was diluted to about 2% with KBr and made into pellets, so that infrared absorption spectrum measurement could be performed (with an FT-IR (Perkin Elmer, 1760X)).

The microstructures of the fractured surface of test pieces after being subjected to a compression test were observed with a scanning electron microscope (Hitachi, S-510).

3. Experimental Results and Discussion

3.1. Molding and Binder Extraction of Mixture of Inorganic Powder and Organic Binder

Figure 2 shows the measurement results for flow behavior of Compounds A and B given in **Table 1**. The measurement was made at 110°C by using a capillary flow tester (Toyo Seiki, Capillograph 1B) with a capillary of L/D=10. Both compounds exhibited non-Newtonian flow behavior. The authors reported that the apparent viscosity at shear rates of 10^2 to 10^3 sec^{-1} was 10^3 to 10^4 poise as the optimum condition in injection molding of ceramics powder.[5] When the apparent viscosity is less than 10^3 poise, a turbulent flow of compound occurs in the mold during molding, which often causes defects in the molded body in the process after debinding. When the apparent viscosity is higher than 10^4 poise, the molding temperature during injection molding increases significantly, which often causes the mold to be insufficiently filled with the compound. For the compounds used in this experiment, the apparent viscosity is 10^3 to 10^4 poise in the shear rate range between 10^2 and 10^3 sec^{-1}. This means that the compounds are suitable for injection molding.

Next, binder extraction was performed on the green compacts after being injection molded. The binder extraction process takes the largest amount of time among the injection molding processes of ceramics, and defects in the compact often occur in this process. Therefore, it is most important to determine the type, composition ratio, and loadings of organic binder blended in ceramics.

When the binder was extracted from the green compacts of A and B compounds molded in this experiment, binder-extracted bodies without cracks and voids were obtained.

3.2. Sintering of Binder-Extracted Sample

3.2.1. Sintering of Binder-Extracted Sample of Compound A

The change in weight of binder-extracted sample during sintering was measured by thermogravimetry. The measurement results are shown in **Figs.3(a)** and **(b)**. This figure indicates that the weight begins to decrease at about 700°C and becomes nearly constant at about 860°C for both compounds. This reveals that the solid phase reaction takes place in the temperature range of about 700°C to 900°C for the binder-extracted samples of both compositions.

Figure 4 shows the X-ray diffraction patterns for the samples obtained by heating the binder-extracted bodies of both compositions to 600°C to 1300°C on the basis of thermogravimetry results. In the X-ray diffraction patterns shown in Figs.4(a) and (b), the difference in peak is not found between the binder-extracted sample that shows no change of thermogravimetric curve in Fig.3 and the sample sintered at 600°C. However, peaks were found for calcium carbonate (at temperatures between the binder extraction temperature (420°C) and a sintering temperature of 600°C) and for γ-calcium pyrophosphate (that seems to change from calcium secondary phosphate). At a sintering temperature of 800°C in the weight loss region in the thermogravimetric curve, the peak that would be for calcium carbonate is greatly reduced, and the peak for β-TCP (calcium tertiary phosphate) is newly found. At a sintering temperature of 1000°C beyond the weight loss region in the thermogravimetric curve, the peak for hydroxylapatite, in addition to that for β-TCP, and also the peak for calcium oxide (that seems to change from unreacted calcium carbonate) are found. As the sintering temperature increases from 1000°C to 1300°C, the peaks for β-TCP and calcium oxide are greatly reduced

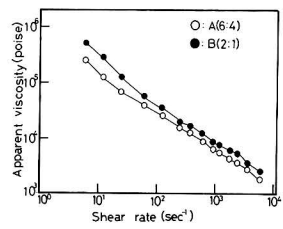

Fig. 2. Dependence of apparent viscosity of shear rate for powder-binder compounds at 110°C.

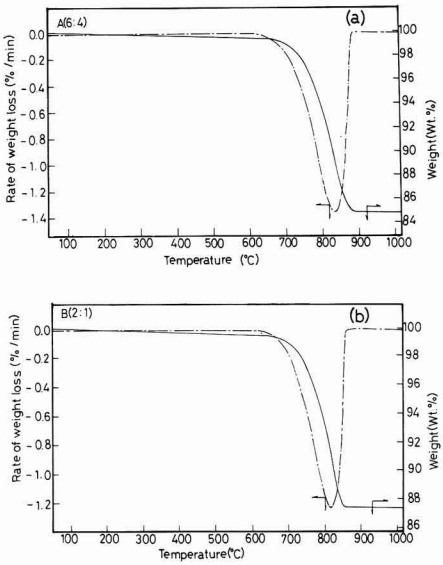

Fig. 3. TGA curves of the binder extracted sample (A) and (B).
(a) : sample (A), (b) : sample (B)

and the peak of hydroxylapatite is found.

Figure 5(a) shows the spectral patterns obtained by using FT-IR. At sintering temperatures between 1000°C and 1300°C, the peak for calcium oxide found at 3650cm^{-1} decreases as the sintering temperature increases, as with the X-ray diffraction data shown in Figs.4(a) and 4(b). The absorbance of calcium oxide is not found at 1300°C. The production of hydroxylapatite is confirmed from the absorbance of OH at 632cm^{-1} and that of PO_4^{3-} at 470, 571, 601, 632, 961, 1045, and 1089cm^{-1}, as well as the absorbance of OH at 3571cm^{-1} found in hydroxylapatite in Fig.5(a). The above result indicates the following: for compound A, the composition of sintered body was unchanged at sintering temperatures up to 700°C; at a sintering temperature of about 800°C, β-TCP was first produced, and then hydroxylapatite was produced as the sintering temperature increased; and the formerly produced β-TCP was changed into hydroxylapatite by reacting with calcium oxide. It was found that a sintered body consisting of hydroxylapatite is obtained at a sintering temperature of 1300°C. As a result of the measurement of Ca/P ratio by fluorescent X-rays, hydroxylapatite with a nearly theoretical ratio of 1.66 was obtained at a sintering temperature of 1300°C. From the above result, it is thought that solid phase reactions of not only Formula (a) but also Formula (b) occur at the same time.[6,7]

$$6CaHPO_4 + 4CaCO_3 \rightarrow Ca_{10}(PO_4)_6(OH)_2 + 2H_2O + 4CO_2 \quad \ldots\ldots(1)$$

$$3Ca_3(PO_4)_2 + CaO + H_2O \rightarrow Ca_{10}(PO_4)_6(OH)_2 \quad \ldots(2)$$

3.2.2. Sintering of Binder-Extracted Sample of Compound B

In the X-ray diffraction patterns shown in Figs.4(c) and (d), peaks are found (as in compound A) for calcium carbonate (at temperatures between the binder extraction temperature (420°C) and a sintering temperature of 600°C) and for γ-calcium pyrophosphate (that seems to change from calcium secondary phosphate). At a sintering temperature of 800°C, the peak that would be for calcium carbonate decreases greatly, and the peak for β-TCP is newly found. At a sintering temperature of 1000°C, a peak for β-TCP containing small amounts of β-calcium pyrophosphate is found. Although the peak for β-TCP is found in the temperature range between 1000°C and 1100°C, no peak for β-TCP is found at sintering temperatures above 1200°C, and the absorbance of α-TCP is found.

Next, in the FT-IR spectral patterns in Fig.5(b), the peaks

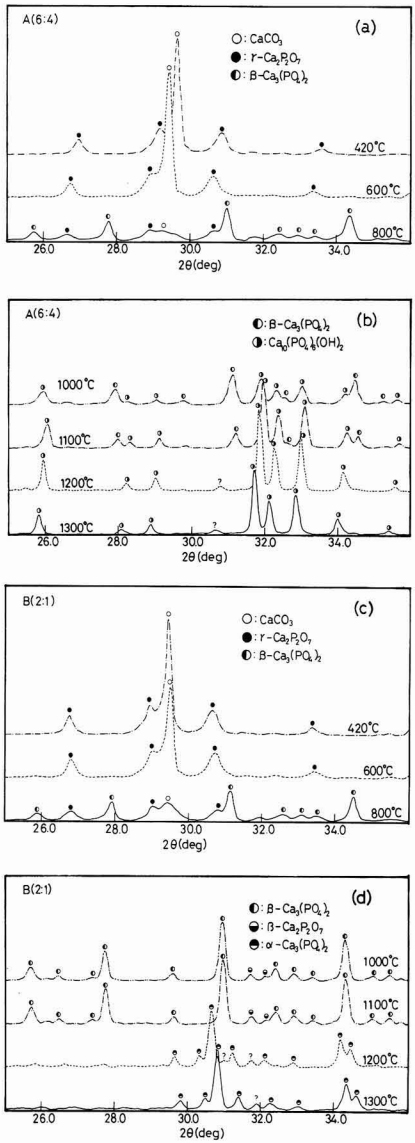

Fig. 4. Change of X-ray diffraction patterns of sample (A) and (B) at various sintering temperatures.
(a) : sample (A) at 420°, 600° and 800°C
(b) : sample (A) at 1000°, 1100°, 1200° and 1300°C
(c) : sample (B) at 420°, 600° and 800°C
(d) : sample (B) at 1000°, 1100°, 1200° and 1300°C

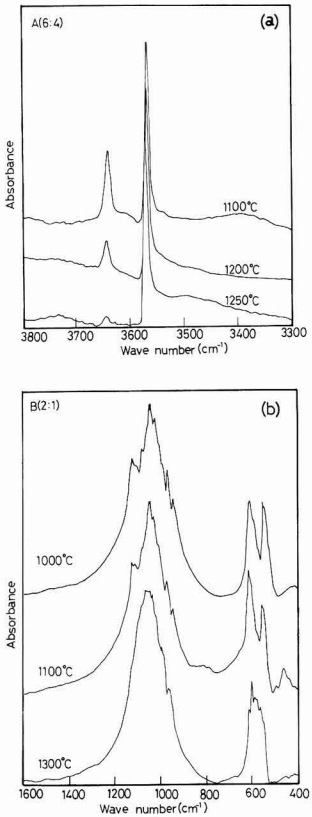

Fig. 5. Change of IR spectral patterns of sample (A) and (B) at various sintering temperatures.
(a) : sample (a) at 1100°, 1200° and 1250°C
(b) : sample (b) at 1000°, 1100° and 1300°C

of phosphoric acid (PO_4^{3-}) at 1600 to 400cm^{-1} at sintering temperatures between 1000°C and 1300°C are considered. The absorbance of β-TCP is found at sintering temperatures of 1000°C and 1100°C, and the absorbance at 1100cm^{-1} and 600cm^{-1} changes at 1300°C. Like the above-described X-ray diffraction pattern, β-TCP changes into α-TCP at sintering temperatures above 1100°C.

From the measurement results of X-ray diffraction and FI-IR, it is considered that the following reaction may take place on compound B.[6)]

$$2CaHPO_4+CaCO_3 \rightarrow Ca_3(PO_4)_2+H_2O+CO_2$$

$$\beta\text{-}Ca_3(PO_4)_2 \xrightarrow{1100℃} \alpha\text{-}Ca_3(PO_4)_2$$

3.3 SEM Observation and Mechanical Properties of Sintered Sample

3.3.1. SEM Observation and Physical Property Measurement of Sintered Sample of Compound A

The fracture surface of the sample sintered at 1000°C to 1300°C and subjected to a bending test was observed with a scanning electron microscope. **Figure 6** shows the SEM photographs. As seen from the figure, the shape and size of grains are uneven, the growth of grain has not proceeded, and the bonding between grains has not proceeded at 1000°C. As the sintering temperature increases, the grain growth proceeds, and the bonding between grains proceeds. It has been found that the sample consisting of hydroxylapatite that was sintered at 1300°C has pores of 5μm or smaller.

Figure 7(a) shows the porosity and bulk density of the sintered sample. The porosity decreases with the increase in sintering temperature, whereas the bulk density increases

Fig. 6. SEM photograph of fracture surfaces of sintered sample (A) and (B) a various sintering temperatures.

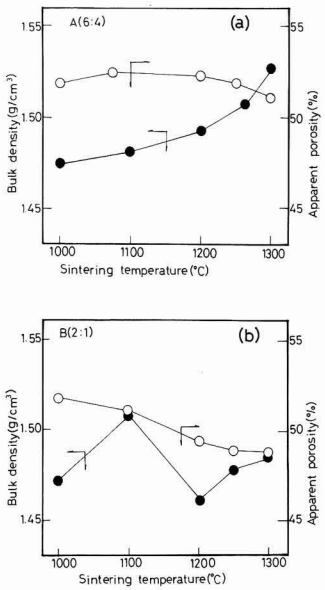

Fig. 7. Bulk density (●) and apparent porosity (○) of sintered sample (a) and (b).
(a) : sample (A), (b) : sample (B)

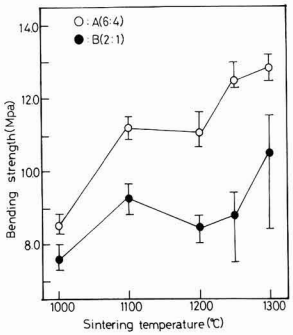

Fig. 8. Compressive strength for rod like test pieces of sintered samples (A) and (B).

with the increase in sintering temperature. This fact agrees with the results of SEM observation. The reason for the decrease in porosity and the increase in bulk density may be that β-TCP, a by-product, disappears as the sintering temperature increases and a sintered body consisting of hydroxylapatite alone is produced.

To determine the strength of the sintered sample, a three-point bending test was conducted on rod-like test pieces that had been sintered at various temperatures and not ground. The result of the bending test is shown in **Fig.8**. The sample sintered at a higher temperature has strong bonding between grains, higher bulk density, and lower porosity. The bending strength is about 12.5MPa at a sintering temperature of 1300°C.

3.3.2. SEM Observation and Physical Property Measurement of Sintered Sample of Compound B

The SEM photographs indicate that, like compound A, the shape and size of grains are uneven, the growth of grains has not proceeded, and the bonding between grains has not proceeded at 1000°C. As the sintering temperature increases, the grain growth proceeds, and the bonding between grains proceeds. It has been found that the β-TCP obtained in this experiment has continuous pores of 5μm or smaller at a sintering temperature of 1300°C.

Figure 7(b) shows the porosity and bulk density of sintered sample. The porosity decreases with the increase in sintering temperature, whereas the bulk density reaches the maximum value at a sintering temperature of 1100°C, then decreases, and increases above 1200°C. The reason for the temporary decrease in bulk density above 1100°C may be that β-TCP changes into α-TCP as the sintering temperature increases in this temperature range.

To determine the strength of a sintered sample, a three-point bending test was made on rod like test pieces that had been sintered at various temperatures and not ground. The results of the bending test are shown in **Fig.8**. The bending strength reaches a peak value at a sintering temperature of 1100°C, then decreases in the temperature range between 1100°C and 1200°C, where β-TCP changes into α-TCP, and increases again above 1200°C, where the porosity decreases.

4. Conclusions

The following conclusions have been drawn from the injection molding of calcium phosphate compounds utilizing the solid phase reaction method.

1) A sintered body consisting of hydroxylapatite, containing almost no by-product, was produced by sintering and binder extraction of injection molded compact consisting of highly-purified calcium secondary phosphate (6mol) and calcium carbonate (4mol). The sample sintered at 1300°C had a bending strength of 12.5MPa.
2) By changing the composition ratio of calcium secondary phosphate to calcium carbonate into 6mol to 3mol, a sintered body consisting of β-TCP, containing small amounts of unreacted β-calcium pyrophosphate was obtained at sintering temperatures below 1100°C. At sintering temperatures above 1200°C, β-TCP changed into α-TCP. The bending strength was 10MPa at 1300°C, which was lower than the above-described sintered body consisting of hydroxylapatite.

References:

1) M. Sakuhana, Ceramics, 24, 601-607 (1989).
2) H. Aoki, M. Akao, M. Higashikata, S. Hasegawa and H. Ukegawa, ditto, 24, 614-617 (1989).
3) S.F. Hulbert, L.L. Hench, D. Forbers and L.S. Bowman, Ceram. Inter., 8, 131-140 (1982).
4) Y. Kankawa, K. Saitou, Y. Kaneko and H. Iwasaki, J. Jpn. Soc. Powder and Powder Metallur. 37, 194-197 (1990).
5) Y. Kankawa, K. Saitou and T. Tanaka, Synthetic Resins, 34, 42-48 (1988).
6) T. Kanazawa and H. Kadoma, Kagaku no Ryoiki, 27, 662-672 (1973).
7) T. Kanazawa and H. Kadoma, ditto, 752-761 (1973).

This article is a full translation of the article which appeared in Nippon Seramikkusu Kyokai Gakujutsu Ronbunshi (Japanese version), Vol.99, No.6, 1991.

A Screening-Diagram for Non-Destructive Inspection

Koichi Kitakami*, Yohtaro Matsuo and Shiushichi Kimura****

* Information Systems Research Center., Canon Inc.
890-12, Kashimada, Saiwai-ku, Kawasaki-shi, 211 Japan
** Department of Inorganic Materials, Faculty of Engineering, Tokyo Institute of Technology
2-12-1, Ookayama, Meguro-ku, Tokyo, 152 Japan

In brittle materials, unstable crack-extension leads to direct fracture. Therefore, some techniques such as X-ray scanning, Ultrasonic microscopy, and Acoustic Emission (A.E.) have been developed for detecting the position and size of defects. However, these techniques do not have high enough precision. We have analyzed crack-size and crack-orientation distributions of fracture origins statistically and proposed an effective method for non-destructive inspection (N.D.I.).

In this paper, joint probability density contour-lines of fracture-location in test pieces subjected to 3-point bending load are shown. Furthermore, "N.D.I.-line" calculated from the joint cumulative distribution function is presented. A more effective "screening-diagram" derived from N.D.I.-line is also suggested.

[Received August 30, 1990; Accepted January 24, 1991]

Key-words: Non-destructive inspection, Structural ceramics, Weibull statistics, Screening-diagram, N.D.I.-line

1. Introduction

As is well known, the fracture of brittle materials including structural ceramics is caused by crack propagation from the weakest defective points (fracture origins) in the materials.

Considering that the shortest way to improving the strength reliability of brittle materials is to correctly recognize the defects as origins of fracture, studies are being widely pursued on nondestructive inspection. They mostly use such measuring techniques as X-ray and ultrasonic flaw detection methods to recognize the size and location of defects. However, there is no sufficient proof that defects detected by such methods are origins of fracture. There is also an acoustic emission method which estimates defect sizes etc. by measuring sounds generated when cracks propagate. From the point of view of screening cost, it is certainly not a realistic method. Approaches by such types of measurement for recognizing defect distribution seem practicable as long as defects in materials such as metals are relatively large but unless used together with other useful information, they seem hardly practicable with fine ceramics in which defects as fracture origins are small.

We have been utilizing an approach which, differing from ones by measurement, recognizes distribution defects as fracture origins by estimating locations of fractures origins stochastically. Being by way of estimating locations of fracture origins, the defect distributions obtained by this approach permit only defects as actual fracture origins to be known. In accordance with probability theory for fracture locations based on competing risk theory, we theoretically derived dimensional distributions of defects as fracture origins and strength distributions after screening for 3-point bending stress fields and proved their validity by applying them to large quantities of test data on 3-point bending of hot pressed silicon nitride.[1-4]

Recently, reviewing the conventional method for operating nondestructive inspection, we have pointed out that conventional nondestructive inspection is not sufficient. We have presented a new effective method of nondestructive inspection,[5] by showing that it is improtant to determine the screening size of defect and the screening area if test pieces have stress gradients.

In this paper, using test pieces subjected to 3-point bending stresses, we show NDI (nondestructive inspection) lines by defining the geometrical shapes of the areas to be actually screened in the two-dimensional coordinate regions specified by the longitudinal and thickness directions of test pieces. We also present a new screening diagram which can immediately determine the screening area for Wiebull shape parameter m≥10.

2. General Theory

We have already presented a "probability theory for fracture locations based on competing risk theory" which deals with different types of fracture origins at once.[1,2] The probability of an object whose reference stress σ_m is (σ_m, $\sigma_m+d\sigma_m$ being fractured at point (ξ, ξ-dξ) in area A_i can be formulated as

$$h_A(\sigma_m, \xi)d\sigma_m d\xi = \prod_{i=1}^{n} R_i(\sigma_m) \times \sum_{j=1}^{n} \lambda_j \, d\sigma_m d\xi \quad \ldots (1)$$

where R_i is the reliability function and λ_i is failure rate, which are given by

$$R_i(\sigma_m) = 1 - \int_0^{\sigma_m} \int_{\xi_i} h_{A_i}(\sigma_m, \xi) \, d\xi d\sigma_m,$$

$$\lambda_j = \frac{h_{A_j}(\sigma_m, \xi)}{R_j(\sigma_m)}$$

$$A = A_1 \oplus A_2 \oplus \cdots A_n. \quad \ldots (2)$$

further

$$h_{A_i}(\sigma_m, \xi) = \exp(-B_i)\frac{\partial}{\partial \sigma_m}(G_i),$$

$$B_i = \int_{\xi_i} G_i d\xi,$$

$$G_i = \left(\frac{\sigma - \sigma_{ui}}{\sigma_{0i}}\right) \cdot \left(\frac{dA_i}{d\xi}\right) \quad \cdots\cdots\cdots\cdots (3)$$

2.1. Joint Probability Density Function for Fracture Locations

In the following, we will proceed with analysis on internal defect (i=1), which takes the 3-point bending test (see **Fig.1**) into account. When a so-called rectangular-cross section beam (one-side span length: L, width: b, height: 2h) is under a 3-point bending load, the stress at a given point inside it is given by

$$\sigma = \frac{\sigma_{max}}{Lh} \cdot x(h - y), \quad \sigma_{max} = \frac{3WL}{4bh^2} \quad \cdots\cdots\cdots (4)$$

Where the origin of coordinate x and y is at one fulcrum of 3-point bending. The location parameter is zero and fractures from the beam sides are neglected. Thus, from eqs.(3) and (4), risk of rupture B_1 can be obtained as

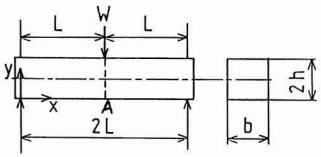

Fig. 1. The coordinage system in the three-point bending test.

$$B_1 = V_{e0}\left(\frac{\sigma_{max}}{\sigma_{01}}\right)^{m_1}, \quad V_{e0} = \frac{2bLh}{(m_1 + 1)^2} \quad \cdots\cdots (5)$$

By using equations (3) and (5), the joint probability density function for fracture location (x, y) due to an internal defect is formulated as

$$h_{A_1}(x, y) = \frac{(m_1 + 1)^2}{Lh}\left(\frac{L-x}{L}\right)^{m_1} \cdot \left(\frac{h - y}{h}\right)^{m_1} \quad \cdots\cdots (6)$$

where L and h are dimensions of the test piece and m_1 is a shape parameter. Here, for convenicence of analysis, the origin of the coordinate axis is taken at the maximum stressed point. From eq.(1), contour maps of the joint probability density function with m_1=5, 10 and 15 were obtained (see **Fig.2(a), (b)** and **(c)**). Each map contains 9 contour lines, which are decasectors of the maximum joint probability density value (the joint probability density value peaks at maximum stress point A. The three maps in Fig.2 also show trends for the maximum joint probability density value to increase with the contour lines becoming denser and for fracture origins to concentrate in a small area around the maximum stress points as the value of the shape parameter increases.

Although it has already been pointed out that where there is a stress gradient in the test pieces (as in 3-point bending tests), the locations of fracture origins are not all over the entire region of the test pieces but rather confined to specific areas, there have been no studies actually showing fracture origin areas qualitatively and quantitatively with the dimen-

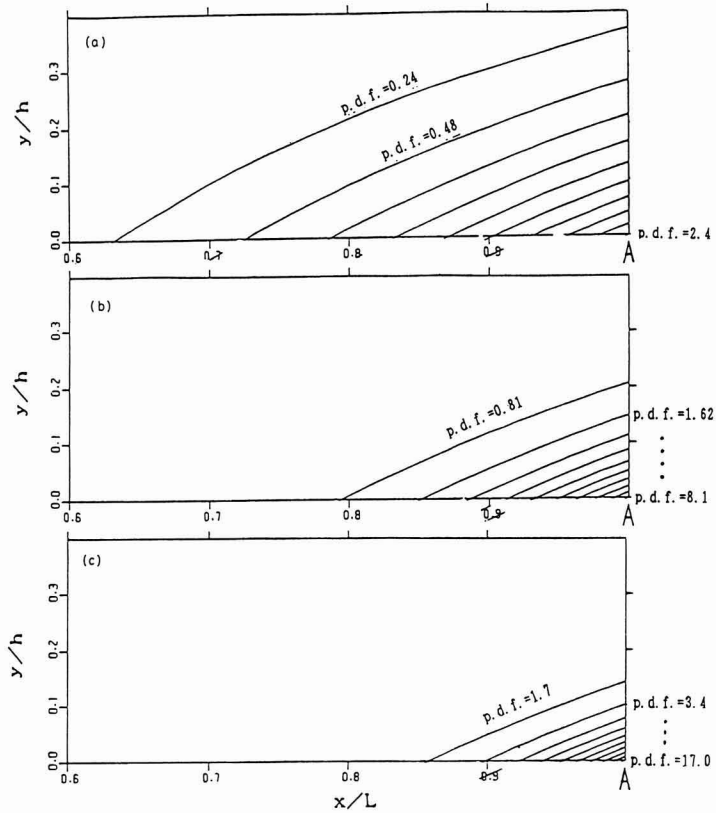

Fig. 2. Contour-lines of probability density function. (a) m_1=5, (b) m_1=10, (c) m_1=15

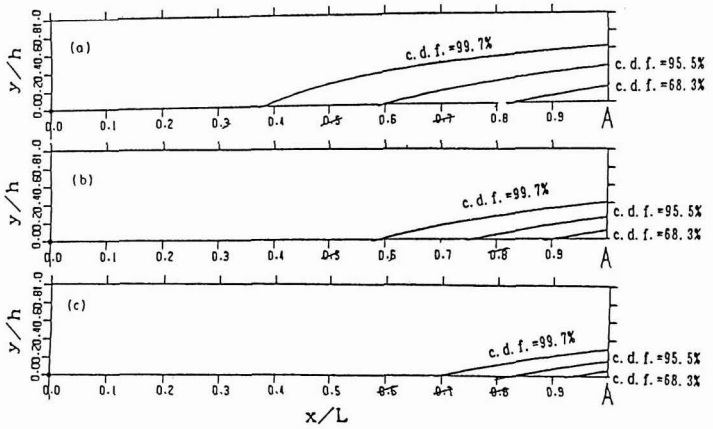

Fig. 3. Contour-lines of cumulative distribution function. (a)m_1=5, (b) m_1=10, (c) m_1=15

sions of test samples and shape parameters as shown in Fig.2. Thus, it was difficult to know to what area fracture origins are confined. In contrast, the recognition of the relation shown in Fig.2 is very useful for nondestructive inspection, since it is possible, when carrying out nondestructive inspection on the assumption of 3-point bending stresses for a group of test pieces, to determine beforehand the screening areas. Fig.2 also shows that the contour lines draw moderate convex curves nearly in parallel.

The above analysis is applicable likewise to stresses which permit joint probability density functions for fracture locations to be derived.

3. Joint cumulative distributions for fracture locations

This chapter deals with joint cumulative distributions in various ways. From the joint probability density function shown in Chapter 2, the joint cumulative distribution function for fracture location (x, y) is formulated by integrating the density function along the contour in Fig.2 as

$$H_{A_1}(x,y) = \int_0^x\int_0^y h_{A_1}(x,y)\mathrm{d}x\mathrm{d}y = \left\{1-\left(\frac{L-x}{L}\right)\right\}^{m_1+1}\cdot\left\{1-\left(\frac{h-y}{h}\right)^{m_1+1}\right\} \quad \cdots\cdots\cdots\cdots\cdots\cdots\cdots\cdots (7)$$

Using equation (7), we present NDI lines and screening diagrams as follow:

3.1. NDI Lines

Using equation(η), we calculated cumulative distribution curves with 3 reliability levels: 68.3% (within ±1σ), 95.5% (within ±2σ) and 99.7% (within ±3σ), where σ denotes standard deviation (see **Fig.3(a), (b)** and **(c)**). Fig.3 shows that as the shape parameter increases, also with cumulative distribution curves, the areas enclosed by the curves decrease. It also clearly shows relative differences in fracture origin areas among the three reliability levels. Such cumulative distribution curves preliminarily prepared for the size of test pieces to be analyzed permit screening areas at required reliability level to be known at once and will possibly be greatly helpful in increasing screening efficiency.

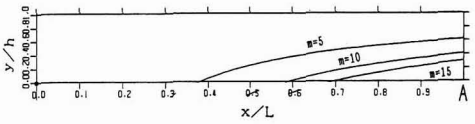

Fig. 4. 99.7% NDI-line.

Figure 4 shows 99.7%NDI lines for different shape parameters. Particularly remarkable is that even with m_1=5 which involves relatively large scatter (wide fracture origin area), the expected area of fracture origins is not as wide as half of the region on the tensile side of the test piece. In other words, we have now recognized with theoretical proof that screening on the assumption of 3-point bending stresses can be confined to a narrow area. This can greatly save time and money.

In addition, for two extremes: $m_1 \to 0$ and $m_1 \to \infty$, 99.7%-NDI lines cover the entire area of the test sample or stand most closely to the maximum stress point A respectively.

3.2. Screening diagrams

Figs.3 and 4 are shown at the same ratio as the aspect ratio of the test pieces. Thus, the curves shown in them are similar to the cumulative distribution curves in actual test pieces. Looking at Fig.4 again from this point of view, we can find an important trend; that is, joint cumulative probability lines with $m_1 > 10$ can be approximated by straight lines. Screening is far easier for an area enclosed by straight lines than for an area enclosed by curves.

Figure 5 shows such linear approximation adjusted for easy use. The horizontal (x/L) and vertical (y/h) axes are graduated by the even scale and half of the tensile area is formed into a square (this figure is called a screening diagram).

The use of the screening diagram will be outlined below by referring to Fig.5(c). Suppose that a sample with shape parameter m_1=20 is tested under nondestructive inspection (screening) at a reliability level of 99.7% (±3σ). The area to be screened is inside the triangular ABC shown in Fig.5(c) (for half of the longitudinal length of the test piece).

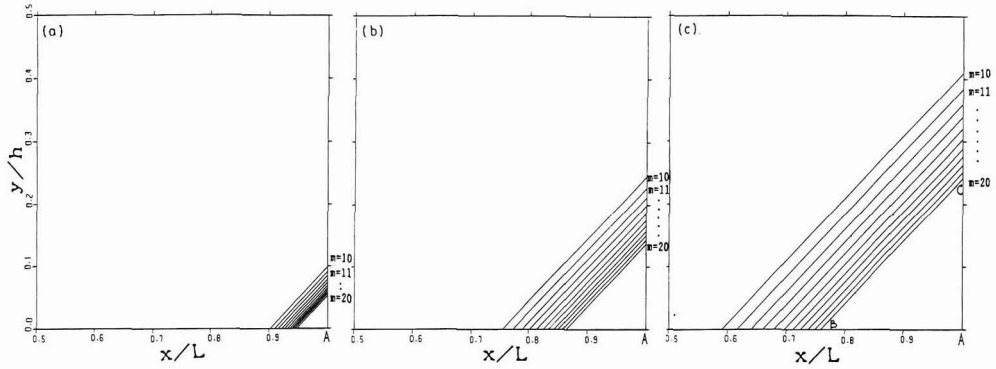

Fig. 5. Screening diagram. (a) 68.3%(±1 σ), (b) 95.5%(±2 σ), (c) 99.7%(±3 σ)

Considering that the vertical and horizontal axes in Fig.5(c) are normalized by sample dimensions L and h respectively, sufficient effect of screening can be obtained by calculating actual dimensions and screening only the area enclosed by these actual dimensions. Thus, the areas to be screened can be estimated easily for different reliability levels: 68.3%(within ±1σ) and 95.5% (within ±2σ).

As in Chapter 2, the analysis in this Chapter 3 can be performed exactly in the same procedure for stress states which permit joint cumulative distribution functions for fracture locations to be derived.

4. Conclusion

With the help of probability theory for fracture locations based on competing risk theory, we studied joint probability density and joint cumulative distribution functions for fracture location (x, y) derived for fractures due to internal defects, reaching the following conclusion:

1) On the basis of joint probability density functions for fracture locations (x, y) in a 3-point bending stress field, contour maps for joint probability density were obtained. With sample dimensions and shape parameters given, they permit actual fracture origin areas to be quantitatively determined.
2) Contour lines in fracture origin areas drew modest convex curves nearly in parallel.
3) On the basis of joint cumulative distribution functions for fracture locations (x, y), we adjusted cumulative distribution functions for different shape parameters with reliability levels: 68.3, 95.5 and 99.7%. This permits the area of screening for the required reliability level to be found visually and enables the operating efficiency of screening to be greatly increased.
4) Finding that joint cumulative probability lines with shape parameter $m_1>10$ could be approximated by straight lines, we presented screening diagrams useful for actual nondestructive inspection. They enable areas to be screened at different reliability levels to be estimated easily.

References:

1) Y. Matsuo and K. Kitakami, Trans. JSME 51-471, A, 2575 (1985).
2) Y. Matsuo and K. Kitakami, Fracture Mechanics of Ceramics, 7, 223 (1986).
3) S. Ito, S. Sakai and M. Ito, Zairyo, 30, 337, 1019 (1981).
4) Y. Matsuo, K. Kitakai and S. Kimura, J. Mater. Sci., 22, 2253 (1987).
5) K. Kitakami, Y. Matsuo and S. Kimura, J. Ceram. Soc. Jpn, 99, 361-364 (1991).

This article is a full translation of the article which appeared in Nippon Seramikkusu Kyokai Gakujutsu Ronbunshi (Japanese version), Vol.99, No.5, 1991.

Characterization of Electrodeposited Gels on Tungsten Heater Coil

Toshiaki Arato, Toshiaki Narisawa, Nobuyuki Koganezawa*, Yoshihiko Nonaka* and Kenji Tochigi**

Hitachi Research Laboratory, Hitachi, Ltd., 3-1-1, Saiwai-cho, Hitachi-shi, 317 Japan
*Mobara Works, Hitachi, Ltd., 3300, Hayano, Mobara-shi, 297 Japan
***Hitachi Research Laboratory, Hitachi, Ltd., 4026, Kuji-cho, Hitachi-shi, 319-12 Japan

Porous insulation films of alumina used in color picture tube heaters for high definition displays have been made by the electrophoretic deposition (electrodeposition) process. In this process, the formation of gels on electrodes and the electrophoresis of Al_2O_3 particles in the solution occur simultaneously. Electrodeposited gels, which are important to control the insulation film structure, were analyzed by powder X-ray diffraction, differential thermal analysis and Fourier transformation photo acoustic spectroscopy (FT-IR-PAS). The X-ray diffraction patterns showed that the electrodeposited gels are amorphous. FT-IR-PAS spectra indicated the presence of hydroxyl and nitrate anions. It is shown that the shape of the gel on an uneven electrode surface depends on the configurations of aluminum and magnesium ions in the electrodeposition solutions.

[Received September 25, 1990; Accepted February 20, 1991]

Key-words: Electrophoretic deposition, Aluminum nitrate, Magnesium nitrate, TG, DTA, Photo acoustic spectra, X-ray diffraction, Amorphous

1. Introduction

An electrophoretic deposition (electrodeposition) process is a well-known method for producing ceramic films about 100μm thick with ease and relative uniformity, which is now used for the formation of superconductive thin films as well.[1,2]

The authors intended to form Al_2O_3 porous insulation films for CRT heaters and studied the phenomenon of film formation by the electrodeposition of Al_2O_3 from an alcohol aqueous solution containing dispersed Al_2O_3 particles with aluminum nitrate and magnesium nitrate as electrolytes.[3] As a result, it was found that film formation have a geat effect on the electrophoresis of ceramic particles onto the electrode surface, but on the gel-like matter (hereafter referred to as electrodeposited gel) formed on the electrode surface by passage on an electric current. Especially in the case of film formation on surfaces with complicated shapes such as a coil, a difference in electrolyte composition in the electrodepositing solution as an origin for electrodeposited gel causes a substantial change in the morphology of the electrodeposited gel.

In this paper, the characterization of electrodeposited gel was tried by Fourier transform infrared photo-acoustic spectroscopy (FT-IR-PAS) that the authors found effective in application to analysis of Al_2O_3 and alumina hydrates,[4] as well as by powder X-ray diffraction and differential thermal analysis (DTA). Moreover, the formation mechanism of the electrodeposited gel was discussed here based on the above results.

2. Method of Experiment

2.1. Composition of Electrodepositing Solutions

The electrodeposition process is that a set of metals are used as electrodes, voltage is applied between both electrodes, and ceramic particles dispersed in an electrodepositing solution are allowed to migrate to the surface of one of electrodes thus covering it to form a film. In this program, a W coil wound to a Mo wire was used as a negative electrode and pure Al as a positive electrode. **Figure 1** shows the appearance of the W coil.

Table 1 lists the composition of electrodepositing solutions used in this study. An electrodepositing solution generally consists of the three components; a dispersion medium, an electrolyte, and ceramic particles such as Al_2O_3, while in this work, electrodepositing solutions not containing ceramic particles were adopted in order to examine the properties of electrodeposited gel formed by electrodeposition.

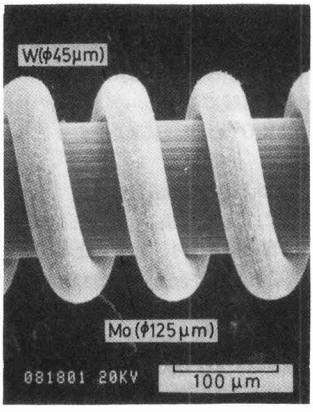

Fig. 1. SEM photograph of tungsten coil electrode.

Table 1. Components and contents of electrodeposition solutions.

components \ sol.No.		1	2	3	4
solvents	ethyl alcohol	80 ml			
	iso-propanol	3.7 ml			
	methyl ethyl ketone	2.0 ml			
	H_2O	80 ml			
electrolytes	dehydrated $Al(NO_3)_3$	2.70 g	2.70 g	–	–
	$Al(NO_3)_3 \cdot 9H_2O$	–	–	4.75 g	–
	$Mg(NO_3)_2 \cdot 6H_2O$	2.50 g	–	–	2.50 g

Among the components of the solutions the composition of the dispersion medium was the same, mainly composed of C_2H_5OH and H_2O. Consequently, the composition of electrolytes is a single variable factor among those of electrodepositing solutions used in this study. First, electrolyte components were dissolved in H_2O heated to about 50°C to the extent that crystals could not be detected visually. This solution was cooled to 20°C and a certain amount of inorganic solvents such as C_2H_5OH were mixed to prepare electrodepositing solutions.

The electrodepositing solutions No.1 contained anhydrous $Al(NO_3)_3$ and $Mg(NO_3)_2 \cdot 6H_2O$ as electrolyte components. The electrolyte of the No.2 solution was $Al(NO_3)_3$ resulted from $Al(NO_3)_3 \cdot 9H_2O$ after dehydration (hereafter dehydrated $Al(NO_3)_3$), that of No.3 $Al(NO_3)_3 \cdot 9H_2O$, and that of No.4 $Mg(NO_3)_2 \cdot 6H_2O$. The molar concentration of Al in No.1 to 3 solutions was set to the constant value (1.3×10^{-3} mol), and that of $Mg(NO_3)_2 \cdot 6H_2O$ in No.1 and 3 solutions 9.9×10^{-3}mol. Dehydrated $Al(NO_3)_3$ was prepared by adding a slight amount of H_2O to special-grade $Al(NO_3)_3 \cdot 9H_2O$, which was thoroughly stirred below 135°C in air, heated at about 135°C and cooled before use. The reason of adopting dehydrated $Al(NO_3)_3$ was to control a hydration state in the solution by removing adsorbed moisture on the surface of the reagent.[5] In this program, $Al(NO_3)_3 \cdot 9H_2O$ and dehydrated $Al(NO_3)_3$ were separately dissolved in solvents and gel structures were compared in order to investigate the effect of dehydration on the morphology and structures of gel. The special-grade $Mg(NO_3)_2 \cdot 6H_2O$ was dissolved in H_2O as it is.

2.2. Samples and Sampling

The W coil was immersed in the electrodepositing solution, connected to a constant voltage power supply, and charged with current at 80V for 5 ~ 50 seconds. As a result, sol containing a large amount of the electrodepositing solution was formed on the surface of the W coil. The coil with the sol was rinsed in acetone and dried at 50 ~ 100°C to form electrodeposited gel (hereafter simply as gel). The gel was obtained by pealing it off the coil. The quantity of gel by a single charge was not enough for analysis, so that the operation was repeated. Obtained samples were held in a desiccator to avoid moisture in air.

Hereafter, the electrodeposited gel samples are called as No.1 ~ 4 gel corresponding to the number of the electrodepositing solution from which they were formed.

2.3. Method of Analysis

Powder X-ray diffraction patterns were obtained with a wide angle X-ray diffraction system (Rigaku Denki; RU-200) using Cu as a target. Cations in the electrodeposited gel were determined quantitatively by atomic adsorption spectrometory after dissolving it in dilute nitric acid. DTA was performed with TG/DTA-300 produced by Seiko Electric Industries. About 0.05 gram of a sample was charged in the Al_2O_3 crucible, and obtained TG and DTA curves were obtained at a heating rate of 5°C/min introducing air with a flow rate of 100ml/min. A reference substance was fully-dried α-Al_2O_3.

Moreover, PAS was carried out with a 170SX Fourier transform infrared spectrometer (NICOLET). Closed containers to house powder samples were cells (MODEL200) produced by M Tech. The outline of this system is omitted since it was stated earlier.[4] A sample (0.1–0.2g) was charged in a sample container in the system, and its spectrum was obtained while performing the correction of light source energy by the spectrum of a perfect absorber using carbon black. Further, the appearance of the electrodeposited gel was observed with a scanning electron microscope (SEM X-650, Hitachi, Ltd.)

3. Resutls and Discussion

3.1. Morphology and Electrodeposition Properties of Electrodeposited Gel

Figure 2 shows SEM images of gel formed on the W coil from each electrodepositing solution as well as a schematic diagram for gel morphology. In the diagram, W denotes the W coil, and Mo the cross section of a Mo core wire to retain the shape of the W coil. In the photos in Fig.2, gel has microcracks which developed after drying, and the diagram gives conditions before drying.

The morphology of gel is classified largely into a type depositing with almost uniform thickness according to the winding geometry of the W coil, and that growing only on the W coil wire. The former includes the cases of $Al(NO_3)_3$ electrolytes (No.2 and 3 electrodepositing solutions), while the latter the cases of $Mg(NO_3)_2$ electrolytes (No.1 and 4

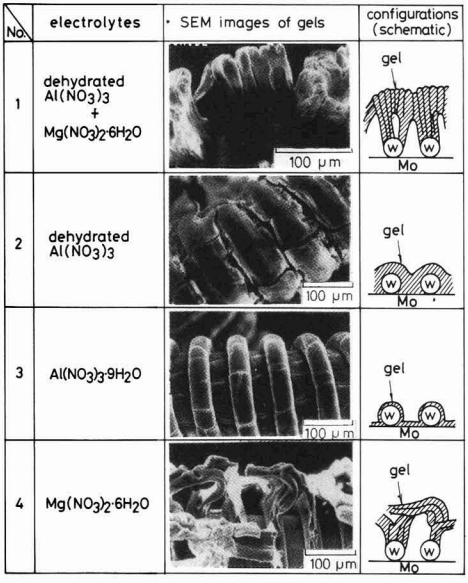

Fig. 2. SEM photographs and schematic configurations of the gel electrodeposited on the coil-type electrodes.

electrodepositing solutions). The No.1 electrodeposited gel provides both features of $Al(NO_3)_3$ and $Mg(NO_3)_2$ electrolytes.

As stated above, the difference of electrolyte used ($Al(NO_3)_3$ or $Mg(NO_3)_2$) make a great difference on gel morphology. It has also been found that this gel morphology affects the shape of Al_2O_3 films electrodeposited using these electrolytes.

Figure 3 presents a relationship between current per unit surface area of the W coil and deposition period when gel was formed by each electrodepositing solution. Applied voltage was 80V (constant), and electrode distance about 15mm. Current decreased with an increase in charging time, which means that gel formation on the W coil heightens electric resistance.

3.2. Results of X-ray Diffraction and Quantitative Analysis

Figure 4 shows the results of X-ray diffraction with electrodeposited gel. No.1 and 2 gel samples have weak diffraction peak at lower diffraction angles, with similar diffraction pasterns. Moreover, the broad diffraction line width suggests glassy structures. As in Fig.4, the No.3 gel sample has diffraction peaks at $2\theta=40°-80°$ which agree with those of α-Al_2O_3, proving that the compound is contained. As stated above, it was found that the structure of formed gel is greatly different between hydrated and anhydrated salts even with the same $Al(NO_3)_3$. On the other hand, the No.4 gel had diffraction peaks as marked with ○ and ● in Fig.4, which were in good agreement with those of $Mg(OH)_2$ and $Mg_6Al_2(OH)_{18}\cdot(4.5H_2O)$ suggesting the presence of both compounds, while peaks with the sign ? were not identified.

In the next step, electrodeposited gel was heated at 1000°C in air and identified by X-ray diffraction. The results are shown in **Table 2.** Two components could be identified from each substance obtained by heating No.1, 2, and 4 gel samples, so that they were listed in Table 2 as a main or secondary compound according to the relative ratio of the peak size. Only α-Al_2O_3 was identified from the heated No.3 gel sample. In comparison between heated No.1 and 4 gel samples, both had MgO and $MgAl_2O_4$, and yet in the No.1 gel the diffraction peaks for $MgAl_2O_4$ were higher than those for MgO, while in the No.4 gel the result was opposite. This indicates that the No.1 and 4 gel samples have two kinds of cations (Al and Mg) and the No.4 is richer in Mg than the No.1. Further, No.2 and 3 have a single cation (Al) but products after heating are not the same. **Table 3** summarizes changes with time in Al and Mg concentration of No.4 electrodepositing solution while forming gel on the W coil. A single batch means electrodeposition for a piece of W coil 15mm long at 80V for 5 seconds. The amount of gel sampled in this study is almost equivalent to 250 batches in this table. The results clearly show an increase in Al concentration by repeated electrodeposition. This indicates that Al dissolves from the Al anode during charging to change the composition of electrodeposited gel.

Table 4 lists the results of quantitative analysis with cations in the electrodeposited gel, accompanied by the amount of Al and Mg in the raw electrodepositing solutions. The

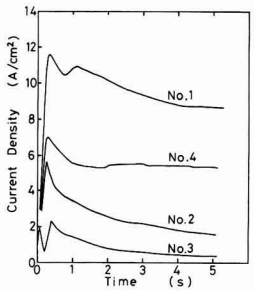

Fig. 3. Relationship between current density and deposition time.

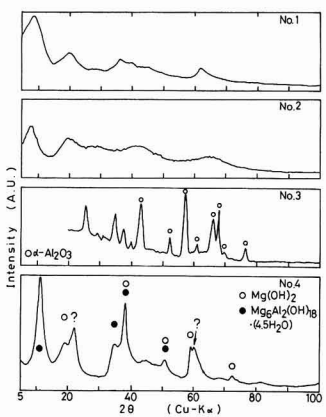

Fig. 4. Powder x-ray diffraction patterns of the gels trodeposited from each solution and dried at 100°C.

Table 2. Components identified from gels heated at 1000°C.

gel	main	sub
No.1	$MgAl_2O_4$	MgO
No.2	$\delta-Al_2O_3$	$\alpha,\gamma-Al_2O_3$
No.3	$\alpha-Al_2O_3$	–
No.4	MgO	$MgAl_2O_4$

Table 3. Al and Mg content changes in electrodeposited solutions of No.4 series. Unit of contents of gels and solution are wt.% and mg/l.

No.	Al	Mg
initial	<0.01	1520
5 batch	1.28	1510
50 batchs	1.72	1460
250 batchs	8.86	1460

Table 4. Al, Mg and unsolved Al contents in electrodeposited gels. Unit of contents of gels and solution are wt.% and mg/l.

gel No.	Al	Mg	unsolved Al
gel No.1	10.8	6.43	–
sol.1	2150	1530	
gel No.2	31.0	0.004	–
sol.2	2180	<0.01	
gel No.3	18.3	0.014	2.13
sol.3	2175	<0.01	
gel No.4	3.03	27.6	–
sol.4	<0.01	1520	

concentration Al/Mg ratio of the No.1 gel is greater than the Al/Mg ratio of the raw solution, supposes that it comes from the contamination of Al from the electrode and a difference in an electrode reaction rate between $Al(NO_3)_3$ and $Mg(NO_3)_2$. A substance which, was not decomposed by dilute acid was detected from No.3 (expressed as insoluble Al in Table 3), and this is considered to correspond to α-Al_2O_3 in No.4 identified by X-ray diffraction. Moreover, the amount of Al is lower than that in No.2, indicting that the amount of anions in gel is relatively great.

3.3. Results of TG and DTA

Figures 5 and 6 present DTA and TG of each electrodeposited gel sample in this study. There are some reports which surmised that the gel formed from electrodepositing solutions with aluminum nitrate as an electrolyte has a structure close to either the existing aluminum hydroxide or alumina hydrates.[6,7] In regard to known substances, TG and DTA for amorphous aluminum hydroxide and alumina hydrates were already reported by Sato et al. in detail[8,9,10] and the results were compared with those of this study. In addition, the results of $Mg(OH)_2$ are given in the figure for comparison with the No.4 gel. SB and AAH in the figure are TG curves for pseudo boehmite and amorphous aluminum hydroxide.

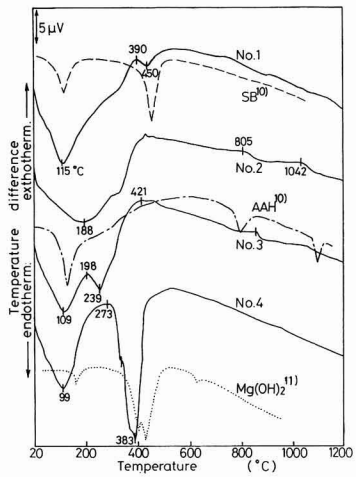

Fig. 5. Differential thermal analysis curves of the deposited gel, phseudo-bohmite[10] amorphous aluminum hydroxide[10] and $Mg(OH)_2$.[11]

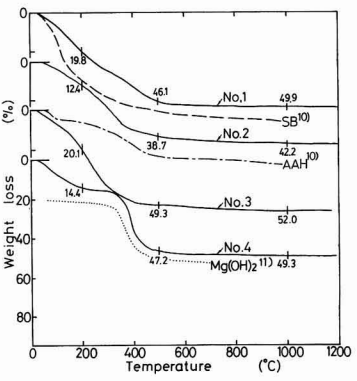

Fig. 6. TG curves of the deposited gel, phseudo-bohmite,[10] amorphous aluminum hydroxide and $Mg(OH)_2$.[11]

The temperatures of endothermic reaction of the No.1 gel (115°C and 450°C) are relatively close to those of pseudo boehmite. With reference to discussion by Sato et al. the endothermic reaction at 115°C is considered to be caused by the desorption of adsorbed water as well as the slight endothermic reaction at about 450°C by the desorption of residual water molecules and dehydration by OH groups. The endothermic reactions of the No.2 gel at 188°C and of the No.3 gel at 109°C are probably due to the desorption of adsorbed water, and yet further behavior of the decomposition of No.2 and 3 gel cannot be surmised by the results of known substances.

According to Hamano,[11] endo-thermic peaks in DTA with $Mg(OH)_2$ are at 150°C (weak) and 400–420°C (strong). In addition, the weight loss as a result of the following reaction is reported to be about 33% at 500°C.[11]

$$Mg(OH)_2 \rightarrow MgO + H_2O \quad \ldots\ldots\ldots\ldots (1)$$

While the weight loss of No.4 gel at 500°C is as high as 47%, and endothermic peaks are located at lower points (99°C, weak; 383°C, strong) than those of $Mg(OH)_2$. Considering these two facts, the content of water and hydroxyl groups in the No.4 gel is higher than that of $Mg(OH)_2$, suggesting weak bonding between –OH and Mg.

3.4. State of Anions in Gel

Figure 7 shows the results of PAS measurement of electrodeposited gel dried at 100°C. Each of the four gel samples has a broad absorption peak at 2800–3700cm.$^{-1}$ This is ascribed to the stretching vibrating ν(OH) of –OH bonding, and yet the considerably broad width means that the structure of electrodeposited gel in this study has poor regularity. Particularly, a spectrum obtained from the No.3 gel provides an absorption range at 2800–3600cm^{-1} broader than those of No.1, 2, and 4 gel samples. This is indicative that in –OH bonding constituting the No.3 gel the deviation of bonding force between O and H is greater than that of other gel – in other words, –OH bonding has high randomness. In particular the peak extends to the side of low

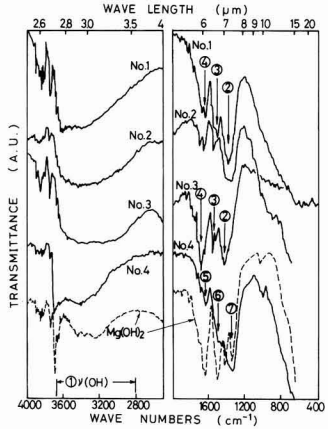

Fig. 7. FT-IR-PAS spectra of the deposited gel dried at 100°C and $Mg(OH)_2$.

wavenumber, suggesting that there is relatively more –OH bonding with weak bonding force between O and H.

In the spectra of No.1, 2, and 3 gel samples, asymmetric absorption peaks are almost commonly present near ② 1300–1400cm.$^{-1}$ ③ 1400–1500,$^{-1}$ and ④ 1600cm^{-1} in addition to the above-stated ① 2800–3700cm.$^{-1}$ The peak ② probably originated from complicated absorption by the stretching vibration of -NO_2, $\nu(NO_2)$, that of -NO_3, $\nu(NO_3)$, and the deformation vibration of N–OH, δ(N-OH),[12,13] ③ from the in-plane deformation vibration of –OH, δ(OH), and ④ from the stretching vibration of –NO_2 due to nitrates $\nu(NO_2)$. Consequently, all of these gel samples are supposed to contain –OH, –NO_2, and –NO_3.

The spectrum of the No.4 gel also has an absorption peak at 2800–3700cm.$^{-1}$ In Fig.5 the spectrum of reagent special-grade $Mg(OH)_2$ (brucite) is shown with a broken line. In comparison, it can be judged that absorption at 3700cm^{-1} (stretching vibration of –OH, this –OH forms a laminar structure coupled with Mg^{2+}) is weak though the spectrum of No.4 gel at 2800–3900cm^{-1} resembles that of $Mg(OH)_2$. The absorption peaks at 1300–1650cm^{-1} denoted by ⑤ and ⑥ in the figure are weaker than that of $Mg(OH)_2$ so that the structure is supposed to have relatively weak in-plane deformation vibration of –OH.

The results of various analyses were summarized to obtain the following qualitative information on the structure of each electrodeposited gel sample.

The No.1 gel probably has a structure in which H_2O and ions such as –OH, –NO_2, and –NO_3 are arranged at random around Al and Mg; the No.2 gel a structure with H_2O and ions such as –OH, –NO_2, and –NO, as in the case of No.1, arranged randomly around a single cation (Al ion); and the No.3 gel a structure with randomly arranged Al ion, H_2O, and other ions such as –OH, –NO_2, and –NO_3 as well as locally a structure connected weakly with the crystal group of α–Al_2O_3 and –OH, –NO_2 or –NO_3. The No.4 gel is relatively similar to $Mg(OH)_2$ and yet it can be judged as an amorphous substance that –OH, –NO_3 or –NO_2 is combined irregularly with Mg.

As a result of the above analyses, it is concluded that each electrodeposited gel has an amorphous structure though with substantial differences. Previously, the substance depositing on the cathode by the electrophoretic deposition of alcohol aqueous solutions (corresponding to electrodeposited gel in this study) was believed to be a hydroxide,[5,6] while various analyses in this work practically revealed that it is not a simple hydroxide but of an amorphous structure including various anions in the solvent.

The results of FT-IR-PAS indicated that electrodeposited gel contains nitrate ions, and aluminum nitrate is dissolved in the solvent as a complex ion,[4,15,16] so that Al ions in the solution probably contributed to electrodeposition as a form of complex ions.

4. Conclusion

In an attempt to clarify the electrophoretic deposition of ceramic particles, gel samples electrodepositing from alcohol solutions containing aluminum nitrate and magnesium nitrate to coil electrodes were obtained to perform qualitative analyses by powder x-ray diffraction, DTA, and PAS.

Gel samples electrodepositing from the alcohol solution with anhydrous $Al(NO_3)_3$+$Mg(NO_3)_2$ as electrolytes to the W coil as well as from the solution with only dehydrated $Al(NO_3)_3$ provide structures in which Al and Mg combine with a large amount of –OH, and moreover there is little regularity among contained –NO_3, –NO_2 and H_2O.

The gel from $Al(NO_3)_3{\cdot}9H_2O$ solutions is of an amorphous structure with Al and –OH, –NO_2, or –NO_3 as well as a local α-Al_2O_3 structure.

The gel from $Mg(NO_3)_2$ solutions is composed of Mg ions in the solution and other anions and resembles the structure of $Mg(OH)_2$, though a slight amount of Al dissolving from the anode is contained in some cases.

References:

1) M.L. Norton, Mat. Res. Bull., 24, 1391-1397 (1989).
2) M. Hein, G. Muller, H. Piel, L. Ponto, M. Becks, U. Klein and M. Peiniger, J. Appl. Phys., 66, 5940-5943 (1989).
3) T. Arato, K. Nakamura, M. Sofue and A. Misumi, J. Jpn. Inst. Metals, 53, 189-194 (1989).
4) T. Arato, K. Tochigi and T. Tamamura, Nihon Seramikkusu Kyokai Gakujutsu Ronbunshi, 98, 726-731 (1990).
5) F. Kitahara and M. Watanabe, Kaimen Denki Gensho–Kiso · Sokutei · Oyo–Kyoritsu Shuppan, (1967), p.201-205
6) Y. Tomita, Hitachi Hyoron, 49, 744-748 (1967).
7) M. Shimbo, K. Tanzawa, M. Miyazawa and T. Emoto, J. Electrochem. Soc., 132, 393-38 (1985).
8) T. Sato, F. Ozawa and S. Ikoma, Shinku Riko Jour., 8, 1, 7-11 (1979).
9) T. Sato, ibid., 8, .2, 10-16 (1979).
10) T. Sato, F. Ozawa, and S. Ikoma, ibid., 9, 2, 2-6 (1980).
11) K. Hamano, Yogyo-Kyokaishi, 71, 101-105 (1963).
12) K. Nakamoto, Infrared Spectra of Inorganic and Coordination Compounds, John Wiley and Sons (1963), 69-161.
13) A Guide to Instrumental Analysis 1 (revised and enlarged ed.) supervised by M. Izumi, M. Ogawa, S. Kato, J. Shiokawa and T. Shiba, Kagaku Dojin (1986), 3-6.
14) K. Nakanishi, P.H. Solomon and N. Fukutani (ed.) Infrared Spectra–Explanation and Exercise–, Nankodo (1986) p.3-59.
15) W. Bol, T. Welzen, Chem. Phys. Lett., 49, 189-192 (1977).
16) S. Shoenherr, F, Forschungsh, A, 616, 87-99 (1979).
17) A.T. Pilipenko, H.F. Falendysh and E.P. Parkhomenko, Khim. Tekhnol. Vody., 4, 136-150 (1982).

This article is a full translation of the article which appeared in Nippon Seramikkusu Kyokai Gakujutsu Ronbunshi (Japanese version), Vol.99, No.6, 1991.

Slow Crack Growth of Mullite Ceramics

Yoshiaki Yamade*, Yoshiaki Kawaguchi*, Nobuo Takeda and Teruo Kishi****

*Sumitomo Metal Industries, Ltd.
16, Sunayama, Hasaki, Kashima-gun, Ibaraki 314-02, Japan
**Research Center for Advanced Science and Technology, The University of Tokyo
4-6-1, Komaba, Meguro-ku, Tokyo 153, Japan

Slow crack growth (SCG) of mullite ceramics was studied by a double cantilever beam (DCB) method. Two types of mullite were fablicated from a high-purity mullite powder and sintered at 1650°C for dense-type specimens (porosity=2.9%), and at 1575°C for porous-type ones (porosity=20.6%). In the DCB testing, crack opening displacements (COD) and applied loads were stored in a computer for detailed analysis. Crack lengths, K values and crack velocities (V) were then calculated with the computer using the stored digital data. The relationship between the compliance and the crack length for this specimen geometry (4.5mm×15mm×60mm with a 20mm-long notch) was obtained using several specimens with different crack lengths. K_{IC} values of two types of mullite were estimated as 2.05MPam$^{1/2}$ (dense-type) and 1.4MPam$^{1/2}$ (porous-type). Mullite was tested in the water, the air and the dry N_2 gas. Mullite showed stress corrosion cracking affected by H_2O. It was found that the plateau regions in K-V diagrams for two different types of mullite appeared in different velocity ranges. The velocity ranges of the two types of mullite were 10^{-4}m/s for dense-type and 10^{-3}m/s for porous-type, respectively. This could be explained by the diffusion of H_2O gas through continuous pores.

[Received October 5, 1990; Accepted February 20, 1991]

Key-words: Mullite, Slow Crack growth, Fracture, Fracture toughness, DCB test

1. Introduction

Mullite ceramics is considered potentially useful as high temperature structural materials and could replace conventional high temperature structural materials of alumina ceramics. Therefore, they have been studied on their properties and applications in various aspects. Several efforts have been made from the aspect of material manufacturing, such as the manufacturing of stoichiometric mullite powders using the coprecipitation method[1] and other methods, and the development of various composite materials reinforced with SiC whiskers and other fibers[2,3] aiming at the improved toughness. Other studies from the aspect of evaluation of material properties are researches on strength and toughness at normal and high temperatures,[4,5] on creep characteristics,[6] on corrosion in hot water,[7] and so forth.

It has been recently reported that mullite shows stress corrosion cracking by H_2O,[9] in the same manner as SiO_2 glasses.[8] According to this report, mullite was found to fracture as a linear elastic body in the environments of air, xylene and water, and was also found to be affected by stress corrosion by water. Stress corrosion cracking is closely related to crack propagation velocity, therefore, one must not only evaluate the K_{IC}, but also investigate Slow Crack Growth (SCG) behaviour. For the evaluation of crack propagation characteristics, specimens for the fracture toughness test are generally used because they are well-suited to stress analysis. Among various test specimens such as the double cantilever beam (DCB) test,[8] the Chevron notch bending test,[10] the compact tension (CT) test,[11] and the double torsion (DT) test,[12] the DCB test specimens have conventionally been used for observation of crack propagation behavior in the case of glass materials. The DCB specimens have the characteristics that the relationship between stress and crack length is stable in a relatively wide range, and that the crack tip is straight and perpendicular to the surface of the specimen. Because of these characteristics, the derivation of K value had been investigated in detail. Therefore, the DCB test is considered more suitable for the quantitative evaluation of crack propagation characteristic than other tests such as the Chevron notch bending and the DT test.

In this study, the authors investigated fracture toughness of mullite ceramics and their crack propagation velocity dependence under various conditions using the DCB test, and clarified stress corrosion characteristics and the effect of pores on these characteristics.

2. Experimental Procedure

2.1. Preparation of Test Specimens

Figure 1 shows the preparation procedure of mullite

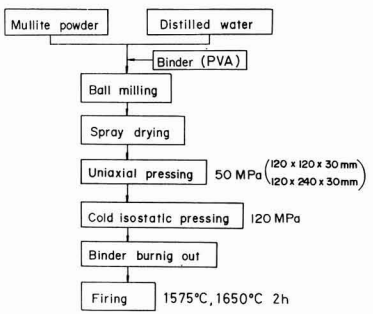

Fig. 1. Sintering process of mullite.

ceramics. Starting with the raw materials of commercially available high-purity mullite powders (manufactured by the sol-gel technique, in content of Al_2O_3=71.80%, SiO_2=28.05%), and firing at 1,575°C and 1,650°C for 2 hours in the air atmosphere. Bulk density of the specimen was measured using the Archimedean method and the average porosity of the specimen was calculated from the ratio between the measured bulk density of the sintered specimen and the true specific gravity of the mullite powder. The two types of sintered bodies were a porous one having porosity of 20.6% (sintered at 1,575°C) and a dense one having porosity of 2.9% (sintered at 1,650°C). As shown in **Fig.2**, the test specimens were prepared by machining in the geometry of 4.5×15×60mm with side groove on both sides of 0.8mm in width and 1.1mm in depth. The slit of 0.3mm in width were machined into the spcimen instead of initial crack

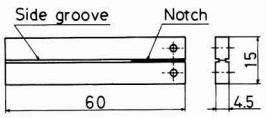

Fig. 2. DCB(Double Cantilever Beam) specimen geometry.

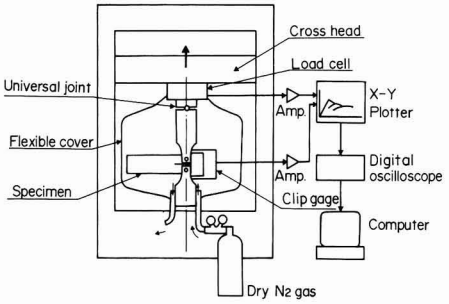

Fig. 3. Schematic diagram of DCB testing system. N_2 gas is filled in the flexible cover to control the humidity.

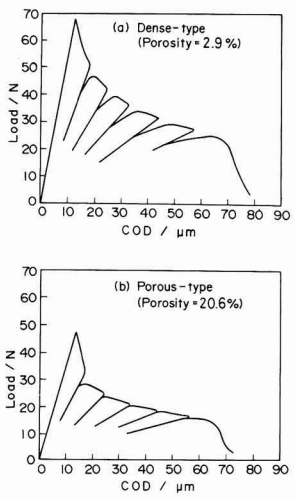

Fig. 4. Typical load-COD curves of two different types of mullite during loading and unloading. (a) dense-type (b) porous-type

2.2. DCB Test

2.2.1. Testing System

Using a universal testing machine, the specimens were pulled through holes drilled on the beam of the test specimen. The change of crack opening displacement (COD) at the loading point were measured by using the clip gage which grasped the specimen from outside, and the change of load by using the load cell. These measured data were stored in a digital storage oscilloscope, from which they were transferred to and recorded into a computer for later calculation.

Relative humidity in the test atmosphere of air was 65%. In the case of test in the nitrogen (N_2) atmosphere, a flexible cover made of vinyl chloride of 0.2mm thick was used to cover the specimen, as shown in **Fig.3**, and filled the cover with dry nitrogen gas (with H_2O concentration of less than 5ppm) in order to provide a dry testing condition. In order to provide a submerged condition in water, the distilled water was supplied continuously from the outside to the slit part and the side groove part of the specimen. All of these tests were carried out in the temperature range of 23±2°C.

2.2.2. Constant Displacement Rate Test

After a pop-in crack was introduced in the specimen by pulling it at a cross-hend speed of 5μm/min, the load was reduced by approximately 30% in order to stop the crack propagation, and then pulled it again at a constant displacement rate. The reduction ratio of load was controlled so that the loading-unloading curve did not show any hysteresis. The displacement rate was 20μm/min as the standard. However, two other rate of 5 and 500μm/min were applied in order to change the range of crack propagation velocity.

2.2.3. Constant Displacement Test (Stress Relaxation Method)

The test of constant displacement type was carried out in order to measure the behavior of the material in the further slower range of crack propagation velocity. A predetermined load was applied in the same condition as the standard DCB test, and then the crosshead was fixed at the position. The load decreased with the crack propagation, so the strains accumulated in the testing machine and the jigs were released and the COD slightly increased. Therefore, a complete constant displacement condition was not realized by this testing method.

2.3. Measurement of Elastic Modulus

Using the bending test specimen of JIS specification, Young's modulus was measured by using the strain gauge method. The 4-point bending test with the outer-span of 30mm and the inner-span of 10mm was calcurated, and the strain was measured with a strain gage (gage length of 5mm), which was adhered on the specimen at the center of its tensile side.

2.4. Fracture Toughness Test

The fracture toughness (K_{IC}) values were measured by using the single edge precracked beam (SEPB) method[13] and the chevron notch bending test method.[14]

In the case of the SEPB test, the K_{1C} value was calculated

from the maximum load and precrack length. In the case of the chevron notch bending test, the crack length was obtained from the COD, and then the K_{IC} value was calculated at the transition point to the unstable fracture, instead of at the P_{max} point.[14]

3. Results and Discussion

3.1. Load-COD Curves

In order to investigate the linearity in fracture of mullite ceramics, the loading-unloading test was carried out by using the DCB testing method. **Figure 4** shows the load-COD curves of two different types of mullite, namely, dense-type and porous-type.

It is seen that all of the direction of unloading are focussed to the origin. This implies that there are no residual strains caused by grain bridging and micro-cracking, which are reported to exist on the fracture surface in the case of alumina ceramics. Consequently, mullite ceramics were confirmed not to show non-linear fracture behavior. The fracture surfaces observed by a scanning electron microscope (SEM) (shown in **Fig.5**), were relatively flat resulting from the mixed of transgranular and intergranular fracture.

3.2. Calculation of Crack Length

The linear relationship between crack length and compliance of mullite were confirmed so that the crack length can be calculated from the change of the compliance. Usually, a master curve for the relationship between compliance and crack length is prepared by using several test specimens with various notch lengths, and the crack lengths are obtained on this curve in correspondence with the compliances measured.[15] In the present study, however, a dimensionless conpliance and crack length master curve (as shown in **Fig.6**) were prepared with 4 pieces of dense-type mullite specimens. The determination of the crack length was carried out using a penetration-type crack detection technique after unloading during crack propagation. This method was similar to that used in the case of fatigue crack.[15] Young's moduli measured by the strain gauge method were 112GPa for the dense-type mullite and 65.6GPa for the porous-type one. As previously described in Section 3.1, mullite ceramics do not exhibit the non-linear fracture. Thus, the crack length were determined from the change of compliance and the Young's modulus using the master curve. It was also found that this master curve can be approximated by equation (1), which is a cubic curve for simple beam.

$$u = 8a^3P/(EBH) \quad \ldots\ldots\ldots\ldots\ldots\ldots (1)$$

u: COD,
a: crack length,
P: load,
E: Young's modulus,
B: thickness of specimen,
H: height of beam

3.3. Preparation of K_I-V Diagram

The crack propagatin per unit time (crack propagation velocity) was calculated using the time dependance of load and COD. K_I values at various time points were calculated using equation (2) proposed by Foote et al.[16]

$$\frac{K_I h^{1/2} B'}{P} = \sqrt{12}\left(\frac{a}{h} + 0.673\right) + \left(\frac{2h}{\pi a}\right)^{1/2} - \left(0.815\left(\frac{a}{h}\right)^{0.619} + 0.429\right)^{-1} \quad \ldots\ldots (2)$$

$$B' = (Bb)^{1/2} \quad \ldots\ldots\ldots\ldots\ldots\ldots (3)$$

In taking account of the effect of side grooves, the plate thickness was assumed by equation (3), which was experimentally confirmed as adequate by Wiederhorn et al..[17]

By plotting the K_I values and the crack propagation velocities at various time points, the K_I-V diagram was prepared.

3.4. Validity of Loading Condition

SCG characteristics of materials are generally evaluated by paying attention to the loading velocity dependence. In both bending and fracture toughness tests, for instance, SCG characteristics closely depend on the loading velocity. In the present experiments, the time dependences of the crack lengths were measured and the results were compiled as a function of crack propagation velocity, so the difference in loading rate resulted in the difference of crack acceleration and maximum crack propagation velocity. However, in the case of the constant displacement velocity test, dK/dt becomes relatively lower with increased crack length, so displacement rate at the loading point is not so important.

Rather important is the relation between the respective K_I-V characteristics which were measured (1) in the process of crack acceleration, (2) in the condition of constant crack velocity, and (3) in the process of crack deceleration.

Meanwhile, Evans reported in his DT(double torsion) test using silica glasses that K_I-V diagrams respectively

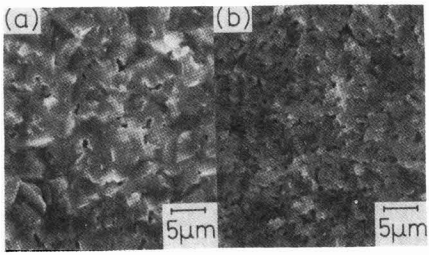

Fig. 5. SEM photographs of fracture surfaces. (a) dense-type and (b) porous-type

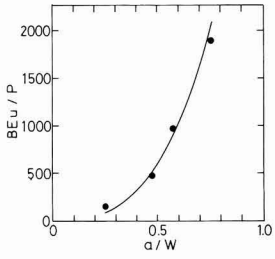

Fig. 6. Master curve of compliance-crack length relation. Crack length can be calculated from each compliance value using this master curve.

measured by the constant displacement rate test and by the constant displacement test (relaxation test) agreed with each other.[12] In the case of the constant displacement rate test, he carried out the DT tests applying a variety of constant displacement rates, from which the K_I-V diagram was determined. This diagram shows the K_I-V characteristics in the condition that cracks propagate at a constant velocity. In contrast, the K_I-V diagram determined by the constant displacement test indicates the K_I-V characteristics in the process of crack deceleration.

In the present study, two types of test were carried out; the constant displacement rate test (which corresponds to the test made in the process of crack acceleration in the present experiment) and the stress relaxation test (which corresponds to the test made in the process of crack deceleration in the present experiment), and successfully measured the K_I-V characteristics in the same crack velocity region, though it was in part of the whole crack velocity range. **Figure 7** shows the typical measured results, in which the results from both tests were plotted nearly along the same line. Thereby, it was confirmed that the K_I-V diagrams for mullite ceramics in the respective stages of acceleration and deceleration of crack propagation nearly agreed with each other within the range of experimental error. However, it is very important to recognize that the respective cracking behaviors in the process of acceleration, at constant velocity and in the process of deceleration, give different physical implication; also, no K_I-V diagram obtained indicates the state in equilibrium.

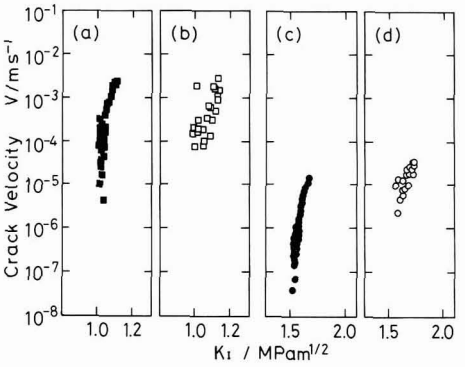

Fig. 7. Comparison between K_I-V diagrams of loading and relaxation tests. Similar diagrams were obtained in both tests. (a) and (b) porous-type mullite in water (c) and (d) dense-type mullite in the air. □, ○: loading test ■, ●: relaxation test

In the present experiments, we applied the constant displacement rate test in high velocity range and the constant dis-placement test in the low velocity range, and compiled the test results into a single K_I-V diagram.

3.5. Influence of Continuous Pores on The Crack Propagation Characteristic

Figure 8 shows the K_I-V diagrams of porous-type mullite ceramics (porosity: 20.6%) and **Fig.9** shows those of dense-type mullite ceramics (porosity: 2.9%). Plateau regions, which suggest the stress corrosion characteristics, are clearly observed in both figures. The respective K_{IC} values determined by the SEPB test and the chevron notch bending test are given on axis X in both figures.

From the studies on glasses by Wiederhorn et al.[8] for the K_I-V characteristics, and by Freiman et al.[18] for the chemical reaction at crack tip, the chemical reaction at crack tip was described as shown in **Fig.10.** It seems the same chemical reaction at crack tip as shown here take place also in the case of mullite ceramics. Evans et al.[12] reported the presence of a plateau region in the K_I-V diagrams of alumina ceramics of 95% purity, but they did not include the investigation on the chemical reaction in this system. The study on the stress corrosion of ceramics, including alumina ceramics, will become more important in the future.

The K_I-V diagram is divided into three regions, amely, region I of low crack velocity, region II of plateau, and region III of high crack velocity. It has been proposed[8] that region I corresponds to the region where the velocity of chemical reaction at the crack tip is dominant to crack propagation. In other words, stress corrosion dominates crack propagation. Region II corresponds to the region where the diffusion velocity of corrosive component and the velocity of crack propagation compete with each other. That is, the balance between mechanical and chemical factors prevail in the region. Region III corresponds to the region where the diffusion velocity of corrosive component is behind the velocity of crack propagation, such that material fracture is caused exclusively by mechanical factors.

It was observed in the K_I-V diagrams in Figs.8 and 9 that

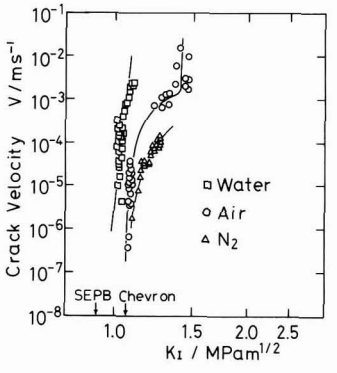

Fig. 8. K_I-V diagrams of porous-type mullite in different environments.

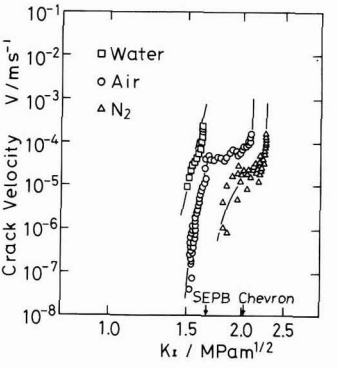

Fig. 9. K_I-V diagrams of dense-type mullite in different environments.

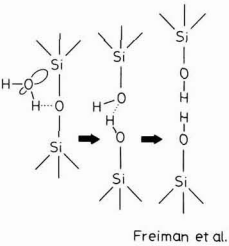

Fig. 10. Chemical reaction model[18] at the crack tip of the glass.

both dense-type and porous-type mullite ceramics were fractured in region I in the case of DCB tests in water. The lower end value in this region I corresponds to K_{ISCC} in general. In the case of tests in an N_2 atmosphere, both dense-type and porous-type mullite ceramics showed the velocity in the plateau region about 1 figure lower than that in the case of tests in an air atmosphere. Compared to test results with silica glasses by Wiederhorn et al.,[8] these velocity values seem to be rather high as data measured in a dry condition as H_2O partial pressure of 5ppm (relative humidity of less than 0.02%). We suppose such high velocity values were caused by a higher H_2O partial pressure in the N_2 atmosphere . Because of the structural feature of the flexible cover used in the testing system, it was difficult to apply vacuum suction to the air in the cover initially. And N_2 gas flow was supplied into the cover to purge the air; in this way the H_2O partial pressure in N_2 atmosphere in the test is supposed to have increased.

A big difference in the fracture behavior between porous-type and dense-type mullite is seen in the velocity in respective plateau regions. A schematic model, as shown in **Fig.11**, is proposed to rationalize this different behavior. In the case of dense-type mullite ceramics, H_2O gas diffuses to the crack tip only through the crack opening, as shown in Fig.11(a). However, in the case of porous-type mullite ceramics which are given with the continuous pores from the specimen surface, not only H_2O gas easily diffuses to the crack tip through these pores with the crack generation, but also H_2O gas initially contained in the pores reaches the crack tip in a shorter time, as shown in Fig.11(b). Thus, the diffusion of H_2O gas appears to be faster. These are assumed to be the reasons for the different velocity in respective plateau regions in the two different K_I-V diagrams as afore-mentioned.

3.6. Correlation Between K_I-V Characteristics and Fracture Toughness Test Results

Table 1 shows the respective measured results of fracture toughness by the DCB test, the SEPB test and the chevron notch bending test. K_{IC} is defined as the K_I value at the point in region III, where a fracture suddenly takes place after cracking is rapidly accelerated. Compared to the K_{IC} values measured by the DCB test, this value for porous-type mullite ceramics and that for the dense-type ones both measured by the SEPB test were lower by 30% and by 20% respectively. The K_{IC} values measured by the chevron notch bending test were relatively close to those measured by the DCB test. It is considered that one of the reasons for the lower K_{IC} values in the case of the SEPB test is that due to SCG (slow crack growth), cracks propagate under the standard loading condition (loading velocity: 0.5mm/min) in the SEPB test before an unstable fracture occurs, thereby, the crack length at the time of final fracture cannot be measured exactly.

Figure 12 illustrates the influence of the plateau to the SEPB test results conceptionally. That is, along with the increase of load, K_I value increased, and when it reached K_{ISCC}, cracks started to propagate slowly. At the time point when the crack length became a+Δa and the K value reached K_{IC}, the cracking behavior transitted to unstable fracture and reached a final failure. Immediately before the final failure, it is assumed that there is a region in which the crack propagation velocity becomes constant in correspondence to the plateau in the K_I-V diagram. If the displacement velocity of the testing machine is not sufficiently high, Δa becomes larger, and K_{IC} is resultingly underevaluated. As previously described, the crack propagation velocity in the plateau region differed by one figure between porous-type mullite ceramics and dense-type ones, so the porous-type mullite ceramics tend to give a larger Δa, and resultantly cause a wide decrease in the apparent K_I value.

When the SEPB test is applied for the evaluation of fracture toughness of the materials which show the SCG, it is necessary to carefully examine the testing condition applied. When the SEPB test is applied for the evaluation of fracture toughness of the different materials which show different crack velocity in respective plateau regions, the evaluated values, even if they were measured under the same testing conditions, cannot be compared with each other immediately without special care. Additional evalution on the crack propagation velocity to the materials will be required, preferably by measuring the COD or by reading the actual crack propagation. Similar special care is necessary in the case of the chevron notch bending test. The stable crack growth and the acceleration of cracking after P_{max} point depend on whether the crack propagation velocity at P_{max} point belongs to the velocity in region I or that in region II. As a result, the K_I value calculated on the basis of P_{max} is not always equal to the K_{IC} value. Thus, to study the materials which apparently show stress corrosion behavior, it seems a special evaluation method on the materials characteristics is necessary by which the K_I-V characteristics can be examined in detail.

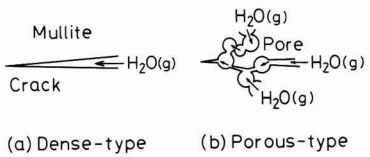

Fig. 11. Schematic model of gas diffusion in two types of mullite. In the porous-type mullite, H_2O gas diffuses faster along many pores.

Table 1. Fracture toughness measured by DCB method, SEPB method and chevron-notch bending method.

Specimen type (Porosity (%))	Fracture toughness measurement method		
	DCB (MPa√m)	SEPB (MPa√m)	Chevron notch bending (MPa√m)
Dense-type (2.9)	2.05	1.66	2.03
Porous-type (20.6)	1.40	0.90	1.08

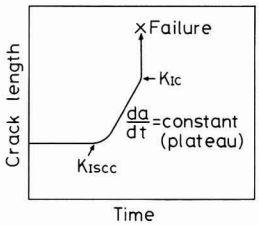

Fig. 12. Schematic model of slow crack growth in the SEPB(Single Edge precracked Beam) testing.

4. Conclusion

Through the investigation of compliances during unloading in the DCB test, mullite ceramics were found fracture as a complete elastic body, and K_I-V diagrams were prepared by using a master curve for compliance-crack length relation of the previous DCB test specimens. Through the examination of these diagrams, the following conclusions were obtained.

1) From the test results respectively carried out in air, N_2 gas and water, mullite ceramics were confirmed to be affected by stress corrosion caused by H_2O gas component.
2) Fracture toughness values of porous-type mullite ceramics and dense-type ones were respectively obtained as 1.4 and 2.05MPa·$m^{1/2}$. Crack velocity values in region II (plateau region) of these two different mullite ceramics tested in air were respectively obtained as approximately 10^{-3}m/s for the porous-type mullite ceramics and approximately 10^{-4}m/s for the dense-type ones. These results differed due to the difference between the respective porosities.
3) A model was proposed to explain the reason why the crack velocity in region II for causing stress corrosion differed between the dense-type mullite ceramics and the porous-type ones. It was attributable to the effect of continuous pores in the latter ceramics as the passage for diffusion of H_2O gas.

(This paper was presented at the Annual Meeting of the Ceramic Society of Japan in May 1990.)

References:

1) K. Hamano, T. Sato and Z. Nakagawa, Yogyo-Kyokaishi, 94, 8, 122-126 (1986), in Japanese.
2) T. Kumazawa, S. Ota, H. Tabata and S. Kozaki, Ceram. Soc. Jpn., Gakujutsu-Ronbunshi, 97, 9, 895-902 (1989), in Japanese.
3) N. Claussen and J. Jahn, J. Am. Ceram. Soc., 63, 3-4, 228-229(1980).
4) D.C. Dokko, J.A. Pask and K.S. Mazdiyashi, ditto, 66, 10, 699-733(1983).
5) Tal-Il Mah and K.S. Mazdiyashi, ditto, 66, 10, 699-733(1983).
6) M. Ashizuka, T. Okuno and Y. Kubota, Ceram. Soc. Jpn., Gakujutsu-Ronbunshi, 97(6), 662-668 (1989).(in Japanese)
7) T. Yoshio, A. Kawano and K. Oda, Proc., Ceram. Soc. Jpn. Annual Meeting, 16 (1989).in Jspanese
8) S.M. Wiederhorn, Fracture Mechanics of Ceramics, 2, 613-640.
9) Y. Okamoto, H. Hattori, Y. Miyata, K. Hayashi and Y. Nishikawa, Proc., Ceram. Soc. Jpn. 1989 2nd. Autumnal Sympo., 610-611 (1989) in Japanese.
10) J.I. Bluhm, Engineering Fracture Mechanics, 7, 593-604 (1975).
11) H. Kishimoto, A. Ueno and H. Kawamoto, Zairyo, 36, 409, 1122-1127(1987) in Japanese.
12) A.G. Evans, J. Mater. Sci., 7, 1137-1146 (1972).
13) T. Nose and T. Fujii, J. Am. Ceram. Soc., 71, 328-333(1988).
14) Y. Kawaguchi, Y. Yamade and T.Kishi, Nippon Zairyo Gakkaishi, in Japanese under application
15) T. Kunio, H. Nakazawa, I. Hayashi and H. Okamura, Hakai-Rikigaku Jikkenho, Asakura Shoten (1984), in Japanese.
16) R.M.L. Foote and V.T. Buchwald, Int. J. Fracture, 29, 125-134 (1985).
17) S.M. Wiederhorn and L.H. Bolz, J. Am. Ceram. Soc., 53, 10, 543-548 (1970).
18) T.A. Mishalske and S.W. Freiman, Nature, 295, 11, 511-512 (1982).

This article is a full translation of the article which appeared in Nippon Seramikkusu Kyokai Gakujutsu Ronbunshi (Japanese version), Vol.99, No.6, 1991.

A Microstructural Study of Mechanical Properties in Si_3N_4 Ceramics

Mikio Sugano, Tadaaki Satake, Hiroyuki Kisuki, Yuuji Fujimoto*, Hiraku Sato and Eiichi Suganuma****

Department of Mechanical Systems Engineering, Faculty of Engineering, Yamagata University
4-3-16, Jonan, Yonezawa-shi, 992 Japan
*Toshiba Inc., 2-4, Suehiro, Tsurumi-ku, Yokohama-shi, 230 Japan
**Yamagata Research Institute of Technology
683, Kurumanomae, Numagi, Yamagata, 990 Japan

To clarify the effect of microstructure on crack growth behavior in Si_3N_4 ceramics, fracture toughness and three point bending tests have been carried out for pressureless sintered (PLS) and hot-pressed (HP) Si_3N_4 specimens. As to the hot-pressed Si_3N_4 ceramics, the specimens were cut out parallel (HP-TL) and perpendicular (HP-SL) to the hot-pressing direction respectively for studying the anisotropy of mechanical properties. Microstructures subsequent to crack growing were characterized on the fracture surface and in the process zone wake by optical and scanning electron microscopies. The anisotropy was discernible in fracture toughness and bending strength, but hardly in microhardness. The process zone wake was damaged more severely in the HP-TL specimen than in the HP-SL one. The X-ray diffraction line profiles and pole figure analyses showed a preferred orientation of the β-phase in hot-pressed Si_3N_4. The HP-TL specimen had a fracture toughness and a bending strength about 10 percent greater than the HP-SL specimen. Pulling-out of elongated grains was more frequently observed on the fracture surface of the PLS specimen. The results obtained were discussed in connection with the preferred orientation of elongated β-phase grains from the microstructural points of view.
[Received October 12, 1990; Accepted March 22, 1991]

Key-words: Microstructural analysis, Anisotropy, Fracture toughness, Bending strength, Hot-pressed Si_3N_4

1. Introduction

Si_3N_4 forms elongated crystal grains of β-phase when it is fired. Lange[1] reported that in the case of hot-pressing Si_3N_4 ceramics c axis of elongated β-phase crystal grains had a tendency of being oriented perpendicular to the pressing direction with mechanical properties showing anisotropy of about 20%, and that the changing of the forms of crystal grains from an equi-axial type to an elongated type resulted in increasing the fracture energy of Si_3N_4 ceramics by about 4 times and the strength by twice.

On the other hand, the anisotropic properties of the mechanical strength is often attributed to the anisotropy of fracture energy when fracture is developed from a potential flaw or inclusions in the materials.[2,3] However, neither theory has come so far as to be established on the origin of strength anisotropy. Moreover, these are chiefly results of investigations on bending strength; reports on other properties seem scarce.[4] Thus accurately understanding the properties of conventional materials is extremely important as a basies for using those materials as well as developing new ones.

Our study is intended to clarify the fracture mechanism of pressureless sintered and hot-pressed Si_3N_4 in relation to their microstructures. Particularly, as to hot-pressed Si_3N_4 ceramics, specimens were cut out in two different directions to the pressing direction and, for each specimen, anisotropies of fracture toughness, bending strength and hardness were investigated and microstructural observations were made of the fracture surface and the periphery of cracks. Based on comparison with those of pressureless sintered ceramics, the results will be investigated in connection with the preferred orientation of elongated β-phase grains from the microstructural points of view.

2. Experimental Procedures

As specimens, pressureless sintered (TSN-03) and hot-pressed (TSN-02) ceramics of Si_3N_4-Y_2O_3-Al_2O_3 system manufactured by Toshiba Corp. were used. To investigate the anisotropy of crack growth properties, SB (Short Bar) specimens with a chevron notch for fracture toughness test were prepared from the hot-pressed (HP) Si_3N_4 ceramics in the shape and dimensions as shown in **Fig.1**. The shape of notch is a_0=6.35mm in depth, t=0.4mm in breadth and α=58.0° in the point angle. Two kinds of specimens were cut out; one (TL) with a test load direction perpendicular and a fracture growth plane parallel to the hot-pressing

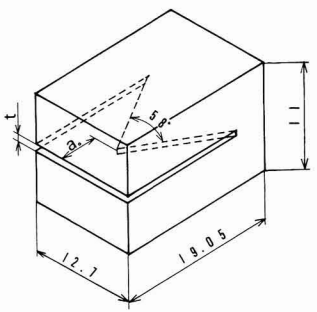

Fig. 1. Shape and dimensions of short bar (SB) specimen with chevron notch. a_0=6.35mm and t=0.4mm.

direction, and the other (SL) with a test load direction parallel and a crack growth plane perpendicular to the hot-pressing direction (**Fig.2(a)**). For fracture toughness tests, a fractometer manufactured by Terra Tek was used. With this measurement apparatus, digital K_{IC} values are output calculated on the basis of maximum load. The experiments were conducted by simultaneously recording the relationship between test load and load point opening displacement. Bending tests were conducted for at least 10 specimens of respective ceramics based on the three-point bending method with the distance between fulcrums set at 15mm. Test pieces 1.5×2.0×19mm were cut out from the surface of fracture toughness test specimens, with the pulling-side surface oriented parallel to the crack growth plane of the fracture toughness test specimens and with the major axes of both specimens orientated to the same direction. The pulling-side surfaces of the specimens were mechanically polished with SiC Emery Paper #1500 and lapping-finished with diamond paste #2000. The surface roughness was R_{max}=0.6μm in the maximum height. The microhardness was measured with a microhardness meter M (manufactured by Shimazu Corp.) at 500g in test load and for 30sec holding time. For microstructure analysis, an optical microscope, SEM (X-560 XMA: Hitachi) and the X-ray diffraction method were used. As for X-ray diffraction intensity, CuKα-ray was measured with RAD-γA (Rigaku) at 40KV in tube voltage and 100mA in tube current. For the measurement of the pole figure, RAD-IIB and a pole figure measurement apparatus (Rigaku) were used. CuKα-ray was measured at 40KV in tube voltage and 30mA in tube current and in the range of α=20-90° based on the Schultz back reflection method. For pressureless sintered ceramics (PLS), experiments were conducted in the same way as the above HP specimens except in the items related to anisotropy.

3. Results and Discussion

3.1. Microstructure Analysis

Fig.2(b) shows the results of SEM observation of the surfaces of HP and PLS specimens parallel to the crack growth plane, etched after mechanical polishing. As a general tendency, for the HP-TL specimen, the number of elongated grains oriented perpendicular to the surface (expressed hereafter as perpendicular-oriented elongated grains) is large while the number of elongated grains oriented parallel (expressed hereafter as parallel-oriented elongated grains) is small. In comparison with the above, for the HP-SL specimen the number of parallel-oriented elongated grains is also considerably large. Also in comparison with the HP specimen, the PLS specimen contains a large number of larger-sized pores. No marked difference was observed between the shapes of elongated grains of the respective specimens; the average larger diamenter of grains was 3μm with an aspect ratio of about 5.

Figure 3(a) shows the results of X-ray diffraction intensity curves measured on the HP specimen surface parallel to the crack growth plane by the diffractometer method. If the three planes of highest diffraction peak value of the β-Si_3N_4 phase (expressed hereafter as the β-phase) are shown, the orders are (101), (200) and (210) for the HP-TL specimen, and (200), (210) and (101) for the HP-SL specimen, showing the difference between the two. Both specimens contain diffraction lines from the α-Si_3N_4 phase (expressed below as the α-phase) besides those from the β-phase. The volume percentage of the α-phase contained in the specimen can be calculated based on the peak value of the diffraction intensity curve by the following equation.[5]

$$C_{\alpha/(\alpha+\beta)} = \frac{I_\alpha(210) + I_\alpha(201)}{I_\alpha(210) + I_\alpha(201) + I_\beta(200) + I_\beta(210)} \times 100$$

When the values obtained from Fig.3(a) are substituted in the above equation, $C_{\alpha/(\alpha+\beta)}$=17.4% for the HP-TL specimen and 11.2% for the HP-SL specimen, thus obtaining different results for respective specimens. The results mean that the α-phase volume fraction of the HP specimen has anisotropy attributable to the direction of cutting out the specimen. The diffraction intensity of the α-phase ($I_\alpha(210)+I_\alpha(201)$) in the above equation is 1125cps for the HP-TL specimen and 1120cps for the HP-SL specimen, showing little difference between both specimens. On the other hand, the diffraction intensity of the β-phase, ($I_\beta(200) + I_\beta(210)$), is 5350cps for the HP-TL specimen and 8860cps for the HP-SL specimen, showing a wide difference between both specimens. Therefore, the anisotropy of the α-phase volume fraction of the HP specimen obtained above is understood to be attributable to the difference of β-phase diffraction intensity curves resulting from the directions of cutting out specimens. Such anisotropy is thought to influence the evaluation of materials

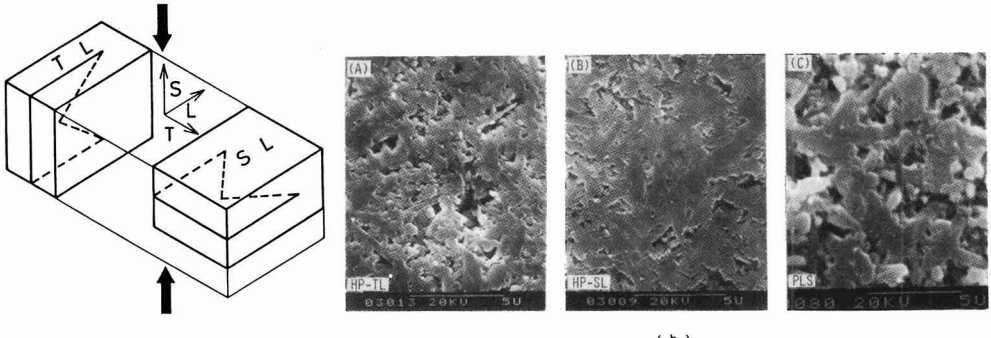

Fig. 2. Specimen preparation from the hot-pressed Si_3N_4 compact (top) and photomicrographs showing surface microstructure obtained from the HP-TL, -SL and PLS specimens respectively (bottom). The arrows indicate the hot-pressing direction.

dealt with on the basis of the mechanical properties and the composite rules of structure-sensitive compound materials.

Similar measurements were conducted on the surface parallel to the crack plane in the PLS specimens and the longitudinal section perpendicular to the crack plane. Fig.3(b) shows the results. For the PLS specimen, little difference is shown between the X-ray rocking curves measured on both measurement planes. And the diffraction intensity from the α-phase is very low in comparison with that for the HP specimen. In the same way as for the HP specimen, the volume percentages of the α-phase obtained with the above equation are 4.4% for the PLS-SIDE surface and 4.1% for the PLS-TOP surface, showing almost the same value. Therefore, it can be judged that there is no anisotropy in the volume percentage in case of the PLS specimen attributable to the direction of cutting out the specimen.

Table 1 shows the diffraction intensity of the β-phase in the HP specimen obtained as relative intensity ratios to the maximum intensity. The comparison between the same face indices of the HP-TL and HP-SL indicates that, in case of the basal or the pyramidal plane of a hexagonal structure for which the index (*hkl*) is $\ell \neq 0$, the relative diffraction intensity of the HP-TL specimen is high and that, in case of the prismatic plane for which the index is $\ell = 0$, the relative diffraction intensity shows a higher value for the HP-SL specimen. This means that the c axis of the β-phase elongated grains in the HP-SL specimen tends to be oriented perpendicular to the pressing axis. This result coincides with those reported by Lange[1] and Iwasaki et al.[6]

In **Fig.4** the same tendency is shown by the results of measurements of the {200} pole figures. The figures are the results of measurements on the surface parallel to the crack growth plane and the values show the contour level of the polar density distribution. That the high level range for the HP-SL specimen tends to distribute more densely around the center than for the HP-TL specimen shows that the HP-SL specimen contains a large number of crystal grains with the prismatic plane oriented nearly parallel to the measuring plane (i.e. the c axis is perpendicular to the crack growth plane).

The above results obtained by the X-ray diffraction method suggest that the material strength properties of the HP-Si_3N_4 specimen has an anisotropy depending on the specimen cutting directions and that, in dealing with the quantative evaluation of the specimen, the anisotropy of the β-phase elongated grains needs to be considered.

3.2. Fracture Toughness, R Curves and Structure Orientation

Figure 5 shows the measured results of fracture toughness (K_{IC}). Measurements were conducted on 15 test pieces for each specimen and the results were indicated by respective average value accompanied with standard deviation (I). It is proved that PLS specimen shows the highest value and that the comparison among HP specimens shows HP-TL>HP-SL, with the K_{IC} value of HP specimen showing anisotropy depending on specimen cutting directions.

Figure 6 shows the typical appearances obtained from the SEM observation of the fracture surface after fracture toughness test for each specimen. In the HP-TL fracture

Table 1 Peak-height ratios from the X-ray diffraction intensity of hot-pressed Si_3N_4 for the surfaces parallel (HP-TL) and perpendicular (HP-SL) to the hot-pressing direction.

h k l	Powder diffraction file I / I I	Specimens HP-TL I / I max	Specimens HP-SL I / I max
1 1 0	2 0	1 3	1 3
2 0 0	8 5	6 4	1 0 0
1 0 1	1 0 0	1 0 0	4 0
2 1 0	1 0 0	5 1	8 8
1 1 1	9	1 7	1 6
2 0 1	3 5	2 2	1 7
2 2 0	5	8	1 0
2 1 1	5	4	8
3 1 0	2 0	2	1 0
3 0 1	7 0	2 9	2 5
2 2 1	2 0	1 2	1 2
3 1 1	9	6	4
3 2 0	3 5	9	1 3
0 0 2	3 5	1 9	1
4 1 0	2 0	8	1 2

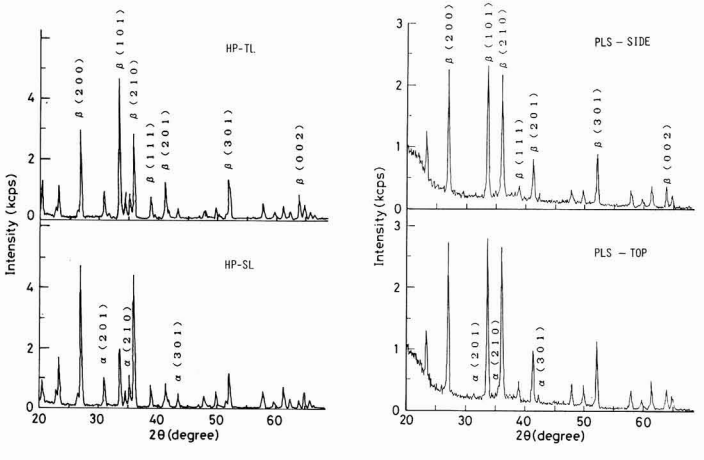

Fig. 3. X-ray rocking curves measured on the surface parallel to crack plane in the HP-TL and -SL specimens (top) and on the top and side surfaces in the PLS specimen (bottom), respectively.

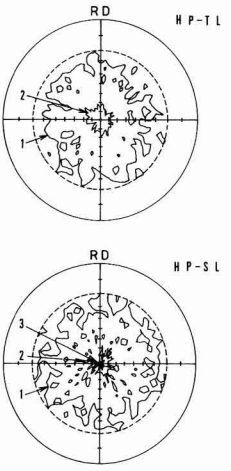

Fig. 4. {200} pole figures of the surface parallel to crack plane of the hot-pressed Si_3N_4 short bar specimens (HP-TL and HP-SL)

surface (Fig.6(A)), fracture surface is composed of the roliefmap according to the shape of grain cross section. This tells that the crack grew with transgranular mode of fracture in perpendicularly oriented elongated grains. In the fracture surface of HP-SL specimen (Fig.6(B)), the pulling-out of parallel-oriented elongated grains is frequently noticed in addition to the cross section of perpendicular-oriented elongated grains. In the case where elongated grains are parallel-oriented at the front of crack, the crack is interpreted to have a tendency to grow along the prismatic grain boundary rather than by transgranular mode of fracture. Similar results were obtained by Bowen et al.[7] and Kisuki[8] in their TEM observation of crack growth behavior. In addition, the pulling-out of perpendicular-oriented grains was less frequently observed for both HP-TL and HP-SL specimens. Although (quantatively) pulling-out tends to be observed a little more frequently for the HP-TL than the HP-SL specimen, no remarkable difference was observed between the two. This seems to be because perpendicular-oriented elongated grains are not so easily pulled out due to the bonding strength of grain boundaries being high even though there is a difference between the above two HP specimens in the perpendicular orientation of the β-phase elongated grains. Therefore, on the fracture surface of the PLS specimen (Fig.(C)) with a lower grain boundary bonding strength than that of the HP specimen, pulling-out of perpendicular-oriented elongated grains is observed considerably more frequently than for the HP specimen. Such a phenomenon as the pulling-out of perpendicular-oriented elongated grains is assumed to effectively act on increasing the fracture toughness value of the PLS specimen as shown in Fig.5.

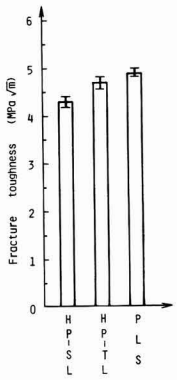

Fig. 5. Comparison of fracture toughness among the variously prepared specimens. I: standard deviation.

Figure 7 shows R-curves for each specimen obtained by the SB method. From the relationship between load and load-point opening displacement simultaneously measured in the fracture toughness test, crack growth resistance (K_R) was obtained by the equation below according to the method of Okada et al.[10] based on Baker's[9] conception.

$$K_I = \chi^{-1/2} P_F [d(r^{-1})/ds]^{1/2}$$

Here, P_F is the load output of the fractometer, r is the ratio of gradient of the load vs. loading point opening displacement curve, s is crack growth area, and χ is the minimum value of $d(r^{-1})/ds$. Each specimen shows a tendency of K_R reaching the minimum at the relative crack length, a/w ≈0.55 (a: crack length including the notch depth, w: specimen length). The slope of the curve for the HP-TL specimen after passing the minimum value is greater than for the HP-SL specimen. Such a tendency of the R-curve is also observed in the results obtained by other researchers who used similar specimens with the chevron notch,[10-12] and is interpreted to be closely related to the microstructure analysis results as described below.

Figure 8 shows the results of observation, using a Normarski contrast optical microscope, made of the appearances of crack initiation at the notch root of the longitudinal section perpendicular to the crack growth plane of the specimen for the fracture toughness test. The observation was made of the longitudinal section cut so as to include the chevron notch root after the crack has grown to midway of the specimen length (corresponding to a/w≈0.6). As shown in the figure, in many cases plural cracks initiate at notch root. Soon after initiation, the cracks grow to merge or only one crack preferable to crack growth continues to grow, leading to a final fracture after passing a stable fracture stage. In the figure, a crack trace (∇mark) that is assumed to have branched from the main crack is observed with an inclination of 15-25°C to the crack growth direction. The length of these branched cracks branchings is about 100μm

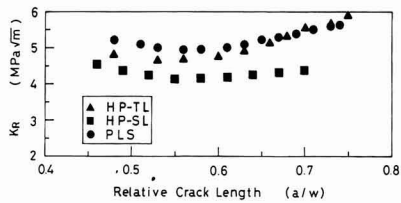

Fig. 7. *R*-curves for the variously prepared specimens. *a*: crack length including the notch depth a_0, *w*: specimen length. The *a*/*w* at notch root is 0.33.

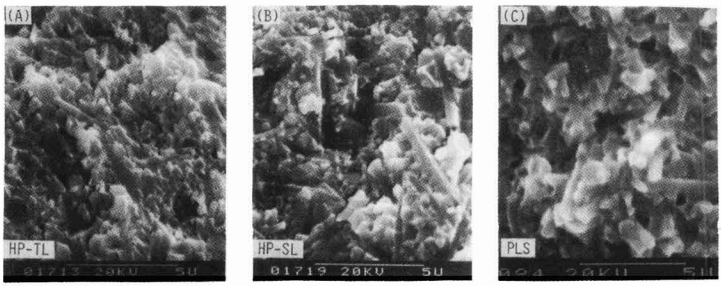

Fig. 6. Fractomicrographs showing appearances characteristics of the fracture surface after fracture toughness test for each specimen.

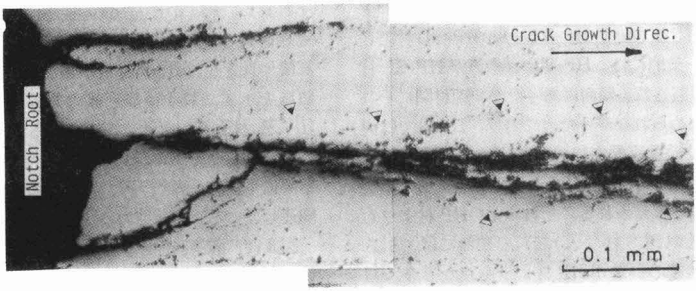

Fig. 8. Nomarski contrast optical photomicrograph taken of a longitudinal section showing appearance of crack initiation at notch root (HP-TL specimen). The symbol (▽) indicates crack branching.

in the vicinity of notch root, but become shorter to about 10μm in places far off the notch root, decreasing in rumbers, (**Fig.9(A)**). The R curve shows a somehow high crack growth resistance in the range of a/w < 0.5 (as shown in Fig.7). This appears to be related to the phenomenon that crack branching occurs more frequently in the vicinity of the notch root while it gradually decreases as the crack grows. Fig.9 shows the appearances of the development of process zone wake (corresponding to a/w=0.6) in the vicinity of crack for HP-TL, HP-SL and PLS specimens observed in the same way as in Fig.8. In the figure, the process zone wake can be distinguished as the width of damage zone developed on the both sides of growing crack. The damage zone width appears most remarkably strong for PLS specimen while it becomes weaker for HP-TL and HP-SL, in this order. Corresponding to this, cracks look more linear. Pores are obserbed along the crack growth path for PLS specimen (Fig.(C) right side). It suggests that a crack grows linking pores in its growth process. The specimen showing a well developed process zone wake includes many microscopic cracks and crack branchings and shows a high fracture toughness value in Fig.5. Therefore, the nature of process zone wake are understood to be an important factor controlling crack growth behavior and fracture toughness. As to factors influencing on process zone wake development, the orientation of β-phase elongated grains in the vicinity of crack is for hot-pressed Si_3N_4 specimen, and the existence of pores and the pulling-out phenomenon of the β-phase elongated grains are for PLS specimen. In the crack growth process of the PLS specimen, when a crack links pores togethr, local stress relief will occur at the crack tip. Because of the formation of a well-developed process zone wake and the local stress relief stated above, the R curve of PLS specimen is understood to generally show higher values than that of HP specimen. Thus, the difference in K_{IC} between HP specimens is assumed to be attributable to the difference of fracture surface morphology chiefly based on the orientation of the β-phase elongated grains; the difference between HP and PLS specimens is assumed to be related to the interaction between pores and crack observed in the PLS specimen and the pulling-out phenomenon of the β-phase elongated grains.

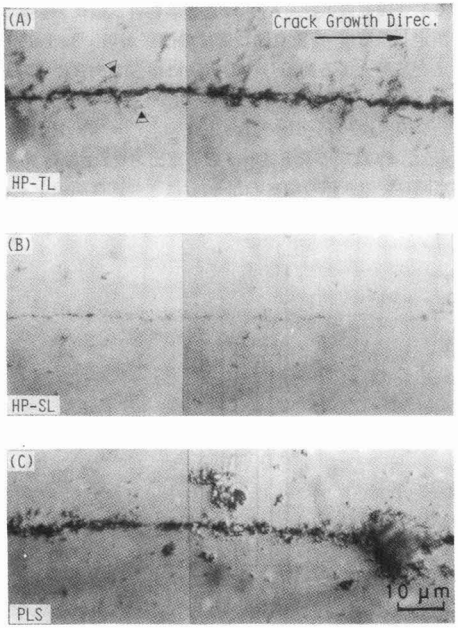

Fig. 9. Nomarski contrast optical photomicrographs (longitudinal section) showing appearances of damage zones formed along a growing crack in each specimen. The symbol (▽) indicates crack branching. The *a/w* is 0.6.

3.3. Bending Strength, Hardness and Microstructure

Figure 10 shows the results of bending strength measured for each specimen with standard deviations appended. To understand the influence of the processing condition on bending strength, as-cut specimens with a diamond cutter and those finished by mechanically polishing the surface with emery paper and lapping were prepared. 10-15 pieces of each specimen were tested to obtain average values. Contrary to the results of K_{IC}, bending strength for the HP specimen showed a higher value than for the PLS specimen. However, the bending strength between HP specimens is also HP-TL>HP-SL, the same relationship of large-and -small as in K_{IC}. In other words, the relationship of large-and-small that depends on cutting-out direction of specimen for testing fracture toughness value and bending strength is preserved between specimens prepared under the same manufacturing conditions independent of cutting-out direction, but not preserved between specimens prepared under different manufacturing conditions. This fact suggests that fracture toughness and bending strength are not necessarily governed by the same factor. Fig.10 shows a tendency of bending strength being higher for the as machined specimen than for the mechanically polished

specimen. It is very interesting to notice that this tendency greatly depend on processing conditions. This suggests that bending strength depends also on processing methods.

Fracture surface morphology and fracture origin were investigated by observing the fracture surface after bending test with an optical microscope and SEM. As shown in the matching pairs of **Fig.11(A)**, the macroscopic fracture surface morphology is composed of mirror, mist and hackle regions. Figs.11(B) and 11(C) show the results of SEM observation of the mirror and hackle regions. The mirror region presents a microscopic morphology consisting chiefly of the transgranular fracture mode of elongated grains and showing that the hackle region was fractured with grains being aggregated. Most fracture origins are defects lying immediately under the surface subjected to tension. **Figure 12** shows an example of the SEM observation of crack origin. The types of defects are chiefly pores and foreign substances, and in this study, surface scratches were scarcely observed (to be a fracture origin). In our experiences, we obtained results that if polishing is parallel to the longitudinal axis of the specimen, surface roughness below R_{max}=3.6μm did not influence bending strength so much.[8] Analyzed with EDX, the foreign substances that exist on the surface or inside (though a very rare case) which initiate the crack were found to consist chiefly of Si containing a trace amount of Al. In the periphery of the inside foreign substances, a cavity of about 50μm in diameter consisting of aggregates of small pores was observed. By the same reason as reported by Itoh et al.,[13] this cavity is assumed to be formed due to the aggregation of Al_2O_3 added as a sintering additive. In the case of a small specimen as used in this study, the bending stress gradient toward the neutral axis if specimen is large, compared with the case of a large specimen. For this reason, the crack growth from a defect existing on the specimen surface is understood to be under mechanically better conditions when proceeding along the surface in the width direction than from the defect root in the thickness direction. Since bending strength is very sensitive to the poperties of the surface subjected to tension, it is assumed that the difference resulting from the difference in processing method as shown in Fig.10 was caused depending on the difference in the depth and magnitude of residual stresses etc. of the process-affected layer.[14,15]

Figure 13 shows the results of Vickers microhardness. Each value was obtained as the average of more than 20 measuring points. Although a slight tendency of HP-TL<HP-SL is noticed in the results, the difference between the two specimens is very small. The hardness of the PLS specimen was considerably lower than that of the HP specimen.

3.4. The Anisotropy of Hot-pressed Si_3N_4 Ceramics

Table 2 shows the degrees of anisotropy of fracture

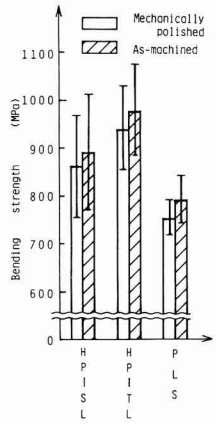

Fig. 10. Comparison of bending strength among the variously prepared specimens. I: standard deviation.

Fig. 12. SEM photomicrographs showing fracture origin observed on the fracture surface after three-point bending test.

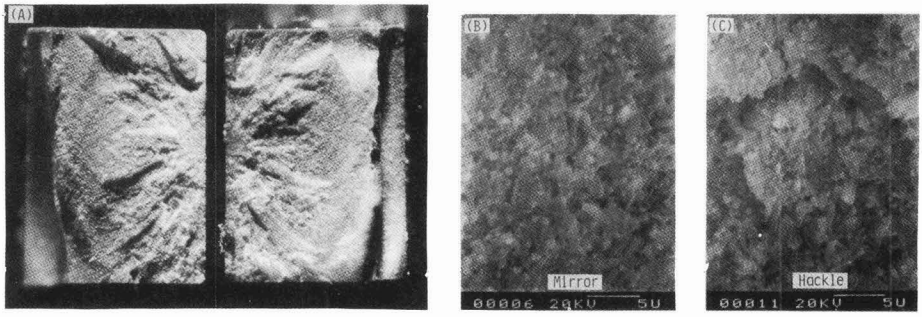

Fig. 11. Optical and scanning electron photomicrographs showing the fracture surface morphology after three-point bending test, in which the specimen broke down at σ_b=952MPa. Matching pairs (A) and SEM photomicrographs taken of the areas corresponding to the fracture mirror and hackle regions in (A) respectively ((B), (C)).

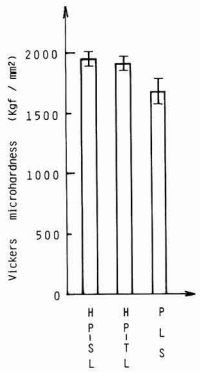

Fig. 13. Comparison of Vickers microhardness among the variously prepared specimens. I: standard deviation.

toughness and bending strength depending on the specimen cutting directions obtained from the results in Fig.5 and 10 as ratios on HP-SL/HP-TL. Both fracture toughness and bending strength were obtained as about 0.9 in the relative strength ratios of the two specimens. Therefore, taking into consideration the crystallographical ainsotropy obtained by the X-ray diffraction method as mentioned above, the anisotropy of mechanical properties of the HP specimen attributable to orientation is recognized to be about 10%. This value is small as compared with the approx. 20% bending strength results obtained by Lange.[1] This is inferred to be attributable to the difference in composition and manufacturing conditions of specimens. Both results show that, in using hot-pressed Si_3N_4 ceramics, consideration of the specimen cutting direction is important.

4. Conclusion

Measurements were taken of the fracture toughness and three point bending strength and hardness of SB specimens cut out with crack growth plane parallel (HP-TL) and perpendicular (HP-SL) to the hot-pressing direction of hot-pressed S_3N_4 ceramics (HP); the anisotropy of the mechanical properties were investigated. As compared with those of microstructure analysis and pressureless sintered ceramics (PLS), the following results were obtained:

1) There was a difference between the HP-TL and HP-SL specimens in the X-ray diffraction intensity curves obtained from the β-Si_3N_4 phase of the HP specimen, whereas little difference between both specimens was observed in the X-ray rocking curves of the α-Si_3N_4. Among the results measured on the top and side surfaces in the PLS specimen, there was no difference either for the α-Si_3N_4 or β-Si_3N_4 phase. Therefore, when the volume fraction of the α- and β-phase and the mechanical properties are quantitatively evaluated from the X-ray rocking curves for the HP specimen, it is necessary to consider the anisotropy in the peak height values of the β-phase in the curves.
2) In the fracture toughness obtained by the SB method and three-point bending strength, 10% anisotropy was observed between the HP-TL and HP-SL specimens. In both fracture toughness and three-point bending strength, HP-TL>HP-SL, thus in both values the HP-TL specimen showed better properties. Though hardness shows a tendency of HP-TL<HP-SL, the difference between both specimens is very small. However, in comparison with the PLS specimen, the HP specimen is superior in bending strength and hardness and inferior in fracture toughness. In other words, correlation between fracture toughness and bending strength is preserved for specimens prepared under the same conditions independent of the specimen cutting direction, but not for specimens prepared under different conditions.
3) The microstructural observation of the longitudinal section of SB specimens revealed that the HP-TL specimen was more remarkable than the HP-SL specimen in the development of process zone wake between the HP specimens, and further that the PLS specimen was more remarkable than the HP specimens. The severity of the process wake zone is closely related to the results of fracture toughness and the crack growth resistance curve.
4) Judging from the fracture surface morphology, transgranular mode of fracture was caused by the crack cutting through perpendicular-oriented elongated grains in the HP-TL specimen while in the HP-SL specimen a crack appeared to have grown along the grain boundary of horizontal-oriented elongated grains. Pulling-out of elongated grains on the fracture surface frequently observed although there was not such a marked difference from the HP-SL specimen. Pulling-out of elongated grains in the PLS specimen was observed much more frequently than in the HP specimen.
5) An anisotropy due to the prefered orientation of the β-phase elongated grains exists in the fracture toughness and three-point bending strength of hot-pressed Si_3N_4 ceramics. But it is not so remarkable in hardness.

Table 2 The ratios of fracture toughness and bending strength between the HP-TL specimen and the HP-SL one in the hot-pressed Si_3N_4 ceramics.

		HP-SL	HP-TL	HP-SL/HP-TL
Fracture toughness (MPa·√m)		4.3	4.7	0.91
Bending strength (MPa)	1)	862	941	0.92
	2)	892	980	0.91

1): Mechanically polished surface. 2): Machined surface.

(The results of the study were partly presented at the 25th-Yogyo Kiso Toronkai, in January, 1987.)

Acknowledgements
This study was partly assisted by the Zairyokogaku Joseikai of Nihon Itagarasu.

References:

1) F.F. Lange, J. Amer. Cer. Soc., 56, 518-522 (1973).
2) Ram Kossowsky, J. Mat. Sci., 8, 1603-1615 (1973).
3) J.E. Weston, J. Mat. Sci., 15, 1568-1576 (1980)
4) H. Suzuki(ed), High Temperature Ceramics Materials, Nikkan Kogyo (1985) p.157-158.
5) O. Yeheskel and Y. Gefen, Mat. Sci. Engng., 71, 95-99 (1985).
6) H. Iwasaki and M. Iaumi, Zairyo, 30, 1044-1050 (1981).
7) L.J. Bowen and T.G. Carruthers, J. Mat. Sci. 13, 684-687 (1978).
8) H. Katsugi, A Master's Thesis in Engineering, Yamagata University, (1987) p.61-62.
9) L.M. Barker, Int. J. Fracture, 15, 515-536 (1979).
10) A. Okada and N. Hirosaki, K. Matoba, Yogyo Kyokaishi, 95, 559-

561 (1987).

11) H. Kobayashi, H. Nakamura, A Kitayama and S. Yamamoto, Trans. JAME, A-54, 1080-1085 (1988).

12) S. Sakaguchi, F. Wakai, H. Kato and T. Shimada, Yogyo Kyokai, Koenyokoshu, 1, (1986) 359-360.

13) M. Ito, K. Sakai and M. Ito, Ziaryo, 30, 1019-1024 (1981).

14) S. Matsuno, M. Ito and H. Okuda, Seramikkusu, 16, 546-553 (1981).

15) H. Okuda and M. Ito, Zairyo, 32, 823-829 (1983).

This article is a full translation of the article which appeared in Nippon Seramikkusu Kyokai Gakujutsu Ronbunshi (Japanese version), Vol.99, No.6, 1991.

Effect of Heating Rate on the Shrinkage of Isothermal Sintering

Yasuo Ikuma, Masaki Nakayama, Yuushi Harada and Takehiro Hiuga*

Kanagawa Institute of Technology
Shimoogino, Atsugi-shi, Kanagawa 243-02, Japan
*Sumitomo Metal Mining Co., Central Research Laboratory, Nakakokubun, Ichikawa-shi, Chiba 272, Japan

Isothermal sintering of $Ba(Mg_{1/3}, Ta_{2/3})O_3$ and ZrO_2 doped with Y_2O_3 was studied at various heating rates. Rapid heating was much effective in promoting densification process of $Ba(Mg_{1/3}, Ta_{2/3})_3$. X-ray diffraction, SEM observation and BET measurement showed that the rapid heating stimulated effectively the sintering of secondary particles whereas the slow heating contributed only to that of primary particles. When specimens were rapidly heated to the sintering temperature, the surface area of specimens did not change during the process of temperature increase. This resulted in a large shrinkage at the sintering temperature. When the specimens were heated slowly to the sintering temperature, the surface area was significantly reduced before reaching the sintering temperature and the densification was retarded.
[Received November 1, 1990; Accepted February 20, 1991]

Key-words: Rapid sintering, $Ba(Mg_{1/3}, Ta_{2/3})O_3$, Y-$ZrO_2$, Surface area

1. Introduction

Several methods have been used to reduce the ceramics processing time. Among them, one method is to shorten the sintering time. The zone sintering[1,2] achieves the densification of β-Al_2O_3 and α-Al_2O_3 in a short time. With this method, a large temperature gradient can be produced in one compact, with the portions of preheating, on-heating, sintering, on-cooling, and postcooling being in one specimen. The plasma sintering[3,4] is similar to the zone sintering, but a large difference is that plasma is used for heating. Considering the retention of specimen shape, the zone or plasma sintering is suitable for sintering of tube- or rod-shaped compacts.

Looking at one point in the compact, these methods achieve rapid heating. Ichimura et al.[5] reported that in sintering $Ba(Mg_{1/3}, Ta_{2/3})O_3$, slow heating of specimen resulted in low density, while rapid heating resulted in high density. They changed the temperature of one compact uniformly, but rapid heating was similar to the zone or plasma sintering. This rapid-rate sintering has been clarified phenomenally and can be explained qualitatively in terms of initial sintering theory[2], but there are disputes over the quantitative explanation[6,7] and the change in specimen is still unknown in many points. The zone and plasma sintering has a difficulty in determining the change of surface area of specimen because a difference in degree of sintering occurs in one specimen with such sintering methods. In the present work, we performed the rapid-rate sintering of $Ba(Mg_{1/3}, Ta_{2/3})O_3$, and ZrO_2 doped with Y_2O_3 by the method of Ichimura et al,[5] in which one specimen was uniformly heated and we examined if there were any changes in specimens depending on the heating rate. $Ba(Mg_{1/3}, Ta_{2/3})$ has been reported to surely have an effect of rapid-rate sintering. However, an effect of the rapid-rate sintering of ZrO_2 doped with Y_2O_3 has not been reported.

2. Experimental Method

$Ba(Mg_{1/2}, Ta_{2/3})O_3$ was prepared as follows: Barium carbonate, magnesium oxide, and tantalum oxide were weighed to the stoichiometric composition. The mixture, to which water was added, was ball-milled for 16hrs, and then calcined at 1100°C for 2hrs in oxygen to form $Ba(Mg_{1/3}, Ta_{2/3})O_3$ powder. The powder was ground in a mortar, and uniaxially pressed under a pressure of 1.5t/cm^2 into a 10mm-dia, about 3mm thick specimen. The powder (TZ-3Y) manufactured by Tosoh Corporation was used as it was for 3mol% Y_2O_3-doped ZrO_2, which was pressed by the above-described method.

The molded specimens of $Ba(Mg_{1/3}, Ta_{2/3})O_3$ were heated in three ways; namely, they were heated from room temperature to the sintering temperature (1450–1600°C) in 1, 5, or 60 minutes (hereafter called 1min heating, 5min heating, and 60 min heating; the corresponding heating rates are about 25Ks,$^{-1}$ 5.1Ks,$^{-1}$ and 0.42Ks^{-1}). The specimens were kept at the sintering temperature for the specified time (0–10min), and then taken out of furnace in 1min for cooling. The thickness of specimen was measured at three points before and after the sintering. The mean value was calculated as the shrinkage from the three measurements. Separate specimens were used for each sintering time.

On the specimens of 3mol% Y_2O_3-doped ZrO_2, the thickness was also measured at several points, and the mean thickness was calculated. The specimens were heated to the specified sintering temperature (1000–1400°C) in 1, 180, or 360 minutes (hereafter called 1min heating, 180min heating, and 360min heating; the corresponding heating rates are about 21Ks,$^{-1}$ 0.12Ks,$^{-1}$ and 0.059Ks^{-1}). After being kept at that temperature for the specified hours, the specimen were taken out of the electric furnace taking 1 minute. After the thickness was measured, the specimens were returned into the electric furnace taking 1 minute. Thus, the measurement was repeated. For both types of specimens, the shrinkage at each sintering temperature was determined as the function of sintering time. After sintering, the SEM observation of some specimens was made, and the particle size was determined by X-ray diffraction. The specific surface areas of some specimens were also measured by the

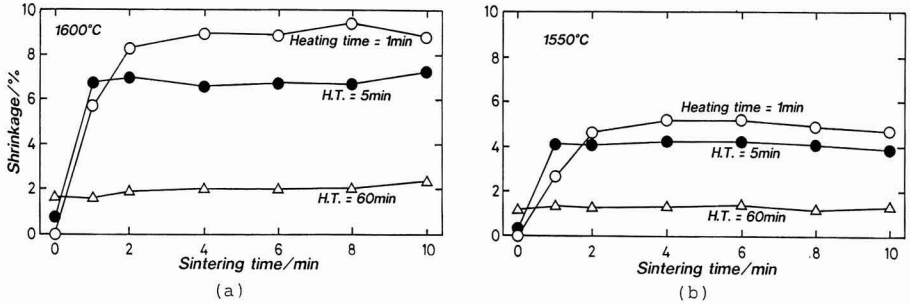

Fig. 1. Shrinkage of $Ba(Mg_{1/3}, Ta_{2/3})O_3$ during the isothermal sintering. Sintering time is the time only when the specimens were at designated temperature. Specimens were heated to sintering temperature with 3 different heating times: 1, 5, and 60min from room temperature to each sintering temperature (heating rate=25Ks,$^{-1}$ 5.1Ks^{-1} and 0.42Ks,$^{-1}$ respectively). Sintering temperature = (a) 1600°C and (b) 1550°C.

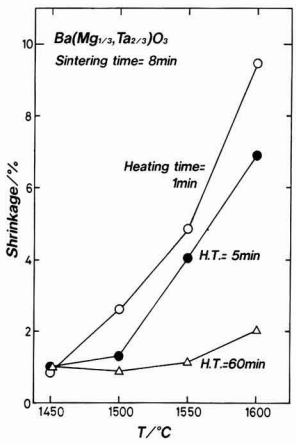

Fig. 2. Shrinkage of $Ba(Mg_{1/3}, Ta_{2/3})O_3$ at sintering time = 8min.

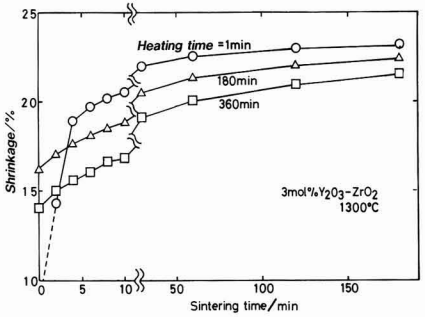

Fig. 3. Shrinkage of ZrO_2 doped with Y_2O_3 at 1300°C. Specimens were heated with 3 different heating times: 1, 180, and 360min from room temperature to sintering temperature (heating rate = 21Ks,$^{-1}$ 0.12Ks,$^{-1}$ and 0.059Ks,$^{-1}$ respectively).

BET method.

3. Experimental Results

Figure 1 shows the shrinkage of $Ba(Mg_{1/3}, Ta_{2/3})O_3$ during the isothermal sintering at various heating rates. At a sintering temperature of 1600°C, the specimen of 60min heating has the smallest final shrinkage; as the heating rate increases from 60min to 1min, the shrinkage apparently increases. The sintering time on the horizontal axis in the figure indicates a time elapsing after the sintering temperature has been reached, excluding the heating time. For example, the point of sintering time=0 means that the specimen is taken out of the furnace when being heated to the sintering temperature. The shrinkage of 1.7% at the sintering time=0 for 60min heating suggests that the sintering proceeds during heating, resulting in shrinkage. For 1min heating, the shrinkage is nearly 0% at the sintering time=0, which means the specimen shrinks less during heating. The change of shrinkage at the sintering time=1–2min, depends strongly on the heating rate. For 60min heating, the shrinkage does not change at this sintering time. For 5min heating, the shrinkage occurs for the first one minute, while for 1min heating, the shrinkage rapidly occurs for the first two minutes or so. This corresponds to the fact that for 1min heating, the specimen is heated to the sintering temperature with the driving force for sintering maintained as will be described later.

At a sintering temperature of 1550°C, the same tendency as that at 1600°C is found (Fig.1(b)); however, the shrinkage generally decreases as compared with the case at 1600°C. A similar tendency is found at a sintering temperature of 1500°C. To clarify this fact, the shrinkage at the sintering time=8min is shown in **Fig.2** as the function of sintering time. At temperatures except 1450°C, the shrinkage apparently increases with the increase in heating rate.

To check whether such an effect of heating rate observed on $Ba(Mg_{1/3}, Ta_{2/3})O_3$ is found on other systems, a similar experiment was performed on Y_2O_3-doped ZrO_2. The result of experiment is shown in **Fig.3**. Unlike $Ba(Mg_{1/3}, Ta_{2/3})O_3$, the heating times of 1min, 180min, and 360min are used. Nevertheless, the specimen shrinks most when being heated rapidly. As compared with $Ba(Mg_{1/3}, Ta_{2/3})O_3$, the difference in shrinkage with the heating rate is relatively small. In particular, the slowly heated specimen (180min heating and 360min heating), though shrinking considerably at the

sintering time=0, shrinks additionally by about 5% at the sintering temperature. For 1min heating, the shrinkage occurs rapidly at the sintering time=0–5min, and the final shrinkage is largest for 1min heating. This means that even for the sintering of Y_2O_3-doped ZrO_2 rapid-rate heating is effective.

To investigate the difference between the rapidly heated specimen and slowly heated specimen, SEM observation was performed. Typical results of SEM observation are shown in **Fig.4**. Comparing with the section of unheated $Ba(Mg_{1/3}, Ta_{2/3})O_3$ specimen (Fig.4(a)), the pores seem to grow on the specimen that has been heated to 1600°C in 60min and held for 4min (Fig.4(b)). The shrinkage in this case is about 2% (Fig.1). The pores have grown probably because the sintering did not take place between secondary particles, though the sintering took place within the aggregated secondary particles. On the other hand, the specimen that has been heated to 1600°C in 1min and held for 5min (Fig.4(c)) has relatively fewer pores. This means that the sintering took place not only within the secondary particles but also between them. This agrees well with the high shrinkage (Fig.1). Although there is such a difference, the primary particles hardly grew on both specimens. This leads to a conclusion that this sintering is not accompanied by the formation of liquid phase. For Y_2O_3-doped ZrO_2, the particle size was estimated from the width at half the maximum intensity of X-ray diffraction peak. The estimated result is that the difference due to sintering temperature is found, but almost no difference due to heating rate is found, the difference being only in the order of error. This suggests that the heating rate has no effect on the particle size.

Although it was considered that the difference in microstructure due to the heating rate could be observed by SEM since the formation of neck proceeded at the initial stage of sintering, the shape of neck could not be determined. When a neck is formed, the surface area of powder decreases. Therefore, the specific surface area of compact was measured by the BET method to know the difference due to the heating rate. **Figure 5** shows the specific surface area of $Ba(Mg_{1/3}, Ta_{2/3})O_3$ measured by the BET method. For 60min heating (Fig.5(b)), the specific surface area of specimen of sintering time=0min decreases slightly as compared with the unfired specimen. In particular, the higher the sintering temperature, the greater the decrease in specific surface area. This may be because of the formation of neck. At all sintering temperatures, the specific surface area of specimen of sintering time=4min changed only by about $0.3m^2/g$ as compared with that of specimen of sintering time=0min. This fact also means that for 60min heating, the sintering has already proceeded when the sintering temperature has been reached, almost no driving force for sintering has remained at the sintering temperature. On the other hand, the specific surface area of specimen of 1min heating (Fig.5(a)) is nearly the same as that of unheated specimen when the sintering temperature is reached (sintering time=0), which means that the specimen is heated to the sintering temperature with the driving force for sintering (proportional to the specific surface area) being sufficiently kept. The change of specific surface area with the change of sintering time from 0min to 4min is as large as 0.8–$1.5m^2/g$, which agrees well with the result of shrinkage measurement. When the specimen is heated to 1600°C or 1550°C in 1min and sintered for 4min, closed pores begin to be formed. The specific surface area measured on these specimens does not show good accuracy.

The specific surface area of Y_2O_3-doped ZrO_2 was also measured by the BET method. The BET method could not be used to measure the surface area of specimen sintered at 1300°C because the final sintering stage was reached. Therefore, the specimen sintered at 1100°C was used to

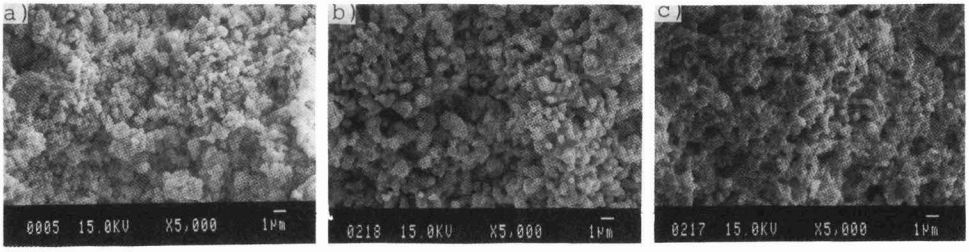

Fig. 4. Scanning electron micrographs of $Ba(Mg_{1/3}, Ta_{2/3})O_3$ compacts: a) without sintering, b) heated to 1600°C in 60min and held the temperature for 4min, and c) heated to 1600°C in 1min and held the temperature for 5min.

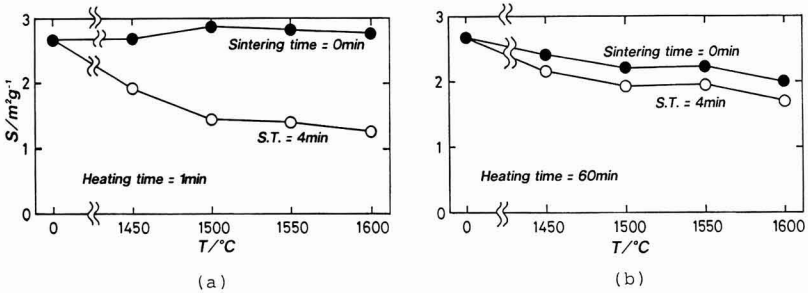

Fig. 5. Specific surface area of $Ba(Mg_{1/3}, Ta_{2/3})O_3$ measured by BET method. Heating time = (a) 1min and (b) 60min.

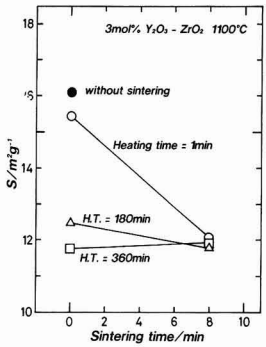

Fig. 6. Specific surface area of Y-ZrO_2 measured by BET method. Specimens were sintered at 1100°C.

measure the specific surface area. The result (shrinkage= about 3–4%) is shown in **Fig.6**. Also in this case, the specimen heated in 1min and having the sintering time=0 still has the original specific surface area, having the driving force for sintering. This is the same as $Ba(Mg_{1/3}, Ta_{2/3})O_3$.

4. Discussion

The initial sintering theory states that the shrinkage is larger when the sintering proceeds by surface diffusion than it does by volume diffusion or grain boundary diffusion. Since the volume diffusion and grain boundary diffusion are the diffusion mechanisms that are important at high temperatures, the shrinkage becomes larger when the specimen is rapidly heated in a shorter heating time. This fact was proven by this experiment. When the sintering proceeds, the specific surface area decreases, resulting in the decrease in driving force for sintering. Therefore, from the result shown in Figs.1 and 5, it is found that,

1) When the specimen is heated slowly, the specific surface area (that is, driving force) decreases before the sintering temperature is reached. Therefore, the sintering is difficult to proceed at the sintering temperature.
2) When the specimen is heated rapidly, the specific surface area (that is, driving force) is almost unchanged even when the sintering temperature is reached. Therefore, the sintering proceeds rapidly, being accompanied by large shrinkage, at the sintering temperature.

There was a difference in the effect of rapid-rate heating between $Ba(Mg_{1/3}, Ta_{2/3})O_3$ and Y_2O_3-doped ZrO_2. This difference is related with the diffusion that governs the sintering mechanism. When Y_2O_3-doped ZrO_2 is heated to 1000–1400°C, monoclinic ZrO_2 or tetragonal ZrO_2 is formed. The diffusion coefficients have not been determined for all crystal structures of ZrO_2, and the difference in diffusion coefficiants between the crystal structures of ZrO_2 is smaller than the difference in diffusion coefficients between ZrO_2 and other compound. For these reasons, the diffusion coefficients of cubic ZrO_2 will be used for the discussion because large amounts of data is available on this crystal structure. The volume diffusion of oxygen in cubic ZrO_2 is fast, its grain boundary diffusion is not promoted over the volume diffusion,[8] and its surface diffusion is only slightly faster than the volume diffusion.[9] The volume diffusion of Zr^{4+} in cubic ZrO_2 is several orders of magnitude smaller than the volume diffusion of oxygen,[10] and its grain boundary diffusion is greater than the volume diffusion by the several orders of magnitude,[10] but there is no data on its surface diffusion. On the other hand, no data is available on the diffusion of $Ba(Mg_{1/3}, Ta_{2/3})O_3$, so that it is impossible to quantitatively discuss the experimental results in terms of diffusion. When $Ba(Mg_{1/3}, Ta_{2/3})O_3$ specimen is slowly heated (60min heating) (Fig.1), almost no shrinkage occurs at the sintering temperature, while, Y_2O_3-doped ZrO_2 specimen, even if being heated for 360min, shrinks considerably. Since the diffusion of a slowly diffusing species (Zr^{4+} in this case) should be considered for compounds, the sintering at high temperature may proceed at a sufficiently high rate by grain boundary diffusion of Zr^{4+}. However, detailed discussion cannot be given because the diffusion coefficient of $Ba(Mg_{1/3}, Ta_{2/3})O_3$ is unknown. We hope that the study on this subject will be actively made.

The absolute values of specific surface areas greatly differ between $Ba(Mg_{1/3}, Ta_{2/3})O_3$ and Y_2O_3-doped ZrO_2. the value of Y_2O_3-doped ZrO_2 is 12–16m^2/g, while that of $Ba(Mg_{1/3}, Ta_{2/3})O_3$ is 1–27m^2/g, one-order lower. This means that the particle size of $Ba(Mg_{1/3, Ta2/3})O_3$ is larger. Since the formula expressing sintering rate shows that smaller particle size results in more rapid sintering, this difference in particle size may be one reason for the difference in experimental results between $Ba(Mg_{1/3}, Ta_{2/3})O_3$ and Y_2O_3-doped ZrO_2.

5. Conclusions

The effect of heating rate on shrinkage in isothermal sintering of $Ba(Mg_{1/3}, Ta_{2/3})O_3$ and ZrO_2 doped with Y_2O_3 was investigated. As a result, it was found that rapid heating produced large shrinkage. This effect was particularly large on $Ba(Mg_{1/3}, Ta_{2/3})O_3$. The SEM observation of specimen revealed that slow heating caused only primary particles to be sintered, but rapid heating promoted the sintering of even secondary particles producing less pores. There was, however, no difference in particle size determined by x-ray diffraction. The BET measurement showed a particularly large difference in specific surface area and revealed the followings:

1) When the specimen was heated slowly, he specific surface area (that is, driving force) decreased by the time when the sintering temperature was reached. Therefore, the sintering was difficult to proceed at the sintering temperature.
2) When the specimen was heated rapidly, the specific surface area (that is, driving force) was unchanged even when the sintering temperature was reached. Therefore, the sintering proceeded rapidly, being accompanied by large shrinkage, at the sintering temperature.

References:

1) S.R. Tan and G.J. May, Sci. Ceram., 9, 103-110 (1977).
2) M. Harmer, E.W. Roberts and R.J. Brook, Trans. J. Brit. Ceram. Soc., 78, 1, 22-25 (1979).
3) J.S. Kim and D.L. Johnson, Am. Ceram. Soc. Bull, 62, 5, 620-22 (1983).
4) E.L. Kemer and D.L. Johnson, Am. Ceram. Soc. Bull., 64, 8, 1132-36 (1985).
5) H. Ichimura, K. Matsumoto and T. Hiuga, Material Forum, Sangyo Chosakai, 3-6 (1986).

6) R.M. Young and R. McPherson, J. Am. Ceram. Soc., 72, 6, 1080-1081 (1989).
7) D.L. Johnson, J. Am. Ceram. Soc., 73, 8, 2576-2578 (1990), R.M. Young and R. McPherson, ditto, 73, 8, 2579-2580 (1990).
8) L.A. Simpson and R.E. Carter, ditto, 49, 3, 139-144 (1966).
9) Y. Ikuma, K. Komatsu and W. Komatsu, Adv. Ceram., 24, 749-758 (1988).
10) W.H. Rhodes and R.E. Carter, J. Am. Ceram. Soc., 49, 5,244-249 (1966).

This article is a full translation of the article which appeared in Nippon Seramikkusu Kyokai Gakujutsu Ronbunshi (Japanese version), Vol.99, No.6, 1991.

Measurement of Thermal Diffusivity of Pyroceram 9606 by the Laser Flash Method

Hiromichi Ohta, Tatuyuki Tsukida, Yo Tomota, Hiroyuki Shibata*,

Gaku Ogura* and Yoshio Waseda*

Department of Material Science, Faculty of Engineering Ibaraki University
Nakanarusawa 4-12-1, Hitachi-shi, 316 Japan
*Research Institute of Mineral Dressing and Metallurgy (SENKEN), Tohoku University
Katahira 2-1-1, Sendai-shi, 980 Japan

Up to date, neither Certified Reference Materials (CRM) nor Standard Reference Materials (SRM) have been available for thermal diffusivity values in the range around $10^{-2}cm^2/s$, which would be useful to advanced ceramics research. Therefore, a round robin test of Pyroceram glass ceramics Corning 9606 for one of the SRMs has been arranged by the subcommittee C-14.91 in National Institute of Standards and Technology (NIST)/ASTM. The results of thermal diffusivity measurement of the Corning 9606 have been described toward the international collaboration to certify Standard Reference Material.

The surface of a disc sample was coated by carbon spray. The apparent thermal diffusivity of an identical sample increased with the number of laser beam flashing because the irradiation of a laser beam burns the carbon coating: (1) a small low temperature rise caused by lower absorption ratio of damaged coating substance increases the apparent thermal diffusivity associated with the negative temperature dependence of thermal diffusivity of Corning 9606 and (2) a burned carbon coating permits the penetration of the laser beam to the sample, which caused fast temperature rise of back surface. For reducing the irradiation damage of carbon coating, a glass cell filled with a $CuSO_4$ solution was inserted in the laser beam path as a variable attenuator. Ninety percent attenuation for the sample 0.97mm thick was found to be favorable to determine the thermal diffusivity value with sufficient reproducibility. The effect of transparency of the sample on the measured thermal diffusivity was also estimated by the theoretical calculation and this clearly confirmed the usefulness of carbon coating. Based on these careful preliminary examinations, the thermal diffusivity values of Corning 9606 in a temperature range between room temperature and 976K were independently determined using two different apparatuses and good agreement was found.

[Received November 7, 1990; Accepted February 20, 1991]

Key-words: Thermal diffusivity, Pyroceram glass ceramics, Standard Reference Materials, Laser flash method, Heat transfer

1. Introduction

A substance which can be used as the standard in measuring heat transfer properties such as thermal conductivity and thermal diffusivity and its properties are indispensable to the certification of measuring instruments and equipment and in estimating their accuracy. Therefore, the U.S. National Bureau of Standard (current National Institute of Standards and Technology), the Information and Numerical Data Analysis Center of Perdue University and others have carried out tests[2] to select standard reference materials and determine their recommended values from an international view-point. However, a standard reference material has not yet been decided for the range of about $10^{-2}cm^2/s$ of thermal diffusivity for the region between austenitic stainless steels and glass fibre boards. Since thermal diffusivity values of many substances among fine ceramics being developed for electronic or structural materials remain in this range, this matter has presented an obstacle in research on thermal properties. At this time, measurements have been carried out through the international collaboration[1] on Pyroceram brand glass ceramics, Code 9606: Corning Glass Works, a polycrystallin ceramics, comprising of SiO_2, Al_2O_3, MgO and TiO_2, in order to certify the standard reference materials for the measurement of thermal diffusivity values in this range.

The thermal diffusivity values of solid substances are often calculated by measuring the temperature responses of infra-red ray detectors using the measuring methods through light heating, such as the laser flash or stepwise heating methods. These methods have advantages such as less error induced by heat leak and short time required for measurement because the heating and temperature measurements are done on a non-contact basis. However, these measurements are based on conditions in which only the surface of the test sample is heated and the surface temperature at the back of the test sample is measured; thus due consideration is required during measurement and analysis concerning the penetration of heating light, radiation from the sample interior and so forth (unless the test sample is opaque). This report describes the measurement of thermal diffusivity values on Pyroceram 9606 glass ceramics ranging from room temperature to 976K using the laser flash method, as one of the international collaboration measurements.

2. Results and Discussions

We obtained a cylindrical block 25.4mm in length and 25.4mm in diameter by courtesy of the National Institute of Standards and Technology/ASTM committee C14.91. The

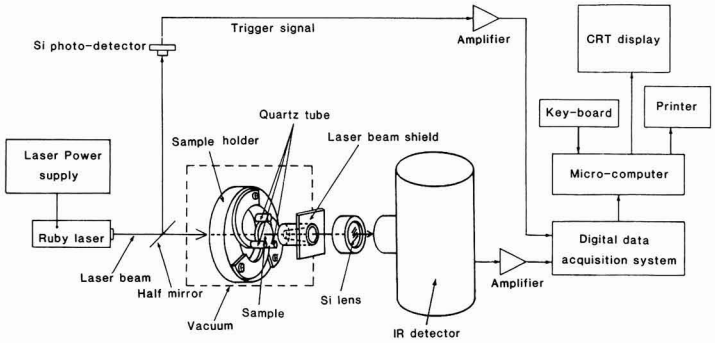

Fig. 1. Schematic diagram of the experimental apparatus for measuring thermal diffusivity of inorganic materials at room temperature.

block was sliced parallel to the bottom surface into discs of given thickness, and these discs were cut and ground into plate from of 10mm in diameter as the test samples. First, we measured the thermal diffusivity of these discs at room temperature by the laser flash method, changing the conditions of beam intensity, coating for beam absorption and so on. Then, we determined the adequate measuring conditions based on these measurements, and carried out the measurement at high temperatures.

2.1. Measurement on the Laser Flash Method at Room Temperature

We used the special measuring equipment shown in **Fig.1** for the measurements at room temperature. We irradiated a laser beam with a pulse width of 1ms and output of 6J on sample surfaces, and measured the temperature rises on their back surfaces with an infra-red detector. The thermal diffusivity values were calculated from temperature responses based on the following equation:[2)]

$$D = 1.38L^2/\pi^2 t_{1/2} \quad \ldots\ldots\ldots\ldots\ldots\ldots (1)$$

where

D: the thermal diffusivity value

L: thickness of the sample

$t_{1/2}$: time for the temperature to reach 1/2 of the maximum temperature rise T_{max} on the back surface of the sample.

To measure the temperature of a restricted portion at the center of the back face, a conical shield tube of inside diameter 3mm on the sample side and 10mm on the detector side was placed behind the sample, and the infra-red ray was focussed into the detector with a non-reflection coated Si lense of 10mm in diameter. Further, in order to raise the sensitivity, the distance between the sample back surface and the detector was set to 40mm, and the sample held in 3 points by quartz tubes, so that the sample was thermally insulated. The measurements were carried out in vacuum of 10^{-3} torr, with the sample holder encased in a container provided with a CaF_2 window for the infra-red ray.

The measurements were done on 4 samples of 0.53, 0.97, 1.51 and 2.02mm in thickness. Since the samples were confirmed to be semitransparent by the preliminary experiment, we coated both surfaces of the samples with graphites by carbon spray (dgf. 123 Miracle Powder Products Corp.), and measured each sample 5 times. The interval of the repeated measurements was set to more than 2 minutes, as normally done in the measurement of metal and other samples.

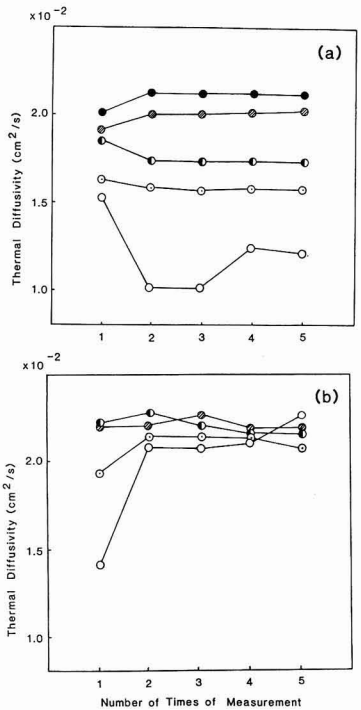

Fig. 2. Apparent thermal diffusivity of Corning 9806 vs number of times of measurement. Sample thickness is ○: 0.53mm ⊙: 0.97mm ◐: 1.51mm and ◍: 2.02mm, ●: 2.51mm respectively. (a) results by using a direct laser beam. (b) results by using a 17% attenuated beam.

Figure 2(a) shows an example of the relationship between the number of times of measurements and measured thermal diffusivity values, and Fig.2(b) the results of measurements through laser irradiation, attenuated by glass filter to 83% (5J). As Fig.2 indicates, the measurement of thermal diffusivity values varies in accordance with the thickness of the samples, number of times of measurements and beam intensity. Thermal diffusivity values tended to increase as the thickness of the sample increased, and this tendency was emphasized at higher beam intensity (a). It is generally known that the laser flash method tends to obtain a thermal diffusivity value at seemingly higher temperature than at

the measured temperature, due to a transient rise in temperature of the sample through the laser irradiation. Since the thermal diffusivity value of this sample has larger negative temperature dependence[3] at room temperature, thermal diffusivity became smaller with the rise in sample temperature through beam irradiation. This tendency became more evident in thinner samples which have smaller thermal capacity and accordingly larger temperature rise. The effect of the thickness in samples is markedly evident in Fig.2(a), where the laser beam was directly irradiated, because of the large temperature rise in the samples.

On the other hand, a tendency was found in the thinner samples (b) toward higher thermal diffusivity values with the repetition of measurements. In these measurements, gradual damage in carbon coating on the sample surface was observed with repeated beam irradiation. Because of the damage, the beam penetrated the sample partially and brought about a quicker rise in the temperature response curve measured at the back surface of the sample. This fact is thought to point to the tendency toward the increase in apparent thermal diffusivity values with the repetition of measurements (especially in thinner samples which are easily affected by beam penetration) in the measurements of samples (b) for which thermal diffusivity values are less affected by temperature rise. To verify this assumption, we carried out the following experiment.

The effect of damage on coating was estimated by altering the laser beam intensity. When the exiting voltage of laser beam was lowered to attenuate the beam intensity, the distribution in the intensity of the laser beam became uneven so that the temperature at the sample center tended to be higher. Therefore, we kept the exiting voltage fixed at the range where there was no unevenness in the distribution of intensity, and inserted a 15mm-thick glass cell filter with parallel sides into the light path and filled the glass cell with copper sulfate solution. Measurement was done by changing the intensity of beam by several percentage for each run through change in concentration of this solution. Thus, we confirmed that the carbon coating was not affected by the irradiation of laser beam when its intensity was attenuated to less than 25%(1.5J), and that we could obtain thermal diffusivity values of about 2×10^{-2}, irrespective of the times of irradiation on each sample, although it should be kept in mind that a reproducible value for thicker samples (2.02 and 1.51mm in thickness in this study) cannot be expected in the measurement at high attenuation, since the intensity of thermal response signal itself became too low by the attenuation of beam intensity.

On the other hand, we calculated the thickness of carbon coating, from the change in weight of the samples after coating, the diameter of the samples and the carbon density, and measured by changing the thickness in the range of 1 to 4×10^{-2}mm. We found that there was no change in the measured values. However, when the samples were sprayed continuously for an unnecessarily long time, there were cases where higher thermal diffusivity values were observed with the beam penetrating into thin parts of the uneven coating as a result of the carbon bearing organic solution flowing-out on the surface of samples.

Regarding the interval of measurements, we first irradiated the laser beam attenuated to 1.5J on samples 0.97mm thick and measured the temperature drop with the infra-red detector; it was confirmed that the temperature returned to the level prior to the measurement about 100 seconds after beam irradiation. Therefore, we think that the interval of more than 2 minutes adopted in this study would not affect the temperature rise on samples by the repetition of irradiation.

The relationship between the attenuation of laser beam and the resulting thermal diffusivity values is showed in **Fig.3**. We also carried out a test on samples coated with gold of 3.4μm on both sides by spattering, in order to confirm that carbon coating by spraying can completely prevent beam penetration into the sample interior. In this case, we noticed peeling-off phenomena in spattered film caused by the unattenuated beam and a large deterioration in signal intensity caused by attenuation (because gold has a low absorption of laser light). Therefore, the attenuation ratios of the laser beam were set at 54% through 83% in the experiment. By the way, carbon was sprayed over the spattered gold layer in the back surfaces of samples in order to raise the radiation of the infra-red ray. As is clear in Fig.3, we judge that the thermal diffusivity value at room temperature of Pyroceram 9606 is a fixed value of $2.15\times10^{-2}cm^2/s$, regardless of the number of measurements and coating material provided that the above experimental conditions were sufficiently taken into account.

It is generally known in the laser flash method that the measured temperature T_{eff} can be expressed in the following equation, under the assumption that the thermal diffusivity value varies linearly with temperature:[2]

$$T_{eff} = T_{amb} + 1.6T_{max} \quad \cdots\cdots\cdots\cdots \quad (2)$$

where, T_{amb} is the sample temperature before laser irradiation, and T_{max} is the maximum rise in the temperature of a measured sample. In order to measure the actual temperature rise of the sample with the beam, we stuck a chromel-alumel thermo-couple of 0.05mm dia. to the back surface of the sample with a bonding agent of cyano-acrylate system and measured the maximum rise in temperature. When we irradiated a laser beam of 90% attenuation on the samples coated with only carbon, the maximum temperature rise was 2.9K at the back surface of the 0.53mm-thick sample. Therefore, no adjustment was done in the temperature using equation(2), since the maximum temperature rise was very

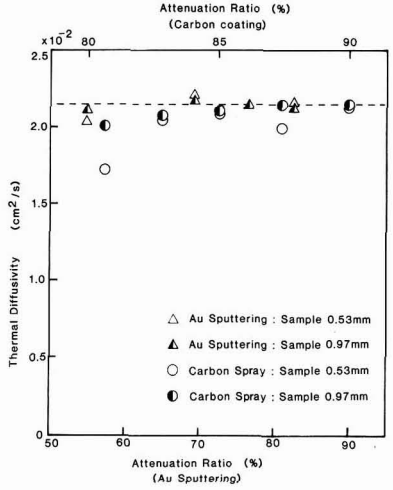

Fig. 3. Apparent thermal diffusivity Pyroceram glass ceramics of corning 9606 as a function of the attenuation ratio of a laser beam.

small in this study.

2.2 Transparency of the Samples

In order to check the actual shielding effect of carbon coating, we measured the transmittance on samples with and without carbon coating.

Regarding the transparency to infra-red rays, we first adopted 0.18mm thick Pyroceram 9606 as the reference sample, and 0.23mm as the measurement sample. Transparency was measured on uncoated samples in the range of 650 through 4000cm^{-1} on an infra-red ray spectrometer, and it was confirmed that the transmittance of infra-red rays remained in the range of 44 to 92%. Here we decided on the thickness of both reference and measurement samples through a preliminary measurement, enough to obtain adequate light and sufficient signals to the detector sensitivity. Then, we sprayed carbon on one side of the 0.23mm-thick samples and measured their transmittance. The transmittance of the infra-red ray was below the detection sensitivity in the whole range of its wave length.

The light shielding against laser beam was tested by measuring the beam intensity passing through the samples, by replacing the InSb detector of the thermal diffusivity measuring equipment with a Si semiconductor light detector. The samples were 1.47mm in thickness, and since the laser beam was monochromatic (wave length 694nm) the beam was attenuated to less than 5% by making use of the reflection of a half mirror. Once irradiated on the samples, the attenuation of its intensity was measured in terms of the change in signal intensity from the Si semiconductor. We confirmed that when a weak beam was used as in this case, we could not detect signals related to the infra-red radiation because of the low temperature rise of samples, but rather only signals related to the intensity of laser beam. When a laser beam was irradiated on samples without carbon coating, we adjusted the sensitivity to get sufficient signal intensity, and measured the samples with carbon coating on one side. In this case, no transmission of laser beam was detected. Taking these facts into consideration, we can safely say that carbon spraying provides sufficient shading.

Although many ceramics are generally semitransparent, there is no definite basis to point to whether or not the coating is necessary and to what extent the transparency of a sample will affect the measurement. Therefore, in order to make this matter clear, we estimated by a calculation the relationship between the apparent thermal diffusivity and the true thermal diffusivity, and investigated the effects of light transparency on thermal diffusivity. When a laser beam is irradiated instantly of the surface of a semitransparent sample of thickness L, the signal $S_R(t)$ is given by the equation (3) of Leung and Tam[4]:

$$S_R(t) = \frac{A}{L}\left[(1-e^{-\alpha L})(1-e^{-\alpha' L}) - 2e^{-\alpha' L}\sum_{n=1}^{\infty}\left(\frac{1-(-1)^n e^{-\alpha L}}{1+\frac{n^2\pi^2}{\alpha^2 L^2}}\right)\left(\frac{1-(-1)^n e^{\alpha' L}}{1+\frac{n^2\pi^2}{\alpha'^2 L^2}}\right)e^{-n^2 t/\tau_L}\right] \quad \cdots\cdots (3)$$

$$\tau_L = \frac{L^2}{\pi^2 D} \quad \cdots\cdots\cdots\cdots\cdots\cdots (4)$$

where

- A : constant depending on the energy of a laser beam, temperature and thermal capacity and emissivity
- α : absorption coefficient of sample against laser beam
- α' : absorption coefficient of infra-red ray in the wave length range measured by an infra-red ray detector.

It is very difficult to know from the expression of this response curve alone to what extent the thermal diffusivity obtained from the actual measurement is affected by the transmitted light. Therefore, we numerically obtained the dimensionless value $D\, t_{1/2}\pi^2/L^2$ for the time in which the theoretical response curve reaches 1/2 of the maximum value, using $S_R(t)$ from equation (3). The result is shown as the function of αL and $\alpha' L$ in **Fig.4**. By the way, the value $D\, t_{1/2}\pi^2/L^2$ was 1.38 on a completely opaque sample which agrees with equation(1). Moreover, the same value was obtained when αL and $\alpha' L$ were interchanged. When $\alpha' L$ or αL exceeds 50, the value converged sufficiently, and we can regard the sample as opaque.

We investigated the effect of transparency on the measured results of Pyroceram 9606 using this chart. The absorption coefficient of the sample against infra-red ray was obtained in the following procedures, so as to avoid the influence of refection on the sample surface. We placed a 0.18mm thick sample in the reference light path, and another of 0.23mm thickness in the measurement path of the infra-red spectral transparency measuring apparatus; the obtained transparency became that for a 0.05mm-thick sample which corresponds to the difference in thickness of these two samples. Based on this value, we obtained the absorption coefficient at every IR wave-length. We calculated the weighted average using the intensity of infra-red ray radiation of the black body at room temperature over each wavelength, and obtained the average absorption coefficient of 14mm^{-1}. Regarding the absorption of laser beam in a sample, we irradiated the same intensity laser beam on samples 0.14mm and 0.35mm thick without carbon coating and measured the intensity of the transmitted light. The ratio of the intensity of the beam transmitted through these two samples was 10.0, from which an absorption coefficient of 11mm^{-1} was obtained.

Next, we irradiated the laser beam attenuated by 90% on a sample 1.25mm thick and measured its thermal diffusivity. When both sides of the sample were sprayed with carbon, the thermal diffusivity value was 2.15×10^{-2}cm^2/s. Thermal

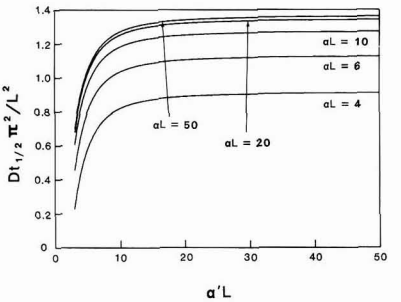

Fig. 4. Theoretical relation between transparency of a sample and apparent thermal diffusivity.

diffusivity values were $2.71\times10^{-2}cm^2/s$ on the same sample without any coating, $2.51\times10^{-2}cm^2/s$ when only the surface was sprayed and $2.29\times10^{-2}cm^2/s$ when only the back surface was sprayed. On the other hand, the results in Fig.4 point to the fact that 8% larger thermal diffusivity values were obtained if only one surface was semitransparent; this figure reached 17% if both sides were semitransparent when the αL and $\alpha' L$ were 10.0, which corresponds with the equivalent semitransparency of this sample. When we compared the above results with the values theoretically obtained, we found that although the same tendency was observed, there is a considerable difference in the apparent thermal diffusivity value when the surface or the back surface of a sample was sprayed with carbon, and the absolute values are slightly different. We presume that the discrepancy may be caused by incident light being attenuated by its scattering in addition to its absorption because Pyroceram 9606 is a crystalized glass, and further by the fact that no consideration was given in the analysis to the distribution in sensitivity on wave-lengths of infra-red detectors for the measurement.

The calculation on the transparency of the light for $\alpha L=10$ showed that only 5×10^{-5} of the light irradiated on the surface of sample reached the back surface, and the sample may actually seem to be almost opaque. However, as made clear by theoretical examinations of equation (3) and actual measurements, due consideration must be given to the accuracy of the measured values on samples without an adequate coating.

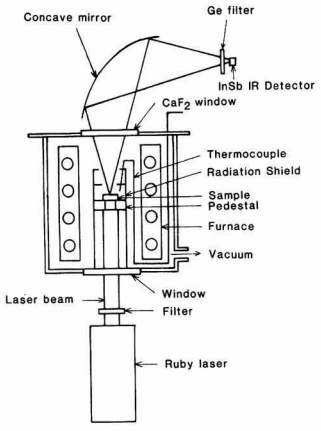

Fig. 5. Schematic illustration of experimental apparatus for measuring thermal diffusivity of inorganic materials at high temperature.

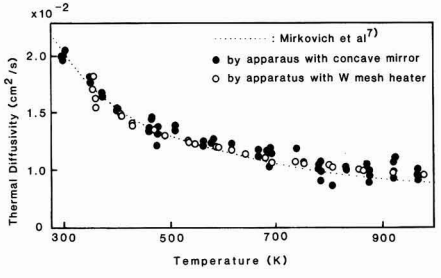

Fig. 6. Thermal diffusivity of Pyroceram glass ceramics Corning 9606.

2.3. Measurements at High Temperature

The measurement of the thermal diffusivity at high temperature was carried out on two systems of equipment different from the one used for the measurement at room temperature, in order to investigate systematic errors intrinsic to the equipment. The first was ultra high temperature equipment equipped with a tungsten mesh heater, the specifications of which were previously reported.[5] This ultra high temperature equipment holds a sample on three alumina pins and sets it at the center of the tungsten mesh heater. The infra-red ray radiated from the back surface of the sample is guided through the pipe beneath the sample and a Si lens to be collected by the infra-red ray detector for measurement. The other device is high temperature equipment heated by a Ni-Cr wire heater; details are shown in **Fig.5**. The sample is placed on an alumina ring of 9.5mm I.D. at the center of the heater, and a laser beam is irradiated onto the lower surface of the sample and the infra-red ray radiated from the upper surface of the sample is focused on the infra-red detector through an aluminum parabolic mirror.

We used samples 10mm in diameter and 0.97mm thick measured at room temperature and a ruby laser (same specifications as the one for measurement at room temperature) whose attenuation was set to 90% from measurement at room temperature. Both sides of samples were sprayed with carbon, and the measurement was carried out in vacuum. Heat loss by radiation was compensated by means of the method of Takahshi et al.[6] to derive the radiative heat loss from decreasing rate of temperature after the maximum point in the temperature responce curve, and using the compensation table by Ohta et al..[5] Since it was necessary to determine the thickness of samples at each temperature to obtain thermal diffusivity values from equation (1), we estimated the thicknesses of samples by measuring thermal expansion coefficient values ranging from room temperature to 1000K using thermal mechanical analysis (TMA) and obtaining the thickness at each temperature from linear thermal expansion coefficient and from thickness at room temperature. In order to ascertain whether change occurred in thermal diffusivity by the progress of sintering and so on during the measurement, we measured thermal diffusivity values by raising and lowering the temperature, and found that the measured values both at the raised and lowered temperatures agreed within an acceptable range of error. Further, there was no reduction in the dimensions of the samples and no temperature hysteresis detected even in the repeated measurement of the thermal diffusivity by thermal mechanical analysis. The thermal diffusivity values obtained by this equipment are shown in **Fig.6**, together with literature data hitherto available.[7] The thermal diffusivity values at room temperature measured by the high temperature equipment shown in Fig.5 agreed well with the values obtained by the room temperature equipment. However, with the ultra-high temperature equipment, we could not obtain signals at room temperature with sufficient intensity to enable analysis because of its low infra-red ray radiation, as its construction can not have a large aperture angle of the infra-red detector to the sample due to the long length heater. Although the error of the order of ±5% was detected in the thermal diffusivity values of the Pyroceram 9606 obtained by two different high temperature apparatus, the values agree well in the wide range of temperatures. In addition, these values agree well with recent measurements[7] by the cyclic heating method on this sample.

3. Conclusion

We measured thermal diffusivity values on Pyroceram 9606, studied internationally in the selection of standard reference materials in terms of thermal diffusivity, by means of the laser flash method, through systematic changes at room temperature, and by varying materials and thickness of shield coating as well as the thickness of samples and laser beam intensity. The following points were made clear. Since Pyroceram 9606 is semitransparent, it requires a coating on its surface for measurements, although the coated film may be damaged by high intensity laser beam and thus precise thermal diffusivity values cannot be obtained due to the change in the absorption and partial transmission of the laser beam. We investigated the carbon sprayed and gold spattered films for coating, and decided on the attenuation ratio of laser beam and conditions for carbon spraying in order to obtain precise thermal diffusivity values. In addition, we obtained a calculation chart to estimate the effects of semitranparency on the samples, and studied the transparency in measurement of Pyroceram 9606. Based on the present results, we systematically measured the thermal diffusivity values of Pyroceram 9606 ranging from room temperature to 976K.

A part of this study was published at the 11th Thermal Properties Symposium held at Tokyo from November 5 to 8, 1990 (Lecture No. A304)

Acknowledgements

Special thanks to Mr. F. Tanji, A. Nishibayashi, post graduate students at Ibaraki University, M. Ishimaru, T. Kimura, students at Ibaraki University, and H. Baba, post graduate student at Tsukuba University who assisted in the experiments at room temperature, and also to Mr. M. masuda, post graduate student at Tohoku University, who assisted in the numerical calculation.

References:

1) Nihon-Netsu-Bussei-Gakkai, Netsu-Bussei-Handobuddu, Youkendou, (1990) pp. 584-588.
2) W.J. Parker, J. Jenkins, C.P. Butler and G.L. Abbott, J. Appl. Phys., 32, 1679-1684 (1961).
3) W.A. Plummer, D.E. Campbell and A.A. Constock, J. Am. Ceram. Soc., 45, 310-316 (1962).
4) W.P. Leung, A.C. Tam, J. Appl. Phys., 56, 153-161 (1984).
5) H. Ohta, Y. Waseda, Yogyo-Kyoukai-shi, 94, 295-299 (1986).
6) Y. Takahashi, T. Azumi and M. Sugano, Netsu-Sokutei, 8, 62-66 (1981).
7) V.V. Mirkovich, P.S. Gaal and H.J. Kareis, Thermal Conductivity 20, ed. by D.P. Hasselman and J.R. Thomas Jr., Plenum (1989) 347-355.

This article is a full translation of the article which appeared in Nippon Seramikkusu Kyokai Gakujutsu Ronbunshi (Japanese version), Vol.99, No.6, 1991.

Cyclic Fatigue Behavior of Pressure-less Sintered Silicon Nitride in Rotating Bending Test

Toshio Ogasawara, Yoshio Akimune and Koji Yoneda

Material Research Laboratory, Nissan Motor Co. Ltd.
1 Natsushima cho, Yokosuka-shi, 237 Japan

Cyclic fatigue behavior of sintered silicon nitride was investigated by the rotating bending test method. The fatigue data were analyzed using Weibull's statistical approach based on the power law crack growth relation. This analysis agreed with experimental results. The relation between the number of cycles to failure and the initial stress intensity factor calculated from the defect size measured by fractography was discussed. As a result, the fatigue failure was caused not only by the surface defects but also by the internal defects. The cyclic fatigue behavior of silicon nitride was explained by the K_I-V diagram, in which the cyclic stress corrosion cracking (SCC) mechanism and the cyclic fatigue crack growth mechanism independent on SCC were taken into consideration.

[Received December 7, 1990; Accepted February 20, 1991]

Key-words: Cyclic fatigue, Rotating bending test, Silicon nitride, Fatigue life distribution, Statistical analysis, K_I-V diagram

1. Introduction

When ceramic matrials are applied as a structural components, it is important to establish a technique for assuring reliability for time-dependent fracture. The fatigue lifetime of ceramics have been often evaluated by bending fatigue tests, however, it is not easy to obtain fatigue data under tension-compression loading. This is because of the difficulty of a bending fatigue test accuratly and experimental difficulties such as fast fracture at the chucked points in tension-compression bending fatigue tests with ceramics.[1)]

A rotary bending fatigue test is the most commonly used fatigue tests with metals specified in JIS-Z 2274 and is used to obtain stress-fatigue lifetime diagrams (SN diagrams). This fatigue test method has the advantage of low cost of equipment and simplicity of testing; permitting tension-compression fatigue tests with a stress ratio R=-1; enabling a high cycle frequency to be employed.

Thus, it is widely used as a method for obtaining basic data necessary for lifetime prediction most simply for metallic materials whose fatigue lifetime can be estimated by using, e.g., modified Goodman diagrams in the case of different stress ratios and mean stresses.

Application of rotary bending tests to ceramics have been reported by Sakai et al., Tanaka et al., Ko and Saruki et al.[2-7)] For fatigue lifetime distributions in rotary bending fatigue tests with alumina, Sakai et al. showed that fatigue lifetime distributions complied with the 3-parameter (rather than 2-parameter) Weibull distribution, and that the larger the applied stress, the larger the value of the Weibull shape parameter (m).[2)] Carrying out a rotary bending fatigue test with silicon nitride, Tanaka et al. reported that the fatigue data scattered so widely that it was difficult to obtain definite *SN* diagrams; fatigue life distributions complied with the Weibull distribution.[3)] Obtaining *SN* diagrams with relatively small scatter by applying rotary bending fatigue tests to alumina and silicon nitride, Ko studied the relation between the minor region and fatigue lifetime by observing fractures of rotary bending fatigue test samples.[6)] Discovering that the rotary bending fatigue strength of silicon nitride was lower than the static fatigue strength, Saruki et al. reported that the experimental results could not be explained only by a volume effect but could be assumed as a result of cyclic loading.[7)]

Fatigue lifetime of ceramics scatter so widely that it is difficult to evaluate the fatigue behavior directly from stress-lifetime diagrams (*SN* diagrams). For this reason, fatigue tests are conducted with fatigue life scatter controlled by precracked specimens by a Vickers or Knoop indentation.[8,9)] This test method is effective in evaluation of fatigue behavior of materials but is not practical for evaluating the lifetime prediction of ceramic components. For evaluation of the *SN* diagrams of components, it is essential to perform a statistical analysis with fatigue lifetime distributions, initial-fractured data and censored data taken into account.[2,10,11)]

Thus, we analyzed rotary bending fatigue data for pressureless sintered silicon nitride in accordance with the fatigue life distribution formula derived for ceramics from the K_I power laws in fatigue crack propagation. Measuring defects as fracture origins of fracture by a fractgraphy, we also analyzed data using stress intensity factors and studied fatigue crack propagation in pressureless sintered silicon nitride in tension-compression cyclic fatigue tests.

2. Experimental Procedure

2.1. Tensile and Constant Loading Rate Tests

The test samples were pressureless sintered silicon nitride ceramics with Y_2O_3 (10wt%) and Al_2O_3 (5wt%) as additives. Young's modulus measured under the resonance method in compliance with JIS-R1602 was 265 (GPa) and fracture toughness measured under the SEPS method in compliance with JIS-R1607 was 5.0±0.2(MPa $\sqrt{m}$)

Tensile strength was measured with a specimen with was stuck with adhesive in SCM440 steel grips as shown in **Fig.1**. This type of specimen is easy to machine and enables aligning accuracy to be improved by the use of adhesive. 10 samples were tested based on JIS-R1606, except for the length of the parallel portion. From the results obtained,

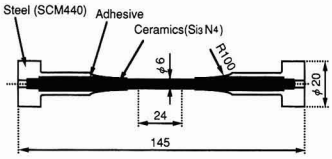

Fig. 1. Geometry and dimensions of tensile test specimen.

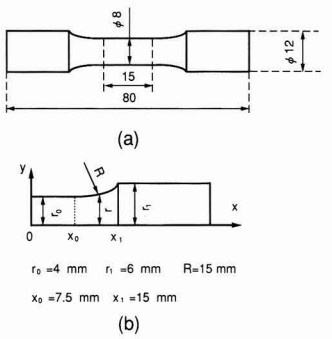

Fig. 2. Rotating bending test specimen
(a) Geometry and dimensions of specimen
(b) Coordinates of specimen for calculating the effective volume

using the method of least squares we estimated Weibull parameters m and σ_0 in

$$F(\sigma_i) = 1 - \exp\left\{-\left(\frac{\sigma_i}{\sigma_o}\right)^m V_{eff}\right\} \quad \ldots\ldots\ldots (1)$$

obtaining m=5.2, σ_0=1478, V_{eff}=678(mm^3) and mean strength=387(MPa). All the specimens fractured within the parallel portion 24mm long.

2.2. Rotary Binding Fatigue Test

We conducted the rotary bending fatigue test in compliance with JIS-Z2274, using No.1-8 shaped specimen as shown in **Fig.2(a)**. The specimens surface was finished a cylindrical grinding to a circumferemtial direction using a #800 diamond wheel.

Ono type rotary bending fatigue tester was used in the experiment. Applying a bending moment load on the specimen held on the tester with springed taper bushes and rotated at a rate of 3000rpm (50Hz), we conducted a complete amplitude fatigue test as shown in **Fig.3**. There were no specimen fractured at grips. An ordinary rotary fatigue test was also applicable to ceramics. The test was successful with the sample deflections kept within a very small range (20/1000mm).

Because of the high cyclic frequency (50Hz), fatigue test results below 10^3 (below 20s) involved a lot of errors, therefore they were treated as initial-fractured data. For the sake of convenience, we halted the fatigue test between 10^7 (2.3 days) and 10^8 (23 days) and treated the data there as censored data. For all the tested samples, we observed fracture origins by an SEM.

3. Test Results and Review

3.1. Relation Between Stress and Fatigue Life (SN diagrams)

Figure 4 shows the relation between maximum stress σ_{max} and fatigue lifetime N (*SN* diagram). The marks ●, ○ and Δ indicate fractured, censored and initial fractured data respectively. The fatigue lifetime obtained here scatter widely, however a general distribution downward toward the right is seen.

To evaluate such widely scattered data, a statistical analysis is necessary. Evans et al. derived a lifetime prediction for glass and ceramics under cyclic loading by integrating the power law for subcritical crack growth (SCG) caused by stress corrosion cracking (SCC) under a constant load[12]

$$da/dt = AK_I^n \quad (K_I = Y\sigma\sqrt{\pi a}) \quad \ldots\ldots\ldots (2)$$

Matsuo et al. calculated based on SCG theory, a fatigue like distribution function udner non-uniform stress states. It is given by

$$F(N) = 1 - \exp\left\{-\left(\frac{N}{N_0}\right)^{m_N} V_{eff}\right\} \quad \ldots\ldots (3)$$

where,

$$m_N = \frac{m}{n-2}$$

$$N_0 = \frac{B}{\sigma_{max}^n \int_0^{2\pi/\omega} (h(\omega t))^n \, dt}\, \sigma_0^{n-2}$$

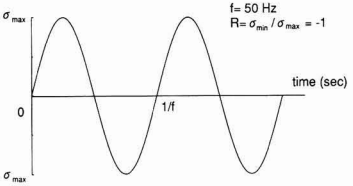

Fig. 3. Stress wave form at the surface of specimen under rotating bending test.

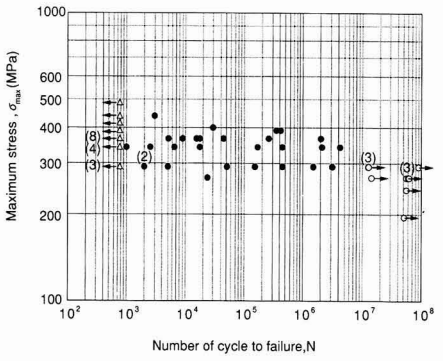

Fig. 4. Maximum stress (σ_{max}) vs. number of cycle to failure (N) representation (*S-N* curve) of sintered silicon nitride under rotating bending test. Left side arrow indicates that number of cycles to failure is less than 10^3. Right side arrow indicates that the tests were suspended at that cycles without failure of the specimen.

$$V_{\text{eff}} = \int_V \{ g(x,y,z) \}^{m'} \, dV$$

$$m' = \frac{n}{n-2} m$$

$$B = \frac{2}{(n-2) A Y^2 K_{IC}^{n-2} \pi}$$

g(x, y, z) : a function for describing the stress distribution of the sample

h(ωt) : a periodic function for cyuclic stress

In accordance with this fatigue lifetime distribution function, we calculate the fatigue lifetime distribution in the present rotary bending fatigue test below. With the coordinate system for the specimen as shown in Fig.2(b), g(x, y, z) is given by

$$g(x, y) = (r_0/r(x))^3 (y/r_0) \quad \ldots\ldots\ldots\ldots (4)$$

where r(x) is the distance between the center and the surface of the specimen, which is given by

$$r(x) = \begin{cases} r_0 & 0<x<x_0 \\ r_0 + R - \sqrt{R^2 - (x-x_0)^2} & x_0<x<x_1 \end{cases} \quad \ldots (5)$$

Thus, the effective volume V_{eff} can be calculated as

$$V_{\text{eff}} = \frac{4\pi}{m'+2} \left\{ r_0^2 x_0 + \int_{x_0}^{x_1} \left(\frac{r_0}{r(x)^{(m'-1)/m'}} \right)^{2m'} dx \right\} \quad \ldots (6)$$

From the effective volume of the rotary bending fatigue test specimen and that of the tensile test specimen calculated from equation (6), their mean strength ratio is given by

$$\overline{\sigma}_{\text{rotating}} / \overline{\sigma}_{\text{tensile}} = (V_{\text{eff(tensile)}} / V_{\text{eff(rotating)}})^{1/m} = (678/233)^{1/5.2} = 1.23$$

Thus, the fast fracture strength in the rotary bending fatigue test can be calculated as 476 (MPa), which nearly agrees with the point in the *SN* diagram in Fig.4 which is extrapolated to 10^0.[2,4]

Equation (3), which is based on the SCG theory under a constant load is also applicable likewise under a cyclic loading. Under a cyclic loading condition, the relation between maximum stress intensity factor (K_{Imax}) and fatigue crack growth rate (da/dN) can be approximately expressed by

$$da/dN = AK_{\text{Imax}}^n \quad \ldots\ldots\ldots\ldots\ldots (7)$$

which is similar to equation (2). Through a calculation using the relation above, an equation close to equation (3) can be derived. Here, however, the stress is represented by $\sigma_{\max}$. This eliminates the necessity of integrating the time term and N_0 is given by

$$N_0 = \frac{B}{\sigma_{\max}^n} \sigma_0^{n-2} \quad \ldots\ldots\ldots\ldots\ldots (8)$$

Here, fatigue parameters A and n are not defined in distinction between SCG effect and cyclic effect. Thus, the fatigue parameters include the effects of cyclic loading condition.

Now, it is evident that a fatigue parameter n can be estimated from the relation ($n=m/m_N+2$) between Weibull shape parameter m_N for fatigue lifetime distributions under maximum stress $\sigma_{\max}$ and Weibull shape parameter m for fast fracture strength distributions obtained from equation(3). Here, we estimated fatigue parameter n from the Weibull shape parameter for fatigue lifetime and fast fracture strength distributions in the experimental results. **Figure 5** shows Weibull plot of fatigue lifetime data with maximum stresses 292, 341 and 366(MPa). The values of Weibull shape parameter m_N and scale parameter N'_0 here were estimated under a least square method, then initial fractured and censored specimens were taken into account. N_0' here was defined in the form involving an effective-volume effect as

$$N'_0 = N_0 V_{\text{eff}}^{(-1/m_N)} \quad \ldots\ldots\ldots\ldots\ldots (9)$$

The values of fatigue parameter n calculated from m_N were nearly constant irrespective of σ_{max}, averaging n=27. From equation (3), $N_0\sigma_{\max}$=constant, which also shows that a fatigue parameter n can be estimated. **Figure 6** shows the relation in logarithmic plotting between σ_{max} and N_0', the gradient of the line representing the inverse of a fatigue parameter n. As a result, fatigue parameter n was calculated as n=25, which agreed with fatigue parameter n estimated by using Weibull shape parameter m_N. Thus, fatigue parameter n can be estimated accurately by using Weibull shape parameter m_N for fatigue lifetime distributions, which is advantageous in reducing the number of samples in fatigue tests.

On the other hand, the value of the fatigue parameter n estimated, as done conventionally, by linear regression from a logarithmical plotted *SN* diagram was about 140, which differed widely from the value by the statistical estimation mentioned above. This is due to the error produced by dropping the information in the initial-fractured data and censored which were neglected. In short, to accurately evaluate ceramics fatigue life statistical processing is essen-

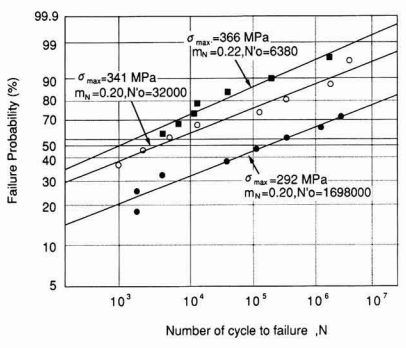

Fig. 5. Weibull plots of number of cycles to failure of sintered silicon nitride under rotating bending test.

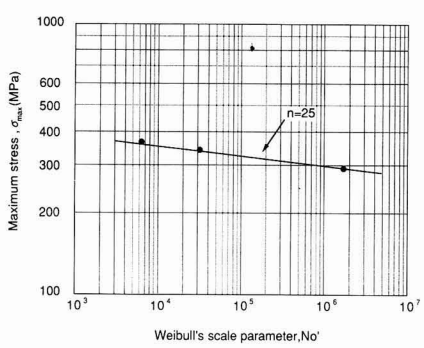

Fig. 6. Log-Log representation of Weibull's scale parameter N_0' in fatigue life distribution as a function of maximum stress $\sigma_{\max}$.

tial.

3.2. Observations of Fracture Origins

Figure 7 shows SEM photographs of typical fracture origins (internal and surfacial defects). Defects here were typical defects possibly produced by vaporizing organic inclusions at sintering. In shape, they were not penny shape cracks but pores. And surface defects are opened pores. In some test samples, no fracture origins were observed which were often found originating on the surface.

The fatigue crack growth mechanism of ceramic is generally recognized as mostly involved with SCG under a constant load in SCC. The acceleration of crack propagation due to cyclic loading is often explained by an effect similar to cyclic or dynamic SCC in metals.[20] According to the fatigue crack propagation due to SCC, there can be no fatigue crack propagation from internal defects, however, in this experiment, a considerable number of fatigue failure from internal defects were observed. A similar result was also observed in tension-compression fatigue tests with silicon nitride by Masuda et al.[13] These facts suggest that there is a fatigue crack growth mechanism instead of SCC.

Thus, we discussed the characteristics of fatigue fractures due to internal defects and those due to surface defects by measuring the size of defects as fracture origins and then calculating initial stress intensity factor K_I. Most of the defects observed in the experiment were pores with various shapes. To deal with them as equivalent cracks, modifiraction had to be made. As a modification where pores are assumed as fracture origins, Baratta's analysis, which assumes a ring crack around a pore is well known.[15] In this model, the size of the crack around the pore depend on grain size. This determination requires a number of assumptions, suggesting that it is not very easy to apply Baratta's analysis. On the other hand, Kishimoto et al. reported that in analysis

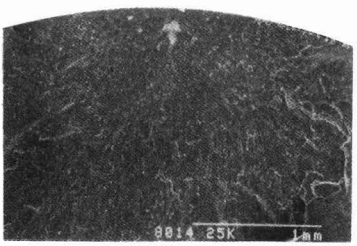

(a) Internal defect

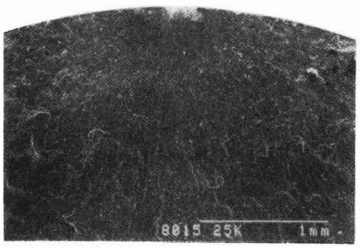

(b) Surface defect

Fig. 7. Typical fracture origins of silicon nitride under rotating bending test. Fracture origins are identified as pores produced by vaporizing of organic inclusions at sintering.
(a) Internal fracture origin, (b) Surface fracture origin

in tensile tests with ceramics actual phenomena can be ascertained relatively well by measuring the area of defects as fracture origins and simply assuming them as penny shape cracks.[14] This method is simple and we appled similar analysis for experimentl results. Measuring the area of a pore as a fracture origin and assuming the pore as equivalent to a penny shape crack, we determined the equivalent radius $a = \sqrt{(area)/\pi}$ as the typical size of a crack. For surface defects, the equivalent radius was determined as $a = \sqrt{2(area)/\pi}$.

Stress intensity factor K_I was calculated for surface semicircle and internal penny shape cracks by the followingequation:

$$K_I = \begin{cases} 1.22\,(2/\pi)\,\sigma\sqrt{\pi a} & \text{(surface defects)} \\ (2/\pi)\,\sigma\sqrt{\pi a} & \text{(internal defects)} \end{cases} \quad (10)$$

For internal cracks, a corrected-stress in the center of a defect was calculated. **Figure 8** shows the relation between initial stress intensity factor and fatigue lifetime. Fracture origins are mainly surfacial defects in the short lifetime region and internal defects in the longer lifetime region. The values of fatigue parameter n for each fracture origin were n=28 for surface defects and n=12 for internal defects, showing that the fatigue crack growth mechanism somewhat differs between the types of fracture origins. Fatigue fractures due to internal defects involve shorter fatigue lifetimes for the initial stress intensity factor than fracture lifetimes involved with fatigue fractures from surface defects, and are found more often on the longer-life side. This suggests that internal defects involve cycle-dependent crack propagation.

From the results of tensile compression fatigue tests with pressureless sintered silicon nitride and TEM observation of the specimens, Masuda et al. considered that microcracking due to stress concentration of pre-existing defects is influential as a fatigue mechanism.[13] It has also been observed in AE measurement by Kishi et al. that micrcracking occurs at crack tip in ceramics.[16] Nonlinear deformations of crack tip due to microcracking possibly cause tensile stresses to remain at crack tip even during unloading , which are involved with fatigue crack propagation.[17-19] However, much remains unknown about the cyclic fatigue crack growth mechanism in ceramics and it is hoped that detailed studies will be made.

3.3. K_I-V Diagram

Figure 9 shows the K_I-V diagram estimated from the ex-

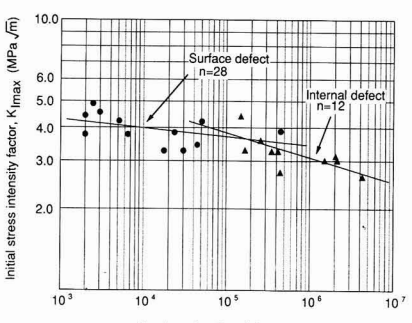

Fig. 8. The relation between the initial stress intensity factor (K_{Imax}) and number of cycle to failure under rotating bending test. The stress intensity factor (K_{Imax}) is calculated by equation 9.

perimental results. Here, cyclic crack growth velocity V is treated as da/dN. It was expected that the K_I-V diagram was composed of line (a) for SCC and line (b) for fatigue crack propagation due to cyclic effect (hereinafter "cyclic FCG (fatigue crack growth)). Crack growth velocity due to SCC, dealt with here, is due to cyclic SCC containing acceleration effect under a cyclic loading. (In the present test, stress ratio R=-1 and frequency t=50Hz.)

With surface defects as origins, fatigue cracks may grow due to the sum of SCC and cyclic FCG, which is given by curve (c). If maximum stress intensity factor $K_{Isurface}$ for surface defects is in the range above the intersection K_{Icross} of line (a) for the SCC mechanism and line (b) for cyclic F(G), a lifetime is governed nearly completely by crack growth due to SCC. In the range of $K_{Isurface} < K_{Icross}$, the effect of SCC may generally be remarkable because SCC shifts from the cyclic FCG dominant zone (K_{Icross}) to SCC dominant zone (K_{Icross}). Here, fatigue life is expected to be shorter because the effect of cyclic FCG in the K_I<K_{Icross} zone is greater than with effect due to SCC only taken into account.

When fracture origins are internal defects, there is no crack growth due to SCC/ crack growth along line(b). Thus, fatigue fractures from internal defects occur only when the maximum stress intensity factor for surface defects $K_{Isurface}$ is smaller than the maximum stress intensity factor for internal defects $K_{Iinternal}$ and $K_{Iinternal}$ is to some extent smaller than K_{Icross}. Here, the crack growth velocity is lower than that due to SCC, extending fatigue life.

Referring to the K_I-V diagram thus estimated, he discuss the experimental results. Where surface defects are origins, fatigue lifetime are shorter and with those surface defects for which load K_I is relatively longer and applied stress intensity factors are found in lower ranges. Fatigue parameter n here is smaller than with surface defects, which suggests that there may be a different fatigue crack growth mechanism. Although the data in Fig.8 scatters because it involves errors in K_I calculation, it shows that the experimental results can be explained by the assumed K_I-V curves.

If fatigue crack growth differs between surface and internal defects, a competition between fracture origins must be taken into account in a statistical analysis of fatigue lifetime data. Fatigue crack growth due to surface defects competes with that due to internal defects and dominant defects as fracture origins are determined by the more significant fatigue crack growth. Ultimate fatigue life depends on the distributions of surface and internal defects sizes and the distributions of location of internal defects. To evaluate the fracture behavior, a multi-modal Weibull distribution must be applied.[10] It may also be important to apply fatigue lifetime analysis about changes in fatigue crack growth characteristics due to load stress intensity factors as with surface cracks.

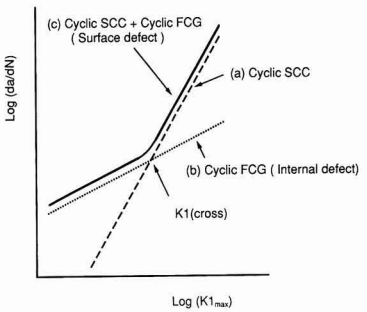

Fig. 9. The K_I-V diagram estimated by the relation between the initial stress intensity factor and number of cycle to failure (see Fig.9).
(a) Crack growth by Cyclic Stress Corrosion Cracking (Cyclic SCC)
(b) Crack growth by Cyclic Fatigue Crack Growth (Cyclic FCG)
(c) Crack growth of surface defects (Cyclic SCC + Cyclic FCG)

4. Conclusion

The results obtained in the present study can be summarized as follows:

1) Rotary bending fatigue tests are also applicable to ceramics. A fatigue test with stress ratio R=-1 can be carried out conveniently.
2) Data in SN diagrams scatter so widely that statistical analysis is essential to evaluate fatigue behavior. Fatigue lifetime distributions conformed to the Weibull distribution, and fatigue parameter n (calculated from Weibull shape factor m_N for fatigue life distributions) and shape parameter m (for fast fracture strength distributions) agreed with parameter n calculated from Weibull scale parameter N_0 and load stress σ_{max}.
3) Observing fracture origins, we found fatigue fractures not only from surface defects but also from internal defects. Fractures from internal defects were often found in data with smaller applied stress intensity factors and longer lifetime, which suggests that there may be a different cyclic crack growth mechanism from SCC.
4) The experimental test results could be explained by K_I-V diagrams assuming crack growth velocity due to cyclic effect for internal defects or SCC and cyclic crack growth together for surface defects.

Acknowledgements
We express our thanks to Prof. E. Yasuda and Prof. Y. Tanabe at Research Laboratory of Engineering Materials of Tokyo Institute of Technology, who gave us useful suggestions in our pursuit of the present study.

References:

1) A.P. Nikkila, T.A. Mantyla, Ceram. Eng. Sci. Proc., 10, 646-656 (1989).
2) T. Sakai, K. Fujitami, Materials, 35, 1371-1377 (1986).
3) D. Tanaka, A. Sakaida, Trans. JSME, A53, 1566-1573 (1987).
4) H.N. Ko, J. Mater. Sci. Lett., 5, 464-466 (1986).
5) H.N. Ko, ditto, 6, 175-177 (1987).
6) H.N. Ko, Yogyo-Kyokaishi 95, 472-475 (1987).
7) K. Saruki, K. Ogawa and T. Asano, Trans. JSME, A54, 2082-2086 (1988).
8) T. Kawakubo and K. Komeya, J. Am. Ceram. Soc., 70, 400-405 (1987).
9) T. Yamauchi, K. Sakai, M. Ito, T. Oji, W. Kenemetsu and M. Ito, Yogyo-Kyokaishi, 94, 631-635 (1986).
10) Y. Matsuo, T. Oida, K. Jinpo, K. Yasuda and S. Kimura, Nippon Seramikkusu Kyokai Gakujutsu Ronbunshi, 97, 136-142 (1989).
11) X. Hu, Y. Mai and B. Cotterell, J. Mater. Sci., 24, 3118-3122 (1989).
12) A.G. Evans and E.R. Fuller, Metal. Trans., 5, 27-33 (1974).
13) M. Masuda, T. Soma, M. Matsui and I. Oda, Nippon Sermikkusu Kyokai Gakujutsu Ronbunshi, 96, 277-283 (1988).
14) H. Kishimoto, A. Ueno, H. Kawamoto and T. Ura, J. Soc. Mater. Sci.

Jpn. 38, 32-38 (1989).
15) F.I. Baratta, J. Amer. Ceram. Soc., 61, 490-493 (1978).
16) T. Kishi, S. Wakayama, Y. Shinozaki, Y. Kagawa and E. Nakata, J. Jpn. Soc. Metallur., 49, 707-713 (1985).
17) L. Ewart and S. Suresh, J. Mater. Sci., 22, 1173-1192 (1987).
18) S. Suresh and J.R. Brockenbrough, Acta metall., 36, 1455-1470 (1988).
19) S. Hattori, Tetsu to Hagane, 75, 578-586 (1989).
20) H. Kobayashi and Y. Kawakubo, Bull. JSM, 27, 757-765 (1988).

This article is a full translation of the article which appeared in Nippon Seramikkusu Kyokai Gakujutsu Ronbunshi (Japanese version), Vol.99, No.6, 1991.

Bending Strength and Microstructure of Commercial Porcelains for Tablewares

Yuichi Kobayashi, Osamu Ohira*, Yasuo Ohashi* and Etsuro Kato

Aichi Institute of Technology
1247 Yakusa-cho, Toyota-shi, 470-03 Japan
*Toki Municipal Institute of Ceramics
1556-2, Dachi-cho, Toki-shi, 509-54 Japan

The bending strength of commercial porcelains for tablewares from ten makers in Tono district, Gifi-prefecture was investigated by using test bars of the same size, non-glazed or glazed and fired in respective markers. An unglazed porcelain body which showed the maximum mean bending strength of 8.9kg/mm^2 had a maximum relative density of 97.5% with pore size less than 20μm. The bending strength of unglazed bodies was in the range from 4.9 to 8.9kg/mm^2 and was increased to the range from 7.0 to 12.0kg/mm^2 by glazing.
In general, when the compressive stress in glaze was over 2.0kg/mm^2, fracture occurred from the origin in the bodies and the glazing increased the bending strength of porcelain bodies by about 3.5kg/mm^2. Especially, pores at the boundaries between glaze and body generated during firing acted as fracture origins and reduced the bending strength.
[Received December 10, 1990; Accepted March 22, 1991]

Key-words: Bending strength, Porcelain, Tableware, Porosity fracture origin, Glaze, Stress in glaze

1. Introduction

For tableware porcelain, importance has been given to appearance rather than to strength. Recently, however, porcelain tableware has come into wider use in places where a lot of people gather such as schools, hospitals, hotels and restaurants and into treatment in automatic washing machines which involve some crushing. Such trends have rapidly invited keen interest in porcelain strength, encouraging high-strength porcelain tableware containing alumina to appear on the market.

While there have been various studies on industrial porcelain bodies such as insulators to improve mechanical strength and a general theory on mechanical strength, there have been few reports on the strength of porcelain tableware partly because there is no unified measuring method for tablewares.[1-4]

With tableware, the strength of glazed products is important but it is difficult to measure the glazed bending strength of samples cut out of products. Also, stresses in glaze are generally studied mostly in relation with the occurrence of crazing.[5] In relation with the bending strength of porcelain, there have been some qualitative studies but none on the quantitative relation between stresses in glaze and increases in strength except for reports on insulators by Yamamoto and those on high-strength porcelain by us.[6]

We have already reported on glazed and unglazed bending strengths of high-strength porcelain containing alumina.[6,7] Using several porcelain bodies for tableware produced in Tono district of Gifu prefecture (currently the site of the world's largest production of tableware porcelain), we molded uniform test samples, fired them under the same conditions as for actual products, and measured their glazed and unglazed bending strength under the method already reported.[6,7] We thus obtained the relation between the results of measurement and such factors as microstructures, stresses in glaze, and fracture origins. To our knowledge, as to the effect of glaze on the body, there is no report on detailed observation of microstructures near the border. Thus, for the glaze, the body and the border between them in particular, we studied the effect of ununiformity on glaze and bubbles in the border between glaze and body.

2. Experimental Method

2.1. Preparation of Test Bars

From the typical tableware porcelains produced in Tono district, Gifu prefecture, we picked up about 10. **Table 1** shows the results of their chemical analysis. Assuming them as 3-component (quartz-feldspar-kaolin) systems, we plotted them on a triangular diagram as shown in **Fig.1**. From these bodies, we prepared test bars under the same casting method shown in the previous report.[6] Before glazing, we biscuit-fired the moldings at 750°C for 30min in an electric furnace and then glazed them using the same glaze used by respective manufacturers under the same method shown in the previous report.[6] In the following paragraphs, the discrimination between nonglazing and glazing is made by using the term "body" for the first and "porcelain for the second, that is, body A, body B etc. for unglazed bars and porcelain A, porcelain B etc. for glazed bars.

2.2. Firing

In a preliminary test to check the effect of the shape and glazed conditions of samples, we heated body B in the electric furnace from room temperature to 1000°C for 2.5h and subsequently at a rate of 200°C/h to 1275°C, held it there for 1h, fired it and then left it to cool down in the furnace.

The test bars of commercial porcelain were fired under the same conditions used by the manufacturers for firing. The temperatures in the manufacturers' kilns fluctuated within ±10° to 20°C. Thus it was not always possible to reflect average firing temperatures and average product

Table 1. Chemical composition of unfired commercial porcelain bodies.

Sample name	A	B	D	E	F	G	I	J	K
SiO_2	67.75	68.61	66.73	67.96	72.50	68.01	67.95	67.33	68.03
Al_2O_3	21.67	21.05	21.33	20.88	18.21	22.59	20.34	20.68	19.71
Fe_2O_3	0.11	0.26	0.61	0.53	0.77	0.33	0.36	0.61	0.62
TiO_2	0.05	0.07	0.26	0.23	0.50	0.14	0.13	0.26	0.33
CaO	0.26	0.50	0.65	1.09	0.15	0.25	0.52	0.39	0.36
MgO	0.05	0.13	0.16	0.16	0.14	0.34	0.10	0.15	0.11
K_2O	3.81	2.90	3.60	3.40	2.02	3.04	3.50	4.09	4.72
Na_2O	1.11	1.26	1.57	0.98	0.77	0.81	1.33	0.71	1.97
Ig.loss	5.21	5.15	5.06	4.71	4.92	4.43	5.06	4.96	4.19
Total	100.02	99.93	99.97	99.94	99.98	99.94	99.29	99.18	100.04
Quartz	28.13	31.59	26.60	31.10	43.39	30.17	30.32	30.23	25.41
Kaolin	38.63	37.98	35.08	34.78	37.15	43.97	34.55	37.05	27.51
Feldspar	33.24	30.44	38.32	34.12	19.46	25.86	35.12	32.71	47.08

strengths but we placed the test samples at the best locations expected to be kept at average temperatures. The unglazed test bars were fired without biscuit-firing after molding.

To compare the firing conditions at the different kilns coordinatively, we fired meβ rings made by Riedhammer (doughnut type inorganic bases for estimating firing temperatures by measuring contraction due to firing) together with the test bars. The meβ rings were fired in an electric furnace charged with air at the specified temperature for 1h, and a very good correlation was obtained between the hold temperature and the temperature measured from the contraction coefficient of the rings. The temperatures measured by the meβ rings, shown below, are distinguished by the symbol (MR) following °C.

The thicknesses of the glaze on the fired test bars ranged approximately from 100 to 150μm.

2.3. Measurement

To measure grain size distribution of the bodies, we used Microscan made by Quanta Chrome. Adding soda pyrophosphate as a deflocculant, we carried out a sufficient dispersion treatment with the help of an ultrasonic washer before measurement. We measured true density, bulk density and porosity by the same method shown in the previous report.[7]

We measured the bending strengths of rectagular test bars with a crosshead speed of 3mm/min by the method using rubber plates employed in the previous report.[7] We set the bars in such a position that a tension acted on its glazed surface. For bending strengths, we obtained arithmetic means from about 10 samples.

For round bars, there is no need to use rubber plates because each sample is held in point contact at two points of the support. We used an ordinary method for measuring 3-point bending strengths. The crosshead speed was 0.5mm/min in compliance with JIS R-1601.

With alumina contained high-strength porcelain bodies, there was little difference in bending strength between samples as fired and polished samples.[7] With ordinary bodies, there might be some difference. So, preparing body B test pars fired and polished with abrasive grain sizes #150, #500 and #1000, we measured their bending strengths and studied the effect of polishing.

To check the sintering of the body and reactions between body and glaze in detail, we mirror-polished the cross-sections of glazed samples and observed their microstructures under SEM. To examine remaining quartz and precipitated mullite in detail, we also observed the samples having the polished surfaces etched in 10% hydrofluoric acid for about 30s.

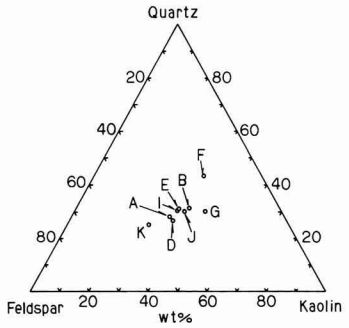

Fig. 1. Composition of unfired commercial porcelain bodies in Quartz-Feldspar-Kaolin system.

3. Results and Discussion

3.1. Effect of Measuring Conditions on Bending Strength

At present, there is no uniform method for measuring the bending strengths of porcelain tableware. This is the main cause of the disagreement among the results of many reseachers.

With ceramics showing a homogeneous texture in general, it is known that the effect of the size of samples on bending strength can be estimated from the effective volume derived from strength theory based on Weibull statistics; and that with the material of the same quality, the smaller the effective volume, the higher the bending strength.

In his book, Shiraki reported that with porcelain, the situation is contrary, that is, the larger the diameter of glazed and unglazed test bars, the higher the bending strength.[8] In porcelain bodies, unlike homogeneous materials, stress distributions are complicated and furthermore stresses (in glaze) are added to them. Thus, it is necessary to examine in detail what effect stresses in glaze have on bending strength.

Using body B, we investigated the effect of the size of samples and processing methods on bending strength.

We fired body B samples at 1275°C for 1h in an electric furnace. We measured the unglazed bending strength of rectangular test bars under the same method using rubber plates as shown in the previous report.[6] With 30 samples, the mean bending strength was 8.7kg/mm^2 with a standard deviation of 3.86%. The strength distribution could be represented in 2-variable Weibull statistics as shown in **Fig.2**, which showed little scatter and a Weibull coefficient of about 32. This proves that the measurement of bending strength was at a high level of accuracy.

With rectangular test bars, the bending strength was 10.8kg/mm^2 for one-side glazing and 10.2kg/mm^2 for overall glazing. The value for one-side glazing is about 5% larger than that for overall glazing. This may be because the glaze on the sides swelled due to surface tension, causing the measured width of the samples to be a little larger. With this value for the width corrected, the bending strength was calculated as about 11.0kg/mm^2, which is close to the value for one-side glazing.

Table 2 shows the measured bending strengths of round and rectargular bars of porcelain B. The values for round bars, both glazed and unglazed, are about 13% larger than those for rectargular bars. With round bars different in diameter, the thinner bars showed higher (though only a little) glazed and unglazed bending strengths than the thicker ones, which is contrary to Shiraki's report. These results can be explained from stress distributions in samples and the concept of effective volumes mentioned above in bending strength tests. In other words, it is assumed that with the same volume, the round bar has a smaller effective volume than the square bar and thus a higher bending strength. Thus, with porcelain body, it can also be represented as dimensional effect of samples under the concept of effective volume based on Weibull statistics.

The effects of glazing also agree very well between round and square bars with strength increases of 23 or 24%. This suggests that the shapes and sizes of sample cross-sections have little effect on stresses in glaze.

Table 3 shows the effect of polishing on the bending strength of samples not glazed after firing. With the high-strength porcelain body contaning alumina in the previous report, in the bending strength range above 20.0kg/mm^2 with sufficient material pulverization, no bending strengths involved with fractures started internally were observed unless the surfaces were polished with abrasive grain sizes #1000 or less. With body B, the bending strength of the samples polished with any abrasive grain size were about 10% higher than of the samples not polished, showing little difference with abrasive grain size. This may be because the grain size of body is so large that even with the largest abrasive grain size of #150, surface cracks are smaller than internal fracture origins in the body. The samples used in the following tests were made by casting the body into rectangular bars and glazing some of them only on one side.

3.2. Unglazed Bending Strength and Pores

From the results of chemical analysis on the assumption that the bases used in the tests are composed of 3 components – quartz, feldspar and kaolin – the contents of these components, except for body F, can be calculated as 25 to 32, 25 to 47 and 27 to 44% respectively, which belong to the composition category called soft porcelain.

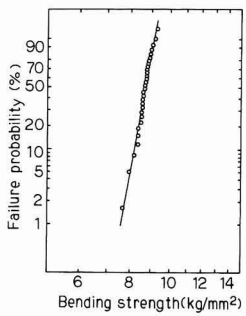

Fig. 2. Weibull plot of bending strength of body B fired at 1275°C for 1 hr.

Table 2. Effect of shape of test bars on bending strength of porcelain B fired at 1275°C for 1 hr.

Shape of test bar	Bending strength(kg/mm^2) Unglazed	Glazed	Ratio Glazed/Unglazed
Rectangular bar (8.4mm×4.2mm)	8.78	10.80	1.23
Round bar (4.5mmφ)	9.95	12.36	1.24
Round bar (6.5mmφ)	9.87	12.15	1.23

Table 3. Effect of lapping of test bars on unglazed bending strength of body B fired at 1275°C for 1 hr.

Condition of surface	Bending strength of unglazed body
Unlapped	8.78kg/mm^2
Lapped (#150)	9.61
Lapped (#500)	10.03
Lapped(#1000)	9.79

Table 4. Firing temperature of commercial porcelains measured by Meβ-Ring.

Firing temperature	porcelains
1250 ~ 1275 ℃(MR)	A K
1275 ~ 1300	B
1300 ~ 1325	E
1325 ~ 1350	D F
1350 ~ 1375	C I J
1375 ~ 1400	G H

The results of X-ray diffraction analysis show that most of the body are composed of quartz, feldspar, kaolin or halloysite and sericite. These bodies differ from the body mainly composed of pottery stone in that they contain ample feldspar and kaolin, and a small amount of silica rock and sericite.

The manufacturers' firing temperatures measured with meβ rings ranged widely (1250° to 1396°C(MR) as shown in **Table 4**.

Figure 3 indicate that the grain size of the bodies ranged narrowly, showing little difference with the bodies. This is because the manufacturers use similar material compositions and manufacturing methods. Only body K is somewhat different from the others, which is due to its particular material composition as shown by the results of chemical analysis.

Figure 4 shows the measured bending strengths of porcelains from the manufactures. The names of the samples are shown by alphabet, from the one having the highest unglazed bending strength at the left and to others in descending order. The lowest and the highest unglazed bending strengths measured in this test were 4.9 and 8.9kg/mm^2 respectively. **Figure 5** shows the frequency distribution of the data.

When studying the sintering of bodies conventionally, only the water absorption was measured in most cases. With the bodies in this study, all of the water absorption were below 0.2%, which makes comparison impossible.

Thus, we measured the bulk densities and true density of the body and calculated total porosities. The results are shown in **Fig.6**. Here, the lower the total porosity, the higher the unglazed bending strength, proving that the body must be sintered densely in order to increase mechamical strength. Most porcelain bodies showed porosities from 5 to 7.5%. The values for bodies A and B were 2.5 and 3.2% respectively. Conventional porosities of porcelain bodies already reported are mostly above 5%. Compared with this, body A and B sintered very densely.

We mirror polished the bodies and observed the size, shape etc. of remaining pores with the SEM. The results are shown in **Fig.7**.

Body A, which showed the highest unglazed bending strength, had been fired at 1275°C (MR), which is relatively low among the others in the present test. Its high bending strength may be the result of the high relative density. From the results of SEM observation, as shown in Fig.7, pores are very few and mostly below 20μm in size.

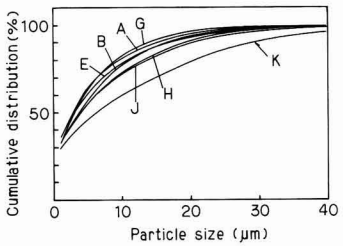

Fig. 3. Particle size distribution of unfired porcelain bodies.

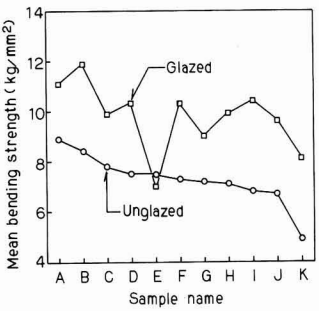

Fig. 4. Unglazed and glazed bending strength of porcelains. Sorted according to unglazed bending strengths.

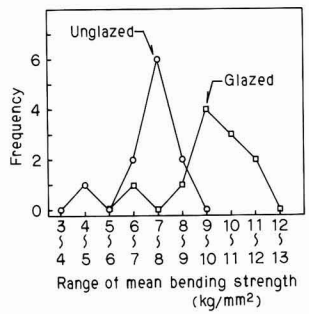

Fig. 5. Frequency distribution of glazed and unglazed bending strength of commercial porcelains.

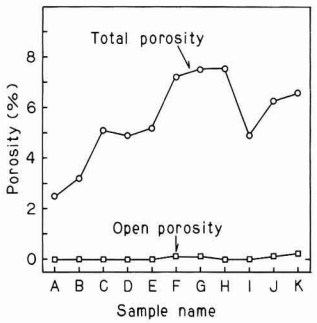

Fig. 6. Porosity of fired bodies.

In these samples, we could not discriminate between quartz and glass-mullite areas. So, we etched their surfaces in a 10% hydrofluoric acid solution for about 30s and observed likewise. The results are shown in **Fig.8**.

Cracks and surroundings of pores appear white because of the edge effect peculiar to the SEM. The portions looking gray are the zones in which mullite is precipitated. Quartz particles look darkest here.

Quartz is hardly affected by etching; around the quartz particles are newly found large annular cracks. This may be the result of large internal remaining stresses due to the difference in thermal expansion between glass-mullite areas and quartz, which promoted selective etching and resultant crack growth. As shown in Fig.8(a), such cracks are generally found around large quartz particles. As shown in Fig.8(b), glass layers about 1μm thick (without mullite) were observed around quartz particles.

They may be the silica-rich glass produced by the reaction between quartz and glass-mullite produced in the reaction between feldspar and kaolin. In body A, the width of the layer is small, showing that body A were not heated so high. As shown in Fig.8(c), the glass-mullite areas contains two zones: one relatively sparsely planted with mullite needless below 0.5μm in dia. and the other covered densely with small mullite crystals.

Body B, which showed the second highest unglazed bending strength of 8.4kg/mm^2, had also been fired at a relatively low temperature of 1288°C (MR). Its porosity was a relatively low 3.2%, comparable with that of body A. From Fig.7, it is evident that pores are few and small. However, large pores, of about 15μm are included, suggesting that pores grow as firing temperature rises.

Body D shows a porosity of about 5% and a bending strength of 7.5kg/mm2, which is average. There are a lot of large pores about 20μm and few small pores.

The widths of the amorphous layers around quartz particles after etching are larger than for bodies A and B, which is consistent with the higher firing temperature than for bodies A and B.

Body F contains only a small amount of feldspar and ample quartz. X-ray diffraction analysis of fired body F detected a trace of cristobalite, which however did not have any particularly large effect on bending strength.

Body H, fired at the highest temperature of 1396°C (MR) in the present test, showed a relatively low bending strength of 7.1kg/mm^2. Its porosity was about 7.5%, the highest of all the samples. As shown in Fig.7, pores are mostly large, above 20μm in dia.

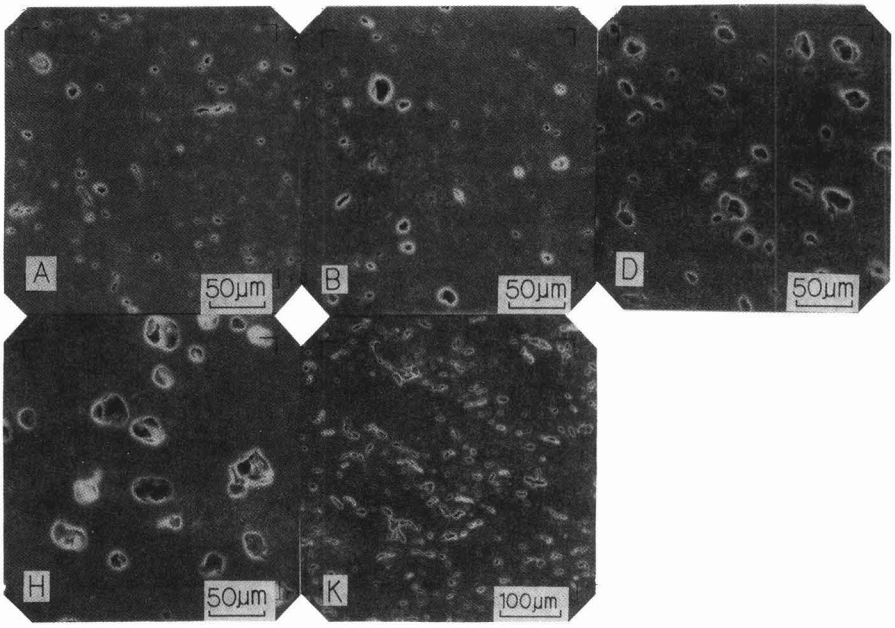

Fig. 7. SEM photographs of lapped surface of fired body A, B, D, H and K: respectively body name.

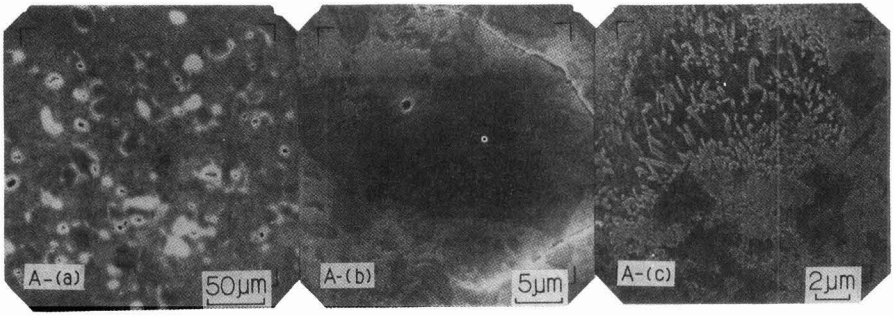

Fig. 8. SEM photographs of lapped surface of fired body A, etched with 10% HF solution.

The results of grain size analysis showed that body K contained the coarsest grains. Thus, it showed the lowest bending strength: 4.9kg/mm^2. Its firing temperature was 1260°C (MR), which was also the lowest. The photograph for this sample in **Fig.7** shows that there are a lot of long voids along the contours of large particles, suggesting insufficient sintering. The total porosity of K was 6.5%, rather high. In other words, it is assumed that melted feldspar is still so viscous that it cannot pervade small cavities or is so scanty that there are still a lot of thin square voids left. Such thin pores are linked together with small stresses, acting as large fracture origins. This may be the cause of only a low bending strength being obtained.

We have looked over bending strengths of bodies including the aspects of microstructure. There is no doubt that firing temperature has a great effect on bending strength. This will be dealt with in detail in another report.

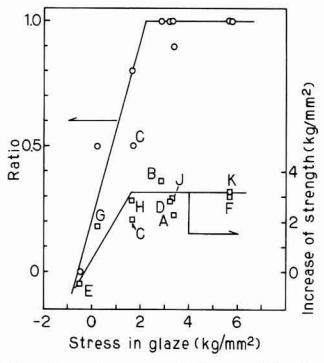

Fig. 9. Effect of stress in glaze on the increase of bending strength and location of fracture origins.
Ratio: (fracture origin in body)/(total test number)

3.3. Glazed Bending Strengths and Microstructures

Microscopically observing the fractures of all samples submitted to the bending strength measurement, we checked in detail whether fracture origins were in the glaze or in the body. We also studied the results in relation with stresses in glaze measured by Inada's method.[5] Glazed bending strengths and frequency distributions are included in Figs.4 and 5 respectively. Fig.9 shows the relations between stress in glaze and increase in strength due to glazing (glazed bending strength-unglazed bending strength, kg/mm^2) and between stress in glaze and ratio of fracture origins in the body (the number of fracture origins in the body/the total measured).

The lowest and the highest bending strengths were 7.0 and 11.9kg/mm^2 respectively. The increases in bending strength due to glazing differed with the bodies, ranging from -0.5 to 3.6kg/mm^2. With porcelain E, which showed a lower glazed bending strength than the unglazed bending strength, there was a tensile stress of about 0.5kg/mm^2 in the glaze. Its low glazed bending strength is possibly because the glaze cannot stand the tensile stress, causing a fracture to initiate in it before the body fractures. With porcelain E, thus all thus fracture origins were in the glaze.

As shown in Fig.9, as the compressive stress in the glaze increases, the fracture origins after gradually from the glaze to the body and when compressive stresses in the glaze are nearly above 2.0kg/mm^2, fractures mostly initiate in the body. As the compressive stress increased, the bending strength also rose but not over 3.5kg/mm^2 with any porcelain sample even when the compressive stress in the glaze was over 2.0kg/mm^2 because of the shift of fracture origins.

Fig.9 shows that in order to increase glazed bending strength, the stress in the glaze must be high, but the glazed bending strengths of all porcelain samples were not raised. With some porcelain samples, there must be other factors which reduce bending strength. Then, using an SEM, we observed the microstructures in the glaze and on the border between glaze and body.

With porcelain E, as shown in **Fig.10**, there are few bubbles on the border between glaze and body and scarcely any in the glaze. Glazing of K caused its bending strength to increase by more than 3.0kg/mm^2.

With porcelain C, which contained a lot of large pores in the body, bubbles were produced on the border between glaze and body as shown in Fig.10. Probably the gas emitted from the body was taken in, making large bubbles at the border between melted glaze and body.

In the glaze, there is some air which turns into bubbles when the glaze melts, but such bubbles are not very large: generally smaller than 30μm. On the other hand, those bubbles produced as the air in the body and the gas emitted from the material are taken into the border when the glaze has melted may grow large depending to a great extent on the properties of the body and firing conditions. Bubbles up to 100μm were observed in porcelain C, as shown in Fig.10. Such large bubbles could be fracture origins, having a great effect on strength. In fact, as shown in Fig.9, despite the glaze stresses over 1.8kg/mm^2, with porcelains A and C, the increases in their bending strengths are only 2.0kg/mm^2, while the bending strengths with other porcelain samples increase by about 3.0kg/mm^2 if the stresses in glaze are above 1.8kg/mm^2. Here, large bubbles at the border between glaze and body may become fracture origins, having an negative effect on glazed bending strengths. This may

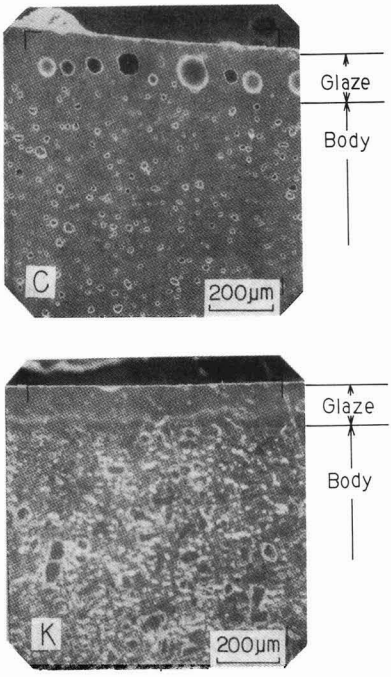

Fig. 10. SEM photograph of boundary of glaze and body.

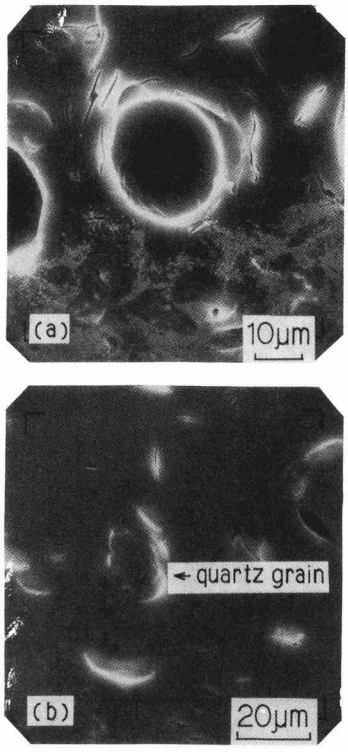

Fig. 11. Crack (a) and unresolved quartz grains (b) in glaze appeared by etching with 10% HF solution.

be why half of the fracture origins with porcelain C are not in the body.

Furthermore, a sign of other fracture origins was found in the glaze. As shown in **Fig.11**, etching the polished surface of porcelaim discovers that there are cracks in the glaze of porcelain H and undissolved quartz particles in the glaze of porcelain G. Such local unevenness of compositions and undissolved particles can possibly become causes of internal stresses or fracture origins or have an negative effect on porcelain strength. This shows that even with large compressive stresses in the glaze, if there are coarse quartz or other particles in the glaze because of insufficient pulverization, they can be fracture origins, preventing porcelain with a sufficient strength from being produced.

3.4. Effect of Glaze Stresses

Studying the effect of glazing on the bending strength of round bars about 1.2cm in diameter, C. Bettary and H.W. Webb reported that bending strength could be raised by about 30% by reducing the coefficient of thermal expansion of the glaze below that of the body but they did not show any values for stresses in glaze.[1] To calculate glaze stress σ_g for glazed round bars from the difference in the coefficient of thermal expansion between glaze and body, W. Spath presented a formula

$$\sigma_g = \frac{E_b\ E_g\ q}{E_b\ q + E_g\ (1-q)} (\beta_b - \beta_g)\ \Delta T$$

where

E_b and E_g : moduli of elasticity of the body and glaze, respectively
β_b and β_g : coefficients of thermal expansion
ΔT : difference (750°C here) between room temperature and the temperature at which the glaze solidifies during cooling
q : thickness ratio of the glaze to the body.[11]

Calculating the difference in the coefficient of thermal expansion as a glaze stress from the results by C. Bettany and H.W. Webb by using the formula above, we find that the bending strength is raised by about 3kg/mm^2 with a glaze stress of about 2kg/mm^2 and that if the glaze stress rises up to 12kg/mm^2, the bending strength will no longer rise. Here the moduli of elasticity of the glaze and the body are assumed as nearly equal: $E_b=E_g=0.8\times10^4$kg/mm^2.[6] Although their reports involve some uncertain factors such as the solidifying temperature of the glaze during cooling and the difference in the coefficient of thermal expansion, their results agree well with ours. However, they show nothing about the mechanisms of strength increases, their relation with fracture origins etc.

For industrial insulator porcelain, Yamamoto explains that because glaze suppress stress concentration by filling up cracks in the body surface, it allows the proper strength of the body to emerge and that the strength of the body without glaze can be increased by 20 to 30% by applying a suitable stress in glaze for the proper strength of the body.[3] He also adds that when fractures initiate in the body as the compressive stress in the glaze increases, a shearing stress is produced by this compressive stress in the glaze, causing the glazed bending strength to turn downward.

Such decreases in glazed bending strength were not observed in our study. This may be because the compressive stresses in the glaze of tableware porcelain concentrated in lower ranges than the results by Yamamoto. However, once the strength reaches its limit, fractures mostly initiate in the body, which somewhat differs from the results by Yamamoto showing that as fractures initiate in the body, the porcelain strength tends to decrease. As for the comparison between unglazed and glazed bending strength, within the scope of the present study, the bending strengths were increased by glazing to 1.65 times, although some scatter was involved, with body K which had a low strength and to 1.42 times with body B which had a high strength. In short, strength increases differed with samples, suggesting that comparison in terms of bending strength ratio are not always suitable. From the results above, with bodies of the quartz-feldspar-kaolin system for tableware, it may be possible to increase unglazed bending strengths by 3.5kg/mm^2 by controlling stresses in glaze within the range of 2.0 to 6.0kg/mm^2.

4. Conclusion

The bending strength of a round bar is about 1.1 times that of a rectangular bar of nearly the same volume.

Irrespective of the shape of samples (prism or round bar) bending strengths are raised by glazing by the same factor.

The measured value of unglazed bending strengths scattered very little. The standard deviations averaged 3.64%.

The bending strengths of polished body samples are up to 14% higher than that of samples as fired.

The unglazed bending strengths of porcelaiun bodies in Tono district, Gifu prefecture ranged widely from 4.9 to 8.9kg/mm^2 and the glazed bending strength ranged more widely from 7.0 to 12.0kg/mm^2.

Under proper composition and firing conditions, porcelain bodies can be sintered up to a relative density of 97.5%.

If air left in the body and gas emitted from the material are trapped into the border between body and glaze during firing, producing large bubbles, they can be fracture origins and cause the strength to decrease.

Glossy glaze made by firing is not always composed of a homogeneous vitreous phase but contains internal stresses due to undissolved quartz and compositional irregularities, which have some effect on glazed bending strength. If compressive stresses in glaze are below 2.0kg/mm^2 in commercial tableware porcelains, fractures initiate in the glaze, not allowing the strengths to rise largely.

Glazing permits the bending strength of tableware porcelain to increase by 3.5kg/mm^2. Strength cannot be raised any more by only increasing compressive stresses in the glaze.

References:

1) C. Bettany and H.W. Webb, Trans. Brit. Ceram. Soc., 39, 312-335 (1940).
2) L.E. Thiess, J. Am. Ceram. Soc., 19, 3, 70-73 (1936).
3) N. Yamamoto, Ceramics, 16, 4, 282-284 (1981).
4) K. Hamano, ibid., 3, 3, 171-179 (1968).
5) H. Inada, Yogyo-Kyokaishi, 85, 489 (1977).
6) Y. Kobayashi, O. Ohira, Y. Ohashi, and E. Kato, Nippon Seramikkusu Kyokai Gakujutsu Ronbunshi, 98, 5, 504-509 (1990).
7) Y. Kobayashi, O. Ohira, Y. Ohashi, E. Kato, Yogyo-KyoKaishi, 95, 9, 887-892 (1987).
8) Y. Shiraki, Glazes and Their Pigments, Gihodo, Tokyo (1977) p.341
9) S.I. Warshaw and R. Seider, J. Am. Ceram. Soc., 50, 7, 337-342

(1967).
10) M.S. Oral, E.M.H. Sallam and P.F. Messer, Trans. J. Br. Ceram. Soc., 82, 31-36 (1983).
11) W. Spath, Ber. D. K. G. 38, 351-359 (1961).

This article is a full translation of the article which appeared in Nippon Seramikkusu Kyokai Gakujutsu Ronbunshi (Japanese version), Vol.99, No.6, 1991.

Structural Change in Plasma-Sprayed Alumina Coatings by Laser Melting (Part I: On Continuous Wave Mode Treatment)

Tetsuya Senda and Chiori Takahashi

Ship Research Institute, Ministry of Transport
6-38-1, Shinkawa, Mitaka-shi, Tokyo 181, Japan

Structural change in the plasma-sprayed alumina coatings by laser melting was investigated. Three layers were observed in the cross-section of laser-treated coatings, melted, heat-affected and as-sprayed zones. X-ray diffraction analysis revealed that both the melted and the heat-affected zones. X-ray diffraction analysis revealed that both the melted and the heat-affected zones were entirely alpha-alumina, while the as-sprayed zone consisted of mainly gamma-alumina. The melted zone, a portion apparently melted by laser with subsequent solidification, had a columnar structure with less porosity but with many cracks. The heat-affected zone is probably a portion which did not melt but underwent the phase-transformation from gamma to alpha phase by laser heating. The relationship between the coating structure and laser parameters, such as powder and beam traverse speed, was also investigated by one-pass treatment under various conditions. When treated under the conditions such that the beam speed is proportional to the laser power, the size of the heat-affected zone increased with the increase both in beam speed and laser power. This indicates that the size of the heat-affected zone depends on the energy density rather than the total energy input. Experiments under various beam traverse speeds revealed that the grain size in the melted zone was inversely proportional to the square root of the beam traverse speed.

[Received December 12, 1990; Accepted February 20, 1991]

Key-words: Laser, Alumina, Plasma spraying, Porosity, Microcrack, Phase transformation

1. Introduction

Ceramic thermal barrier coatings of jet engines are porous because they are prepared by plasma-spraying.[1] The presence of pores contributes to the improvement of thermal shock resistance, but lowers the corrosion resistance of substrates because those pores are open pores. Since pores on the surface can be considered a type of flaw, such pores may lower the strength of the coatings. In order to improve such defective points, attempts have been made to melt and re-solidify the surfaces of thermal-sprayed coatings by irradiation of a laser and achieve the densification and smoothness of the surfaces.[2-8]

However, laser-treated ceramic coatings tend to contain a large number of surface cracks which are probably caused by thermal stresses, and these problems have not yet been solved. Structural changes in laser-treated coatings depend on treating conditions, but details of such structural changes are not known. Besides, the influence of each treatment condition is not fully understood. By using alumina-sprayed coatings as specimens, the present study was carried out by laser-treating the specimens through simplification of irradiation conditions and then investigating experimentally how the resulting structural changes would depend on the treating conditions. In this report, changes in laser-treated coating structures were investigated in detail. Relations between treating conditions and coating structures were also examined by carrying out one-pass treatment using beams of the continuous wave mode.

2. Experimental Method

Alumina coatings as specimens were produced by the ordinary atmospheric plasma-spraying. Alumina powders as a spray material were over 99.6% pure, had an average diameter of some 19μm, and their diameters ranged from 10μm to 44μm. A torch, Plasmadyne SG-100 model, was used for spraying, and its gas for creating a plasma jet was a mixture of argon (50 L/min) and helium (13 L/min), with argon (8.2 L/min) as the powder transporting gas. The input of the torch was 31V and 900A. The distance between the torch and the substrate was 90mm. The substrate was made of mild iron of 60mm x 60mm x 2mm whose surface was treated by sand-blasting. The substrate was cooled by air from the back surface while the spraying was carried on. **Figure 1** shows a photomicrograph by the scanning electron microscope of the surface of the sprayed coating as a specimen and a micrograph by an optical microscope of its polished cross section. The thickness of the coating was approx. 0.35mm. The sprayed coating is formed by accumulation of the particle flattened and solidified from melting. The dark areas inside the coating as seen in the cross-sectional photomicrograph are considered to represent scars caused by the pull-out of alumina grains during grinding.

The laser apparatus employed for the experiment was composed of a carbon dioxide laser with the maximum output of 1kW and a work table having the maximum moving speed of 5m/min. Although the laser could be used with either a continuous wave (CW) mode or a pulsed mode (100 to 3000Hz), only the continuous wave mode was used in the experiment for this report. Surface treatment is usually accomplished by laser irradiation of two-dimensional scanning. In this study, however, the laser scanning was done

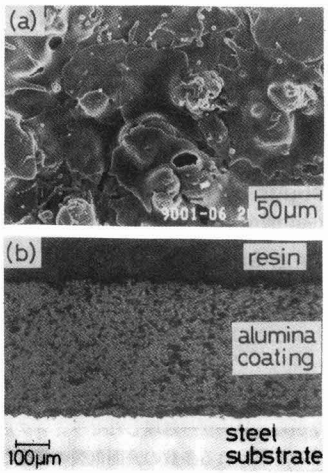

Fig. 1. Photomicrographs of as-sprayed alumina coating.
(a) Scanning electron micrograph of top surface, (b) Optical micrograph of cross section.

once in one direction (one-pass treatment) in order to evaluate the effect of each condition with simplified parmeters. In this case, such parameters as laser power, beam diameter, and the traverse speed (scanning speed) of the beam become important. In case one-pass treatment is carried out in the continuous wave mode, both the beam diameter and laser power affect energy density. In this experiment, only the laser power was varied, while the beam diameter was kept constant. The focal distance of the lens was 127mm, and the specimen was placed 28mm from the focal point. The scanning of the beam was accomplished by moving the table on which the specimen was mounted. The laser power ranged from 40W to 300W, while the beam traverse speed was in the range from 0.4m/min to 4m/min. The exit of the laser beam was in the shape of a nozzle, and argon gas was blown (0.01MPa) toward the surface of a specimen in order to protect the lens.

A specimen which underwent laser irradiation was cut at right angles to the direction of the beam traverse. The cross section was then polished, observed with an optical microscope, and scanning electron microscopic (SEM) observation was then made to investigate changes in the coating structure. Polishing was accomplished with the use of emery paper and diamond past. The final finish was obtained using diamond paste of 1/4μm. X-ray diffraction was also carried out to investigate changes in the crystal structure.

3. Experimental Results and Discussions

3-1. Structural Changes of Coating

Figure 2(a) is an optical microscopic picture showing a cross section of a one-pass treated coating. The beam was irradiated from the top of the picture downward and moved at the right angle to the picture surface. The areas irradiated by the laser were found to have three layers. The first layer was found to have cracks and to be denser than the original coating. This is considered to represent that area which was melted by the laser irradiation and then solidified (to be discussed later). The surface of this area was hump-like and uneven. The second layer was found enclosing the first layer and represented by a rather dark area in the photomicrograph. This area, having higher apparent porosity than the original coating, is regarded to have been affected in some way by the laser irradiation. The third layer was not different from the original coating, and is considered to have not been affected by the laser treatment.

Figure 2(b) shows an SEM image of the fracture surface of the coating. Columnar crystals are seen in the area corresponding to the first layer of Fig. 2(a), and finer crystals are seen closer to the second layer. The picture of the fracture surface does not any clear distinction between the second and third layers, both of which have a structure of flattened particle accumulation.

Figure 3 shows SEM images of zones appearing on the surfaces of the first and second layers. The first layer of Fig. 3(a) shows no structure of flat grains, and is totally different from the surface of the original coating shown in Fig. 1. Although the surface is similar to a sintered body, cracks were observed. The second layer shown in Fig. 3(b)

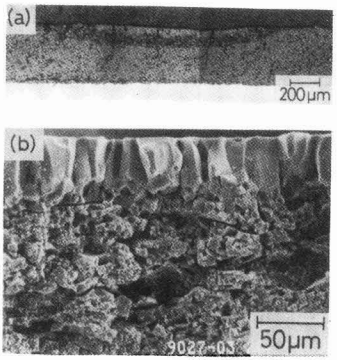

Fig. 2. Photomicrographs of cross-section of laser-treated coating (70W, 0.4m/min).
(a) Optical micrograph of polished cross-section, (b) Scanning electron micrograph of fracture surface.

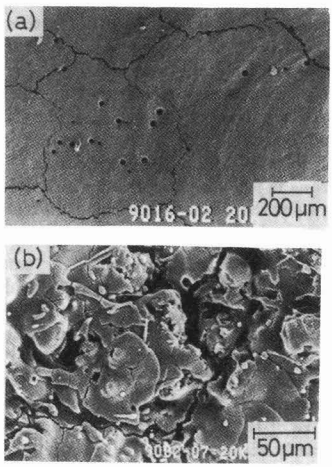

Fig. 3. SEM images of top surface of laser-treated coating.
(a) Laser-melted zone, (b) Heat-affected zone.

does not appear to be different from a sprayed but untreated surface in terms of a macroscopic structure of particle accumulation; it seems to have many more microcracks inside the grains compared to Fig. 1, and those cracks are wider.

Figure 4 shows results of X-ray diffraction of the first layer, a zone of the second layer obtained by eliminating the first layer by polishing, and the sprayed coating surface before laser irradiation. The sprayed but untreated surface is made of γ-alumina containing α-alumina as shown in Fig. 4(a), while the first (pattern b in the figure) and the second layer (pattern c) are α-alumina which does not contain a γ-phase.

Although the powder before the spraying was α-alumina (hexagonal structure), the main component of the sprayed coating was γ-phase. Presumably this is because the γ-phase (cubic structure), a metastable phase, was formed due to an extremely high cooling rate (over 10^6K/s) of melted particles solidifying on the substrate; the presence of α-phase is considered to have been caused by the particles in imperfect melting.[10] It has been reported that by setting up spraying conditions (carefully), a film of nearly 100% γ-phase can be obtained.[11] In contrast, it is thought that the first layer, considered as a melted layer formed by the laser, has been solidified as a stable α-phase from room temperature to the melting point because the cooling rate in the case of laser irradiation is slower compared with the case of spraying. The slow cooling rate can be presumed from the fact that the first layer has grains of far greater size than those of fine crystals observed in the second and third layers.[11]

These results have confirmed that the first layer is a zone which was re-solidified after being melted by laser irradiation. There appear fine crystal grains near the second layer. Because it is assumed that the slower the solidification speed is the finer those grains are, the cooling and solidifying processes are presumed to begin from near the substrate rather than the surface. Those humps on the surface can be considered to have been formed due to the presence of a surface tension at the time of melting or because of the gas being blown from the nozzle near the laser beam exit.

In contrast, the second layer has no sign of having melted, but is changed to α-phase. It is reported that γ-alumina is transformed into α-alumina at over 1000°C to 1200°C.[12] As for sprayed coatings which mostly contain γ-phase, Thompson and Whittemore have made detailed investigations and found that these coatings also undergo phase transition by a heat treatment.[13] More specifically, it has been reported that under the heat treatment of 4h at 1149°C, a phase transition takes place to α phase and δ phase which contain minute amounts of K phase and θ phase and, further, that a heat treatment that at over 1260°C for 1/2h causes a complete transition to α phase. Similarly, Heintze and Uematsu have obtained α-alumina coatings first by spraying in a ordinary atmosphere and then heating the coatings with a plasma torch.[11] Since the density of α-alumina is approximately 4.0g/cm^2 while that of γ-alumina is 3.65g/cm^2,[12] the transition from γ phase to α phase is accompanied with a volume reduction of nearly 10%. For this reason, the porosity increases due to a heat treatment as reported by Thompson and Whittemore,[13] and Heintaze and Uematsu reported that a large number of microcracks have been observed within the particles of α-alumina coatings which were re-heated after spraying.[11]

In view of these reports, the second layer may be considered to be a zone which had a phase transition completed from γ to α phase by the effect of laser heating though not melted by the heat. The time duration for which laser irradiation exerts a thermal influence is short, as compared to experiments indicated in the above reports. Because the phenomenon is probably a thermal activation process, it is considered quite possible for a phase transition to complete in a short time, as in the present research, if the temperature is sufficiently high. The microcracks observed in Fig. 3(b) are the same as those observed by Heintze and Uematsu, which are considered to have been caused by a reduction in volume associated with the phase transition. It seems also to be related to an increase in the dark zones in the second layer of Fig. 2(a). In fact, the measurement of porosity by processing the SEM image of a cross section indicated that the porosity of the third layer or as-sprayed coatings was 5%, while that of the second layer increased to 13%, with the difference precisely representing the volume change. Nevertheless, the comparison of Fig. 1(a) and Fig. 3(b) seems to indicate that an increase in porosity associated with a volume change brings about the enlargement of microcracks within the particles, so that only a minor increase in the number of macroscopic pores as seen in Fig. 2(a) is considered to occur. On the other hand, the generation or enlargement of microcracks may weaken the bonding force among sprayed particles so as to possibly cause an increasing number of particles to drop off during the process of specimen polishing. An apparent increase in porosity is considered to be caused both by a volume change and by grains dropping off due to this volume change.

In summarizing the preceding results, the structure of an alumina-sprayed coating which underwent a one-pass laser treatment can be represented schematically as in **Fig. 5**; the coating has a three-layer structure, with the first layer being a zone which was melted by laser irradiation and re-

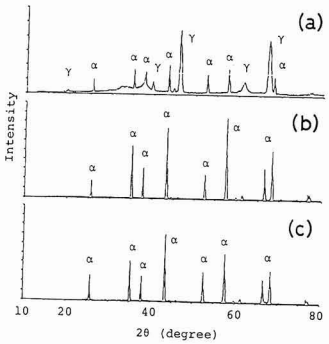

Fig. 4. X-ray diffraction patterns.
(a) As-sprayed surface, (b) First layer (laser-melted zone), (c) Second layer (heat-affected zone).

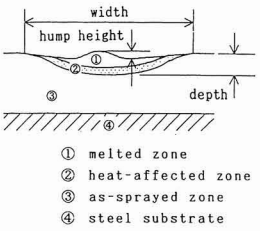

Fig. 5. Schematic of cross-section of laser-treated coatings.

solidified (melted zone), the second layer being a zone in which a phase transition took place as a result of the heat to increase microcracks (heat-affected zone), and the third layer being a zone which was not affected at all (as-sprayed zone).

3-3. Relationship between Coating Structure and Laser Treatment Conditions

The structure shown in Fig. 5 can be evaluated using parameters such as widths and depths of the melted zone and the heat-affected zone, the size of crystal grains in the melted zone, and lengths of cracks per unit area. In the following, the relationship between these parameters and laser treatment conditions will be discussed.

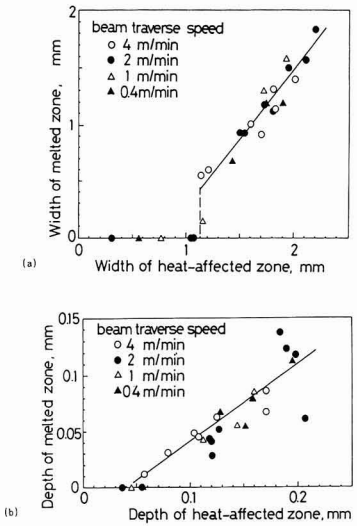

Fig. 6. Relationship between melted zone and heat-affected zone. (a) Width, (b) Dept.

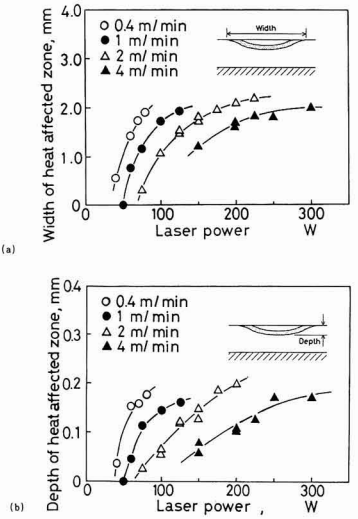

Fig. 7. Relationship between laser power and size of the heat-affected zone. (a) Width, (b) Depth.

Figure 6 shows relationships between the widths of the melted zone and the heat-affected zone of the coating treated by changing the laser power and the beam traverse speed and also between the depth (thickness) of the melted zone and the depth (from the surface) of the heat-affected zone. Although there is some scattering, particularly in depth, the size of the melted zone is generally related to that of the heat-affected zone almost linearly. In consequence, both zones need not be evaluated independently. Hence the width and the depth of the heat-affected zone will be evaluated because of the ease with which observations can be made at low laser power levels.

Figure 7 illustrates the relationship between the width or the depth of the heat-affected zone and the laser power, using the beam traverse speed as its parameter. As examined in Fig. 6, exactly the same tendency was revealed for the relationship between the width or the depth of the melted zone and the laser power. If the laser power is increased while keeping the beam traverse speed constant, then both the width and the depth of the heat-affected zone become larger, but each seems to reach a saturation point somewhere. When the laser power is increased beyond the range indicated in the graphs, the coating is destroyed probably because it starts to boil, thereby making it impossible to carry out a normal treatment. If the beam traverse speed is increased while keeping the laser power constant, then both the width and the depth become smaller, but this seems obvious because the faster the beam traverse speed the smaller the time integral value of the incident heat on a unit area, namely, the total imputenergy of irradiation.

Therefore, the total amount of incident heat can be made constant by increasing the laser power in proportion to the increasing of the beam traverse speed. In this case, the relationship between the width and the depth of the heat-affected zone is established as shown in **Fig.8**. Both the width and the depth can be made bigger by increasing both the laser power and the beam traverse speed. In other words, the width and the depth of the heat-affected zone can be considered to depend rather on the energy density than on the total energy irradiated. It can also be said that the short-time irradiation of high-density energy can treat a bigger volume than the long-time irradiation of low-density energy. In this case, both the width and the depth have exactly the same tendency as shown in Fig. 8.

For each beam traverse speed, laser power output condition was chosen in such a way that the width of the heat-affected zone was nearly the same in reference to Fig. 7(a). **Figure 9** shows SEM images of the surface of the melted

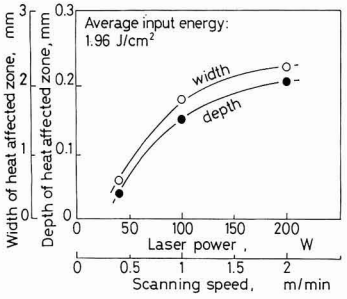

Fig. 8. Effect of energy density on the size of the heat-affected zone.

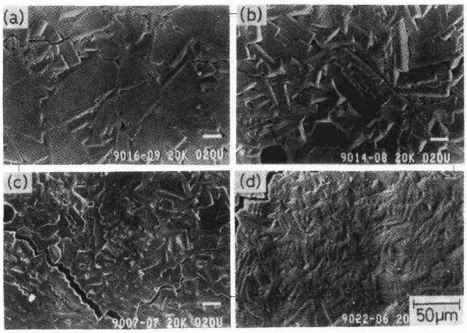

Fig. 9. SEM images of top surfaces of the melted zone.
(a) Beam traverse speed of 0.4m/s, laser power of 70W; (b) 1m/s, 100W; (c) 2m/s, 150W; (d) 4m/s, 225W.

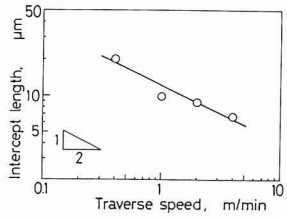

Fig. 10. Effect of beam traverse-speed on the grain-boundary intercept length.

zones which were laser-treated under these conditions. In this case, the laser power was also varied, thereby changing the energy density. However, it is considered that the density change essencially represents the effect of the beam speed. The size of crystal grains becomes smaller as the beam speed becomes higher. The shapes of the grains are close to an equilateral polygon when the beam speed is low, but become almost rectangular at higher speeds. Although cracks appearing on the surface were evaluated in terms of crack length per unit area on the SEM images, these four conditions did not really yield any clear distinction.

As seen from the photomicrograph of the cross section in Fig. 2(b), the grains seen from the surface are columnar crystals, and the definition of their size is difficult because the shapes of the grains are anisotropic. For this reason, an attempt was made to carry out relative comparison of grain sizes based on the average value of the lengths of those line segments crossing the grain boundaries (intercept length) which were produced by arbitrary straight lines drawn on the photomicrograph, and the results are shown in **Fig. 10**. The grains clearly become smaller as the beam speed gets higher, and the grain size (intercept length) is inversely proportional to nearly the square root of the beam traverse speed. The beam traverse speed is inversely proportional to the residual time of the beam at a certain point on the specimen, and is deeply related to the time duration for which the specimen is maintained at a high temperature. In other words, it can be assumed that the longer the grains are kept at a high temperature, the bigger their size becomes.

5. Conclusions

Investigations were carried out on the structural change in alumina-sprayed coatings which underwent mainly one-pass treatment by laser. As a result, it was found that the laser-treated alumina coating had a three-layer structure, consisting of a melted zone formed by the melting from the surface and re-solidifying, a heat-affected zone formed by phase transition by heat, and an unaffected zone. When the change in the width and the thickness of the heat-affected zone was examined by varying the laser power and the beam traverse speed, it was found that as long as the total energy irradiated on the coating was constant, the short-time irradiation of the beam of high energy density produced a heat-affected zone of bigger volume. The grain size in the melted zone became smaller as the beam traverse speed was increased. In the ranges used for this experiment, the treatment conditions did not particularly affect the generation of cracks.

The present research was conducted under the auspices of the Special Research Fund for Atomic Energy of the Science and Technology Agency. A part of the results presented at the 1990 Annual Meeting of the Ceramic Society of Japan (Lecture No. 2B39).

Acknowledgements
The authors would like to express their sincere appreciations to Dr. Shigeyasu Amada, (currently at the Institute of Technology, Gumma University) and Dr. Susumu Uematsu, Ship Research Institute, for their many valuable words of advice and instances of cooperations.

References:

1) T. Senda, S. Amada, S. Uematsu and S. Sato, J. Jpn. Thermal Spraying Soc., 24, 1296-1300 (1988)
2) I. Zaplatynsky, Thin Solid Films, 95, 275-284 (1982).
3) A. Adamski and R. McPherson, Advances in Thermal Spraying, Pergamon Press (1986) pp.555-562.
4) M. Havrda et al., Advances in Thermal Spraying, Pergamon Press (1986) pp.569-575.
5) R. Sivakumar and B.L. Mordike, Surface Engr., 4, 127-140 (1988).
6) R. Sivakumar, Cryst. Prop. Prep., 22/25, 671-692 (1990).
7) N. Iwamoto et al., Surface and Coatings Tech. 34, 59-67 (1988).
8) T. Suzuki, M. Ito, M. Nakahashi and H. Takeda, Ceramics Ronbun shi, 97, 571-577 (1989)
9) A. Kobayashi, Correspondence from Heat Source Center, 5, pp. 31-33 (1989)
10) R. McPherson, Thin Solid Films, 83, 297-310 (1981).
11) G.N. Heintze and S. Uematsu, Thin Solid Films, submitted for publication
12) D.N. Polbyarinoff, High Fire-resistant Oxide Ceramics, Japan-USSR Communications, (1977) p. 67
13) V.S. Thompson and O.J. Whitemore, Jr., Am. Ceram. Soc. Bull., 47, 637-641 (1968).

This article is a full translation of the article which appeared in Nippon Seramikkusu Kyokai Gakujutsu Ronbunshi (Japanese version), Vol.99, No.6, 1991.

Preparation of ZrN Fine Powders from ZrO_2 by Reduction with Mg and Their Recovery

Hidehiko Kobayashi, Miyuki Katou, Yoshihide Kamiyama* and Takashi Mitamura

Department of Applied Chemistry, Faculty of Engineering, Saitama University
255 Shimo-ohkubo, Urawa-shi, 338 Japan
*Fujisawa Research Laboratory, Tokuyama Soda Co., Ltd.
2051 Endo, Fujisawa-shi, 252 Japan

Preparation conditions of ZrN fine powders from ZrO_2 by the thermite method using Mg under a nitrogen flow (200cm^3/min) have been investigated. Operation conditions for acid washing and the electrophoretic deposition of ZrN to obtain well defined ZrN powders have also been studied. The Mg/ZrO_2 molar ratio was kept constant at 5 but the charge varied from 1 to 7g. No unreacted ZrO_2 was observed in the products. ZrN fine powders of single phase have been synthesized at 600° ~ 800°C in a relatively short time. On the other hand, about 0.5 ~ 0.8wt% of Mg remained at the ZrN particles after acid washing with 1 ~ 2M HNO_3. The amount of Mg was not affected by synthetic temperature. It was found that the electrophoretic deposition method is a convenient and effective means for the recovery of ZrN fine powders from the products suspended in ethanol after acid washing.

[Received December 20, 1990; Accepted February 20, 1991]

Key-words: ZrN powder, Thermite method, Mg, Electrophoretic deposition

1. Introduction

The thermite process is known to release, in general, large quantities of heat generated by the reactions between a metal oxide and an active metal mixture when heated, because of the rapid propagation of the combustion (redox) reactions.[1] This process produces powdered products efficiently in a short time with only small quantities of external heat, in which the active metal works as the reducing agent. The normal reducing metals are Mg, Al and Zn, Mg being superior to the others for various reasons; (1) it is more reducing thermodynamically, (2) by-product oxides derived from the reducing metal can be easily removed by elution with an acid, and (3) it has a relatively low melting point (649°C) which allows it to be molten and mixed with metal oxides well at a relatively low temperature. These characteristics make Mg a desired active metal for the thermite process.

Meerson et al. first discussed synthesis of ZrN powder from ZrO_2 by the Mg-aided thermite process, but the particles prepared at 1100°C for 2h were fairly coarse at 5μm on the average.[2] The authors have investigated the synthesis conditions for the production of ZrN powder using ZrO_2 as the starting material and Mg as the reducing metal,[3-5] to find that the fine ZrN particles (30 to 100nm) can be prepared at a lower temperature (600°C) in a shorter time (1h).[4] The fine particles are more sinterable than the commercial powder.[5]

In this study, an attempt was made to investigate the effects of increased charge of the starting material on the synthesis conditions of fine ZrN particles and their characteristics, in considering that the thermite process is accelerated by the propagating heat of reaction. Increased charge of starting material was accompanied with the increased quantities of Mg-derived by-products (such as MgO and Mg_3N_2). Furthermore, the combination of acid washing and electrophoretic deposition was investigated as the solid-liquid separation process to recover the fine ZrN particles efficiently by removing these by-products.

2. Experimental Procedure

2.1. Synthesis of Fine ZrN Particles

The starting materials were commercial ZrO_2 powder (Tosoh, TZ-0, purity: 99.9%, average particle size: 0.1μm) and Mg powder (Kojundo Kagaku Kenkyusho, particle size: −150 meshes). They were well mixed by an agate mortar, and 0.2 to 7g of the mixture (Mg/ZrO_2=2 to 5) was placed in a graphite boat and put in a quartz reactor tube, which was then sufficiently purged with nitrogen gas. It was then admitted in a horizontal electrical furnace kept at a given temperature (600° to 1000°C), held for a given time (15 to 360min) under a nitrogen flow (200cm^3/min), and then quenched. Temperature was measured and controlled using the chromel-alumel thermocouple and PID type temperature controller. The powdered product was treated with 2M HNO_3 (acid washing) to remove the by-products, and washed with water and then dried, to prepare the fine ZrN particles. The X-ray diffraction analysis was made to determine quantities of the crystalline phases produced by their relative intensities, with NaCl as the internal standard. The lattice constants and crystal sizes of ZrN were determined by the diffraction lines of the (200), (220), (311), (222), (400), (331), (420) and (422) planes. A transmission electron microscope (TEM) was used to observe the morphologies and grain sizes of the ZrN particles. The samples were measured by the differential thermal and thermogravimetric analysis (TG-DTA). Nitrogen and remaining Mg were determined by Kjeldahl and atomic absorptiometric analyses, respectively.

2.2. Electrophoretic Deposition for Recovering Fine ZrN Particles

A given quantity (0.25 to 2g) of the synthesized ZrN

particles, treated with 1 to 2M HNO_3, was dispersed in 100cm^3 of special reagent-grade ethanol to prepare a suspended solution. A trace quantity of HNO_3 as the electrolyte was added to the suspension, to measure its conductivity and ξ–potential at 25°C. The electrodes were specially configured in the cell, to prevent nonuniform deposition by direction of electrophoresis; cylindrical platinum plates as the anode were fixed to the cell wall and a Ti wire as the cathode was arranged at the cell center concentrically. The ZrN particles were deposited electrophoretically on the Ti cathode in the cell. Each Ti wire (purity: 99%, diameter: 3mm, length: 50mm) working as the cathode was coated with a thermo-contractive Teflon tube in such a way as to leave a 30mm length uncoated. It was etched with a 4% HF solution and hot H_2SO_4 water solution (1+1), in this order, to make its surfaces rougher. The electrophoretic-deposition recovery was effected under the conditions of 20V DC voltage at room temperature, and 15 to 300sec deposition time. Quantity of ZrN deposited was measured by weighing after the deposited sample was dried.

3. Results and Discussion

3.1. Thermogravimetric Changes of Starting Materials

The starting mixture molar ratio of (Mg/ZrO_2=2 to 5) was analyzed by TG-DTA analysis under a nitrogen flow (200cm^3/min). There was only one, sharp exothermic peak at 593° to 600°C, associated with a sharp increase in weight, found in a temperature range from room temperature to 1000°C, irrespective of the molar Mg/ZrO_2 ratio tested. One typical example of the results is shown in **Fig.1**. These results indicated that the reduction and nitridation reactions of

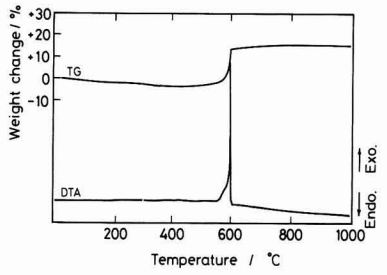

Fig. 1. TG-DA curves of ZrO_2-Mg mixed powder (Mg/ZrO_2 molar ratio=5) in N_2.

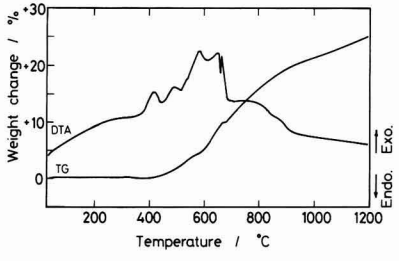

Fig. 2. TG-DTA curves of ZrO_2-Mg mixed powder (Mg/ZrO_2 molar ratio=5) in air.

ZrO_2 by Mg and nitrogen progressed rapidly in a short time, and ZrN was possibly synthesized at around 600°C. Furthermore, the unsymmetric nature of the exothermic peak suggested that the reaction proceeded in two or more stages, and that reduction of ZrO_2 slightly preceded in the reduction-nitridation process represented by $ZrO_2 \rightarrow ZrN$. The following two reactions are considered to represent the overall process:

$$ZrO_2 + 2Mg \rightarrow Zr + 2MgO \quad \ldots\ldots\ldots (1)$$

$$Zr + 1/2N_2 \rightarrow ZrN \quad \ldots\ldots\ldots\ldots (2)$$

No consideration was given to the reactions involving the Zr-Mg alloy in the $ZrO_2 \rightarrow ZrN$ process, because Zr is dissolved in molten Mg to 0.6wt% at most in a temperature range from 650° to 800°C,[6] and Mg is dissolved only sparingly in Zr.[6]

The reduction of ZrO_2 with Mg (eq.(1)) was investigated under an Ar gas flow (100cm^3/min) for the case of Mg/ZrO_2 molar ratio=5. The TG-DTA curves are given in **Fig.2.** Another atmosphere of an argon or helium (95vol%) and hydrogen (5vol%) mixture flowing at 100cm^3/min gave the similar TG-DTA results.

These results indicate that a very reactive reducing agent is formed by Reaction (1) and that it is difficult to maintain a stable atmosphere reducing system. Only TG-DTA results with the argon atmosphere are presented in this article.

The exothermic peak on the DTA curve is generally broader than that under a nitrogen flow, and quantity of the heat generated was one-tenth or less of that shown in Fig.1. A sharp endothermic peak resulting from melting of Mg was observed at 656°C. It was Mg left by Reaction (1) completed with an excessive quantity of Mg. Reaction (1) was considered to proceed at a temperature lower than the melting point of Mg under an argon flow, as was the case with a nitrogen flow. This means that melting of Mg is not essential for the reduction of ZrO_2, although it is necessary for Mg and ZrO_2 to contact sufficiently with each other, and Mg should be used excessively at lower than its melting point.

A by-reaction, represented by Equation (3) below, will be observed, in addition to eq.(1) and (2), when an excessive quantity of Mg is used under a nitrogen flow.

$$3Mg + N_2 \rightarrow Mg_3N_2 \quad \ldots\ldots\ldots\ldots (3)$$

Figure 3 presents the TG-DTA curves of Mg treated under a nitrogen flow (200cm^3/min). The sharp exothermic peak resulting from nitridation of Mg (eq.(3)) is observed at 657°C, 50 to 60°C higher than temperature at which an exothermic peak occurs in the ZrO_2-Mg-N_2 system (Fig.1). Unsymmetric nature of the exothermic peak, however, is

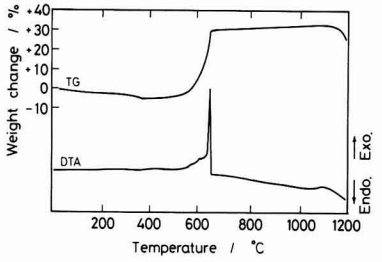

Fig. 3. TG-DTA curves of Mg powder in N_2.

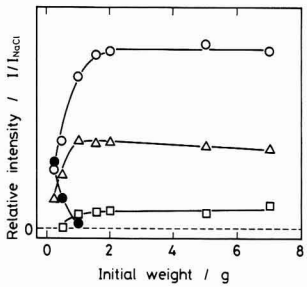

Fig. 4. Change in relative XRD intensities of products as a function of initial weight.
Composition of starting powder: Mg/ZrO_2 molar ratio=5,
Synthesis conditions: 600°C, 60min
○: ZrN, △: MgO, □: Mg_3N_2, ●: ZrO_2

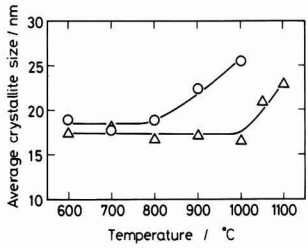

Fig. 5. Change in average crystallite size of synthesized ZrN as a function of synthesis temperature.
○: This work, △: Ikeda et al.[4]

similar, indicating that the reduction of Mg is accelerated with molten Mg. Dubovik et al. also observe that Mg is nitrided rapidly at above its melting point.[7] The TG curve shows a weight loss at above 1100°C, attributable to decomposition of Mg_3N_2. In summary, the Mg-aided thermite process to produce ZrN powder is controlled by Reaction (1) under a nitrogen flow, and Reactions (2) and (3) occurring subsequent to Reaction (1) proceed rapidly in the presence of molten Mg, which accelerates the overall reaction process rapidly by accelerating Equation (1). Use of an excessive quantity of Mg to increase contact points between Mg and ZrO_2 and thereby accelerate Equations (1) and (2), starting at below the melting point of Mg, will invariably increase production of Mg_3N_2 (Equation (3)), increasing Mg consumption.

3.2. Effects of Increased Feed Charge on Production of ZrN

Figure 4 shows the effects of the feed charge on relative X-ray diffraction intensity of the product, where the mixed feed (molar ratio of Mg/ZrO_2=5) was treated at 600°C for 60min. Under these conditions, MgO and Mg_3N_2 were formed, in addition to ZrN. Relative intensity of ZrN increased sharply with the feed charge rate up to 2g. Those of MgO and Mg_3N_2, on the other hand, increased as that of ZrO_2 decreased, each attaining a constant level at above 1g, accompanied by disappearance of the peaks of ZrO_2. At a feed charge of 2g or more, the product powder consisted of ZrN, MgO and Mg_3N_2, acid treatment of which gave the single-phase microparticles of ZrN. It has been thus demonstrated that, in the Mg-aided thermite process to produce the single-phase ZrN microparticles, increasing feed charge rate brings favorable effects, because of the increased heat of reaction in the system.

Next, the effects of temperature on average crystallite size were investigated under the ZrN producing conditions, where heating time was set at 60min, because no heating time effect was observed in a range from 15 to 360min. **Figure 5** shows the effects of heating temperature on average crystallite size for two levels of feed charge 1g[4] and 5g, where the feed mixture (molar ratio of Mg/ZrO_2=5) was treated at 600° to 1000°C for 60min. In the case of higher feed charge, average ZrN crystallite size was constant at around 18nm in a temperature range from 600° to 800°C, and then increased as temperature increased from 800°C. In the case of lower feed charge,[4] on the other hand, it was constant at around 17nm in a temperature range from 600° to 1000°C, and increased thereafter as temperature increased, as was the case with higher feed charge rate. These results indicated that the increased heat of reaction as a result of the increased feed charge caused system temperature to exceed set temperature of the furnace by roughly 200°C, as shown in Fig.5.

Figure 6 presents the TEM photographs of the fine ZrN particles prepared at 800° and 1000°C for 15min. The particles, agglomerated to a notable extent, were close to spheres, and the primary particles, whose sizes corresponded to those of the crystallites, were grown significantly at 1000°C. The desired temperature level for the production of the single-phase ZrN microparticles therefore will be in a range from 600° to 800°C.

The lattice constants of the single-phase ZrN microparticles prepared at 600° to 1000°C were measured. They were almost constant at a=0.4575 ±0.0001nm, which is in agreement with the literature values of a=0.4570 to 0.4578nm.[8-10] It is known that zirconium nitride has a fairly wide range of dissolution of nitrogen atom, and an attempt was made to determine nitrogen content in zirconium nitride using the relationship between lattice constant of zirconium nitride and N/Zr ratio.[11] Nitrogen content thus determined was 102% at a ZrN lattice constant of a=0.4570nm, and 83% at a=0.4578nm. The predicted nitrogen content, therefore, is 86 to 90% for the samples prepared in this study having a lattice constant of a=0.4574 to 0.4576nm.

Nitrogen content of the single-phase ZrN microparticles determined by the Kjeldahl method was 11.6 to 12.1wt%, or 87 to 91% that of the stoichiometric ZrN composition (13.3wt%). These are in good agreement with the results by the lattice constants. Thus, it can be concluded that the ZrN microparticles prepared in this study are fairly close to stoichiometric ZrN in chemical composition.

3.3. Acid Washing of Refining ZrN Microparticles

The Mg-aided thermite process will produce MgO and

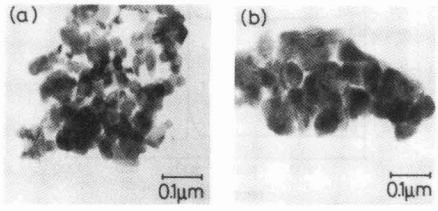

Fig. 6. TEM micrographs of ZrN powders. (a): 800°C, 15min, (b): 1000°C, 15min

Mg_3N_2 as by-products derived from Mg and they must be removed from the target product. The ZrN product can be refined by acid treatment, in which difference in solubilities of these components in the acid is utilized. In this study, the effects of acid concentration on refining performance were investigated.

Figure 7 presents the XRD patterns of the powders treated with 1 to 5M HNO_3. No diffraction peak of MgO or Mg_3N_2 was detected by any acid treatment used in this study, indicating that these by-products were eluted out. It should be noted, however, that part of ZrN was oxidized into ZrO_2, when 3M or more concentrated HNO_3 was used. The single-phase ZrN microparticles, therefore, will be produced by the acid treatment with 1 to 2M HNO_3. Elution of Mg from the ZrN product treated with 1 or 2M HNO_3 increased with treatment time, but attained a constant level in 1h.

Next, 2g of the ZrN powder product was treated with 1M HNO_3 in multi-stage for 1h for each cycle. **Figure 8** shows the effects of acid washing cycle on eluted Mg quantity. Mg was removed by the different mechanisms as cycle number increased; by the conventional water-replacement washing up to third cycle, and by water-diffusion washing thereafter. In other words, MgO and Mg_3N_2 present in the product powder were mostly removed by the third cycle, but small quantities of the residual Mg compounds were difficult to remove by the cyclic acid treatment. Concentration of the Mg residue was roughly 0.8wt% at the third cycle and 0.5wt% at the 8th cycle. There was little possibility that Mg or MgO was dissolved in, or bonded to, the ZrN particles, because the residual concentration was almost irrespective of temperature at which the feed mixture was heated.

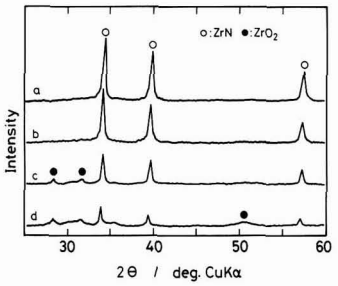

Fig. 7. X-ray powder diffraction patterns for ZrN powders after washing with various concentrations of HNO_3.
a: 1M, b: 2M, c: 3M, d: 5M

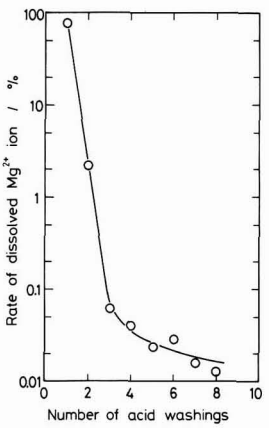

Fig. 8. Relationship between proportion of extracted Mg^{2+} and number of acid washing.
Condition of acid washing: 2g powder/100cm^3 HNO_3, 1h

3.4. Recovery of ZrN Microparticles by Electrophoretic Deposition

As discussed earlier in Section 3.3, MgO and Mg_3N_2 present in the ZrN powder could be removed by acid washing process. However, it was found that the ZrN particles were too fine at 30 to 100nm to be recovered sufficiently by the centrifugal solid-liquid separation, subsequent to water washing to remove the residual acid over the particles. Furthermore, increasing acid treatment and water washing cycles reduced the recovery rate of ZrN. An attempt was made, therefore, to apply electrophoretic deposition to the recovery of the ZrN particles.

Electrophoresis normally uses an electrolyte added to a suspension to charge the particles with electricity.[12-15] In this study, HNO_3 was used as the electrolyte and ethanol as the disperse medium to recover the single-phase ZrN microparticles.

Figure 9 shows the conductivity of two types of ethanol solution, one added with varying concentration of HNO_3 and the other the HNO_3-containing one to which acid-treated ZrN microparticles were added. Conductivity of the former solution increased linearly as HNO_3 concentration increased, whereas that of the latter suspension solution was higher than that of the former at a HNO_3 concentration of 5×10^{-4}mol/dm^3 EtOH or lower. These results suggested that the H^+ ions of roughly 10^{-3}M remained on the acid-treated ZrN particles. The ξ-potential of these particles present in the ethanol solution was positive. The ZrN particles synthesized were sufficiently conductive (resistivity: 13.6μΩcm) to be electrically deposited at a voltage of several tens of volts,[16] and a relatively low voltage of 20V was used for the electrophoretic deposition process to recover the ZrN particles in order to prevent codeposition of traces of Mg^{+2} ions remaining in the suspension.

Figure 10 shows the effects of ZrN particle concentration

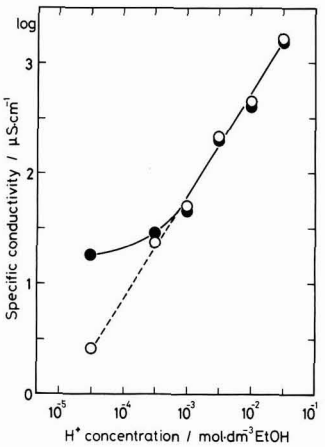

Fig. 9. Effect of H^+ concentration on specific conductivity of electrophoretic bath.
○: with only HNO_3, ●: with ZrN powder after acid washing

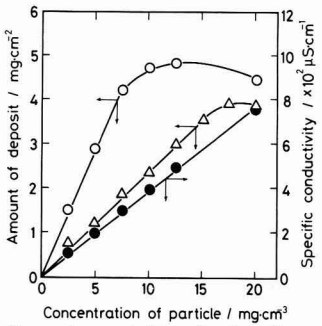

Fig. 10. Changes in amount of deposit and specific conductivity as a function of concentration of particle.
○, ●: acid washing with 1M HNO_3, △: acid washing with 2M HNO_3

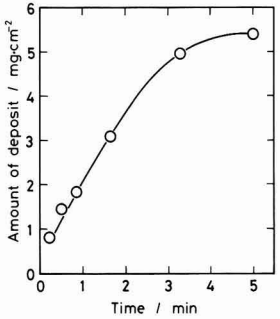

Fig. 11. Relationship between amount of deposit and deposition time.
Applied voltage: 20V, Particle concentration: 20mg/cm^3 EtOH

in the disperse medium on electrically deposited quantity of ZrN for the acid washing process with 1 and 2M HNO_3. Deposited ZrN quantity increased linearly as ZrN concentration in the solvent increased, and tended to attain a constant level eventually for each acid concentration. Deposited quantity of the ZrN particles was smaller for the sample acid-washed with 2M HNO_3 than with 1M HNO_3, conceivably resulting from agglomeration of the particles in the suspension. It was also observed that conductivity of the suspension increased with ZrN particle concentration linearly, indicating that H^+ ions were remaining on the as-treated ZrN particles.

Figure 11 shows the effects of deposition time on deposited quantity of the ZrN particles which were treated with 1M HNO_3 and were present in the ethanol solution at a concentration of 20mg/cm.[3] The deposited quantity increased with time linearly during the initial stage, but later attained a constant level. Thus, it has been demonstrated that the ZrN particles can be recovered sufficiently in a short time even at a low voltage of 20V by the electrophoretic deposition process, without using an electrolyte additive, because the particle surfaces are always charged positive with the H^+ ions adsorbed on, or attached to, them during the acid washing process. It is therefore considered that electrophoretic deposition is a useful solid-liquid separation process for the acid-treated products of the Mg-aided thermite process.

4. Conclusions

The Mg-reduced thermite process was used to prepare ZrN microparticles from the ZrO_2-Mg-N_2 feedstock, and the product was refined by a combination of acid treatment and electrophoretic/deposition to prepare the single-phase ZrN microparticles.

1) The single-phase ZrN microparticles were produced at a relatively low temperature (600° to 800°C) and in a short time from the starting material of molar ratio of Mg/ZrO_2=5; no unreacted ZrO_2 was found to remain, even with increased feed charge.
2) Mg remained in the single-phase ZrN microparticle product to 0.5 to 0.8wt%, even after repeated acid treatment cycles. The residual Mg content was irrespective of temperature at which the feed mixture was treated.
3) Electrophoretic deposition was found to be a useful means for the recovery of the ZrN microparticles from the ethanol suspension in which the acid-treated ZrN particles were dispersed.

References:

1) S. Takeda, New Ceramics, 6, 73-79 (1990).
2) G.A. Meerson and S. Roy, Poroshkovaya Met., Akd. Nauk Ukr. USSR, 3, 71-77 (1963).
3) T. Ikeda, T. Mori, T. Iida and T. Mitamura, Yogyo-Kyokaishi, 93, 108-109 (1985).
4) T. Ikeda, T. Mori, F. Noguchi, T. Iida and T. Mitamura, Yogyo Kyokaishi, 93, 505-510 (1985).
5) H. Kobayashi, H. Hoshino, T. Ogata and T. Mitamura, Seramikkusu Ronbunshi, 97, 1189-1194 (1989).
6) M. Hansen and K.P. Anderko, Constitution of Binary Alloys, McGraw-Hill, New York (1957), 932-933.
7) T.V. Dubovik, V.S. Polishchuk and G.V. Samsonov, J. Appl. Chem. USSR, 37, 1812-1814 (1964).
8) Y. Okabe, J. Hojo and A. Kato, Yogyo Kyokaishi, 85, 173-180 (1977).
9) A. Wilcokson and R.E.W. Casselton, J. Am. Ceram. Soc., 53, 293 (1970).
10) L.E. Toth, Transition Metal Carbides and Nitrides, Academic Press, New York and London (1971) 88-89.
11) A.J. Perry, M. Georgson and M.D. Sproul, Thin Solid Films, 157, 255-265 (1988).
12) Y. Tomita, Hitachi Hyoron, 49, 40-44 (1967).
13) K. Anzai, Denki Kagaku, 53, 63-67 (1985).
14) N. Koura, ibid., 56, 208-209 (1988).
15) N. Koura, Hyomen Gijutsu, 40, 819-824 (1989).
16) H. Kobayashi, M. Katoh, H. Hoshino and T. Mitamura, ibid., 40, 1144-1145 (1989).

This article is a full translation of the article which appeared in Nippon Seramikkusu Kyokai Gakujutsu Ronbunshi (Japanese version), Vol.99, No.6, 1991.

Kinetics of Curing of Polycarbosilane Fiber by Oxidation Treatment

Toshio Shimoo*, Masaki Sugimoto and Kiyohito Okamura***

*Department of Metallurgical Engineering, College of Engineering, University of Osaka Prefecture
4-804, Mozu-Umemachi, Sakai-shi, 591 Japan
**Graduate Student, University of Osaka Prefecture
4-804, Mozu-Umemachi, Sakai-shi, 591 Japan

The mechanism of curing polycarbosilane (PCS) fiber has been investigated. Polycarbosilane has been melt-spun to fibers in the diameter range of 21-113μm. The rate of curing of PCS fiber was measured with a thermo-balance in Ar-O_2 gas mixtures with 5-100kPa O_2 at temperatures from 413K to 463K.

The rate of curing increased with increasing curing temperature and Po_2 and with decreasing fiber diameter. The fiber melted to agglomerate in a mass, depending on the curing temperature, Po_2 in Ar-O_2 gas mixtures and the size of fibers. A cured layer, through which oxygen molecules can advance and reach the reaction interface, was formed around the fiber. The reaction interface receded towards the center of the fiber as the curing progressed.

In the early stage of curing, the kinetics followed the contracting-disc formula: $1-(1-X)^{1/2}=kT$. The apparent activation energy was 87.7kJ/mol. The rate constant k was proportional to Po_2 and was inversely proportional to the diameter of the fiber. It is considered that the curing of PCS fiber is controlled by the interfacial reaction. In the late stage of the reaction, curing is controlled by the diffusion of oxygen through the reaction layer.

[Received December 25, 1990; Accepted February 20, 1991]

Key-words: Polycarbosilane fiber, Oxidation treatment, Curing Kinetics, Thermogravimetry, Reaction mechanism, Rate-determining step

1. Introduction

One of the greatest disadvantages of silicon carbide fibers is their rapid reduction in mechanical strength at high temperature (1573K or more) due to pyrolysis.[1,2] The pyrolysis-related problems must be solved before these materials can be extensively used industrially, whether they are used alone or in combination as a reinforcement for the composite ceramics of recent interest. The authors have been investigating the reaction mechanisms involved in the pyrolysis of various types of silicon carbide fibers,[3-6] and clarified that the pyrolysis is characterized by crystallization of the amorphous fibers into β-SiC, which is accompanied by release of SiO and CO gases. It is also found that pyrolysis rate is largely determined by the quantity of oxygen present in the fibers.[6]

The production process of the commercial silicon carbide fibers consists of (1) melt spinning of the organic silicon polymer, (2) thermo-oxidation/curing and (3) firing.

Step (2) is an important process in which the melt-span fibers are heated and converted into inorganics without fusing, thus silicon carbide fibers are obtained. The curing process is represented by cross-linking reactions in the presence of oxygen, and the cured fibers are invariably contaminated with oxygen.[8] It is essential to control oxygen content in the cured fibers to a proper level, in order to efficiently control pyrolysis of the final silicon carbide fibers. Rate of, and the reaction mechanisms involved in, the oxidation/curing process therefore must be clearly understood.

Many researchers have been discussing the reactions involved in the curing process and characterization of the cured fibers. However, few have attempted to analyze the kinetics of the process, though Ichikawa et al. have investigated oxidation of the polycarbosilane powder.[12] In this study, the authors have measured the rate of isothermal oxidation/curing of the melt-spun polycarbosilane with a thermobalance. The effect of curing temperature, partial pressure of oxygen in the atmosphere, and diameter of the fibers were investigated in detail, and mechanisms and controlling stage of the reaction were elucidated.

2. Experimental Procedure

For the production of the polycarbosilane fibers (PCS fibers), polycarbosilane (Shin-Etsu Chemical) was melt-spun at 573 to 603K in an Ar gas atmosphere. The spinning rate was varied to control the fiber diameter at 21 to 113μm.

Two types of experiments were conducted to investigate the oxidation/curing mechanisms of the PCS fibers.

2.1. Measurement of Oxidation Rate of PCS Fibers Under Isothermal Conditions

A carbon crucible containing 1g of the PCS fibers was suspended in the constant-temperature section (kept at a given temperature) of a Kanthal oven, after having been connected to an automatic balance (measurable limit: 100g, sensitivity: 0.1mg), to continuously monitor the mass gain of the fiber sample as a result of oxidation/curing. The atmosphere gas was a mixture of Ar and O_2, kept at a total pressure of 100kPa, where oxygen partial pressure p_{O_2} was varied in a range from 5 to 100kPa. The mixed gas flowed at $1.67\times10^{-5}m^3/s$ from the oven bottom. A number of pores were provided in bottom and side wall of the crucible to allow the mixed gas to pass through the crucible sufficiently.

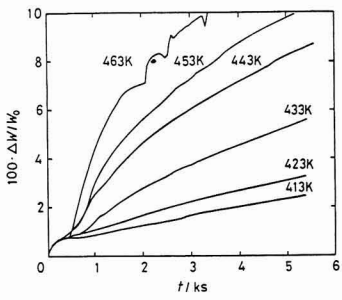

Fig. 1

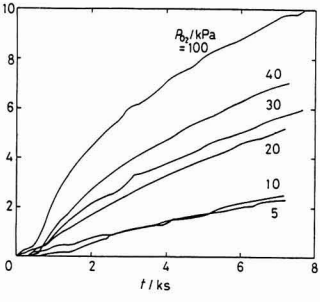

Fig. 2

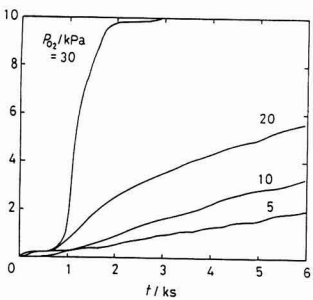

Fig. 3

Fig. 1. Mass gain with curing of PCS fibers (d/μm=113) heated isothermally at various temperatures in 80%Ar-20%O_2 gas mixture.

Fig. 2. Effect of p_{O_2} in Ar-O_2 gas mixture on mass gain with curing of PCS fiber (d/μm=113) heated isothermally at 423K.

Fig. 3. Effect of p_{O_2} in Ar-O_2 gas mixture on mass gain with curing of PCS fiber (d/μm=65) heated isothermally at 423K.

No weight change was observed in the crucible in the temperature studied.

2.2. Measurement of Oxidized Quantity of PCS Fibers by Continuous Heating

PCS fibers of 113μm in diameter were heated at 40K/hr in a pure oxygen atmosphere for the oxidation/curing treatment. They were held for 1.8ks at a curing temperature of 423 to 483K, and then allowed to cool. The oxidized quantity of the fibers was determined by measuring the weight change before and after the treatment.

Growth of the oxidized layers over each fiber was observed for the two types of the PCS fibers cured at different temperature levels, 443 and 483K.

First, the fiber sample was fired by heating it to 1473K in an Ar gas atmosphere. Later, it was pyrolyzed at 1973K in an Ar gas atmosphere, and the fracture faces were analyzed by a scanning electron microscope. It was a method using the fact that growth behavior of β-SiC crystallites accompanied to pyrolysis depends on the concentration of oxygen in the fibers.

3. Results

3.1. Effects of Temperature

Figure 1 shows the effects of oxidation/curing temperature in a range from 413 to 463K on mass gain of the PCS fibers, where ΔW is the mass gain determined by a thermobalance, and W_0 is the original mass of the fiber sample. The fibers used in the tests had a diameter of 113μm. The atmosphere was of a mixture of oxygen (p_{O_2}=20kPa) and argon (p_{Ar}=80kPa). The mass gain of the sample resulted from introduction of oxygen into the sample during the curing treatment. Curing rate of the fiber sample would be assessed by mass gain rate. No effect of curing temperature on curing rate was found at the initial stage of reaction, until the sample was heated to a certain level at which the thermal oxidation process proceeded steadily. Curing rate increased naturally with curing temperature. It was frequently noted that curing rate increased sharply at 463K at a curing time greater than 2ks, on account of the accelerated oxidation caused by temperature runaway, discussed later. Finally, the

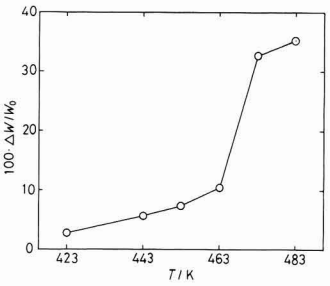

Fig. 4. Mass gain with curing of PCS fiber (d/μm=113) heated continuously at 40K/h and held at various curing temperatures for 1.8ks in a pure oxygen atmosphere.

PCS fibers were molten to stick to each other. It was difficult to measure curing rate at 463K or more, because of melting and combustion of the fibers.

3.2. Effects of Oxygen Partial Pressure and Fiber Diameter

The PCS fiber sample was treated at 423K under an oxygen partial pressure in a range from 5 to 100kPa, to observe curing behavior of the fibers. **Figures 2** and **3** show the results for fibers having an diameter d of 113μm and 65μm, respectively. In each case, the curing process was accelerated as oxygen partial pressure increased. Melting and combustion of the fibers prevented measurement of curing rate at p_{O_2}>20kPa with the finer fiber sample. A sharp mass gain was noted at p_{O_2} = 30kPa and around 1ks (Fig.3), due to the temperature runaway caused by accumulated heat in the sample during the curing process, as discussed later.

Comparing the results shown in Fig.2 with those in Fig.3, it was obvious that the finer sample was cured faster at the same oxygen partial pressure.

3.3. Thermal Oxidation of PCS Fibers by Continuous Heating

Curing rate of the PCS fibers by isothermal heating has been discussed so far. However, these fibers are commercially cured by continuous heating from room temperature to curing temperature. Therefore, an attempt was made to find the relationship between mass gain of the fibers and

curing temperature by the procedure described in Section 2.2. The results are shown in **Fig.4**. It has been found that mass gain of the fibers $100\Delta W/W_0$ almost corresponds to increase in oxygen content (mass % O) of the fibers.[12] Mass gain rate increased slowly as curing temperature increased up to 463K, but sharply (around 3 times) from 463 to 473K, presumably resulting from curing temperature runaway. Unlike the isothermal heating case, however, these fibers were not fused to stick to each other.

3.4. Observation of Oxidized Layers over PCS Fibers

As shown in Fig.4, mass gain (corresponding to increased oxygen content) of the fibers cured at 443K was 4.5%, which was much lower than that of the fibers cured at 483K (28.9%). These fibers were fired at 1473K and then further heated to 1973K. The amorphous silicon carbide fibers containing oxygen are pyrolyzed at high temperature, and this process is characterized by the crystallization accompanied by the release of SiO and CO gases.[3-6]

$$SiC_{1+x}O_y \text{ (amorphous)} \rightarrow \beta\text{-SiC} + SiO\ (g) + CO\ (g) \quad \ldots\ldots\ldots\ldots (1)$$

The fiber containing a larger quantity of oxygen was pyrolyzed faster, and the SiC grains were grown faster.[6] On the other hand, the oxygen-free PCS fiber turned into β-SiC and carbon when treated at high temperature:[14]

$$SiC_{1+x} \text{ (amorphous)} \rightarrow \beta\text{-SiC} + C \text{ (amorphous)} \quad \ldots\ldots\ldots\ldots\ldots\ldots\ldots\ldots (2)$$

The SiC grains in the oxygen-free fibers were grown differently from those in the oxygen-containing fibers during the firing process, because of the different reactions they underwent. It is therefore possible to grasp the extent of oxygen penetration into the fibers by observing the growth behavior of the grains on the fiber cross-sections.

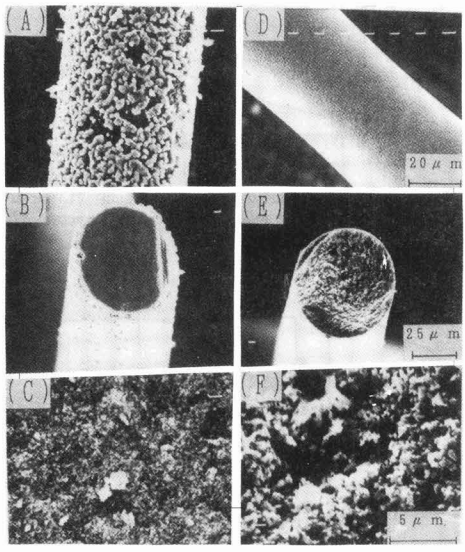

Fig. 5. SEM photographs of PCS fibers decomposed at 1973K after curing at 443K and 483K in an oxygen atmosphere and heating at 1473K in an argon atmosphere.
curing temperature=443K, $100\Delta W/W_0$=4.5: (A) surface, (B) cross section and (C) center of fiber
curing temperature=483K, $100\Delta W/W_0$=28.9: (D) surface, (E) cross section and (F)center of fiber.

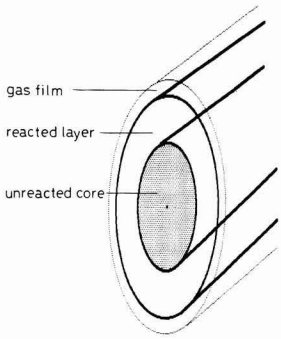

Fig. 6. Schematic representation of curing of PCS fiber.

Figure 5 presents the SEM photographs of the fiber cross-sections. The grains were grown and coarsened only on the fiber surface (A) and on the thin layer (B) in the vicinity of the surface in the fiber cured at 443K. The grains were small at the fiber center (C) and scarcely coalesced into larger ones. This probably resulted from the reactions represented by equation (1) in the layers near the surfaces, and by equation (2) inside. In the fibers containing a high proportion of oxygen cured at 483K, the grains were grew significantly during the pyrolysis process throughout the cross-section (D, E and F). This suggested that reaction (1) proceeded both on the surfaces and inside. It is worthy of attention, though not understood why, that the grains on the fiber surfaces are smaller than those on the surfaces cured at 443K. These fibers were crushed for the X-ray diffraction analysis. β-SiC of the sample cured at 483K had sharper X-ray diffraction patterns, which was in agreement with the SEM analysis results. It is therefore considered that the curing process proceeded while the reaction interfaces were similar to the outer peripheries of the fiber cross-sections.

4. Discussion

4.1. Kinetic Analysis

Figure 6 illustrates the oxidation/curing model of the PCS fiber, based on SEM analysis of the pyrolyzed fiber cross-sections. In other words, the curing process is considered to consist of the following three steps:

① transport of oxygen towards the surfaces through the gas film around the fiber,
② transport of oxygen towards the unreacted core through the surfaces and the reacted layers, and
③ chemical reactions at the reaction interfaces.

The curing process was discussed for the cases of the different rate-determining steps, considering the cylindrical fiber model shown in Fig.6.

1) Diffusion of oxygen through the gas film as the rate-determining step:
Curing rate of the fiber n/mol·s^{-1} will be given by eq.(3).

$$n = 2\pi r_0 l k_g (p_{O_2} - p_{O_2}')/RT \quad \ldots\ldots\ldots\ldots (3)$$

where,
r_0 and l : radius and length of the PCS fiber

k_g : mass transfer coefficient
p_{O_2} and $p_{O_2}^i$: oxygen partial pressures in the bulk gas and on the fiber surface
R : gas constant

Combining eq.(3) with eq.(4) will give eqs.(5) and (6), considering that p_O^i is negligibly small as compared with p_{O_2}:

$$n = d\{(\pi r_0^2 l - \pi r_i^2 l)\, d_O\}/dt$$
$$= -2\pi r_i l d_O (dr_i/dt) \quad \cdots\cdots (4)$$
$$X = k't \quad \cdots\cdots (5)$$
$$k' = 2k_g p_{O_2}/RTr_0 d_O \quad \cdots\cdots (6)$$

where, r_i is radius of the unreacted core, d_0 is oxygen content (mol/m^3) of the oxidation-cured fiber, and X is conversion, defined by eq.(7):

$$X = 1 - (r_i/r_0)^2 \quad \cdots\cdots (7)$$

Equation(5) and (6) suggest that the curing process is accelerated as p_{o2} increases and r_0 decreases, which almost corresponds to the experimental results shown in Figs.1 and 3. It should be noted, however, that the linear relationship of eq.(5) is contradictory to the observed results where the relationship between pyrolysis-induced mass gain and time is represented by a curve. The linear relationship of eq.(5) was used to determine reaction rate during the intial stage only. The reaction rate was assessed by $d(\Delta W/W_0)/dt$. **Figure 7** presents the Arrhenius plot of the $d(\Delta W/W_0)/dt$ values, which gave an apparent activation energy of 94.2KJ/mol. The results by Ichikawa et al. for powdered polycarbosilane[12] are also shown in the figure, for comparison. It is interesting to note that the activation energy values are essentially the same as their value of 84.5kJ/mol, in spite of the different conditions under which the experiments were conducted. This suggested that the two reaction systems shared the common reaction mechanisms and rate-determining step.

According to the film theory, mass transfer coefficient k_g is given by eq.(8):

$$k_g = D/\delta \quad \cdots\cdots (8)$$

where,

D : diffusion coefficient of oxygen in gas, and
δ : thickness of the gas film

It is generally accepted that diffusion coefficient of a gas is in proportion to $T^{1.5}$ or $T^{1.8}$.[15] This temperature-dependence relationship, when substituted into eq.(6) or (8), gives an activation energy of 1.8 to 2.9KJ/mol in a temperature range between 413 and 463K. The above value is much lower than 94.2KJ/mol, from which it is judged that step ① is not the rate-determining step.

2) Diffusion through Reacted Layer as Rate-Determining Step

Diffusion of a mass from the surface of a cylindrical sample (such as the PCS fiber) towards the inside will be represented by eq.(9), when it is the rate-determining step:[16]

$$(1-X)\ln(1-X) + X = k't \quad \cdots\cdots (9)$$

where, k' is rate constant.

Conversion X can be found from mass gain ΔW of the PCS fiber sample by Equation (10):

$$X = \Delta W/\Delta W^f \quad \cdots\cdots (10)$$

where ΔW^f is the mass gain when the curing process is completed (when mass gain is no longer measuable).

The fiber sample was cured for a long time at 423K and p_{o2}=20kPa, to find the ΔW^f value. **Figure 8** plots $\Delta W/W_0$ against time. It also plots conversion X against time where X was determined from the $\Delta W/W_0$-time relationship and eq.(9). A linear relationship was not noted during the initial stage of the oxidation/curing process ($t \leq 6$ks, $X \leq 0.55$), from which it is judged that step ② is not the rate-determing step. However, a linear relationship was noted during the later stage of the process ($0.55 \leq X \leq 0.70$), due to increased thickness of the reacted layer that prevents diffusion of oxygen.

3) Reaction at Interface as Rate-Determining Step

Rate of the reaction n/mol·s^{-1} at the interface will be represented by eq.(11), on the assumptions that it is of first order and the reverse reaction is negligible:

$$n = 2\pi r_i l k_r p_{O_2}/RT \quad \cdots\cdots (11)$$

where, k_r is rate constant.

The following equations are derived from equations (4), (7) and (11):

$$1-(1-X)^{1/2} = k''t \quad \cdots\cdots (12)$$
$$k'' = k_r p_{O_2}/r_0 d_0 RT \quad \cdots\cdots (13)$$

Applicability of eq.(12) is shown in Fig.8. The reaction is represented by a linear relationship during the initial stage, but the plot is curved downward as the reaction proceeds ($X \leq 0.55$). The reaction at this stage is represented by eq.(9) derived on the assumption that the reaction rate is determined by diffusion. It is thus considered that the curing of the PCS fibers is determined by the different mechanisms

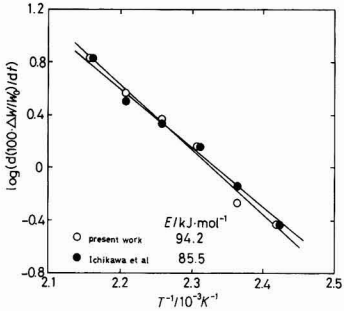

Fig. 7. Temperature dependence of initial rate of curing, $d(\Delta W/W_0)/dt$.

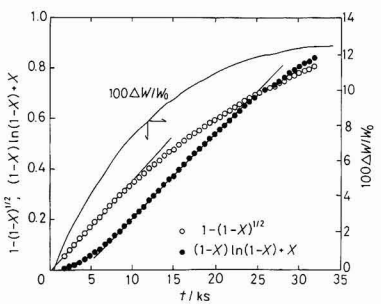

Fig. 8. Mass gain with curing of PCS fiber (d/μm=113), $1-(1-X)^{1/2}$ vs time and $(1-X)\ln(1-X)+X$ vs time plots in 80%Ar-20%O_2 gas mixture at 453K.

during the initial and later stages of the reaction. In other words, the reaction at the interfaces is the rate-determining step during the initial stage, where the cured layer is sufficiently thin to allow diffusion of oxygen easily through it, and the reaction tends to be limited by diffusion during the later stage, where the cured layer becomes sufficiently thick. The experimental results are analyzed using eq.(12) for the case of the reaction at the interfaces as the rate-determining step.

The ΔW^f value, an important parameter to find the X level, was determined by trial and error to satisfy eq.(12). The estimated ΔW^f value at 453K is almost compatible with the results shown in Fig.8. This type of analysis produced the reasonable results discussed below.

Equation (12) was applied to the results shown in Fig.1, and the results are presented in **Figure 9**. The data for each temperature level are well represented by a linear relationship, except for those obtained during the initial stage of the reaction process, which gives rate constant k'' from its slope. Equation (13) is rearranged into equation (14):

$$k = k''T = k_i p_{O_2}/r_0 d_0 R \quad \ldots\ldots\ldots\ldots \quad (14)$$

Temperature-dependence of the reaction process was assessed using the k value. **Figure 10** shows the Arrhenius type plot for the k-value, and the linear relationship gave an apparent activation energy of 87.7KJ/mol. This level is within the reasonable range as the activation energy for the reactions in which organic compounds are involved.[17]

Figure 11 shows the effects of partial pressure p_{o2} of oxygen present in the atmosphere gas on rate constant k''. There is a linear relationship in a $k''\leq 0.06$ range for each fiber diameter:

$$k''/ks^{-1} = 27.7 \times p_{O_2}/MPa \text{ for } d = 113\mu m \quad .(15)$$

$$k''/ks^{-1} = 15.6 \times pVo2/MPa \text{ for } d = 113\mu m \quad (16)$$

which are the results of the analysis by the least-square method.

These correlations correspond well to the relationship of eq.(13). Increasing p_{o2}, however, would not increase the k'' value beyond 0.06, because of accelerated oxidation of the fibers to cause temperature runaway, and eventually fusion and combustion of the fibers. Especially, the fine fibers (d=65μm) were burned at p_{o2}=20kPa or more so that their oxidation rate could not be measured. It is apparent from eqs.(15) and (16) that the finer fibers had a larger k'' value at the same oxygen partial pressure. This also corresponds well to the relationship of eq.(13).

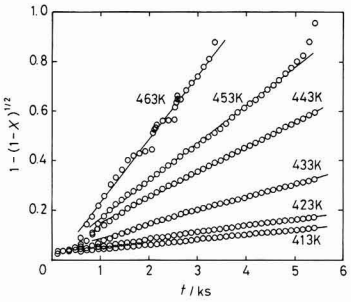

Fig. 9. Application of rate equation (12) to data shown in Fig.1.

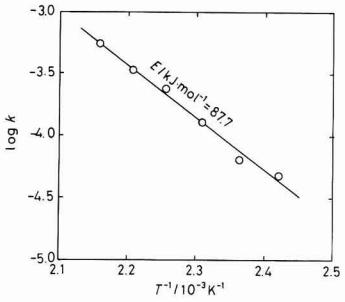

Fig. 10. Arrhenius plots of rate constant k.

4.2. Fusion and Combustion of PCS Fibers

As discussed earlier, the PCS fibers will be fused or even combusted, depending on conditions of thermo-oxidatun/curing e.g., high curing temperature, high oxygen partial pressure and fine fibers. The fine fibers (d=20μm) were completely combusted at 453K and $p_{o2}\geq$50kPa. In addition, the fibers of 65μm were mostly fused into blocks at 423K and p_{o2}=20kPa. On the other hand, no fusion was observed in the thicker fibers (d=100μm) cured at 463K and po_2=20kPa, or at 423K and p_{o2}=100kPa. Fusion and combustion of the PCS fibers during the thermo-oxidation/curing step are very important problems. As discussed above, there is a restriction in temperature, oxygen partial pressure and fiber size, for the curing process. In this study, the fiber sample was thrown directly into the curing oven kept at a given temperature. In a commercial plant, where the fibers are heated slowly and continuously, the conditions resulting in fusion and combustion of the fibers will be substantially relaxed.

The PCS fibers were found to fuse and combust at a temperature below their melting point of 506K, conceivably because of the combustion of the volatile matter released from the fibers, which increased temperature beyond their melting point.

The curing reactions of the PCS fibers will start to proceed at around 373K.[7] In other words, the Si-O-Si bonds are formed within the fibers by the following cross-linking reactions:

$$\equiv SiH + HSi\equiv + O_2 \rightarrow \equiv Si\text{-}O\text{-}Si\equiv + H_2O \quad \ldots(17)$$

$$\equiv SiOH + HOSi \equiv \rightarrow \equiv Si\text{-}O\text{-}Si\equiv + H_2O \quad \ldots(18)$$

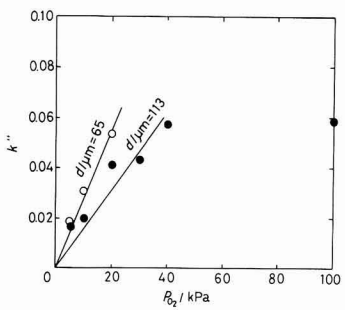

Fig. 11. Relation between rate constant k'' and p_{O_2}

These reactions are exothermic.13) Furthermore, hydrogen may be formed during the curing process,[13] and temperature will be further increased if it is oxidized. Temperature will be sufficiently high, if heat is not removed adequately, to fuse the fibers.

In an extreme case, the fibers were completely burned out because of the temperature runaway caused by the combustion of the volatile matter. CH_4 may be formed when fiber temperature exceeds 823K, and the combustion of CH_4 and H_2, if it occurs, will further increase their temperature to eventually combust the solid components. Increasing quantity of the PCS fibers in the crucible tended to prevent heat release, accelerating temperature runaway.

5. Conclusions

The laboratory-prepared PCS fibers were cured under an oxidative atmosphere to measure curing rate by a thermobalance and to observe penetration of oxygen into the fibers. The effects of curing temperature, oxygen partial pressure and fiber size on curing rate were investigated to understand the reaction mechanisms involved.

1) Increasing temperature accelerated curing, but fusion of the fibers was observed at 463K or higher.
2) Increasing oxygen partial pressure (p_{o2}) accelerated curing, and fusion of the fibers was observed at above a critical p_{o2} level, which decreased as fiber size decreased.
3) Decreasing fiber size accelerated curing, eventually causing fusion and combustion of the fibers.
4) Oxygen penetrated into the fiber concentrically from the surface towards the center.
5) Curing rate of the PCS fibers was determined by the two-dimensional, interfacial reactions within curing time used in this study. An observed apparent activation energy was 87.7kJ/mol. Rate constant k'' of the overall interfacial reaction was in proportion to p_{o2}, and almost inversely proportional to fiber size.
6) It is considered that curing of the PCS fiber is governed by the rate of interfacial reactions, in which the unreacted portion of each fiber is oxidized with oxygen diffusion through the already reacted layers. In the later stage of the curing process, the cured layer will be sufficiently thick to make oxygen diffusion the rate-determining step.

References:

1) Y. Sasaki, Y. Nishina, M. Sato and K. Okamura, J. Mater. Sci., 22, 43-48 (1987).
2) D.J. Pysher, K.C. Goretta, R.S. Hodder, Jr and R.E. Trssler, J. Am. Ceram. Soc., 72, 284-288 (1989).
3) S. Shimoo, M. Sugimoto and K. Okamura, J. Jpn. Inst. Metals, 54, 802-808 (1990).
4) S. Shimoo, M. Sugimoto and K. Okamura, Seramikkusu Ronbunshi, 98, 1324-1329 (1990).
5) S. Shimoo, Y. Kakei, M. Sugimoto and K. Okamura, J. Jpn. Inst. Metals, 55, 294-303 (1991).
6) S. Shimoo, Y. Kakei, M. Sugimoto and K. Okamura, Seramikkusu Ronbunshi, 99, 401-406 (1991).
7) S. Yajima, Am. Ceram. Soc. Bull., 62, 893-898 (1983).
8) S. Yajima, Y. Hasegawa, J. Hayashi and M. Iimura, J. Mater. Sci., 13, 2569-2576 (1978).
9) Y. Hasegawa and K. Okamura, ibid., 18, 3633-3648 (1983).
10) Y. Hasegawa and K. Okamura, ibid., 21, 321-328 (1986).
11) Y. Hasegawa and K. Okamura, J. Chem. Soc. Jpn. 564-571 (1985).
12) H. Ichikawa, H. Teranishi and T. Ishikawa, ibid., 4, 696-704 (1987).
13) Y. Hasegawa, J. Mater. Sci., 24, 1177-1190, (1989).
14) S. Shimoo, M. Sugimoto and K. Okamura, Powder and Powder Metallurgy, 37, 1132-1137 (1990).
15) J. Szekely, Rate Phenomena in Process Metallurgy, Wiley-Intersci., New York (1971) p.369.
16) E. Hashimoto, Kagaku Sosetsu, 9, (1975) 215.
17) Chemical Handbook, Basis, Vol.2, ed. by Chem. Soc. Jpn., Maruzen, (1975) p.107-115.

This article is a full translation of the article which appeared in Nippon Seramikkusu Kyokai Gakujutsu Ronbunshi (Japanese version), Vol.99, No.6, 1991.

Growth of PZT Crystal by Using PbO-KF-$PbCl_2$ Flux

Satoshi Fujii, Yosohiro Sugie, Yusuke Takahashi and Hiroshi Fujiwara

Department of Applied Chemistry, Faculty of Engineering, Himeji institute of Technology
2167, Sosha, Himeji-shi 671-22, Japan

Single crystal of lead zirconium titanate (PZT) were grown by slow cooling method from fluxes of PbO-KF-PbF_2 and PbO-KF-$PbCl_2$ system. (1) Single crystals of PZT with a size smaller than 1mm were grown from the flux of PbO-KF-PbF_2 system. (2) Single crystals of PZT of a maximum size 1.7×1.7×0.9mm were grown from the flux of PbO-KF-$PbCl_2$ system. The obtained crystals were reddish brown in color and their composition was determined to be $Pb(Zr_{0.52}Ti_{0.48})O_3$ by EDX.
[Received August 24, 1990; Accepted February 20, 1991]

Key-words: PZT, Single crystal, PbO-KF-$PbCl_2$ flux, $Pb(Zr_{0.52}Ti_{0.48}O_3$

1. Introduction

A solid solution of lead zirconium titanate $(Zr_xTi_{1-x})O_3$ (PZT) is a terroelectric substance possessing a perovskite structure, and has a boundary phase from tetragonal crystal to trigonal crystal, particularly at x 0.55. Since this solid solution displays an excellent piezoelectric characteristic in the neighborhood of this boundary, it is now widely used for supersonic oscillators and piezoelectric firing devices.

When PZT single crystals are grown in fusion or by a fusion method, the vaporization or dissolution fusion? (bunkai yokai) of their main component PbO can easily occur during the fusion process. For this reason, growth is accomplished mainly by flux methods. There have been reports[1-3] on the use of two-component fluxes of PbO-PbF_2, KF-PbF_2, and the like and a report[4] on the use of fluorides as starting materials, but large and good quality single crystals have not been obtained, indicating that research on the physical properties of single crystals has not been advanced much. Moreover, since PbF_2 evaporates a great deal at high temperatures, requiring the crucible to be sealed tightly, it cannot easily be treated as a flux. Under these circumstances, the present study was an attempt to grow single crystals by using three-component flux of PbO-KF-PbF and PbO-KF-$PbCl_2$ which has not been reported before.

2. Experimental Procedures

2-1. Preparation of Starting Material and Flux

The starting material was prepared as follows. PbO (massicot) powder, TiO_2 (anatase) powder, and ZrO_2 powder (all produced by Nakarai Tesk Co., top grade) were mixed at a molar ratio of 2:1:1 and ground, put in a platinum crucible, sintered at 900°C for 3h, then ground using an agate mortar to obtain powder of less than 200 mesh (74μm). This raw material was identified by X-ray diffraction to be a PZT-phase.

For the flux, powders of KF, PbO, PbF_2 and $PbCl_2$ were used. All of the powders were top-class reagents made by Nakarai Tesk Co.

2-2. Method for PZT Single Crystal Growth

The starting raw material and the flux were weight by chemical balance so that the relative weight was 0.33 and the total weight was 12.0g. The materials were mixed, and 0.5g of B_2O_3 was added to this mixture in order to control the evaporation of the flux. These were put in a lidded platinum crucible of 50ml in volume. This crucible was placed inside a vertical electric furnace having kanthal lines as a heat source to conduct growth experiments according to a prescribed schedule of temperatures. After the experiments, the flux was dissolved using warm dilute nitric acid and filtered to take out crystals grown.

2-3. Method for Examining Grown Crystals

The rate of flux vaporization during the growth process was calculated based on the difference from the total amount inside the crucible before the growth began. The crystal yield? (shuritsu) was computed from the ratio of the crystal harvest to the total amount of starting raw materials. Since crystals had to be at least 1mm for the measurement of their physical properties, all the crystals grown were divided into those bigger and others smaller than 1mm. The crystals were identified by the X-ray powder diffraction method (XRD) and observed using a scanning electron microscope (SEM).

3. Results and Discussions

3-1. Growth Using PbO-KF-PbF_2 Flux

Under the conditions of 1100°C for holding temperature, 10h for holding time, and 20°Ch^{-1} for slow cooling speed, the growth of crystals was attempted using single fluxes of PbO, KF and PbF_2 and also the flux of PbO-KF system, but no crystals were grown. Consequently, a further attempt was made using a two-component and a three-component flux containing PbF_2, and crystals were grown using flux containing more than 50mol% PbF_2, as shown in Fig. 1. Crystals were obtained when the molar ratio of PbO:KF:PbF_2 was 1:1:2, 1:10:15 or 1:14:40, with a particularly good yield (Table 1) at the ratio 1:10:15. All of these crystals were identified by XRD to be PZT. Figure 2 gives an SEM image of crystals obtained when the molar ratio of PbO:KF:PbF_2 was 1:10:15. The crystals yielded were all very small and included many which were chipped. This is presumably because most of the flux evaporated during the crystal growth, as inferred from the fact that the rate of PbF_2 vaporization was as much as about 70% as shown in Table 1.

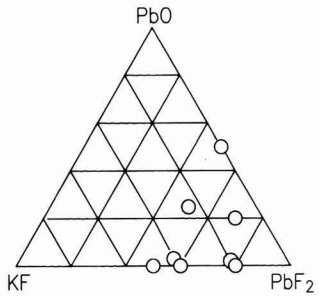

Fig. 1

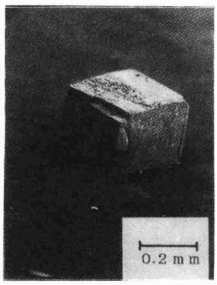

Fig. 2

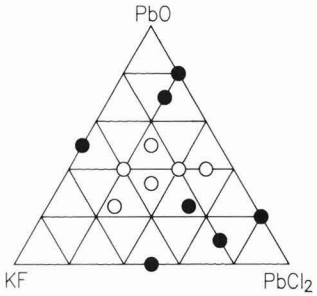

Fig. 3

Fig. 1. Composition of PbO-KF-PbF_2 flux and PZT crystal growing region.

Fig. 2. SEM photographs of PZT crystal obtained from PbO-KF-PbF_2 flux whose molar ratio was 1:10:15.

Fig. 3. Composition of PbO-KF-$PbCl_2$ flux and PZT crystal growing region. ○ and ● show larger and smaller crystal than 1mm, respectively.

Table 1. Growth of PZT crystal with PbO-KF-PbF_2 flux.

No.	Flux mol. ratio PbO:KF:$PbCl_2$	Yield (%)	Sieve analysis (%) 2.0mm~1.0mm	1.0mm pass	Flux loss (wt%)
1	1 : 2 : 1	48.7	40.1	59.9	43.2
2	2 : 1 : 1	55.4	32.3	67.7	42.5
3	2 : 2 : 1	50.2	27.8	72.2	45.1
4	4 : 1 : 5	50.4	45.8	54.2	49.2
5	2 : 1 : 2	63.7	48.3	51.7	47.8
6	1 : 1 : 1	55.1	38.6	61.4	49.7

Table 2. Growth of PZT crystal with PbO-KF-$PbCl_2$ flux.

No.	Flux mol. ratio PbO:KF:PbF_2	Yield (%)	Sieve analysis(%) 1.0mm pass	Flux loss (wt%)
1	1 : 1 : 2	44.0	100	68.7
2	1 :12 :49	50.4	100	72.7
3	1 :10 :15	55.5	100	70.5

3-2. Growth Using PbO-KF-$PbCl_2$ Flux

Figure 3 shows the relationship between components of PbO-KF-$PbCl_2$ flux and the crystal size obtained. The symbol represents fine crystals of less than 1mm in size or their collective bodies, while indicates single crystals of more than 1mm. The conditions under which the growth is attempted are the same as those given in paragraph 3-1; namely, holding temperature of 1100°C, holding time of 10h, and slow cooling speed of 20°C/h. As seen from the diagram, PZT single crystals could be obtained over a wide area of the composition. When the molar ratio of PbO:KF:$PbCl_2$ was 1:1:1, 2:1:2, and 4:1:5, the yield and ryudo? showed best levels (Table 2). In particular, the molar ratio of 2:1:2 had the best results. Consequently, an examination was made to create conditions for growth of single crystals using flux of molar ratio 2:1:2. First, if the holding temperature was dropped to 1000°C, then crystals obtained became smaller, and at 900°C no crystals were obtained. Next, when the slow cooling speed was changed to 30°C/h, crystals became smaller and the yield also decreased. Moreover, when the holding time was reduced to 5h, then crystals often became lumpy. As a result, it was considered that the conditions established at the outset were good for growth of crystals.

When crystals grown by PbO-KF-$PbCl_2$ flux were identified by XRD, they were all found to be PZT.

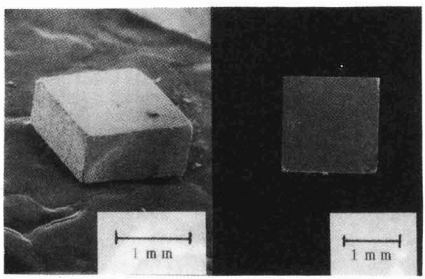

Fig. 4. SEM photographs of crystal obtained from PbO-KF-$PbCl_2$ flux whose molar ratio was 2:1:2.

Table 2 shows the yield and other results for crystals of more than 1mm in size were obtained. In view of these results, PbF_2 was substituted for $PbCl_2$ and the resulting flux evaporated approximately 20% less. In this case, crystals of 1 to 2mm in size were obtained. Figure 4 shows an SEM image of one of those crystals obtained using the flux whose molar ratio was 2:1:2. They were all plane-shaped crystals measuring 1.7 X 1.7 X 0.9mm and reddish brown. As seen from this photograph, the crystals had better surface characteristics than those obtained using PbF_2 flux (Fig. 2). These crystals were examined semi-quantitatively by EDX analysis and found to have an atomic ratio of Zr:Ti equal close to 52:48 displaying excellent piezoelectric characteristics, namely, $Pb(Zr_{0.52}Ti_{0.48})O_3$ single crystals.

4. Conclusion

An investigation was conducted on the growth of PZT single crystals from three-component fluxes of PbO-KF-PbF_2 and PbO-KF-$PbCl_2$. The results are summarized as follows:

1) Single crystals of PZT grown from the flux of PbO-KF-$PbCl_2$ were less than 1mm.
2) Three-component flux of PbO-KF-$PbCl_2$ system was effective for growing single crystals of PZT, and crystals

of over 1mm were obtained.

3) When the molar ratio of PbO:KF:$PbCl_2$ was 2:1:2, crystals were obtained which had excellent surface characteristics. Those crystals were plane-shaped (1.7 X 1.7 X 0.9mm) and consisted of $Pb(Zr_{0.52}Ti_{0.48})O_3$.

Acknowledgements

The authors would like to express their sincere appreciations to Dr. Yasu-Yuki Takatani and Mr. Tomoki Tomita of the Industrial Technology Center of Hyogo Prefecture for their valuable assistance during EDX analysis.

References:

1) S. Fushimi and T. Ikeda, J. Apply. Phys., 3, 171-172 (1964).
2) S. Fushimi and T. Ikeda, J. Phys. Soc. Jpn. 17, 1202-1203 (1962).
3) S. Fushimi and T. Ikeda, J. Am. Ceram. Soc., 50, 129-132 (1967).
4) C. Sakamoto and T. Honjo, Yogyo-Kyokai-Shi, 84, 118-124 (1976).

This article is a full translation of the article which appeared in Nippon Seramikkusu Kyokai Gakujutsu Ronbunshi (Japanese version), Vol.99, No.6, 1991.

Mechanical and Electrical Properties of Al_2O_3/SiC Nano-Composites

Akihiro Sawaguchi, Kohji Toda and Koichi Niihara*

Department of Electronic Engineering, The National Defense Academy
Hashirimizu, Yokosuka-shi, Kanagawa 239, Japan
*ISIR, Osaka University
Mihogaoka, Ibaraki-shi, 567 Japan

Mechanical and electrical properties of nano-composite ceramic materials composed of Al_2O_3 matrix and nanometer size SiC particles are described. The composites including less than 5vol% SiC particles have the same order of resistivity and dielectric constant as those of the non-SiC material, while keeping highly improved-mechanical properties. The incorporation of 5vol% SiC into Al_2O_3 matrix might be promising for materials used under harsh circumstances.

[Received November 16, 1990; Accepted February 20, 1991]

Key-words: Al_2O_3/SiC nano-composites, Electrical property, Mechanical property

1. Introduction

In recent years, the remarkable advancement of leading technology has brought about, in the field of electronics, a need for materials which show superior properties under harsh circumstances. In order to miniaturize and increase capacity of ICs or to accomplish multi-lamination of capacitors, it is necessary to improve mechanical and electrical properties of materials for substrates and packages or for capacitors. It is desirable that this need is satisfied while keeping the natural functions of the materials intact.

Al_2O_3 ceramics are anti-corrosive to matters neutral, acidic, or basic, and very strong and hard, so that they are useful as structural ceramics.[1] Moreover, they show excellent insulating and high-frequency properties. As a result, they are most frequently used as insulating ceramics indispensable for electrical machinery.[2]

In controlling the microstructure of ceramics, improving their various functions, or building new functions into them, composition is one of the most important techniques. As for Al_2O_3 ceramics, a number of studies have been reported on composition by dispersion of the second phase.[3] As one of such composition techniques, a close attention has been paid to nano-composite materials having particles and whiskers, which are far smaller than matrix, dispersed at the grain boundaries or inside the grains.[4]

The purpose of this study is to study causal relations between electrical and mechanical properties of Al_2O_3/SiC nano-composite and composite structures and to discuss its possibility as an electronic material superior in mechanical strength.

2. Experimental Method

2-1. Production of Nano-Composite

As starting powders for Al_2O_3/SiC nano-composite, γ-Al_2O_3 (average particle diameter: 0.4μm) made by Asahi Chemical Co. and β-SiC (average particle diameter: 0.3μm) of Ibiden Co. were used. Powders of Al_2O_3 and SiC were prepared at their composition ratios and mixed in a wet-type bowl mill for 12h inside ethanol. After drying, the powders underwent further dry-type mixing for 24h and all the lumps were sufficiently ground. This powder mixture was hot-pressed in nitrogen atmosphere at the sintering temperature at 1500 to 1800°C and the pressure of 28MPa to obtain nano-composite.

2-2. Evaluation of Properties

Hardness, one of mechanical properties, was measured under loads of 300 to 1000g using a Vickers test machine. Fracture toughness was evaluated by the IM method (Indentation Microfracture method). Hardness was measured by the 3-point bending method with the span of 20mm and the crosshead speed of 0.5mm/min.

In order to measure electrical properties, a disk of 10mm in diameter and 1mm in thickness was cut and metallic electrodes were vapor-deposited on both sides by sputtering. Resistivity was measured by the two-terminal method using a high-resistance meter (Yokogawa-Hewlett-Packard:4329A). Moreover, the frequency properties of impedance were measured using an impedance analyzer (Yokogawa-Hewlett-Packard: 4192A). The dielectric constant was calculated from the measurement of capacity based on the two-terminal method.

For observation of the microstructure, a transmission-type electron microscope (TEM), a high-resolution electron microscope (HREM), and the like were used.

3. Experimental Results and Discussions

3-1. Microstructures

The specimen thus prepared was observed by TEM. It was found that in the range where SiC additive was little, a majority of SiC particles of several ten nanometers in diameter were dispersed inside Al_2O_3 particles and formed nano-composite, as shown in **Fig. 1**. **Figure 2** is an HREM image of Al_2O_3/SiC nano-composite. As a result of this HREM observation, it was confirmed that no big reactive phase existed at the boundary between SiC particles dispersed inside particles and the matrix.

3-2. Mechanical Properties

Figure 3 shows the relationship between SiC addition in Al_2O_3/SiC composite and the mechanical properties. For reference purposes, results for the case in which SiC particles of 2μm in average diameter were used as a starting raw material are also included. The fracture toughness and the bending strength assumed the highest values at 5vol% for SiC. Since the bending strength increased nearly 3-fold compared to the case of 0vol% for SiC, it is apparent that the mechanical properties were greatly improved. This is presumably because compressed residual stresses generated around the minute SiC particles scattered throughout the Al_2O_3 particles strongly restrain the generation of destructive sources inside the Al_2O_3 matrix. Thus, it is clear that this composite can have its mechanical properties improved effectively even with the addition of a small amount of SiC.

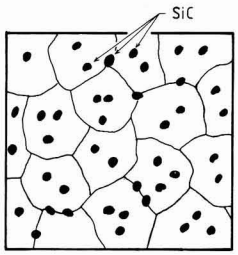

Fig. 1. Structure of Al_2O_3/SiC nano-composite.

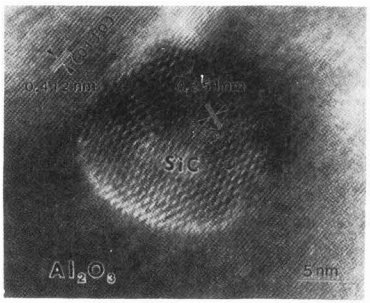

Fig. 2. HREM image of Al_2O_3/SiC nano-comitrposite.

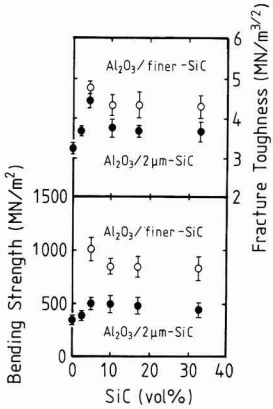

Fig. 3. Fracture toughness and strength of Al_2O_3/SiC nano-composite on the relation of SiC addition volume.

3-3. Electrical Properties

Figure 4 shows the relationship between the volume resistivity of the Al_2O_3/SiC composite and the addition of SiC. When the addition of SiC was within 10vol%, then the resistivity remained almost constant at the order of 10^{13} cm, but decreased abruptly when the addition was over 15vol%, and went below 10^6 cm when the addition exceeded 20vol%. The resistivity ratio of the single substances Al_2O_3 and SiC was greatly different by the order of 10^9. This is presumably because of the fact that while the addition of SiC was still small, SiC particles stayed within crystal grains, but the increasing addition above 15vol% brought about dispersion of SiC particles around grain boundaries, thereby causing the resistivity to fall abruptly. From the point of view of resistivity, the new composite can be treated as an insulator when the addition of SiC is below 10vol%, and as a semiconductor above 20vol%. When the addition of SiC is within 10vol%, the composite has excellent mechanical properties, so that it can be expected as an insulating material.

Figure 5 shows the temperature dependence on the resistivity of Al_2O_3/SiC nano-composite. It is seen that the resistance temperature coefficient is negative. It is clear that for a specimen in which the addition of SiC ranges from 0 to 10vol%, its gradient is relatively large and the composite insulating, while the addition is over 20vol%, the gradient

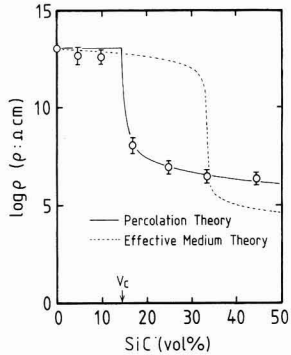

Fig. 4. Experimental relation between resistivity and SiC vol% for nano-composite.

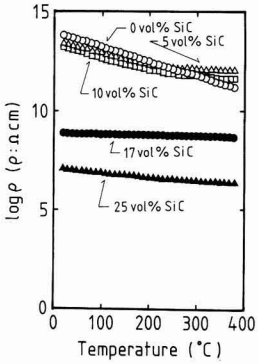

Fig. 5. Temperature dependence on resistivity of Al_2O_3/SiC nano-composite.

is small and the composite semiconductive.

Figure 6 shows the measured frequency characteristics of impedance. For a specimen whose SiC addition is 5vol%, it was capacitive with its phase almost at -90° and effective as an insulating substrate. The phase of a specimen whose SiC addition was large came close to 0°, and the specimen was purely resistive. By drawing the complex impedance plot for such a specimen, two separate arcs were verified, indicating the existence of at least two or more phases which are represented by different electrical properties.

The relationship between relative dielectric constant and the SiC addition at a frequency of 1MHz is given in **Fig. 7**. It was found that when the addition was small, the dielectric constant did not change much, as in the case of volume resistivity.

3-4. Conduction Models of Nano-Composite

An attempt was made to compare the newly obtained nano-composite with conduction models of composites in terms of elemental compositions. The models employed were the effective medium theory and the percolation theory.

(1) Effective Medium Theory

Landauer's effective medium theory presupposes a specimen which has two types of grains with conductivities

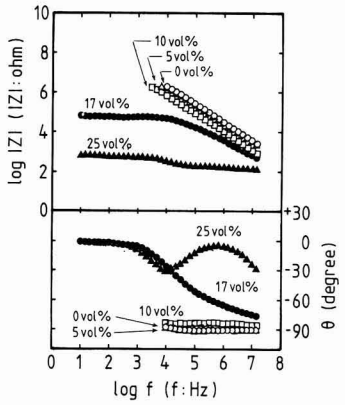

Fig. 6. Frequency characteristics of impedance for nano-composite.

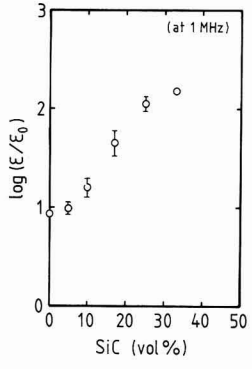

Fig. 7 Relative dielectric constant of nano-composite as a function of SiC vol%.

(inverse of resistivity) σ_1 and σ_2 dispersed randomly without any interrelationship and which is sufficiently large compared to the grain sizes.[6] Grains are assumed to be spherical. Then, with x_1 and x_2 ($=1-x_2$) representing the volume ratio of the two types of grains, the conductivity σ_m of the system as a whole can be expressed by the followins, equation:

$$\sigma_m = [(3x_1 - 1)\sigma_1 + (3x_2 - 1)\sigma_2 + [\{(3x_1 - 1)\sigma_1 + \{(3x_2 - 1)\sigma_2\}^2 + 8\sigma_1\sigma_2]^{1/2}]/4 \quad \ldots\ldots (1)$$

By substituting the conductivities of Al_2O_3 and SiC into σ_1 and σ_2 the relations between their respective volume ratiso and σ_m can be calculated. As a result, the resistivity of the composite, ρ, can be obtained as the inverse of σ_m.

In an ordinary sintered body consisting of Al_2O_3 and SiC, particles of Al_2O_3 and SiC are scattered around, as in the case of two types of particles with conductivities σ_1 and σ_2. If the conductivities of $A\lambda_2O_3$ and SiC are used as the values for σ_1 and σ_2, then the inverse of σ_m for different volume ratio can be obtained, as plotted in **Fig. 4**. The actual measurements of the inverse of the resistivity for the case where the volume ratio of SiC was 0.1% were adopted as the values for σ_1 and σ_2. As is clear from the graph, the theoretical values do not agree with the actual measurements. Since the conductivity of SiC is extremely larger than that of Al_2O_3, the resistivity of the entire system can only be determined with the conductivity and the volume ratio of SiC, as long as the volume ratio of SiC is over 34%, as easily understood from equation (1).

This model does not apply properly to structures such as nano-composites. Based on the effective medium theory, it is considered that an electric current flows uniformly through the particles of SiC and Al_2O_3 according to their resistivities. In practice, however, it is considered that in this region, a current flows more selectively through the connections of SiC particles, since they have a lower resistance.

(2) Percolation Theory

When insulating particles are mixed with conductive particles, an electric current flows selectively through the connections of the conductive particles. This implies that a current flow depends on a geometric state. The percolation theory treats such situations based on probability.[7]

Kirkpatrick has obtained the following equation for the case of simple cubic lattices by means of computer simulation:

$$\sigma(V) \propto (V - V_c)^t, \; t \sim 1.5 \quad \ldots\ldots (2)$$

where V represents the volume ratio of the conductive particles. The above equation can be rewritten in terms of resistivity as follows:

$$\rho(V) \propto (V - V_c)^t, \; t \sim 1.5 \quad \ldots\ldots (3)$$

The resistivity for the cases in which this model holds is related linearly with $\log(V-V_c)$, and the absolute value of the slope angle is t.

According to the percolation theory, if the volume ratio of SiC is over a certain critical value V_c, then equation (3) applies to the resistivity of a composite. If the results of the measurement of volume resistivity in Fig. 4 are plotted against the relation between $\log\rho$ and $\log(V-V_c)$, then nearly a straight line is obtained, as shown in **Fig. 8**, and it is found from the slope angle that t=1.52. Therefore, the model based on the percolation theory holds for this case.

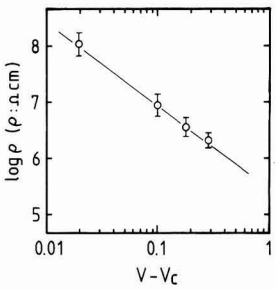

Fig. 8. log ρ vs. log (V-V_c) of Al_2O_3/SiC nano-composite ceramics.

If this straight line is expressed in terms of the relation between ρ and V, then it becomes a solid curve in Fig. 4. It is clear that the theoretical values agree very well with the actual measurements above the critical volume ratio V_c.

In the regions where from the point of view of composition, the conductivities of Al_2O_3 and SiC must be reflected on the entire system according to the effective medium theory, the conductivity of the system as a whole is controlled by SiC in practice, because the conductivity of SiC is extremely higher than that of Al_2O_3. In this experiment, the value V_c=0.15 was obtained. But this critical volume ratio was the volume ratio for the precise moment when conductive channels began to be formed throughout the entire specimen. Above this V_c, the characteristics of SiC must become predominant. These results show that while the characteristics of Al_2O_3 also affect the resistivity of the system as a whole when the volume ratio of SiC is 15%, the characteristics of SiC become dominant when the SiC volume ratio exceeds 30%. As a result, it is considered that the value V_c=15% obtained experimentally based on the percolation theory is equivalent to the volume ratio for the moment when the characteristics of SiC begin to become more or less predominant, and is also a meaningful value in reality.

In contrast, no conductive channels are formed inside a specimen below V_c, so that the percolation theory cannot fully explain the phenomenon. In this case, Al_2O_3 is considered to contribute considerably to the conductivity of the system, so the effective medium theory is more realistic. As seen from Fig. 4, however, the actual measurements of resistivity are somewhat lower than theoretically calculated values. The possible cause of this is that the very resistivity of Al_2O_3 which is a large contributor has lost some of its value as a result of the composition with SiC.

4. Conclusions

Nano-composites were produced having a structure in which nano-meter size SiC particles were dispersed in the matrix of Al_2O_3 and the relations between their mechanical and electrical properties and the volume ratio of SiC were examined. It was found that materials with the SiC addition of less than 5vol% showed little changes in resistivity or conductivity and displayed excellent mechanical properties. Therefore, such materials are considered to be promising as outstanding insulating ceramic substrates. The measurements of resistivity were examined by comparison with theoretical values based on conduction models of composites. It was found that by setting the critical volume ratio at 15% for which SiC particles dispersed around the boundaries of Al_2O_3 particles began to form conductive channels throughout the specimen, the percolation theory stood up where this critical volume ratio was surpassed. Because it is simple and inexpensive, the production process for such particle-dispersed nano-composites is considered to be an effective technique in the future development of materials.

References:

1) G. Grosch and G.J. Brockmann, Powd. Met. Int., 13, 146-151 (1981).
2) P.N. Venkatachalam, Am. Ceram. Soc. Bull., 63, 577-579 (1984).
3) R.P. Wahi and B. Ilschner, J. Mater. Sci., 15, 875-885 (1980).
4) K. Niihara, A. Nakahira, T. Hirano, K. Ojima, K. Izaki and M. Kawakami, Proc. MRS Meeting on Advanced Materials, Tokyo (1988).
5) K. Niihara, R. Morena and D.P.H. Hasselmann, J. Mater. Sci. Lett., 1, 13-16 (1982).
6) R. Landauer, J. Appl. Phys., 23, 779-784 (1952).
7) S. Kirkpatrick, Rev. Mod. Phys., 45, 574-588 (1973).

This article is a full translation of the article which appeared in Nippon Seramikkusu Kyokai Gakujutsu Ronbunshi (Japanese version), Vol.99, No.6, 1991.

Preparation of $BaTiO_3$ Films by CVD

Hidenobu Nakazawa*, Hisanori Yamane and Toshio Hirai

Institute for Materials Research, Tohoku University
2-1-1 Katahira, Aoba-ku, Sendai-shi, 980 Japan
*Kawasaki Technical Research Laboratory. Asahi Chemical Industry Co., Ltd.
1-3-1 Yakou, Kawasaki-ku, Kawasaki-shi, 210 Japan

Thin films of $BaTiO_3$ were prepared by CVD using barium β-diketonate chelate {$Ba(C_{11}H_{19}O_2)_2$} and titanium tetraisopropoxide {$Ti[OCH(CH_3)_2]_4$} as precursors. $BaTiO_3$ films deposited from 700° to 1000°C on MgO(100) substrates showed prominent a-axis orientation. X-ray pole figure measurement by Schulz's reflected method indicated that the CVD-$BaTiO_3$ films deposited from 900° to 1000°C grew epitaxially on MgO(100) substrates. SEM observation showed that rectangular grains aligned two dimensionally in the plane of the films deposited at 1000°C.
[Received December 16, 1990; Accepted February 20, 1991]

Key-words: Thin film, CVD, $BaTiO_3$, β-diketonate chelate, epitaxial growth, a-axis orientation

1. Introduction

Barium titanate ($BaTiO_3$) of tetragonal perovskite structure is known as a ferroelectric having a polarization axis in the direction of c-axis and a high dielectric constant in the direction of a-axis, and has been studied extensively for its sinters, single crystals and thin films.[1,2]

Recently, a number of researchers are trying to prepare the thin films by various methods, including physical vapor deposition (PVD) (such as deposition,[3-7] sputtering,[8-12] and laser ablation[13,14]) to meet the increasing demand for more compact, integrated elements.

Chemical vapor deposition (CVD) is also extensively being applied to the production of thin films, together with PVD, for semiconductor devices. However, few researchers have discussed CVD as a method for preparing thin films of barium titanate, mainly due to the lack of proper barium sources for CVD. More recently, however, Yamane et al discussed β-diketone chelate as a barium source for the preparation of oxide-base superconducting thin films (Y-Ba-Cu-O films) by CVD.[15]

In this study, the authors attempted to prepare a Ba-Ti-O film on a MgO(100) substrate by the CVD method, using β-diketone chelate as the barium metal source and titanium alkoxide as the titanium metal source, to investigate the crystal orientation and surface morphology of the deposits prepared at varying temperatures.

2. Experimental Procedure

Figure 1 illustrates the hot-wall type CVD apparatus used in this study, where a quartz tube (inner diameter: 20mm) was placed horizontally, and the feed evaporation and substrate-holding sections were heated separately by electrical heaters. The β-diketone chelate as the barium source was $Ba(thd)_2${bis(2,2,6,6-tetramethy3.5-heptanedionato)barium(II)}, supplied by Tosoh-Akzo. Roughly 60mg of $Ba(thd)_2$, placed in a quartz glass boat, was heated to 250°C[15] and carried to the substrate by an Ar gas flowing at 50ml/min. Titanium tetraisopropoxide {TTIP: $Ti(OCH(CH_3)_2)_4$, supplied by Wako Junyaku} was carried from the evaporator by an Ar gas flowing at 100ml/min. The TTIP evaporator was kept at 25°C.[16] Oxygen was used as the oxidation gas, admitted into the reactor tube at 250ml/min. The other reaction conditions were a total gas pressure of 6mmHg and a reaction time of 1h. The substrate was of single crystalline, mirror-polished MgO(100), 10×10×0.3mm in size, kept at 600° to 1000°C.

The films prepared were analyzed by various methods: X-ray diffraction analysis (XRD) with CuKα ray to investigate the crystalline phases and orientation; the Schulz's reflection method with CoKα ray to draw the pole figures (in an attempt to clarify the relationship between the crystalline phase and orientation for the films deposited at 900° and 1000°C); analysis by a scanning electron microscope (SEM) to observe the film surface structures; and electron probe microanalysis (EPMA) with a $BaTiO_3$ sinter as the standard to determine the film compositions.

3. Results and Discussion

The thin film prepared was white and semitransparent, approximately 1μm in thickness. **Figure 2** presents the X-ray diffraction analysis results of the thin films deposited at 600° to 1000°C on the MgO substrates. The cubic or tetragonal $BaTiO_3$ (100) or (101) was detected in the film deposited at 600°C, though only to a small extent (Fig.2(a)). The (*h*00) or (00*l*) peak was detected in the film deposited

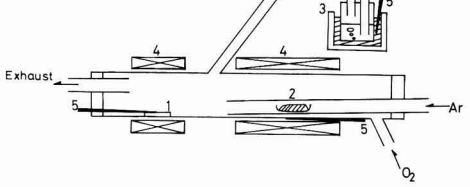

Fig. 1. Schematic diagram of the hot wall type CVD apparatus for the synthesis of $BaTiO_3$ films.
(1) MgO substrate, (2) $Ba(thd)_2$ boat, (3) $Ti[OCH(CH_3)_2]_4$ bubbler in a water bath, (4) resistance furnace, (5) thermocouple

at 650°C (Fig.2(b)). For the films deposited at 700°C and higher (Fig.2(c), (d) and (e)) intensity of the (h00) or (00ℓ) peak increased, and intensity of the (101) or (212) was 5 or less relative to that of the (200) or (002) peak.

Next, the XRD peaks of these orientated films, observed at 2θ=99 to 102°, were investigated, to find that each peak was positioned at 101.0° with a tail to the lower-angle side. The peak position was closer to that of the tetragonal (400) peak at 2θ=100.96° (JCPDS5-0626) rather than to that of the cubic $BaTiO_3$ (004) peak at 99.69° (JCPDS31-174).[17,18]

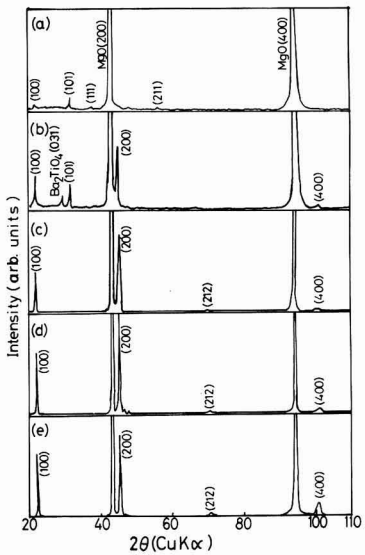

Fig. 2. XRD patterns of $BaTiO_3$ films deposited on MgO(100) substrates at various deposition temperatures. (a): deposited at 600°C, (b): deposited at 650°C, (C): deposited at 700°C, (d): deposited at 900°C (e): deposited at 1000°C

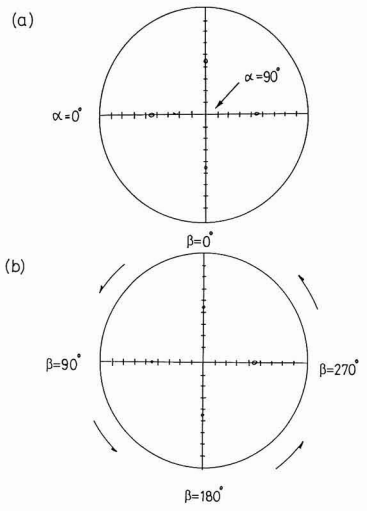

Fig. 3. X-ray pole figures taken about the (101) peak for the $BaTiO_3$ film deposited at 1000°C (a) and taken about the (220) peak for the MgO(100) substrate (b)

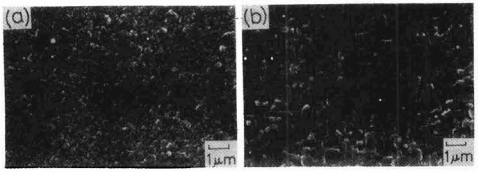

Fig. 4. SEM photographs of the $BaTiO_3$ films deposited at 900°C (a) and at 1000°C (b)

And the tail at lower angle side of the peak was attributed to tetragonal (004) (2θ=99.45°). Thus the $BaTiO_3$ films prepared in this study are considered to be of the tetragonal phase whose a-axis is oriented to the direction perpendicular to the substrate, because the (400)/(004) peak intensity ratio will be 2:1 when the tetragonal $BaTiO_3$ phase is not oriented.[18] Peaks of the Ba_2TiO_4 and unidentified phases were detected at 2θ=46 to 48° in all of the thin films prepared, though very slightly; relative intensities of these peaks were 5 or less.

The EPMA results indicated that thin films had excess quantities of titanium (Ba/Ti≤0.5) than the stoichiometric $BaTiO_3$ composition.

The half-width of the rocking curve of the (200) plane was measured to assess the crystal orientation. It was around 0.9° for the films deposited at 700° to 1000°C, sufficiently small in comparison to that of the rocking curve of the substrate (0.5°), indicating that its crystallinity was high.

Figures 3(a) and **(b)** present the pole figures of the (101) and (220) reflections at 2θ=36.9 and 73.8° for the $BaTiO_3$ film deposited at 1000°C and MgO substrate, respectively.

The $BaTiO_3$ (101) diffraction poles were detected at a inclination angle (α) of 45°, and at rotation angles (β) of 0, 90, 180 and 270° around the normal line to the substrate. These were in agreement with the angles of the MgO substrate (220), from which it was judged that the $BaTiO_3$ film was grown epitaxially with the substrate. Similar results were observed with the film deposited at 900°C. This film, however, had wider peaks, and hence slightly more irregular crystalline configuration in the substrate plane than the one deposited at 1000°C.

Figures 4(a) and **(b)** present the SEM photographs of the thin films deposited at 900° and 1000°C, respectively. Grains of around 500nm were found on the surface of the film deposited at 900°C. The film deposited at 1000°C, on the other hand, had a dense surface, with rectangular grains of 1μm extending two-dimensionally. Growth of the rectangular grains was considered to correspond to their epitaxial relation with the substrate. Single-crystalline LiF[3,13] and $SrTiO_3$[5,7] were known as substrates on which a $BaTiO_3$ film was grown epitaxially. An oriented $BaTiO_3$ film was deposited on a MgO(100) substrate by sputtering,[12] but the report did not mention whether or not the film was grown epitaxially.

It is thus clarified that a $BaTiO_3$ film was grown epitaxially also on a MgO (100) substrate, though misfit of the lattice constant of the tetragonal $BaTiO_3$ (100) system with that of MgO (100), which ranges from 4.1 to 5.0%, is larger than those with LiF (100) and $SrTiO_3$ (100) substrates, ranging from 0.3 to 0.6% and from 2.2 to 3.3%, respectively.

4. Conclusions

The thin $BaTiO_3$ films oriented to the a-axis were prepared at 700° to 1000°C by the thermal CVD method, using a β-diketone chelate as the barium source and titanium alkoxide as the titanium source. $BaTiO_3$ is highly ferroelectric, having a dielectric constant of 2000 or more in the direction of the a-axis,[2] and its film is expected to be used for large-capacity capacitors.

The $BaTiO_3$ grains were grown in the films deposited at 900° and 1000°C epitaxially with the MgO (100) substrates, as revealed by the pole figures drawn by Shulz's reflection method. The film deposited at 1000°C consisted of rectangular grains extending two-dimensionally on the film surface.

Acknowledgements
The authors thank Dr. J. Tanaka of Tohoku University's Faculty of Engineering for his valuable suggestions in drawing the pole figures. Part of this study was financially supported by subsidies granted by the Ministry of Education (A-02855172 and B-02555146).

References:

1) M.E. Lines and A.M. Glass, "Principle and Applications of Ferroelectrics and Related Materials," Clarendon Press, Oxford (1977) 241-245
2) S.E. Wemple, M. Didomenico, Jr. and I. Camlibel, J. Phys. Chem. Solids, 29, 1797-1803 (1968)
3) E. Muller, B.J. Nicholson, and G.L'E. Turner, J. Electrochem. Soc., 110, 969-973 (1963)
4) J.R. Slack and J.C. Burfoot, Thin Solid Films, 6, 233-237 (1970)
5) M.A. Sevost'yanov and Y.Y. Tomashpol'skii, Sov. Phys. Crystallogr., 24, 115-117(1979)
6) Y. Iijima, Jpn. J. Appl. Phys., 24, 403-404 (1985)
7) Y. Iijima, T. Terashima, K. Yamamoto, K. Hirata and Y. Bando, Appl. Phys. Lett., 56, 527-529 (1990)
8) M. Wohlecke, V. Marrello and A. Onton, J. Appl. Phys., 48, 1748-1750 (1977)
9) T. Nagano, T. Kosaka, S. Omori and O. Omoto, Ferroelectrics, 37, 681-684 (1981)
10) J.C. Olson, D.F. Stevison and I. Bransky, Ferroelectrics, 37, 685-687 (1981)
11) V.S. Dharmadhikari and W.W. Grannemann, J. Vac. Sci. Techonl., A1, 483-485 (1983)
12) K. Fujimoto, Y. Kobayasi and K. Kubota, Thin Solid Films, 169, 249-256 (1989)
13) G.M. Davis and M.C. Gower, Appl. Phys. Lett., 55, 112-114 (1989)
14) R. Nawathey, R.D. Vispute, S.M. Chaudhari, S.M. Kanetkar and S.B. Ogale, Solid State Commun., 71, 9-12 (1989)
15) H. Yamane, H. Kurosawa and T. Hirai, J. de Physique., C5, 131-140 (1981)
16) K.J. Sladek and W. Wayne Gibert, Proc. 3rd Int. Conf. on Chemical Vapor Deposition (1972) 215-231
17) JCPDS file, No.31-174
18) JCPDS file, No.5-0626

This article is a full translation of the article which appeared in Nippon Seramikkusu Kyokai Gakujutsu Ronbunshi (Japanese version), Vol.99, No.6, 1991.

Preparation of Heat Resistant Microporous Ceramic Membranes for Selective Gas Permeation

Maorong Chai, Koshi Sekizawa, Masato Machida, Koichi Eguchi and Hiromichi Arai

Department of Materials Science and Technology, Graduate School of Engineering Sciences, Kyushu University
6-1 Kasugakoen, Kasuga-shi, 816 Japan

Microporous membranes of hexaaluminates (Ba- and La-Al_2O_3) showed heat resistance much higher than that of the conventional Al_2O_3 membrane. Although the Al_2O_3 membrane cracked by heat treatment above 1000°C due to γ-α transformation, Ba- and La-Al_2O_3 membranes retained a crack-free microstructure and exhibited excellent selective gas permeation after calcination up to 1000°C.

[Received April 1, 1991; Accepted May 23, 1991]

Key-words: Hexaaluminate, Membrane, Sol-gel, Heat resistance, Selective gas permeation

1. Introduction

Microporous ceramic membranes have been extensively investigated for the separation of gaseous mixtures because of many advantages in their thermal and chemical stabilities.[1,2] One of the most important applications of gas-separative ceramic membranes is for high-temperature catalytic reactions. Actually, however, most conventional membrane materials, i.e., Al_2O_3, SiO_2 and SiO_2-Al_2O_3, are easily thermally damaged because of crack formation or pore growth above 1000°C. For the improvement of membrane heat resistance, the investigation should be directed to the development of a new membrane material, which has hardly been examined so far. In previous studies,[3,4] we developed fine particles of hexaaluminate with excellent heat resistance. This material can retain the particle size by an order of magnitude smaller than pure alumina after calcinating above 1100°C, and is expected to be suitable for heat-resistant ceramic membranes. In this study, the preparation and thermal stability of hexaaluminate membranes were examined by the modified sol-gel method. The thermal stability of the membrane was evaluated by measuring microstructure and gas permeability after sintering at different temperatures ranging from 500 to 1300°C.

2. Experimental Procedure

Microporous membranes with a composition of hexaaluminate ($BaAl_{12}O_{19}$ and $LaAl_{11}O_{18}$) were prepared by repeated dip-coating (20 times) of a coarse porous substrate (Al_2O_3 76%, SiO_2 23%, Nippon Kagaku Togyo Co. Ltd., 16×16mm, thickness 2mm, pore size 500nm, porosity c.a. 45%.) with alkoxide-derived sol prepared by the following procedure. Aluminum isopropoxide, $Al(OC_3H_7)_3$, was introduced into an excess hot water (80°C, 100mol/mol-alkoxide) under vigorous stirring. The clear sol was obtained by the addition of HCl (0.1mol/mol-alkoxide) to the alkoxide-water slurry. Finally, a corresponding amount of $Ba(NO_3)_2$ or $La(NO_3)_3$ was added to the sol. Prior to the dipcoating process, the sol was diluted six times with water to reduce viscosity. These membranes were dried at room temperature in air and calcined at 500°C for 5h after a single dip-coating process. After heat treatment at 1000-1300°C, microstructures and gas permeability of the La-Al_2O_3 and Ba-Al_2O_3 membranes thus prepared were compared with those of the pure alumina membrane, which was prepared from boehmite sol as described by Leenaas et al.[5] The dip-coating of the alumina membrane was repeated 10 times. The gas permeation measurement was performed at room temperature as was described by Burggraaf et al.[6]

3. Result and Discussion

Microstructure of Al_2O_3, La-Al_2O_3 and Ba-Al_2O_3 membranes was observed with a scanning electron microscope (JEOL JSM-330T) after heating at 500, 1000 and 1300°C in air (**Fig.1**). We confirmed that the microstructural change of the porous alumina support was scarcely observed in this temperature range. The surface of the three types of membranes as deposited are smooth and flat, i.e., neither cleavages nor cracks were observed. From the cross-sectional view of the membranes, the thickness of the membranes is about 3-5μm. The heat treatment above 1000°C changed the microstructures of membranes in a different way. Significant shrinkage and grain growth of Al_2O_3 resulted in crack formation in the membrane calcined above 1000°C. In contrast, the La-Al_2O_3 and Ba-Al_2O_3 membranes could maintain the initial microstructures up to 1000°C. Heating at 1300°C led to crystallization of the hexaaluminate, which was indicated by the formation of place-like particles.

An effect of heat treatment temperatures on the H_2 permeability of three types of membranes is shown in **Fig.2.** The permeability of pure Al_2O_3 membrane steeply increased with a rise in heating temperature. On the other hand, the permeability of Ba- and La-Al_2O_3 membranes increased gradually up to 1000°C but rose drastically above 1000°C due to the crystallization of hexaaluminate. From the pure gas (H_2 and N_2) permeation measurement, the permeability ratio of H_2 to N_2 is plotted as a function of heat treatment temperatures (**Fig.3**). For the Al_2O_3 membranes prepared, the gas permeabilities are proportional to the reciprocal square root of the molecular weight of examined gas (H_2, He, N_2, CO_2), indicating that Knudsen flow should dominate

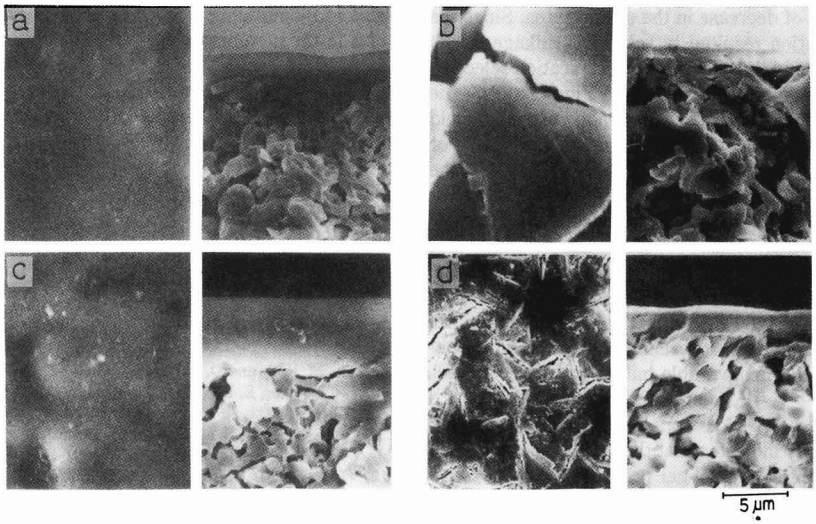

Fig. 1. SEM micrographs of surface and cross-sectional views of microporous membranes after heating at respective temperatures a) Al_2O_3, 500°C, b) Al_2O_3, 1000°C, c) Ba-Al_2O_3, 1000°C and d) Ba-Al_2O_3, 1300°C

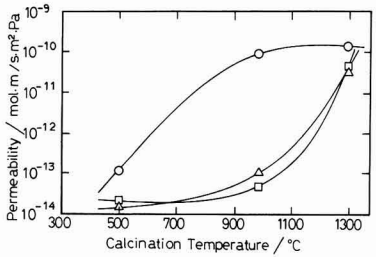

Fig. 2. Hydrogen permeability of microporous membranes after heat treatment
△ Ba-Al_2O_3, □ La-Al_2O_3, ○ Al_2O_3

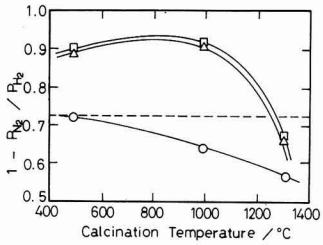

Fig. 3. Permeability ratio of H_2 to N_2 as a function of heat treatment temperature of membranes. The broken line shows a theoretical value of the Knudsen diffusion mechanism.
△ Ba-Al_2O_3, □ La-Al_2O_3, ○ Al_2O_3

gas permeation through the membranes. The gas permeation of the Al_2O_3 membrane deviated from Knudsen flow after heat treatment above 1000°C because of the crack formation. For the hexaaluminate membranes, however, the observed gas selectivities were much higher than expected from Knudsen flow after calcination at 500-1000°C (Fig.3). This is probably due to the existence of smaller pores than in the pure alumina membranes. These small pores possibly led to the contribution of an other permeation mechanism. It is noted that the Ba- and La-Al_2O_3 membranes retained the selective permeation, which is expected from Knudsen mechanism, after crystallization of hexaaluminate at 1300°C. These outstanding properties appear to result from the excellent heat resistance of hexaaluminate fine particles against crystal growth and sintering.

It is well known that the γ-α phase transformation of Al_2O_3 significantly accelerates grain growth with two orders of decrease in the surface area. Since the transformation resulted in volume shrinkage, crack formation, and thus a decrease in permeation selectivity of the membrane (as shown in Figs.1 and 3), the operation temperature of alumina membrane should be limited to well below 1000°C. Some alkaline earth or rare earth oxides were reported to suppress the phase transformation and sinterability of Al_2O_3 at 1000-1200°C.[7-10] Moreover, Matsuda et al. and the authors have previously reported that the addition of these oxides produces the hexaaluminate phase, which can retain a surface area 10 times larger than Al_2O_3 above 1200°C.[11,3,4] The present study revealed that such a heat resistant material is quite suitable for a thermally stable microporous membrane.

4. Conclusion

This study shows that hexaaluminate membranes prepared by the sol-gel process possess a much higher heat resistance than conventional alumina membranes, which indicates that selective gas permeation could be applicable to high-temperature processes. The formation of hexaaluminate is effective not only in inhibiting crack formation, but also in maintaining the fine grain size of primary particles in the membranes.

References:

1) L.C. Klein and N. Giszpenc, Ceramic Bull., 69, 1821-1825(1990)
2) A. Larbot, J.P. Fabre, C. Gurzard and L. Cot, J. Am. Ceram. Soc., 72, 257-261(1989)
3) M. Machida, K. Eguchi and H. Arai, J. Catal. 103, 385-393(1987)
4) M. Machida, K. Eguchi and H. Arai, Bull. Chem. Soc. Jpn., 61, 3659-3665(1988)
5) A.F. M.Leenaars, K. keizer and A. Burggraaf, J. Mater. Sci. 19, 1077-1088(1984)
6) Y. Lin and A. Burggraaf, J. Am. Ceram. Soc., 74, 219-224(1991)
7) R.M. Revy and D.J. Bauer, J. Catal., 9, 76-86 (1967)
8) H. Schaper, E.B.M. Doesburg, and L.L. Van Reijan, Appl. Catal., 7, 211-220(1983)
9) H. Schaper, E.B.M. Doesburg, P.H.M. Dekorte and L.L. Van Reijan, Solid State Ionics, 16, 261-265(1985)
10) I. Amato, D. Martorama, and B. Sliengo, Sintering and Catalysis, ed by G.C. Kuczubski, Plenum Press, New York and London(1975) 187-197.
11) S. Matsuda, A. Kato, M. Mizumoto and H. Yamashita, Proc. 8th Int. Cong. on Catal., Berlin(1984), Vol. 4, 879-889

This article appeared in English in Nippon Seramikkusu Kyokai Gakujutsu Ronbunshi (Japanese version), Vol.99, No.6, 1991.

Information & Communications

News

10-Fold Production Speed Increase of Ceramic Thin Films

The Basic Technology Research Promotion Center has developed, jointly with RIMS is (comprised of 17 private enterprises including Ishikawajima-Harima Industries) an apparatus capable of producing thin ceramic films 10 times faster than the conventional one. It has a function to perform coating, and produces ceramic material by reacting a metal as the starting material, evaporated with an electron gun, with ionized gas (plasma) of nitrogen, oxygen or carbon. The ceramic plasma is deposited over an object under a given voltage. It has been demonstrated that a stainless surface is coated with a thin titanium nitride film at 1.7μm/sec, a speed which is 9 to 10 times faster than that obtained by conventional apparatus. The apparatus will be applicable to coating automobile and machine parts to make them wear-resistant.

Non-Linear Optical Materials

Asahi Glass has developed, jointly with Nagoya University's Faculty of Engineering, a material dispersed with superfine semiconductor particles which has a 3-dimensional non-linear optic effect (rate at which refractive index is changed when the material is irradiated with light) 100 times higher than the conventional one. Cuprous bromide is used as the semiconductor material, the superfine (100Å) particles of which are dispersed in glass. The device operates with laser beams of 410nm wavelength. The 3-dimensional non-linear optic effect allows high-speed optical logic elements such as those provided with switching or memory functions to operate only with light. Realizing a high 3-dimensional non-linear optic effect level, in particular that produced by a practical wavelength, is the key to developing optical computers.

Apatite Sheet

The Fukuoka Prefectural Industrial Technology Center has developed, jointly with the Government Industrial Research Institute, Kyushu, a method to make sheets from fibers coated with apatite, and jointly applied for patent. The process is based on the wet synthesis of apatite in which a phosphoric acid solution is added drop by drop to a calcium ion solution, and the fibers of various materials, such as pulp, bamboo, straw and so on, are added to the reaction solution to deposit and crystallize apatite over the fiber surfaces. The coated fibers thus prepared are then made into sheets by the standard method. No additive (such as polymer fixing agent) is used. Quality of apatite to be deposited over the fiber surfaces can be freely controlled up to 0.8mg/g of fiber by adjusting concentrations of calcium ions and phosphoric acid. Controllable range can be further widened by adjusting pH of the reaction solution and operating temperature. The researchers are now looking for applicable areas.

Gyrotron-Aided Ceramic Producing Apparatus

Tomen, Fuji Denpa Kogyo and Continental Electronics (US) have jointly developed and plan to sell the world's first apparatus to produce fine ceramics in which works are heated by high-power microwaves. The apparatus employs a gyrotron (used for the research of nuclear fusion), and is expected to find use in the development of high-temperature superconducting materials and ceramic-ceramic joining. The gyrotron, supplied by Barian, heats the works uniformly by high-power microwaves of 28GHz to produce ceramic parts of high accuracy. Barian and Continental Electronics have already supplied the new apparatus to research organizations in the USA. The three companies are jointly producing apparatus for commercial purposes with gyrotrons supplied by Barian. The price will be 100 to 150 million yen. They also plan to commission tests and research for the development of new ceramic materials, and are expecting annual sales of at least 200 million yen.

Ceramic Die

The Agency of Industrial Science and Technology's Mechanical Engineering Laboratory has produced a prototype ceramic die for constant-temperature forging, a technique to produce highly heat-resistant alloys for aircraft parts, in which an object is forged in a die at around 1000°C. The conventional die for this process is of molybdenum alloy, which, however, cannot be used under any condition except vacuum. This tends to make the forging system very large. The ceramic die, on the other hand, allows the system to operate at atmospheric pressure, which is a great advantage. It is approximately 25cm in diameter, and of electrically conducting Sialon to allow electrical discharge machining. The circular die consists of fan-shaped sections, each being fit in a base of nickel alloy. The strains and stress distributions of the die and the object being forged are analyzed by a supercomputer using the finite element method to prevent heat-induced cracking. The research group expects that when fully developed, it will replace dies of molybdenum alloy.

Rod of Single-Crystalline Synthetic Diamond

Sumitomo Electric has developed a method which produces a rod of single-crystalline synthetic diamond in a short time at a high yield. The crystals are machined to incise slightly in the crystal direction, and stainless wedges are driven into the breaks to dress the crystals. The conventional method in which the crystals are ground by a disc-shaped blade of phosphor bronze into a rod takes approximately 70h. The newly developed method produces the rod in 10min or so, at twice or more the yield, thus greatly reducing the cost. The diamond rod is characterized by uniformity both in size and crystalline direction. It is suitable for grindstones dressers because of its constant dressing resistance for stable grinding. The price varies from 1,600 to 8,000 yen, depending on size. The company has already started selling the diamond rods, and is expecting to attain initial sales of 100 million yen.

Resistivity of Sintered $YBa_2Cu_3O_{7-x}$

Takahashi and Suga of the University of Tokyo have reported that three steps of resistivity transition were observed in sintered $YBa_2Cu_3O_{7-x}$ under large current densities of j= to 100A/cm^2 as the temperature was lowered, as follows. (1) A sharp drop appeared at T=93K, corresponding to superconducting transition of the material; (2) a broad shoulder appeared at T=92K to 82K, with the gradual decrease in resistivity likely due to the weak intergranular compling at grain boundaries; (3) the resistivity became almost constant and a finite value was detected over 77K, which suggests that extremely weak grain boundaries are present in sintered specimens.

The experiments to measure current dependence of resistivity in sintered YBCO were carried out in zero external field, particularly in the region of 100A/cm^2. The J_c of sintered YBCO was substantially lower than that of single crystal or thin film, the former of which has not exceeded 500A/cm^2 thus far. At present the researchers predict that the J_c value at T=0K of the specimen might not reach 200A/cm^2 because residual resistance becomes finite (but constant) after general boundaries transit to the superconducting state.

$YBa_2Cu_3O_{7-x}$ Junction

Takahashi and Suga also reported a low

resistivity junction method for $YBa_2Cu_3O_{7-x}$ and indium metal.

The junction of high T_c superconductors with metal is an important superconductor application technology for the manufacture of devices. When an external current flows through a junction to a superconductor, Joule loss of $q=\rho ij^2$ is generated (ρi=boundary resistivity) to destroy superconductivity of the area near the junction. Junction resistance must as a result be under $pi=10^{-5}\Omega.cm^2$ for practical use.

On the other hand, the $YBa_2Cu3O7-x$ (YBCO) superconductor permits a wide range of oxygen defects from x=0 to x=0.9 (characteristics of superconductivity largely depend on oxygen quantity). Therefore it is important to join YBCO with metal at room temperature to prevent changes in characteristic because absorption or a decrease in oxygen is caused when the joining process generates heat.

Takahashi and Suga tried to prepare junctions by the evaporation method, that is, they deposited metallic thin film on YBCO with vacuum evaporation which was then joined by solderless contact. This method is applicable for a wide area range (from very small to large). Contact characteristics are shown in Table 1.

Table 1. Contact chracteristics

Sample	Evaporation condition (torr)	Contact area (cm^2)	Contact resistance 77K ($\mu\Omega$)	Contact resistivity 77K ($\mu\Omega$)
#1	Silver (4.0×10^{-6})	0.0550	76.1	4.18
#2	Silver (1.8×10^{-6})	0.0594	32.2	1.91
#3	Gold (2.4×10^{-6})	0.0728	70.6	5.14
#4	Gold (2.8×10^{-6})	0.1008	74.7	7.53
#5	Copper(4.0×10^{-6})	0.0416	95.0	3.95
#6	Copper(2.4×10^{-6})	0.0864	42.2	3.65
#7	Indium(2.0×10^{-6})	0.0899	1.30×10^{4}	1.16×10^{3}

New Classification System

Wada et al. of the Superconductivity Research Laboratory have proposed a new classification system for copper-based superconductor consisting of 3 categories or "blocks." According to the new classification, the main block is perovskite ($ACUO_{3-8}$), followed by a rock salt block (AO) and fluolite block (AO_2). The pervoskite block contains four types, full pervoskite structure ($ACUO_3$) and three types of oxygen defficient pevroskite blocks; the series of superconducting compounds such as $La_2Ca_{n-1}CunO_{2n+2}$ and $MmA_2Ca_{n-1}Cun$-$Cu_3O_{2n+4-1}Z$ (R: rare earth element, A=Sr or Ba) consist of pervoskite blocks, rock salt blocks and fluorite blocks. The electroneutrality conditions in the crystal were taken into account.

The characteristic charge for each structural block was calculated using an ionic model. In La_2CuO_4, the perovskite block $[La^{3+}Cu^{2+}(O^{2-})_3]$ has a negative charge and the rock salt block $[La^{3+}O^{2-}]$ a positive charge. The negative perovskite block is considered to be a hole acceptor. On the other hand, in Nd_2CuO_4, the oxygen deficient perovskite block $[Nd^{3+}Cu^{2+}(O^{2-})_2]$ is positively charged and the fluorite block $[Nd^{3+}(O^{2-})_2]$ is negatively charged. Consequently, the perovskite block readily accepts an electron. The rock salt block usually has a positive charge and works as a hole donor for the CuO_2 planes in the perovskite block. The fluorite block has usually a negative charge and so works as a hole acceptor. A variety of new layered copper oxides which may turn into new high-T_c superconductors can be designed by employing the basic principles of the present block model and taking into account the lattice constant matching and the electroneutrality condition between the blocks. Thus the block model provides a guiding principle for the preparation of new layered copoper compounds.

$Y_{1-x}CaxBa_2Cu_4O_8$ ($0 \le x \le 0.1$) Films

Manabe and his colleagues at the National Chemical Laboratory for Industry have prepared $Y_{1-x}CaxBa_2Cu_4O_8$ superconductor film by the dipping-pyrolysis process. According to the Journal of the Ceramic Society of Japan (international edition, vol.99/no.5), films of the 1-2-4 phase with $T_{c,zero}$=70K and 55K were prepared by direct heat-treatment of (Y_2O_3-$BaCO_3$-CuO) precursor films (Y: Ba: Cu=1:2:4 in molar ratio) in O_2 at 780°C for 24-72h followed by slow-cooling and quenching, respectively. Both films showed metallic behavior above the transition temperatures, indicating the formation of the 1-2-4 phase. On the other hand, once a mixture of $YBa_2Cu_3O_7$(1-2-3) and CuO was formed by the heat-treatment at 820°C, $p(O_2)=10^{-3}$ atm or at 700°C, $p(O_2)=10^{-2}$–10^{-4} atm, conversion into the 1-2-4 phase was very difficult after the subsequent heat treatment within the stability region (780°C, $p(O_2)$=1 atom) of the 1-2-4 phase. The $Y_{1-x}Ca_x$-$Ba_2Cu_4O_8$ (x=0.05 and 0.1) films exhibited higher $T_{c,onset}$ values, however, the film of lx=0.1 was found to contain only a small fraction of the 1-2-4 phase. Moreover, when the Ca-content precursor films were fired in an atmosphere with $p(O_2)$ of 10^{-3}–10^{-4} atm at 700°C, the product films gave an XRD pattern of (1-2-3) + (1-2-4) mixture.

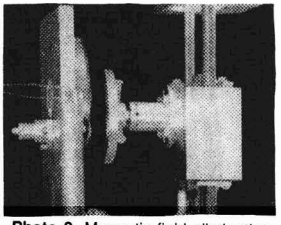

Photo 2 Magnetic field elimination equipment

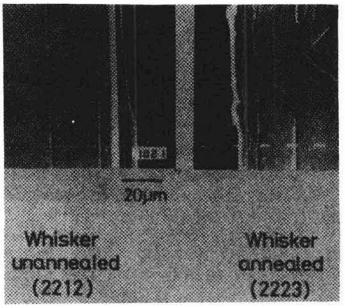

Photo 1. Microgram of Bi system ceramic cyristal

Large Bi System Superconductor Single Crystal

The Government Industrial Research Institute(GIRI), Osaka, and Assoc. Prof. T. Kawai of Osaka University have jointly developed a large single crystal Bi system superconductor. This single crystal was originally prepared as a 90K superconductor and was converted to 110K through a CAP process developed by GIRI. Its size is 3mm wide, 3mm long and several micrometers thick. The low temperature phase crystal is composed of Bi, Sr, Ca, and Cu at 2:2:1.2, and the high temperature Tc crystal is 2:2:2:3.

Complete Elimination of Magnetic Field by Superconductor

The Research Development Corporation of Japan(RDCJ) has developed magnetic field elimination technology by completely eliminating "trap" magnetic field. Trap magnetic field is the largest cause of decreased reliability in superconductors and magnetic shield materials. The process sweeps away residual magnetic field on superconductors by means of a scanning laser beam, achieving an ideal phase in which the internal magnetic field is zero. This prevents malfunctions in high speed Josephson elements and will lead to the development of high performance magnetic field shielding device.

The Magnetic Flux Quantum Information Project team headed by Prof. E. Goto applied a 488nm Ar ion laser, which can flux focus on an area of 0.1mm in diameter to scan the surface of superconductors. During this process, the superconductor at the heated point converts to ordinary conductive material, and trap magnetic field gathers at these points. If the ordinary conductive points are moved slowly to the external area of the superconductor, no trap field remains at the center of the superconductor.

An experiment employing Nb, which converts to a superconductor at liquid helium temperature, has shown that the method facilitates complete elimination of trap fields. The team expects that this method will be

applicable to any superconductive material because all convert to ordinary conductive material when heated.

Mixer Employing High Temperature Superconductor

Few studies have been reported on applications of high temperature superconductors to electromagnetic wave sensors, compared with the vigorous R&D on elucidation of the superconducting mechanism and exploration of new superconductors.

The National Research Laboratory of Metrology (NRLM) has reported a study on the application of high Tc superconductors to a mixer. High performance mixers do not only permit simplification of a frequency measurement system, but also permit dramatic progress in synthesis and branching.

The construction of the mixer is simple, consisting of 2mm long needle-like tungsten wire having a diameter of 25μm. The needle-like wire is installed vertically against a single crystal of Bi or Y system high Tc single crystal. The mixer can detect a 10MHz beat signal.

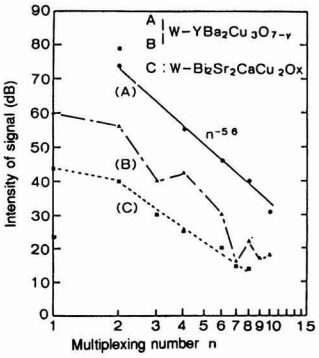

Fig. 1. Relation between multiplexing number vs intensity of beat signals

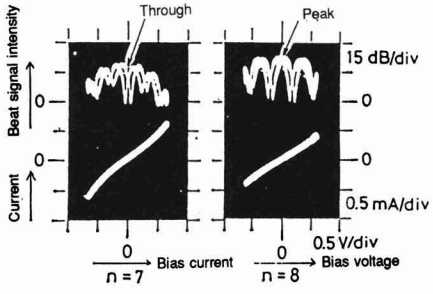

Fig. 2. Dependency of beat signal intensity on bias current and bias voltage

Abstracts of Articles on Ceramics from the Selected Journals of the Academic Societies

TETSU_TO_HAGANE
Vol.77, No.3, 1991
p.361-368

O, P and S Distribution Equilibria between Liquid Iron and $CaO-Al_2O_3-Fe_tO$ Slag Saturated with CaO

Shiro BAN-YA, *Mitsutaka* HINO, *Atsushi* SATO and *Osamu* TERAYAMA

Equilibrium oxygen, phosphorus and sulphur distribution between liquid iron and $CaO-Al_2O_3-Fe_tO$ slag saturated with CaO has been studied at the temperature range from 1 550 to 1 650°C in order to know the applicability of the slag to secondary refining of steel and the approximate validity of the regular solution model for the aluminate slag.

As the results, it is guessed that CaO saturated $CaO-Al-_2O_3-Fe_tO$ slag would be useful the secondary refining of steel. It was confirmed that regular solution model was satisfied for oxygen distribution between liquid iron and aluminate slag as well as that between liquid iron and silicate or phosphate slag in our previous work. Sulphur distribution ratio and sulphide capacity of the aluminate slag were determined as the function of slag composition and temperature.

Key words: secondary steelmaking; ladle metallurgy; slag; physical chemistry; oxygen distribution; dephosphorization; desulphurization; aluminate slag; sulphide capacity; regular solution model.

TETSU_TO_HAGANE
Vol.77, No.3, 1991
p.391-397

Dynamic Wearing Test for Magnesia-Carbon Refractories Using Induction Furnace

Akio IKESUE, *Jhouki* YOSHITOMI and *Hiroshi* SHIKANO

The chemical corrosion (static wearing condition) and the mechamo-chemical corrosion (dynamic wearing condition) on magnesia-carbon refracrories were investigated by a high capacity induction furnace. In comparison with respective experiments, the specimens after dynamic wearing had large wearing rates and showed specific corrosion mechanism on microscopic observation. The corrosion resistance of specimen was determined by base material of refractories under static wearing condition. Through dynamic wearing condition, it was possible to mention that the corrosion resistance has influenced by both factors as base matetial and hot modulus of rupture.

Key words: steel making; refractory; corrosion; abrasion; erosion; simulation.

Zairyo-to-Kankyo
Vol.40, 1991
p.96-102

Forms of Corrosion of Sintered Silicon Nitride Ceramics in Aqueous Environment at High-Temperatures and Pressures*

Tetsuo Yoshio** and Kohei Oda***

** Department of Engineering Science, Faculty of Engineering, Okayama University
*** Department of Industrial Chemistry, Yonago National College of Technology

Pressureless-sintered Si_3N_4 with additives (Y_2O_3-Al_2O_3 and MgO) prepared with imide decomposed Si_3N_4 powder was severely corroded in water at high-temperature and pressure (300°C and 8.6 MPa), resulting in weight loss and formation of corrosion product layer. The purpose of this work is to correlate the formation of corrosion product to the formation of pits and discuss on an aqueous corrosion pit as the fracture origin. After removal of corrosion product by ultrasonic cleaning in water bath, pits up to about 100 μm in diameter were found distributed over the Si_3N_4 surface. Pit features in these sintered Si_3N_4 are different depending on the species of oxide additives; Si_3N_4 with Y_2O_3-Al_2O_3 forms deep pits with a thin protective corrosion product layer and that with MgO forms shallow pits with a thick non-protective corrosion product layer. This result in higher corrosion resistance for the former than the latter. Based on these results, schematic model for pitting corrosion of Si_3N_4 was proposed. The results also suggest that aqueous corrosion attack is practically important because it can lead to a strength degradation of engineering ceramics.

Key words: Si_3N_4 ceramics, aqueous corrosion, high-temperature and pressure, pitting corrosion, oxide additives, corrosion product, strength degradation

Japanese Journal of Applied Physics
Vol. 30, No.2, Feb., 1991
p.246-250

Superconductivity of $YBa_2Cu_3O_{7-x}$ by Addition of Reactive Fine Powders

Takenobu SAKAI, Kozi NISHIO, Naoyuki OGAWA, Izumi HIRABAYASHI and Syoji TANAKA

Superconductivity Research Laboratory, ISTEC, 2-4-1 Mutsuno, Atsuta-ku, Nagoya 456

We report a new method for introducing pinning centers by partial melting processing using reactive fine powders, such as SiC, SiO_2, Al_2O_3, and ZrO_2. Since this method lowers processing temperature, it may become a useful technique for the production of high-J_c metal-sheathed tapes and wires. YBCO powders were mixed with 25 mol% SiC powder of 0.3 μm, sintered at 980°C for 15 min and cooled at 3°C/h under flowing oxygen gas. The obtained samples show prominent grain growth and reacted phases (Y_2BaCuO_5, Ba_2SiO_4) which are of submicron size and uniformly dispersed in the YBCO matrix. Magnetic measurements show the improvement of the critical currents (over 7500 A/cm^2 at 77 K 0.04 T), and the sample shows the so-called fishing behavior at 77 K. It seems that the reacted phases (Y_2BaCuO_5, Ba_2SiO_4) work as effective pinning centers.

KEYWORDS: high-T_c superconductors, critical current density, flux pinning

Japanese Journal of Applied Physics
Vol. 30, No.2, Feb., 1991
p.251-257

Growth, Structure and Properties of $La_{2-x}Sr_xNiO_4$ (x=0 to 0.3) Single Crystals

Wen-Jye JANG and Humihiko TAKEI

Institute for Solid State Physics, the University of Tokyo, Roppongi, Minato-ku, Tokyo 106

Large, homogeneous single crystals of $La_{2-x}Sr_xNiO_4$ (x=0, 0.1, 0.2, 0.3) of 7 mm in diameter and 20 mm in length have been obtained by using a lamp-image type floating-zone furnace under oxygen atmosphere. The chemical and X-ray diffraction analyses reveal the presence of excess oxygen with a presumed form of peroxide ion in the crystals of x=0 and 0.1. Small magnetic susceptibility and obvious deviation from the Curie-Weiss law are observed, whereas the diamagnetic signals from superconductivity are not detected on heating from 4 K to 300 K. The resistivity is semiconductive at room temperature and becomes insulative below 100 K.

KEYWORDS: $La_{2-x}Sr_xNiO_4$ (x=0 to 0.3), FZ single crystals, magnetic and electrical properties, superconductivity, excess oxygen

Japanese Journal of Applied Physics
Vol. 30, No.2, Feb., 1991
p.258-262

Characteristics of the Switching in a Superconducting Y-Ba-Cu-O Thin Film by Laser Irradiation

Keizo KATO, Kuniharu TAKAHASHI†, Kazuo MINAMI, Noriki HAYASHI††, Shigeru OKUDA††, Satoshi TAKANO††, Mieko OHTSUKA††† and Mitsuru AWANO††††

Department of Electrical and Electronic Engineering, Faculty of Engineering, Niigata University, 8050, Ikarashi 2-no-cho, Niigata 950-21
†*Graduate School of Science and Technology, Niigata University, 8050, Ikarashi 2-no-cho, Niigata 950-21*
††*Osaka Research Laboratories, Sumitomo Electric Industries Ltd., 1-1-3, Shimaya, Konohana-ku, Osaka 554*
†††*Experimental Center for Very Low Temperature and Energy Technique, Tokyo Institute of Technology, 2-12-1, O-okayama, Meguro-ku, Tokyo 152*
††††*Department of Mechatronics, Faculty of Engineering, Tokyo Engineering University, 1404-1, Katakura-cho, Hachiohji, Tokyo 192*

Radiation-induced switching of a Y-Ba-Cu-O thin film sample is studied using a 1.06 μm pulsed Q-switched Nd:YAG laser with a duration of 10 ns. The results of the switching from the super- to normal conducting states in our sample caused by laser irradiation are attributed to a bolometric effect, i.e., heating of the sample by radiation. The response time of the switching is less than 30 ns and it almost agrees with the relaxation time of the thermal conduction in the film. Using a simple model assuming uniform distribution of energy through the film thickness, the specific heat of the film is also estimated and a clear jump in the specific heat at the critical temperature is shown.

KEYWORDS: Y-Ba-Cu-O, superconducting thin film, switching, optical response, bolometric effect, specific heat, laser irradiation

Japanese Journal of Applied Physics
Vol. 30, No.2, Feb., 1991
p.263-273

Structure-Parameter Dependence of Modality of Macroscopic Quantum Effect in Superconductor Junction (II) —Linked Junction—

Masanori SUGAHARA and Nobuyuki YOSHIKAWA

Faculty of Engineering, Yokohama National University, Tokiwadai 156, Hodogaya, Yokohama 240

Quantum behaviors of linked junctions of superconductor and normal metal are theoretically studied with the following results. They are classified into two types: type 1 with normal conductance $G > G_c$ and type 2 with $G < G_c$, where G_c is the critical conductance. Ideal models of type 1 and type 2 are, respectively, prescribed with a set of parameters ($g_p \gg 1$, $g_s = 1$) and ($g_p = 1$, $g_s \gg 1$), where g_p (parallel mode number) is the number of electronic quantum modes over the cross section of the link and g_s (series mode number) is the number of loss oscillators (phonons or photons) which perform energy-exchange interaction with a transitting electron. In the case of superconductor junctions, type 1 shows the Josephson effect and type 2 shows the PQT effect (duality of Josephson effect). The PQT effect is also expected in some normal type 2 junctions.

KEYWORDS: macroscopic quantum effect, coherent state, superconducting linked junction, weak link, Josephson effect, PQT effect, phase quantum tunneling (PQT)

Japanese Journal of Applied Physics
Vol. 30, No.2, Feb., 1991
p.274-279

Boron Ion Doping Effects on Superconductivity of $YBa_2Cu_{3-x}B_xO_{7-y}$ Ceramics

Hiroshi KATSURA*, Takasu HASHIMOTO and Yasutaka SUEMUNE†

Department of Applied Physics, Tokyo Institute of Technology, Ohokayama, Meguro-ku, Tokyo 152
†Compound Semiconductor Device Division, NTT Electronics Technology Corporation, Morinosato-Wakamiya, Atsugi-shi, Kanagawa 243-01

Impurity effects of small ionic size, light atomic weight boron ions on the superconductivity of $YBa_2Cu_3O_{7-y}$ are investigated. The doped boron content x is from 0.00 to 0.52 in $YBa_2Cu_{3-x}B_xO_{7-y}$ as a nominal composition, and the ceramic samples fired in air or annealed in high-pressure oxygen gases are examined with X-ray diffraction, dc electrical resistivity, and ac magnetic susceptibility. The crystal lattice is found to shrink due to the boron doping and to deform from orthorhombic to tetragonal form for values of x of more than about 0.2. Superconductivity is found to be modified by the partial B^{3+} replacement for Cu(1) ions so as to lower the critical temperature T_c and to broaden the transition width. Change from metallic behavior to semiconductive behavior is accompanied by the boron incorporation of x above 0.30 in the normal electrical conduction states. Steep transition is revealed on the high-pressure oxygen gas annealed samples.

KEYWORDS: superconductivity, high-T_c oxide, impurity effects, lattice constants, Meissner effect

*Present address: Sumitomo Electric Industries, Yokohama.

Japanese Journal of Applied Physics
Vol. 30, No.2, Feb., 1991
p.280-281

Variation of Transport Properties with Density of $YBa_2Cu_{3-x}M_xO_{7\pm y}$ ($M=Ti^{4+}$, V^{5+}, Cr^{3+} or Mn^{4+} and $x=0.0$–0.1 g atom)

P. Umadevi MURALIDHARAN and A. D. DAMODARAN

Regional Research Laboratory (CSIR), Trivandrum 695 019, Kerala, India

The effect of the sintered density on the transport properties like normal state resistivity, T_c (superconducting transition temperature) and absolute thermopower has been studied for doped YBCO ($YBa_2Cu_{3-x}M_xO_{7\pm y}$, where $M=Ti^{4+}$, V^{5+}, Cr^{3+} and Mn^{4+} and $x=0.0$–0.1 g atom). The sintered density of the sample depends on the valency of the substituent. The density increases in the order pure YBCO < Cr^{3+} doped YBCO < Ti^{4+} doped YBCO < Mn^{4+} doped YBCO < V^{5+} doped YBCO. The resistivity as well as absolute thermopower decreases with increasing density. The significance of these results for the technological applications of granular superconductors is briefly discussed.

KEYWORDS: Y-Ba-Cu-oxide, doped YBCO, sintered density, resistivity, absolute thermopower

Japanese Journal of Applied Physics
Vol. 30, No.2, Feb., 1991
p.L272-L275

Effect of Reduction on Superconductivity and Electronic State of Nd-Ce-Cu-O System

Yuko YOKOYAMA, Toshikazu KATAYAMA, Hiroyuki OYANAGI, Yuichi HASUMI† and Yoshikazu NISHIHARA

Electrotechnical Laboratory, Tsukuba, Ibaraki 305
†Faculty of Science & Technology, Meiji University, Kawasaki 214

The effect of reduction on the superconductivity and electronic state of $Nd_{2-x}Ce_xCuO_{4-\delta}$ has been investigated by measurements of the magnetization and X-ray absorption near-edge structure of the Cu K-edge for specimens annealed at various oxygen pressures and temperatures. The superconducting onset temperature and diamagnetization increase with decreasing oxygen partial pressure of annealing. We find that the electron density estimated from the edge shift of the Cu K-edge absorption increases with the increase in the degree of reduction and that the magnitude of superconductive diamagnetization becomes constant above a certain degree of reduction. It is concluded that the electron density beyond a certain critical value is necessary for the occurrence of the superconductivity in this system.

KEYWORDS: superconductor, $Nd_{2-x}Ce_xCuO_{4-\delta}$, magnetization, X-ray absorption

Japanese Journal of Applied Physics
Vol. 30, No.2, Feb., 1991
p.L276-L279

Cryogenic Scanning Tunneling Microscopy and Spectroscopy on the Cleaved Surface of Bi-Sr-Ca-Cu-O Down to 4.2 K

Tetsuya HASEGAWA, Masashi NANTOH and Koichi KITAZAWA

Department of Industrial Chemistry, University of Tokyo, Bunkyo-ku, Tokyo 113

Atomic resolution has been achieved by a scanning tunneling microscopy (STM) system for the first time on an oxide superconductor at cryogenic temperatures. The atomic corrugation with a periodicity of 0.35 nm and the modulation along the *b*-axis with a superlattice periodicity of about 2.7 nm have both been clearly observed on the cleaved *a-b* plane of a Bi-Sr-Ca-Cu-O single crystal. Furthermore, it is found that some features of the spectrum, including the shape of the superconducting gap, depended significantly on the distance between the probe tip and sample surface. Wide scattering of the results so far reported for various types of tunneling methods can be interpreted in terms of this distance dependence of the tunneling spectrum. We conclude that the superconducting gap structure in the spectrum is by far different from the prediction of the BCS weak-coupling theory.

KEYWORDS: cryogenic STM, Bi-Sr-Ca-Cu-O, high-temperature superconductor, tunneling spectroscopy, superconducting gap

Japanese Journal of Applied Physics
Vol. 30, No.2, Feb., 1991
p.L298-L301

Processing of Perovskite $Pb(Zn_{1/3}Nb_{2/3})O_3$ by Hot Isostatic Pressing and Its Dielectric Properties

Takamitsu FUJIU, Akira TANAKA and Tadashi TAKENAKA†

Opto-electronic Materials Laboratory, Nikon Corporation, 1-10-1 Asamizodai, Sagamihara, Kanagawa 228
†Faculty of Science and Technology, Science University of Tokyo, Noda, Chiba 278

Perovskite $Pb(Zn_{1/3}Nb_{2/3})O_3$ (PZN) was obtained by first fabricating pyrochlore PZN ceramics and then converting pyrochlore to perovskite using HIP. PZN ceramics containing as much perovskite as 96% were fabricated under 200 MPa at 1150°C for 1 h. The electromechanical coupling factors and the piezoelectric constants were lower than expected, probably due to the low relative density of the specimen measured.

KEYWORDS: lead zinc niobate, perovskite, pyrochlore, hot isostatic pressing, dielectric constants, electromechanical coupling factors, piezoelectric constants

Journal of Physical Society of Japan
Vol.60, No.2, 1991
p.384-386

Uniaxial Stress Effect on the Superconductivity of Grain-Aligned Composites of $La_{2-x}Sr_xCuO_4$

Yuichi MOTOI, Katsumi FUJIMOTO, Hiromoto UWE and Tunetaro SAKUDO

Institute of Applied Physics, University of Tsukuba, Tennoudai 1-1, Tsukuba, Ibaraki 305

The uniaxial stress effect on the superconductivity of grain-aligned samples of $La_{2-x}Sr_xCuO_4$ prepared by a "magnetic-field-induced alignment" method has been investigated. The T_c decreases with increasing uniaxial stress along the "c-axis". The result indicates that the in-plane O–O or Cu–O bond length should significantly affect its superconductivity.

[$La_{2-x}Sr_xCuO_4$, uniaxial stress effect, superconductivity, magnetic-field-induced alignment, grain-aligned composite, bond length, Cu–O plane]

Bibliographic Information

1. Title	Journal of Ceramic Society of Japan, International Edition	ISSN : 0912-9200
2. Frequency	Monthly	1 volume per year (No.1 Jan. - No.12 Dec.)
3. Volume No.	100	
4. Cover data of (Vol. 95, No1)	January 1987	Vol.95 No.1 is the first Issue of English version
5. Index of contents	Given annually	bound in
6. Size	21cm×29.7cm	1700 pages per annum
7. Subscription rates (Air speed)	¥200,000	(12 issues)

ORDER FORM

To: Circulation Div., the Journal of Ceramic Society of Japan, International Edition
c/o Fuji Technology Press Ltd.
Daini Bunsei Bldg., 1-11-7 Toranomon
Minato-ku, Tokyo 105, Japan

Date: _____

Please enter my subscription to the **Journal of Ceramic Society of Japan, International Edition**
(for _____ copy/ies)

Name: _____
Position: _____
Address: _____
Signature: _____

☐ Payment enclosed
(Payment by credit card is preferred)

☐ Bill me
Air speed ¥200,000

Attention: Please indicate our ref. No.(AUTO, TEC, TECJ, CER, ROB, ...) when you make the remittance.
All subscriptions can be paid in advance through any of the following methods.

1) Charge my:
☐ AmEx ☐ Visa ☐ MC
Card No. . . . . .Exp. Date . . . . . .
Mr/Mrs./Ms. . . . . .
Address . . . . . .City . . . . . .
Zip code . . . . . .Country . . . . . .
2) Transfer to Fuji Technology Press Ltd A/C No.10667 Fuji Bank Toranomon Branch, Minato-ku Tokyo
3) Bank Draft
4) Transfer to Fuji Gijyutsu Shuppan K.K.(Fuji Technology Press Ltd.) A/C No. Tokyo 7-145130, Postal Saving

Attention!!

You are now able to make remittance by credit card!
You can enter subscriptions with only your name, card number and its expiry date. No bank charge nor preparation of Japanese yen bank draft is necessary.

What is the English Monthly Journal TECHNO JAPAN?

It is a professional international periodical designed to cater to people in a wide variety of key industrial and government positions. Its carefully selected contents, including complete reports, for example, on the current status and new developments in Japanese industry and technology, are tailored to meet the information needs of specialists all over the world. Each news article includes an expert's commentary based on in-depth data analysis and also incorporates sufficient data to enable readers to make their own independent judgements on various issues and topics. Techno Japan is a monthly journal whose reports contain information indispensable for those overseas specialists who keep track of current conditions and must project future Japanese and international economic and industrial trends. It is the most authoritative source of information about the most recent technological advances in virtually all fields of industry.

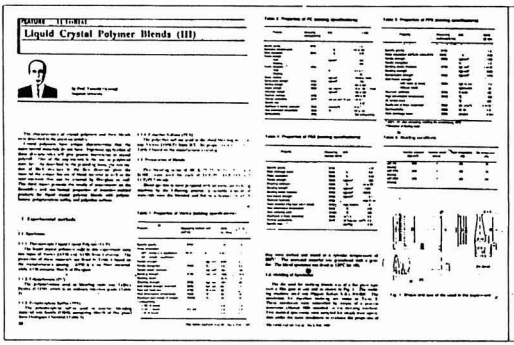

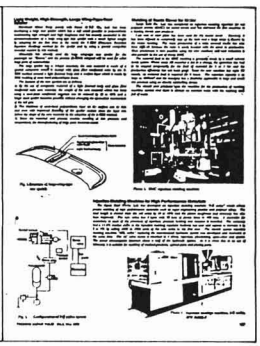

Contents of TECHNO JAPAN

Industrial & Technological News Articles

Every issue of Techno Japan contains more than 300 pieces of information.

News articles are classified as follows:

Basic Industries:	*Energy, Steels & Metals, Ceramics & Materials Science, Superconductivity*
Machinery Indu	*Miscellaneous Machines, Precision Engineering & Fine Finishing, Factory Automation, Transportation & Materials Handling*
Electronics Industries:	*Electronic Devices, Telecommunications, Information Processing, Home Automation & Broadcasting, Electronics Instruments, Medical Engineering, Electronic Machine Manufacturing & Assembly*
Chemical Industries:	*Chemicals, Polymers, Biotechnology*

Disaster Prevention, Agribusiness Systems Industries:

Feature Articles

Long, highly informative feature articles of crucial interest to overseas governments and industries appear each month. As many as 55 pages in one issue may be devoted to such important and fascinating articles which enlarge the depth and breadth of readers' knowledge about subjects of current interest. Such high news value feature articles are carried individually or in a series.

Economic Report and Statistics

Techno Japan's economic report and statistics is officially provided by the Economic Planning Agency. These reports help to promote mutual understanding among various nations.

Research Institutes in Japan

TECHNO JAPAN *FUJI TECHNOLOGY PRESS LTD.*
Daini Bunsei Bldg., 11-7, Toranomon 1-chome, Minato-ku, Tokyo 105, Japan.